Experimental Investigation of Advanced Film Cooling Schemes for a Gas Turbine Blade

Mohamed Gaber Ghorab

A Thesis

in

The Department

of

Mechanical and Industrial Engineering

Presented in Partial Fulfillment of the Requirements
for the Degree of Doctor of Philosophy (Mechanical Engineering) at
Concordia University
Montreal, Quebec, Canada

December 2009

Your file Votre référence
ISBN: 978-0-494-67349-2
Our file Notre référence
ISBN: 978-0-494-67349-2

Abstract

Experimental Investigation of Advanced Film Cooling Schemes for a Gas Turbine Blade

Mohamed Gaber Ghorab Ph.D.

Concordia University, 2009

Advanced cooling techniques are essential for further improvement in the efficiency and the power output of gas turbines. Turbine inlet temperatures of 1900 K are typical of current gas turbines, and there is an interest in increasing the temperatures for the next generation of gas turbine engines. Over the past decades, significant effort has been devoted to increase the turbine efficiency and to develop effective cooling strategies to maintain the blade temperature below the melting point of the alloys used to construct the airfoils. As a result, various cooling strategies have been developed such as film, impingement, and muti-pass cooling for the blades, and evaporative cooling for the inlet air.

In this work, a state-of-the-art thermal turbomachinery test rig was designed and constructed to investigate the film-cooling performance of advanced film cooling schemes over a flat plate. Designing and constructing mechanical parts, as well developing software codes (Labview and image processing) for transient film cooling measurement was the foremost part of the current experimental work. The thermochromic liquid crystal (TLC) technique was used to measure wall surface temperature. A circular film hole was used to validate the current experimental technique and methodology. The validation results showed that the current experimental technique and methodology were deemed reliable.

Subsequently, the film cooling performance of the louver and new hybrid schemes were investigated, experimentally. The louver scheme was proposed by Pratt and Whitney Canada (PWC) to allow the cooling flow to pass through a bend and to encroach an airfoil material (impingement effect), then exit to the outer surface of the airfoil through a designed film hole. Immarigeon and Hassan (2006) then Zhang and Hassan (2006) numerically investigated the film cooling effectiveness performance of the louver scheme. The hybrid scheme was proposed in the current study, which includes two consecutive film hole configurations with interior bending. The cooling performances for the two advanced schemes have been analyzed experimentally over a flat plate across blowing ratios of 0.5, 1.0 and 1.5 at a density ratio of 0.94. The results showed that the louver and the hybrid schemes enhanced the local and the average film cooling performance in terms of film cooling effectiveness, and the net heat flux reductions are better than other published film hole configurations. In addition, both schemes provided an extensively wide spray of secondary flow over the outer surface, and thus enhanced the lateral film cooling performance over the downstream surface area. Moreover, the two schemes produced an average heat transfer coefficient ratio near unity at low and high blowing ratios. As a result, the louver and the hybrid schemes are expected to reduce the temperature of the outer surface of the gas turbine airfoil and to provide superior cooling performance, which increases airfoil lifetime.

In addition, the adiabatic film cooling performance and flow characteristics for the hybrid scheme were investigated numerically. The numerical investigation was analyzed across blowing ratio of 0.5, 1, and 2. The flow structures of the hybrid scheme are presented at different blowing ratios to provide a better physical understanding. The

results showed that the hybrid scheme directed the secondary flow in the horizontal direction and reduced the jet liftoff at different blowing ratios. Finally, conjugate heat transfer (CHT) and film-cooling analyses were performed to investigate the hybrid scheme performance with different flow configurations. Different geometries of parallel flow and jet impingement with different gap heights as well as the adiabatic case study were investigated at blowing ratios of 0.5 and 1.0. The results showed that the adiabatic case provided downstream centerline superlative cooling performance near the hybrid film hole exit compared to other conjugate geometries studied. At the downstream location, the impingement configuration with a large gap height provided the highest downstream performance at blowing ratio of 0.5 and 1.0 with respect to other cases studied. Moreover, the downstream film cooling performance was enhanced far along the spanwise direction for the CHT cases studied and it has the highest value near the scheme exit for parallel configuration. In addition, the impingement configuration enhanced the upper stream cooling performance compared to parallel flow and it was further enhanced for large gap heights.

Keywords: film cooling effectiveness, heat transfer coefficient ratio, louver, hybrid, TLC, NHFR, CHT.

Acknowledgments

Praise be to GOD, who gave me the success to finish my thesis.

Completing the work presented in this thesis would not have been possible without the help and support of a number of people. My deepest appreciation and gratitude go to my supervisor and mentor, Professor Hassan, who has been my source of guidance and support at every step of my degree program. I am also grateful to Pratt and Whitney Canada (PWC) and NSERC for their financial support. Specially thanks to Mr. Terry Lucas for his input and support.

I thank my family members, especially my mother, sister and brother, as well as Fred and Inge for their moral support and their encouragement during my studies. My wife deserves heartfelt thanks for standing by my side throughout my degree program as does the little princess who has recently brought her light into my life, my sweet daughter Tasnim.

Also, I would like to thank my research colleagues including Dr. R. Muwanga, X., Zang, P., Phutthavong, T., Ahmed., Dr. W. Saleh., and M.D. Rahman., as well as the present research group members, R., Bowden, A., Megahed, T., Elnady., K., Cook and Y. Fan. My deepest appreciation to MIE Admin. and Tech. staff for their help including Dan, Henry, Leslie, Sophie, Maureen and Arlene.

Table of Contents

List of Figures

List of Tables

Nomenclature

Symbols

Br	blowing ratio ($\rho_j u_j / \rho_m u_m$)
Cp	specific heat at constant pressure (J/kg.K)
d	film hole diameter (m)
D_h	hydraulic diameter (m)
Dr	density ratio (ρ_j / ρ_m)
F_n	Frossling number = $Nu/\sqrt{Re_{Dh}}$
H	gap height (m)
h	heat transfer coefficient (W/m^2 K)
H^*	dimensionless gap height (H/d)
Hue	hue color component
I	momentum flux ($\rho_j u^2_j / \rho_m u^2_m$)
k	thermal conductivity (W/m K)
L	length of film hole offset distance (m)
L^*	dimensionless length of offset distance (L/d)
Nu	Nusselt number (hD_h/k)
P	film hole pitch
p	flow pressure (N/m^2)
P^*	non-dimensional pressure ($P^* = p/ \rho U^2_m$)
Pr	Prandtl Number ($\mu C_p /k$)
q	heat transfer flux (W/m^2)
R	reference coordinate (x,y,z)
Re	Reynolds number ($\rho U_m D_h / \mu$)

St	Stanton Number (Nu/RePr)
T	temperature (K)
t	time (s)
T^*	temperature ratio at constant pressure (ρ/ρ_m)
T.K.E.	turbulence kinetic energy (m^2/s^2)
Tu	turbulence intensity $\sqrt{2/3*k}/U_m$
U	normal velocity in x direction (m/s)
u ,v,w	velocity components (m/s)
Vr_x	velocity ratio in x direction (u/U_m)
Vr_y	velocity ratio in y direction (v/U_m)
Vr_z	velocity ratio in z direction (w/U_m)
W	cross section width (m)
x,y,z	coordinates
y^+	non-dimensional wall distance ($\rho u_\tau y/\mu$)

Greek symbols

$\bar{\alpha}$	thermal diffusivity (m^2/s), ($k/\rho Cp$)
μ	dynamic molecular viscosity (kg/m.s)
α	injection (or inclination) angle for first stage holes
ε	least square error
η	local film cooling effectiveness $[(T_f-T_m)/(T_j-T_m)]$.
η_{aw}	local adiabatic film cooling effectiveness, $(T_{aw}-T_m)/(T_j-T_m)$
η_{av}	averaged film cooling effectiveness $=(\bar{T}_w-T_m)/(T_j-T_m)$).
η_c	non dimensional temperature $(T_w-T_m)/(T_j-T_m)$.

θ	non-dimensional surface temperature $(T_m-T_j)/(T_m-T_w)$.
ρ	density (kg/m^3)
τ	time step (s)
φ	over all film cooling effectiveness in the practical engine $=1/\theta$

Subscripts and superscripts

m	free mainstream conditions
av	average
aw	adiabatic wall
c	centerline
e	refers to exit
f	refers to film
i	initial
j	refers to jet
o	without film cooling
s	solid
w	refers to wall

Abbreviations

ACFM	actual cubic feet per minute (CFM)
AFH	arrowhead fanshaped hole
CDH	conical diffused hole
CHT	conjugate heat transfer
CYSA	cylindrical simple angle
DAQ	data acquisition system
DJFC	double jet film cooling
FDCA	forward diffused compound angle
FDSA	forward diffused simple angle
HSV	hue saturation value
HTC	heat transfer coefficient
HTCR	heat transfer coefficient ratio
LDCA	lateral diffused compound angle
LDSA	lateral diffused simple angle
NHFR	net heat flux reduction
PSP	pressure sensitive paint
RGB	red, green, blue
ROI	region of interest
SCFM	standard cube feet per minute
TLC	thermochromic liquid crystal

Chapter 1

Chapter 1 Introduction

Gas turbines play a major role in modern aeronautical propulsion and power generation. A key parameter that greatly affects the design characteristics of turbine engines is efficiency, or thrust to weight ratio. One of the main factors affecting efficiency is the gas turbine inlet temperature. Increasing the inlet temperature increases the efficiency; however, the properties of the turbine blade alloys limit the maximum allowable temperature. Through the development of advanced materials and cooling schemes, high turbine inlet temperatures above 2500 K can be adopted. The airfoil of gas turbines should be cooled sufficiently for safe operation and for long-term durability and reliability. Therefore, over the past decades, many studies have devoted significant efforts to the development of effective cooling schemes. Internal convection, jet impingement, and external film cooling or their combinations are available cooling techniques applied to turbine airfoil cooling. Internal cooling occurs where secondary cooling air passes through internal flow passages, which decreases the material temperature of the airfoil by conduction. Film cooling occurs by injecting the cooling air from tiny holes onto the airfoil surface, which forms a thin thermal insulation against hot gases.

1.1 Motivation

Advanced film cooling techniques are vital to increase cooling performance, thus increasing the gas turbine efficiency and thrust–to-weight ratio. Throughout the last three decades, film-cooling strategies have been developed to maintain an airfoil temperature below the alloy melting point. Film hole geometries play a very important role in

enhancement film cooling over a turbine airfoil surface. Different film hole shapes were designed with different exit shapes and configurations in order to provide a uniform momentum injection and reduce the jet lift-off, hence enhancing the coolant spray over the airfoil surface (Taslim et al., 2005; Zhang and Hassan, 2006; Miao et al., 2006; and Dhungel et al., 2007). Consequently, creating new film hole geometry is one of the major methods to improve airfoil cooling performance and reduce aerodynamic losses, thereby increasing the gas turbine efficiency and power output. Pratt and Whitney Canada (PWC) proposed a novel impingement film cooling scheme to prevent jet lift-off for the coolant flow with respect to standard round holes, hence improving the film cooling performance (Immarigeon and Hassan, 2006). The anti vortex hole is another advanced technique for round shaped film cooling. It has anti vortex branched holes which provide good results for covering coolant flow over the surface. The original idea for anti vortex film holes was established at NASA Glenn Research Center (Dhungel, et al., 2007).

Creating and developing new film hole geometries is the approach taken to improve film cooling performance since other parameters are still restricted from film cooling applications under actual operating conditions. Advanced hybrid and louver film cooling schemes are employed throughout the present experimental work. In addition, the hybrid scheme is simulated to investigate the adiabatic flow structure and film cooling effectiveness performance at different blowing ratios. Afterwards, the conjugate heat transfer is combined with film cooling effectiveness to investigate the cooling performance of the hybrid scheme with different flow configurations. The cooling performance of the proposed scheme for the parallel flow configuration and impingement jet with different gap heights will be evaluated.

1.2 Objective and organization

Based on the literature review in Chapter 2, advanced cooling schemes are essential for the next generation of gas turbine engines. The experimental and computational studies using advanced film-cooling schemes have been tested over a flat plate. The novel schemes (louver and hybrid) allow optimization of the cooling effectiveness by enabling less jet lift-off at the exit of the cooling holes and wide downstream lateral spreading. The principal objective of this study is to experimentally investigate the film cooling effectiveness and the heat transfer coefficient performance of the two schemes. The Thermochromic Liquid Crystal (TLC) technique is used to provide global surface temperature measurements over the target surfaces downstream of the film cooling holes. In addition, the performance of the hybrid scheme and the understanding the flow structure will be investigated numerically. The film cooling effectiveness performance of the hybrid scheme with conjugate effect for different flow configurations will then be presented through this study.

The following are the specific objectives through the current study are:

1. To design and construct hardware and automated data acquisition systems for a state-of-the-art thermal turbomachinery test rig using Thermochromic Liquid Crystal technique.
2. To develop the software codes for labview, image processing, solving nonlinear data reduction equations and posting data.
3. To validate the test rig for film cooling effectiveness and heat transfer coefficient and to investigate the film cooling and heat transfer coefficient performance of the louver

over a flat plate then compare its performance with other advanced published film hole geometries.

4. To investigate the cooling performance of the hybrid cooling schemes over a flat plate under different blowing ratios and compare results with other film hole configurations at different blowing ratios.
5. To Investigate the cooling performance analysis of the hybrid cooling scheme by combining the film cooling and conjugate heat transfer values for different flow configurations at low and high blowing ratios.

The thesis consists of seven chapters. This chapter presents the motivation and objective of the current study. Chapter two will cover the literature review regarding the effect of design and operating parameters on film cooling effectiveness and heat transfer coefficient performance for gas turbine applications. At the end of the literature review, a summary will be provided for the effect of different operating conditions and advanced published film hole geometries on the film cooling performance. The thermal turbomachinery test rig will be described entirely in chapter three. The test rig has been built to investigate the film cooling effectiveness and heat transfer coefficient performances of different film hole geometries on flat plates and airfoil surfaces for gas turbine applications. The description of the design, construction, and development of the mechanical, instrumentation, and automated data acquisition systems will be clarified in Chapter three. In addition, this chapter will be closed by a discussion of the uncertainty analyses, experimental procedure and validation study. Chapter four will include the output performance results of the louver scheme investigation across blowing ratios of 0.5 to 1.5, at a density ratio of 0.94. The chapter will close with a

summary of louver scheme film cooling and heat transfer performance. Furthermore, chapter five will cover the performance of film cooling effectiveness and heat transfer for the new hybrid scheme, which will analyze experimentally for blowing ratios of 0.5 to 1.5, at a density ratio of 0.94. Later, the performance of the scheme will compare with other film cooling configurations, followed by a conclusion of the cooling performance of the hybrid scheme.

Chapter six will discuss the adiabatic film cooling performance and flow structure of the hybrid scheme compared to the circular hole at low and high blowing ratios. Afterward, a three-dimensional conjugate heat transfer model will be presented to investigate the hybrid scheme performance by including the conjugate heat transfer in addition to film cooling for parallel and impingement flow configurations with different gap heights. The summary of the adiabatic and conjugate film cooling performance for numerical study will be presented at the end of Chapter six. A conclusion of the current work and recommendation for future studies will be presented in Chapter seven.

Chapter 2

Chapter 2 Literature Review

The cooling process of gas turbine airfoils (nozzle vanes and blades) has been studied computationally and experimentally. The aim of film cooling is to create thermal protection over the airfoil surface and to keep the coolant flow attached to the surface. For a better understanding of the complex mixing flow and heat process, film cooling should be investigated by studying the mixing phenomena of the main and secondary flows. The outcome objective of this study is to propose the best possible cooling schemes. The current literature review will focus mainly on experimental and numerical studies for different film cooling schemes over either a flat plate or an airfoil surface, and their effect on the performance of film cooling effectiveness and heat transfer coefficient. In addition, the effect of operating parameters such as blowing ratio, density ratio, turbulence intensity, and surface roughness on adiabatic film cooling effectiveness and heat transfer performance will be presented. Finally, the literature review will demonstrate previous conjugate heat transfer studies for gas turbine cooling applications.

Measured temperatures and heat transfer coefficients over the surface depend on flow conditions and geometry design parameters. Many studies have been concluded to investigate the effect of film cooling design parameters on a flat plate and on scaling up actual airfoils, as well as using a flow conditions close to the actual gas turbine engine. The results are presented and correlated in dimensionless groups such as Reynolds number, Nusselt number, Stanton number, blowing ratio, density ratio and temperature ratio as a function of spanwise and downstream distance.

2.1 Effective parameters on adiabatic film cooling effectiveness and heat transfer coefficient

This section presents a survey on the effect of traditional and advanced film cooling hole configurations, operating conditions, and surface finishing on the film cooling effectiveness and the heat transfer coefficient performance over a flat plate and airfoil surface. Studying film cooling over a flat plate is a way to study endwall film-cooling performance, as well as to investigate the effect of different parameters on film cooling and heat transfer coefficient performance. The output results such as heat transfer coefficient, film cooling effectiveness and Nusselt number using a flat plate, can be presented in correlated equations as a function of downstream distance, blowing ratio, density ratio, momentum flux, turbulence intensity, and temperature ratios. These correlated equations for the flat plate test can be applied to actual airfoils under real engine conditions by including other correction factors for real parameters.

The airfoil cooling is applied at different regions such as leading edge, trailing edge, pressure and suction sides, and blade tip. The flow characteristics at each region are completely different with respect to the other regions. Therefore, many researchers studied the effect of design parameters such as film hole configurations and operating conditions at different airfoil regions on film cooling performance. They also considered the rotational effect on the airfoil surface (blade). The flow structure at each region of airfoil has specific optimum parametric study. Therefore, specific film hole configurations should be used for the film holes at each region, such as circular hole at the leading edge, as this area has higher pressure and lower Mach number values.

The investigation of film cooling effectiveness and heat transfer coefficient performance under actual turbine engine conditions is very important. However, these values are difficult to measure as the instruments for measuring temperature and pressure cannot provide acceptable accuracy, especially at high rotational speed. Therefore, the operating conditions are trimmed down. The results were then presented in dimensionless forms. Heat transfer distribution for three-vane cascades under steady state conditions has been studied by Nearly et al. (1985). They investigated the basic parameters: which affect film cooling: Mach number, Reynolds number, turbulence intensity, and wall to gas temperature ratio. By using a large scale model consisting of a complete gas turbine stage, Blair et al. (1989) studied the effect of inlet turbulence, stator-rotor axial spacing and relative circumferential spacing of the first and second stators on heat transfer distribution for an airfoil blade. On the other hand, Martinez-Botas et al. (1995) and Baines et al. (1982) studied the heat transfer characteristics in an annular cascade vane. Ames and Plesniak (1997) simulated a four-vane cascade and moved the turbulence generator close to the vane to generate different levels of turbulence. They discovered from their study that the heat transfer was increased and boundary transition was created earlier on the suction surface by increasing the turbulence levels. Garg and Gaurgler, (1997) investigated the effect of different operating parameters on film cooling performance, such as the blade rotational effect and coolant flow direction from shower-head holes. In addition, Garg and Gaurgler (1997) studied the effect of the coolant to the main stream mass and temperature ratios on film cooling at the hole exit. Later, Garg and Rigby (1998) reported that the heat transfer had a majorly significant effect on the

coolant velocity and temperature approximately 60% on the blade suction side and 50% on the pressure side.

Thermochromic Liquid Crystal and Infrared (IR) Thermography are two techniques used to calculate the film cooling effectiveness and heat transfer coefficient by measuring surface wall temperatures. Ling et al. (2004) developed a new technique for processing transient heat transfer using TLC by considering the effect of conduction in three dimensions, for a single transient test, to measure the local heat transfer coefficient and adiabatic film cooling effectiveness. Vogel et al. (2003) studied the influence of heat flux distributions on film cooling effectiveness by using TLC over four different heater-foil configurations with film cooling holes. Another contribution came from Baldauf et al. (2001), who used the Infrared Thermography technique to measure surface temperature with high resolution and then finite element analysis to obtain the local heat transfer coefficient downstream of a row of cylindrical film holes.

The effect of the design and operating parameters on film cooling and heat transfer coefficient performance are presented in the following subsections:

2.1.1 Advanced film hole geometries

Film hole geometry is one of the most effective parameters that influences the film cooling performance. Early studies used slot configuration to investigate film cooling effectiveness. Goldstein et al. (1974) was one of the first groups that studied adiabatic film cooling using film holes. They investigated the effect of film hole geometry and flow parameters on film cooling performance.

Eriksen and Goldstein (1974) experimentally investigated the effect of the blowing ratio on the centerline film cooling effectiveness for injection film holes having

a 35° inclination angle and lateral expansion angle of 10° at a distance of 1d from the entrance of the film hole, as shown in Fig.2.1a. The film cooling effectiveness along the centerline increased with blowing ratio until a peak value was reached at a particular downstream location, after which it decreased for any increase in blowing ratio. Film holes having 10° lateral expansion angles have significant effects on spreading the secondary flow downstream of the film hole injections. Furthermore, the fan shaped hole decreased the exit velocity of the secondary flow thereby reducing its penetration into the main stream.

Goldstein and Taylor (1982) investigated the regions around the injection hole, which have low and high heat transfer coefficients. The heat transfer coefficient has a higher value on the region between two contiguous holes at high blowing ratios, and decreases at low blowing ratios. Also, it has higher a value at exit regions along the film hole sides due to the interaction between the main and injection flow, which creates eddies and high shear stresses. At high blowing ratios, once the cooling jet partially reattaches to the airfoil surface, the heat transfer coefficient increases; however, it decreases further downstream of the film hole (x/d >10). Later on, Goldstein and Jin (2001) studied the performance of film cooling and the heat transfer coefficient using one row of holes with a 35° inclination, 45° compound angles, 3d hole spacing, and a hole length to diameter ratio of 6.3.

Makki and Jakubowski (1986), and Kohli and Bogard, (1999) found that forward-and-laterally positioned film holes have lower heat transfer coefficients and higher film cooling effectiveness when compared to round holes. Makki and Jakubowski's conclusion arose after comparing the cooling performance for forward-and-laterally expended holes

with circular film hole geometries using a 35° inclination angle and a pitch to diameter ratio of 3. The effect of film hole spacing arrangements (staggered and in line) on film cooling performance was studied by Ligrani et al. (1992). They reported that there was no significant effect of film hole rows on the heat transfer coefficient at low blowing ratios, while at high blowing ratios, the heat transfer coefficient increased with increasing number of film rows. Furthermore, Ligrani et al. (1994) investigated the effect of three different hole configurations on the heat transfer coefficient and film cooling effectiveness; one with a simple angled hole and two with compound angled hole using different pitch to hole diameter ratios. The compound angled hole configuration had a higher film cooling effectiveness than the simple hole due to a large spreading area over the span-wise region. In addition, Sen et al. (1996) investigated the effect of three different compound angles (CA) on the heat transfer coefficient. The first case was a circular hole with a 0° CA, the second hole had a 60° CA in the lateral direction, and third hole had a 15° forward expansion with a 60° CA,. They reported that the heat transfer coefficient is enhanced by increasing the momentum flux for 0° CA and 60° CA. The forward expansion increased the lateral mixing, such that the heat transfer coefficient further increases by increasing momentum flux.

Schmidt et al. (1996) reported that the film cooling performance was small but the heat transfer coefficient was high for compound angle injection at high momentum ratio (coolant to mainstream). The effect of a 45° and 90° compound angle in the span wise direction for holes with a 35° inclination angle in the stream-wise direction, on the heat transfer coefficient was investigated by Ekkad et al. (1997) using TLC technique. The compound angle provides high mixing between the main and jet streams hence the heat

transfer coefficient increases due to the turbulent flow over the surface. Gritsch et al. (1998) investigated the film cooling effectiveness for different shaped holes with 30° inclination angles for a blowing ratio ranging from 0.25 to 2.0 and density ratio of 1.85. From their results, the film cooling performance increases with increasing exit area, leading to a wider spray and the coolant flow remaining attached to the downstream surface. Gritsch et al. (1998) studied the performance of the heat transfer coefficient for the previous geometries, for a 1.85 density ratio at a blowing ratios ranging from 0.25 to 1.75. They noted that the heat transfer coefficient decreased with increasing cross sectional area at the hole exit, consequently reducing the coolant exit momentum. Therefore penetration with main stream flow reduces. Moreover, the heat transfer coefficient is lower at low blowing ratios.

Ligrani et al. (1992) studied the effect of pitch to film hole ratio for staggered configurations (one and two rows) with a 35° inclination angle on adiabatic film cooling effectiveness and Stanton number downstream of the film holes. They reported that a small pitch to film hole diameter ratio for the staggered arrangements provides a higher spanwise average effectiveness than the in-line film hole arrangement. The effect of the staggered and in-line configurations for two circular rows with opposite orientation angle on film cooling performance was investigated by Ahn et al. (2000). Each row had five holes with a 35° and 45° inclination and orientation angle, respectively. They noted that the heat transfer coefficient for the staggered arrangement was lower than that of the inline arrangement; however, the inline arrangement produced a higher film cooling performance, for blowing ratios 1.0 and 2.0. Goldstein (1982) and Ammari et al. (1990)

reported that mixing increases, by increasing the inclination angle, hence increasing the turbulence boundary layer displacement thickness.

Lateral and forward diffused film holes with simple and compound angles (LDSA, LDCA, FDSA, FDCA) film cooling holes beside cylindrical round simple angle (CYSA) film holes were studied experimentally by Bell et al. (2000) to investigate the effect of shaped holes on film cooling performance. The inclination angle for the five film hole configurations was 35° and L/d = 3.0. They presented the data for blowing ratios from 0.4 to 1.8, momentum flux ratios from 0.17 to 3.5, and density ratios from 0.9 to 1.4. They noted that the configuration of LDCA and FDCA had the highest value of spanwise averaged Stanton number downstream the film hole (from x/d = 0 to 20) for blowing ratios from 0.7 to 1.8; however, the LDCA gave the highest values. Moreover, the spanwsie average adiabatic effectiveness for simple angle film hole configurations (CYSA, FDSA, LDSA) increased by increasing the density ratio from 0.9 to 1.4 for Br = 0.7 and this effect was smaller for the other two film holes with the same compound angle. In addition, Kim and Kim (2004) studied the effect of shaped injection holes on turbine blade leading edge film cooling. They simulated five different cylindrical hole models. The parametric study was conducted with a mainstream turbulence intensity of 0.2%, mainstream Reynolds number of 7.1×10^4 based on cylinder diameter, blowing ratio of 0.7, 1.0, 1.3 and 1.7, and density ratio of 1. They concluded that a conical-diffused hole (CDH) provided the best cooling performance. Bell et al. (2000) performed a similar experiment and noted that the film hole geometry with laterally diffused compound angle (LDCA) demonstrated the highest cooling performance.

Lee (2000) studied the effect of orientation angle for film cooling holes on the boundary layer temperature distribution and film cooling effectiveness. The film cooling results were obtained using five film holes designed with an inclination angle of 35° and orientation angles of 0°, 30°, and 60°. They presented the film cooling effectiveness distribution with respect to the velocity ratio and orientation angles. From their results, the compound angle produced more sprayed coolant over the surface, which affects the coolant flow from the neighboring jet. Consequently, the sprayed coolant became more uniform and the film cooling performance increased.

Cho et al. (2001) studied the effect of the film hole shape on heat transfer characteristics and film cooling effectiveness, using a 30° inclination angle and 0°, 45° and 90° compound angles,. Their first geometry was a circular hole, and the second film hole was conical with a 4° angle. The third film hole configuration used a film hole that was tilted 4° along its central axis, but was more conically shaped with an 8° angle downstream at L/d = 5.4. The three different film hole geometries were investigated with Br = 0.5, 1.0, and 2 at a density ratio of 1.0. Higher film cooling effectiveness was found by increasing the lateral injection angle. The film hole with 4° conical angle, as shown in Fig.2.1b, provided the best cooling performance compared to other film holes under all conditions.

The film cooling and heat transfer performances of three different film hole configurations were analyzed experimentally by Yu et al. (2002). The first configuration used baseline circular injections with 30° in the streamwise direction and L/d = 10. The second configuration's hole shape was similar to the baseline circular, but it had a 10° forward diffusion angle starting at distance of 0.79d below the test surface. The hole was modified by adding an extra 10° diffusion angle in the lateral direction for the third hole

configuration. The three configurations were tested for two blowing ratios (Br = 0.5 and 1.0), with Reynolds numbers ranging from 2300 to 4300, based on the hole diameter. They observed that the third configuration (Fig.2.1c) provided the highest film cooling effectiveness. However, the heat transfer coefficient was close to the second configuration and lower than the circular scheme.

Sargison et al. (2002) experimentally investigated the film cooling performance and aerodynamics loss for a converging slot-hole (Console) over a flat plate, as shown in Fig.2.1d. This scheme was designed to provide cooling and aerodynamic performance using slot geometry. The console cross section was changed from circular shaped at the hole inlet to slot shaped at the hole exit. The hole's wall was convergent in the streamwise direction and divergent in the lateral direction. The cross section decreased from the inlet to the exit so that the flow accelerated toward the exit. The accelerated flow provided a lower and more stable jet turbulence, which reduced secondary and mainstream penetration. Reynolds number was 1.44×10^5, based on the slot height, with a mainstream momentum flux ratio of 1.1. The console film hole provided good lateral uniformity of adiabatic effectiveness, which approached the slot effect. The console's laterally averaged heat transfer coefficient was also similar to that produced by the slot hole. The console film hole yielded less aerodynamic losses when compared to the circular and fan shaped holes, but it showed higher thermal stress concentrations, particularly at the exit area. Liu et al. (2009) investigated the effect of exit-entry area ratios of 0.67 and 1.33 for console film hole on film cooling performance. They noted that smaller exit-entry area ratios produced a better thermal protection due to higher film cooling effectiveness with minimum discharge

coefficient. A small exit-entry area promoted the acceleration of flow with low-turbulence, providing stable film cooling over the wall surfaces.

Saumweber et al. (2003) used fan shaped, laidback fan shaped, and circular holes to study the film cooling performance experimentally using turbulence ratios of 3.5, 7.5, and 11%. Both fan shaped holes were expanded laterally with an angle of 14°, and the laidback fan shaped hole included a 15° expansion in the streamwise direction, as presented in Fig.2.1e. They used a length to diameter ratio of 6 with blowing ratios of 0.5, 0.75, 1.0, 1.25, and 1.5. They reported that both shaped holes provided similar characteristics and there was no benefit in using the laidback configuration. Due to the lateral expansion at the hole exit of shaped holes, the film cooling effectiveness interacted with each other then sprayed a closed film cooling effectiveness.

Dittmar et al. (2003) investigated the film cooling performance of four different film hole configurations using infrared thermography. Double rows of cylindrical injection holes and discrete slots were used along with a single straight fan shaped hole and compound angle fan shaped holes. From their results, the four film holes provided the same film cooling effectiveness at low blowing ratios. However, the fan shaped hole with a compound angle (Fig. 2.1f) provided the highest film cooling effectiveness at high blowing ratios compared to other film holes.

Taslim and Khanicheh (2005) analyzed the effects of two different compound hole angles on the film cooling performance. The setup involved a single row of 90° compound angle circular film holes (d = 7.5 mm), and 45° compound angle for shaped film holes, with a 25° inclination angle in the downstream direction. The two film hole schemes were analyzed for blowing ratios ranging from 0.7 to 4.0. They noted that the highest overall film

cooling effectiveness over a wide range of blowing ratios was achieved with the diffuser shaped hole, which is presented in Fig. 2.1g. They concluded that increasing the exit cross-sectional area led to less jet penetration into the main flow due to a reduction in momentum flux, which produced a higher cooling effectiveness.

Miao and Wu (2006) numerically investigated the effects of blowing ratio and hole shape on the adiabatic film cooling effectiveness and distribution of flow fields over a flat plate with a density ratio of 1.14. The plate had two rows of injection holes in a staggered arrangement. Three different film holes were used; circular, forward diffused, and laterally diffused simple angles with a diameter of 5.0 mm and a 35° streamwise injection angle. It was revealed that the geometry of the hole shape plays a major role on adiabatic film cooling effectiveness, especially in the vicinity of the cooling holes. It was also proven that the highest cooling effectiveness was witnessed with laterally diffused simple angle geometry at a blowing ratio of 1.5. The laterally diffused simple angle provided superior cooling due to its ability to reduce the momentum of the cooling flow at the exit of the hole and penetrate into the main stream. This phenomenon was also observed experimentally by Taslim and Khanicheh (2005).

Immarigeon and Hassan (2006) numerically investigated the film cooling performance for the louver scheme. They inspected four different geometries using a different number of pedestals. The operating conditions consisted of 0.87 to 5.22 blowing ratios, 3% turbulence intensity and a density ratio of 1.73. They reported that at high blowing ratios, the pedestals have a negligible effect on the laterally averaged film cooling effectiveness near the hole exits ($x/d < 2$), yet they spread the coolant downstream. Zhang and Hassan (2006) extended the numerical investigation for the

louver scheme without including the pedestals and by using a single entrance hole. They compared the output results for the louver scheme with traditional circular and shaped film holes using single and multiple rows in staggered and in line arrangements. They noted that the louver scheme provided the highest performance for the average and local film cooling effectiveness with lower heat transfer coefficient ratios at low and high blowing ratios.

Kusterer et al. (2007) enhanced film cooling performance by using a new film hole arrangement which named double-jet film cooling (DJFC), of a circular hole. The interaction of two neighboring cooling jets created an anti-kidney vortex pair, which had improved film cooling effectiveness. In addition, the DJFC arrangement provided a good distribution of cooling air in a lateral direction. Moreover, Dhungel et al. (2007) and Heidmann and Ekkad (2008) studied computationally the effect of antivortex film hole design on film cooling performance. The principle concept of the antivortex film cooling moderates was the effect of the counter-rotating vortex pair. They investigated the performance of film cooling effectiveness and heat transfer coefficient for different vortex designs at unity blowing ratio and a density ratio of 1.05 and 2.0. Created vortices from round hole allowed the secondary flow to remain attached to the surface and hence improved the film cooling performance. Koc (2007) experimentally and numerically investigated the film cooling effectiveness performance of rectangular injection holes for blowing ratio from 0.5 to 2.0. He noted that the injection temperature, momentum flux ratio, and blowing ratio were affected the film cooling effectiveness. The highest performance in the streamwise and lateral directions was shown to be a blowing ratio of 0.5 and it decreased with further increase in blowing ratio.

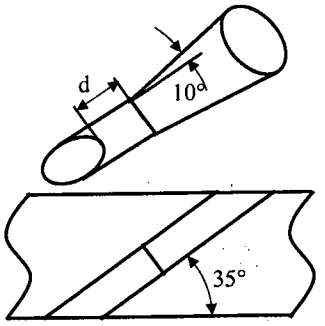

a) Eriksen and Goldstein (1974)

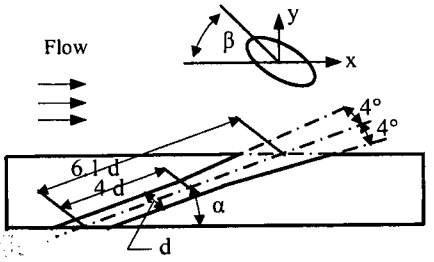

b) Cho et al. (2001)

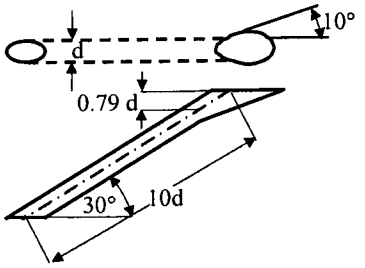

c)Yu et al. (2002)

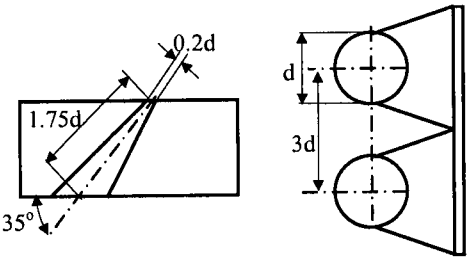

d) Sargison et al. (2002)
Console film hole

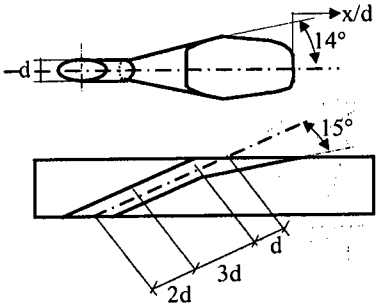

e) Saumweber et al. (2003)
Laidback fanshaped

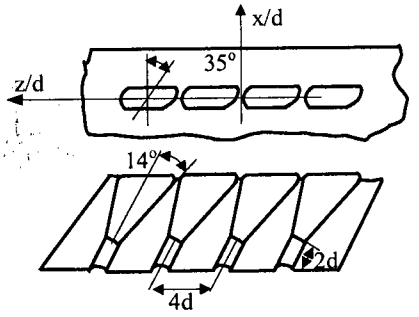

f) Dittmar et al. (2003)

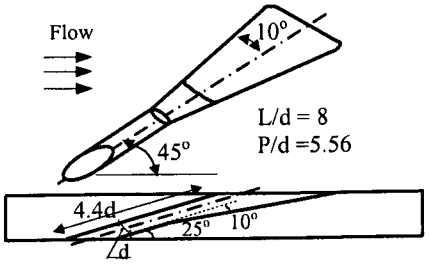

g) Taslim and Khanicheh (2005) CAFSH

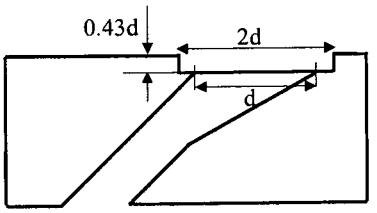

h) Baheri et al. (2008)

Figure 2.1. Advanced published film hole configurations.

On the other hand, investigating the effect of different hole geometries on the film cooling effectiveness performance and the heat transfer coefficient for an actual airfoil was studied. Studies were done both numerically and experimentally, under the same conditions or close to actual operating conditions. Weigand et al. (2000) studied the adiabatic film cooling effectiveness on a convex surface for zero pressure gradient flow. They tested five different injection configurations; three of which were cylindrical holes, and two had different shaped holes. A higher film cooling effectiveness and lower heat transfer coefficient were obtained by using a shape hole compared to of a circular hole. The secondary flow passed from the pressure side toward the suction side by decreasing the blowing ratio. Martin (2001) studied the thermodynamic measurements in order to determine the heat transfer surface and adiabatic film-cooling effectiveness at dimensionless engine conditions using a Mach number and Reynolds number of 1.0 and 850,000, respectively. The downstream heat transfer was affected by the vortex passage, while the heat transfer in the wake region downstream was augmented by increasing the downstream Mach number from transonic to supersonic.

Martini et al. (2003) studied, experimentally and numerically, the trailing edge film cooling downstream using a double in-line rib array. The experimental results indicated that the ribs had a significant effect on local and average adiabatic film cooling effectiveness. However, there was a significant deviation between the numerical and experimental results for adiabatic film cooling effectiveness. The CFD simulation could not capture the appropriate mixing turbulence process.

Jackson et al. (2000), and Kim and Kim (2004) studied the effect of shaped injection holes on turbine blade leading edge film cooling. Kim and Kim (2004)

simulated five different cylindrical hole models with various injection holes. The operating conditions were a 0.2 % main stream turbulence intensity, a $7.1x10^4$ main stream Reynolds number based on cylinder diameter, a blowing ratio of 0.7, 1.0, 1.3 and 1.7, and a unity density ratio. They deduced that the two span-wise diffused (laidback) film holes enhanced the film cooling effectiveness with respect to other film hole types.

Okita and Nishiura (2007) examined the film cooling effectiveness performance of arrowhead fan shaped hole (AFH) and fan-shaped hole with laidback (FSH) geometries on pressure and suction sides of airfoil. From their results, the AFH provided higher film cooling effectiveness at high blowing ratios (Br > 1.5) than the FSH on the suction side of the airfoil. At low blowing ratios, there was no significant difference between the AFH and FSH geometries. Also, the performance of the AFH compared to the FSH on the pressure side was similar to the suction side with less improvement.

2.1.2 Blowing ratio

The blowing ratio is another important parameter that has a significant effect on the performance of the heat transfer coefficient and film cooling effectiveness. Goldstein et al. (1974) studied the effect of the blowing ratio on the center film cooling effectiveness for injection film holes with a 35° inclination angle. They found that the film cooling effectiveness downstream of the film holes increased with increasing blowing ratio until it reached a maximum value (peak), where it then decreased for any increase in blowing ratio. The coolant flow attached to the downstream target surface at low blowing ratios, and lifted off from the surface at high blowing ratios (Bergeles et al., 1977). Close to the film hole, the heat transfer coefficient was higher where there was a 3-D nature of the jet; further, downstream the flow becomes mainly a 2-D structure. The

inclination angles for the film hole and the blowing ratios have an effect on the jet mixing between main and cooling streams. By increasing the blowing ratio, the heat transfer coefficient ratio increases. Furthermore, it approaches unity for low blowing ratios (Hay et al. 1985). Makki and Jakubowski (1986) concluded that increasing the coolant to mainstream ratio decreases the film cooling effectiveness. In 1991, Sinha et al. studied the effect of the blowing and density ratios on film cooling effectiveness over a flat pate. For the same density ratio, they reported the same conclusion as Goldstein et al. (1974).

Drost et al. (1997) studied the effect of operating conditions on the film cooling effectiveness and heat transfer coefficient for flat plate and turbine airfoil by using the transient liquid crystal technique; Mach numbers of 0.3 and 0.5, blowing ratios between 0.3 and 1.5, and a density ratio of 1.6. From their results, the maximum film cooling effectiveness was obtained for double row holes on the suction side of the airfoil in comparison with single hole. The high cooling momentum reduced the film cooling effectiveness on the pressure side of the airfoil. On the other hand, due to the increased shear between the injection and main flow, the heat transfer coefficient increased between the holes.

Goldstein and Jin (2001) studied the effect of film hole location on the heat transfer coefficient distribution to determine the regions that have higher and lower heat transfer coefficients. At low blowing ratio (Br < 0.8), the injection did not affect the mainstream at the hole location or on the blowing ratio inside the stagnation region. The mainstream jet collaboration created large eddies that led to shear stress, increases the coefficient of heat transfer. In addition, they investigated that the tangential injection

extends the temperature field for a blowing ratio equal to 0.5, although higher blowing ratios, the peak of film cooling effectiveness decreases.

Miao et al. (2006) numerically investigated the blowing ratio and hole shape effects on the adiabatic film cooling effectiveness and distribution of flow fields over a flat plate with a density ratio of 1.14. The plate had two rows of injection holes in a staggered arrangement. Three film holes with simple angle were used: cylindrical, forward diffused, and laterally diffused, with diameters of 5.0 mm and an injection angle of 35^{o} in the stream-wise direction. It was revealed that the geometry of the hole played a major role on the adiabatic film cooling effectiveness, especially in the vicinity of the cooling holes. It was also proven that the highest cooling effectiveness exists with laterally diffused and simple angle geometry for a blowing ratio of 1.5. The laterally diffused simple angle provided superior cooling due to its capability to reduce the momentum of the cooling flow at the hole exit, hence reducing the penetration into the main stream. Taslim et al. (2005) also observed this phenomenon experimentally.

Knost and Thole (2005) studied adiabatic film cooling effectiveness by measuring two end wall film-cooling hole patterns combined with cooling from a flush slot, which was simulated as leakage flow between the turbine and combustor. By increasing the momentum flux of the cooling jet, the cooling impacts the vane and swab (clean) down to the end of all surfaces. Liu et al. (2004) studied local film cooling effectiveness and the heat transfer coefficient with cooling injection by using single and double rows at blowing ratios of 1.0, 2.0, and 3.0. The secondary flow and the coverage of cooling on the end-wall have a major effect on film cooling. The coverage of cooling on the end-wall can be enhanced by increasing the blowing ratio. Knost and Thole (2005) concluded

that the film cooling momentum flux ratio had a significant effect on the cooling performance. Film cooling was enhanced by increasing the momentum flux ratio.

2.1.3 Density ratio

The effect of the density ratio (coolant to mainstream ratio) on the heat transfer coefficient and film cooling effectiveness over the downstream surface film holes was studied through previous research. The film cooling effectiveness decreases by increasing the density ratio (Makki and Jakubowski, 1986). To achieve the required density ratio experimentally, foreign gases are used as a coolant flow such as helium, nitrogen, CO_2, refrigerant or a mixture of two types of gases. Ammari et al. (1990) investigated the effect of two different density ratios (1.0 and 1.52) for a 35° inclination angle and unity blowing ratio. They reported that lower density ratios provided high heat transfer coefficients where higher turbulence eddies were produced at the jet hole. However, for various density ratios, the blowing ratio has a significant effect on the heat transfer coefficient. Chen P. et al. (2001) preformed two separate tests with different injection conditions to evaluate the heat transfer coefficient using the TLC technique. In addition, they found that there was an error in evaluating the film cooling effectiveness, which can be reduced by selecting an adequate pair of heated injection temperatures.

Sinha et al. (1991) studied the effect of the mainstream Reynolds number, the blowing ratio, and boundary layer displacement thickness to hole diameter ratio on the heat transfer coefficient using circular film holes with a 35° inclined angle along the stream wise direction. They noticed that a small difference, approximately 10% of the heat transfer coefficient, could be produced by changing the density ratio from 1.0 to 1.52 for a 1.46 blowing ratio.

Li et al. (2005) explored film-cooling enhancement using mist injection into the cooling air while comparing the various effects of different modeling setups. It was established that an injection of 2% mist could provide a 45% downstream cooling enhancement through a 2-D slot simulation. The focus of this study was to simulate the effects of turbulence models and numerical modeling schemes on the dispersed-phase. They also noted that a higher concentration of mist generates a better cooling effect. For the 2-D slot, a 5% concentration of injected mist containing 10 μm droplets increased cooling up to 65%. Li et al. (2006) extended their study by examining the effect of mist injection on film cooling performance using different film hole geometries. They used round and fanshaped holes and found that there was a 30 to 50% cooling enhancement due to 2% injection of the coolant flow rate. The fanshaped hole provided the highest peak cooling enhancement, with an increase of 52% compared to 50% for the 3-D round hole and 38% for the 2-D slot.

2.1.4 Turbulence intensity

The main and coolant flows turbulence intensity has a significant effect on film cooling performance and the heat transfer coefficient over the target cooling surface. For high mainstream turbulence intensity, the film cooling effectiveness over the downstream surface will decay (Jumper et al., 1991). They investigated the effect of a mainstream turbulence intensity of 14 and 17% for round film holes with a 30^{o} inclination angle. Bons et al. (1994) also studied the effect of high mainstream turbulence intensity. The turbulence intensity ranged from 0.9 % to 17%, with varying blowing ratios from 0.55 to 1.85, for constant mainstream Reynolds number. From their results, at low blowing ratios (Br = 0.75), by increasing the turbulence intensity, the maximum downstream film

cooling effectiveness significantly decreased. The coolant jet structure did not totally formulate due to high mainstream turbulence intensity. However, at high blowing ratios, the jet momentum was higher than the main stream; hence, jet left-off was increased, which reduced the reattachment of the jet flow to the target surface, further reducing the film cooling effectiveness. At low mainstream turbulence intensities and low blowing ratios (< 1.5), the span-wise adiabatic film cooling effectiveness was higher. However, at high blowing ratios, the film cooling effectiveness downstream increased by increasing the turbulence intensity (Drost et al., 1997). The same conclusions were noted by Mayhew et al. (2003) and Saumweber (2003) through experimental investigation of the free stream turbulence effect on the film cooling performance, using the infrared technique.

Jenkins et al. (2004) presented the combined effect of high turbulence and film cooling on the dispersion of a simulated hot streak passing over a nozzle guide vane. They reported that the additional turbulence exiting in the wake region does not appear as a result of increasing turbulence conditions. Because of the non-existence of any turbulence inside the wake region, no significant effect was noticed on decreasing the hot streak. Film cooling reduces the peak temperature in the hot streak by 75%, compared to the upstream peak temperature.

Ou and Rivir (2001) studied the effect of turbulence intensity (1% and 20%) and blowing ratios (1.0, 1.5, 2 and 2.5) on film cooling effectiveness and the heat transfer coefficient for a circular leading edge using the TLC technique. They used a circular film hole with a 20^{o} injection angle and a 7.86 hole pitch to diameter ratio. They reported that the turbulence had a significant effect on the film cooling effectiveness and Frössling

number ($Nu/\sqrt{Re}$), for all blowing ratios. In addition, Reynolds number had a significant effect on film cooling for a unity-blowing ratio with high turbulence intensity. In stagnation regions, the film cooling effectiveness and heat transfer coefficient are affected by blowing ratio, Reynolds number and turbulence intensity (Ou and Rivir 2001).

2.1.5 Surface roughness

Surface finishing has a significant effect on both the film cooling effectiveness, and the heat transfer coefficient. In 1986, Goldstein et al. reported that at low blowing ratios, the surface roughness decreases the film cooling effectiveness by 20 %; however, it increases by 50 % at high blowing ratios. Sen and Bogard (1996) found that the surface roughness had a significant effect on film cooling by studying different cases of hole geometry: a round hole with 30° inclination angle, a 60° angle away from the main stream in the lateral direction, and a 15° forward expansion with an orientation angle of 60°. Barlow and Kim (1995) found that for a small level of roughness the film cooling effectiveness was lower than for higher surface roughness. Additionally, the film cooling effectiveness was corrupted farther downstream and enhanced the heat transfer coefficient by 50 % for rougher surfaces (Schmidt et al., 1996).

In a real case, a gas turbine airfoil operates under several environments with high temperature and stress, and the airfoil has clear-off roughness. There are many causes for increasing airfoil surface roughness and they depend on the processes, which create the rough surface. Airfoil surface roughness can be created from fuel deposits, LE erosion and deposits, hot corrosion and erosion, pitting, and mild and large spallation (Bons et al. 2001). They measured the roughness for the end-wall to be 28 μm. They stated that the

roughness level was 4 to 8 times greater than the levels for a production line airfoil, which is less than 1 μm. Moreover, the erosion grooves close to the film hole have a significant effect on the film cooling effectiveness. Cardwell et al. (2006) investigated the effect of a mid-passage gap and roughness on the end-wall film cooling using a large-scale turbine vane. They noted that adiabatic film cooling effectiveness decreased by increasing the surface roughness at high blowing ratios; although at low blowing ratios there was no significant effect from surface roughness.

2.2 Conjugate heat transfer

Protecting gas turbine blades from overheating is required in order to circumvent the creation of hot spots inside the airfoil. The main parameters which affect overheating are internal and external heat transfer, metal temperature distributions, film cooling methods with different film holes, coating the outside airfoil surface, and the rotational effects. Through the last few decades, the study of conjugate heat transfer calculations for gas turbine applications has started. Conduction heat transfer has a significant effect on airfoil life, and by creating internal cooling passages, the airfoil life will be increased.

Rhee et al. (2004) installed square ribs with different arrangements and attack angles on an effusion plate in order to investigate the effect of ribs on impingement and effusion cooling systems with cross flow. The ribs improve the heat transfer on the effusion surface, and although it increases for a small pitch of the ribs, the pressure drop increases by 15% of the total loss due to the installed ribs.

Analyzing conjugate heat transfer is required to couple fluid flow and the airfoil body of a turbine system. Heidmann et al. (2003) investigated numerically the conjugate heat transfer and showed that it produced a lower outer wall temperature compared to an

adiabatic wall temperature. This is due to heat losses from the outer wall to the plenum. They used two different vane materials throughout their study; high thermal conductivity Inconel nickel alloy, and low thermal conductivity silicon nitride ceramic. High thermal conductivity is predicted without upheaval of the vane surface temperature. They reported that film cooling is considered a two-temperature problem, which causes heat flux at the wall. The conjugate heat transfer cannot be considered one-dimensional conduction heat transfer but it should be three-dimensional heat conduction where there is conduction heat transfer along the vane as well as from the outer to inner wall. In addition, high heat flux was discovered on the impingement side of the film cooling holes (round shaped). Lu et al. (2005) investigated, experimentally and numerically, the effect of downstream conjugate heat transfer on film cooling for round holes with 30° inclination angles over a flat plate. The conjugate heat transfer creates a varying heat flux distribution over the wall compared to adiabatic wall temperature. Additionally, they studied the effect of mesh size and turbulence model (k-ε model with wall function) on the accuracy results, numerically, using CFD code STAR-CD 3.1. They noted that the two-layer model, $y^+ = 1$, gives more accurate results compared to experimental data, but consumes more computational time compared to other cases for $y^+ = 10$, 30, and 100.

Film cooling performance for different film hole configurations (cylindrical, diffuser, and fanshaped) over a flat plate, for both adiabatic wall temperature and conjugate heat transfer; have been studied by Bohn et al. (2005). From their results, the conjugate heat transfer had a large variation on the heat flux distribution. Also, the fan-shaped hole provided a film cooling effectiveness three times higher than the round hole configuration. Kusterer et al. (2006) extended the work of Bohn et al. (2005) to improve

the film cooling performance over a blade by investigating the regions for the highest thermal loads. They included all internal flow passages and used the film hole shapes. As a result, the leading edge and blade tip regions had high thermal loads, therefore the redesign and relocation of the film hole shapes in these regions were proposed to protect these areas. Mazur et al. (2006) used steady state CFD simulations to analyze conjugate heat transfer for a nozzle vane. They carried out the thermal load analysis by investigating the temperature distribution around the nozzle, and hence estimated the life of the nozzle. As well, they investigated the step change in material properties due to the flow and solid heat interference Wu and Miao (2006) numerically investigated the effect of conjugate heat transfer of fanshaped film cooling over a concave plate. They used three different conjugate materials under four different blowing ratios (0.5, 1.0, 1.5 and 2.0). They noted that the blowing ratio had a significant effect on the lateral film cooling effectiveness.

2.3 Summary

Many experimental and computational studies have been done to investigate the cooling process of gas turbine airfoils with the objective of understanding this complex flow and heat process, and to devise the best possible cooling schemes.

The above investigations can be summarized as follows:

1. Hole geometries are important because they can affect the film cooling performance. Laterally and forward expanded holes provide higher values of spanwise averaged effectiveness and lower values of span-wise averaged heat transfer coefficients than round holes. Moreover, the advanced film cooling holes reduce jet lift-off hence

increasing the film-cooling performance and reducing the heat transfer coefficient over the target surface and downstream of the film holes.

2. Compound angle injection leads to an increase in spanwise averaged effectiveness compared to holes with a 0^{o} compound angle. However, compound jet angles generally produce high values of heat transfer coefficient due to an increase in the turbulence over the surface.
3. Hole spacing affects the spanwise film cooling performance. Small hole spacing provides better coverage of the wall, and thus higher effectiveness values than larger space. A pitch to diameter ratio of 3 was commonly used in film cooling studies.
4. There is no significant effect of the number of film hole rows on the heat transfer coefficient at low blowing ratios, however, at high blowing ratios, the heat transfer coefficient increases with increasing number of film rows. A small pitch to film hole diameter ratio for staggered arrangements provides a higher span-wise average effectiveness than the inline film hole arrangement.
5. At low blowing ratios, the film cooling performance for the majority of film holes is almost the same, but expanded exit holes yield higher performance compared to round holes. For high blowing ratios, the coolant jet undergoes lift-off. Therefore, the interaction between the two streams increases, hence causing a reduction in film cooling effectiveness.
6. A decrease in density ratio causes an increase in the downstream heat transfer coefficient on the film-cooled surface for inclined hole angles less than 90^{o}, however no significant effect on heat transfer coefficient for 90^{o} inclined holes (normal injection) was observed. Reducing the density ratio has the same effect as increasing

the momentum flux ratio. It reduces the lateral spreading of the jet, thus lowering the spanwise averaged adiabatic film cooling effectiveness. Moreover, the density ratio provides a high heat transfer coefficient while producing higher turbulence eddies at the jet hole.

7. The free-stream turbulence is very important parameter that affects significantly on film cooling performance. At low blowing ratio, the film cooling effectiveness increases with decreasing the turbulence intensity. While, at high blowing ratio, the effect of turbulence intensity is insignificant on film cooling effectiveness. On the other hand, for high turbulence intensity, the heat transfer coefficient reduced according to blowing ratio for circular holes. For shaped holes, the blowing ratio becomes more significant at high mainstream turbulence intensity.
8. Large mainstream length scale enhances the turbulence mixing and carets a strong vortex, which increases with increasing blowing ratios, thereby the heat transfer coefficient increases.
9. The span-wise adiabatic film cooling effectiveness is increased at low main stream turbulence and blowing ratios, however film cooling effectiveness increases at high blowing ratios by increasing the main stream turbulence intensity.
10. There is a heat transfer enhancement benefit in roughening the internal surface of the turbine blades. At low blowing ratios, the film cooling effectiveness decreases by 20% due to surface roughness, but increases by 50% at high blowing ratios.
11. Mist injection is another method that allows for cooling improvements. Cooling improvements of 30-50 % can be obtained with an injection of 2 % coolant flow rate.

3-D round and fan-shaped diffusion provide the best overall cooling with roughly 50 % improvement, while 2-D slots allow for an improvement of about 30-40 %.

12. Double jet film cooling hole configurations and antivortex film holes enhance the film cooling performance in downstream and lateral directions.
13. Arrowhead-shaped holes (AFH) improve film cooling effectiveness more than shaped film hole on the pressure and suction sides of airfoil.
14. Ribs enhance heat transfer in internal cooling passages. It serves as a vortex generator and thus promotes the turbulent mixing in the bulk flow, and accordingly, enhances the heat transfer from all participating walls.
15. The conjugate heat transfer decreases the outer wall temperature due to heat losses from the external wall to the coolant air through the blade body. Moreover, it has a significant effect on varied heat flux over the external wall.
16. Using fanshaped holes provides film cooling effectiveness three times higher than round shaped for the conjugate study.
17. Due to the heat losses from the external surface to the blade body, the leading edge and blade tip regions have the highest thermal load and should be redesigned for those shaped hole configurations and locations to protect against high thermal loading.

Chapter 3

Chapter 3 Test Facility and Methodology

3.1 Experimental test facility

Figure 3.1 presents a schematic diagram of a new open loop turbomachinery film cooling test rig established at Concordia University. The test rig is designed in order to provide a subsonic inlet Mach number. The air supplied to the test rig is provided by a compressed air tank at regulated pressure of 700 kPa. The tank has dimensions of 1.22 m in diameter and a 2.88 m height. The test rig consists of mechanical and thermography systems. The thermography system includes a Data Acquisitions System (DAQ), light sources, camera and computing workstation. The mechanical system consists of main and secondary flow loops. The entire test rig is pipelines are made of stainless steel 410 of 5 cm, 7.62 cm, and 15.24 cm pipe diameters. The secondary air is heated while the main stream was kept at the supply temperature. Each loop includes a pressure controller to maintain a steady operating pressure at a preset value. A Rosemount Multi-Variable Mass Flow Meter (3095MV) and rotameter (FL-1502A) are used to measure the main flow, and the secondary flow rates respectively. The flow rate in each loop is adjusted manually through gate and needle control valves. The main flowmeter records the load pressure and temperature to correct for density variations for measuring the flow rate. A divergent-convergent nozzle is designed to settle down the main flow before entering the test section. A honeycomb is installed at the exit of the convergent nozzle to create a more uniform velocity distribution for the main flow entering the test section. The divergent-convergent nozzles and the main duct are made from cast acrylic sheets, 1.27

cm thick, with 91% light transmittance. The main duct cross section has dimensions of 11 cm x 5 cm and total length of 150 cm. The plenum is made from cast acrylic, and is insulated to reduce heat losses to the surroundings. An electrical variable power air heater with a maximum capacity of 1200 Watts is installed upstream of the plenum to heat the secondary flow. A fast acting two-way solenoid valve routes the flow through a bypass until steady state conditions are achieved, then the secondary flow is allowed to pass the test section through the plenum. The following section will describe more information and specifications for the test rig components.

Pressure controller

The mainstream line is connected with a 1098-EGR-6351, 3" pressure regulator including 6351 pilot type (FISHER) with high sensitivity feedback, as shown in Fig. 3.2. It has the capability of controlling the downstream main pressure with an outlet pressure range of 0.35 to 2.4 bar. This range of pressure can be changed by replacing the adjusting spring. While the R18-C05RG-LA (NORGREN) pressure regulator is connected before the air heater in order to control the secondary flow pressure with a range of 0.35 to 8.6 bar. The main objective of using individual pressure controllers in each line is to obtain more flexibility to control the pressure at each line.

Air flow measurement:

A multi-variable mass flow meter (Rosemount 3095) is used to measure the mainstream flow rate through a 15.24 cm (6") plate orifice diameter. On the other hand, the airflow rotameter is installed in the secondary loop to measure the secondary flow rate. The backpressure of the rotameter is at atmosphere pressure. Therefore, the standard

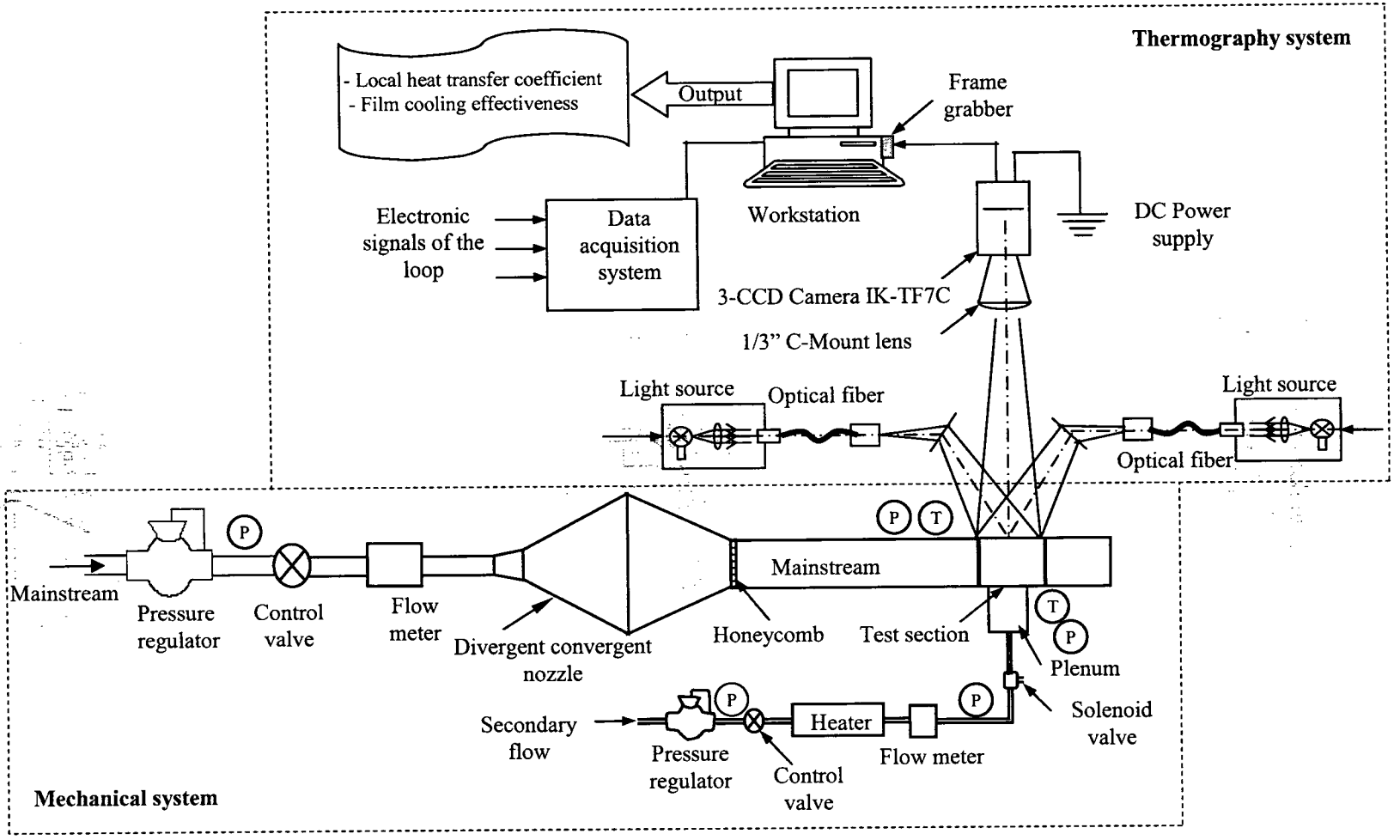

Figure 3.1. A schematic diagram of designed turbomachinery film cooling test rig.

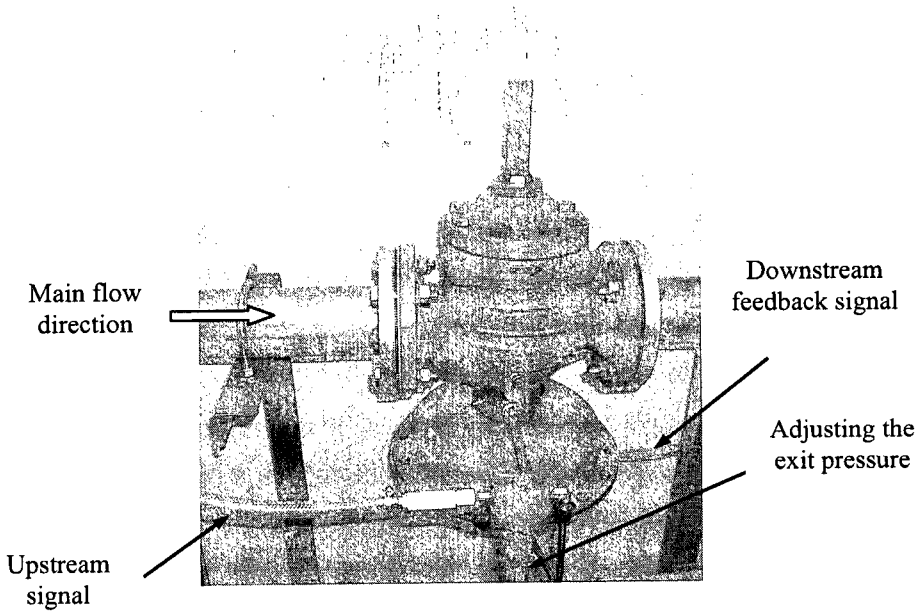

Figure 3.2. Main stream pressure controller.

cubic feet per minute (SCFM) is the same as actual cubic feet per minute (ACFM). The flow rate is adjusted by using the downstream manual control valves (gate and needle). The effect of changing air density due to air temperature is considered by measuring the downstream air temperature by using a RTD probe for the main flow and a T-type thermocouple for the secondary flow. MV Assistant Engineering Software and AMS were provided by Rosemount. The software is used to calculate the flow rate after receiving the signals for absolute pressure, air temperature, and pressure difference cross the orifice plate. The specifications of the orifice plate, such as orifice dimensions, beta factor (ratio of the orifice bore and pipe line diameter), and orifice material are set in the flow meter's processor using EA software. The Rosemount 3095 multi-variable mass flow meter provides two output signals; a digital indicator and analog for 4-20 mA. The minimum time response for the air flow meter is 2 seconds and it has an accuracy of 0.5% from span. The flow meter has the ability to work up to 250 in H_2O pressure difference around the orifice plate. The orifice plate is selected according to the required maximum flow rate with a larger orifice plate diameter for higher flow rates.

Plenum

The plenum is a connecting part between the air heater and the film holes. The plenum has a rectangular cross section of 7.5 cm x 20 cm with a 20 cm height. It is made from cast acrylic (Plexiglas) with a 1.27 cm thickness. A honeycomb is inserted inside the plenum to prevent a swirling flow pattern inside the plenum and to break down large turbulent structures. An electrical rope heater is put inside the plenum to warm it up during the heating process of the secondary flow. In the meantime, the secondary flow is routed through a fast acting 2-way bypass solenoid valve until steady state conditions are

achieved. In addition, the plenum is insulated in order to reduce the heat loss to the surroundings.

Divergent-convergent nozzles and main duct

The main flow is supplied through a 316L stainless steel schedule 10S pipe line with a 15.24 cm (6") inner diameter. Afterwards, the main flow is passed through the adaptor which changes the pipe line shape from a round (15.24 cm diameter) to a square cross section (15.24 cm x 15.24 cm) before entering the divergent-convergent nozzles, followed by the main duct, as shown in Fig.3.3. The divergent-convergent and main ducts are made of a cast acrylic material with 1.27 cm thickness. The main function of the divergent-convergent nozzle is to settle down the main flow, and to make it uniform before entering the test section. A CFD model is created to simulate the divergent-convergent nozzle for designed cross section and length dimensions. Different dimensions are investigated numerically before the manufacturing process to investigate and achieve the optimal design dimensions, which would give a more uniform velocity profile at the exit area of the divergent duct. The optimal output dimensions for a divergent nozzle, based on numerical simulation, were 15.24 by 15.24 cm, and 50.8 cm by 27.5 cm for the inlet and exit cross sections, respectively. In order to allow a smooth transition from the inlet to the outlet cross sections, the divergent section has a length of 70 cm. In addition, the cross sectional dimensions for the convergent section changed from 50.8 by 27.5 cm to 5 cm (height) 11 cm (width), with a length of 70 cm. The profile for a divergent-convergent duct should be at least a 4^{th} order polynomial curve to construct smooth transition for the width and the height. However, it is very difficult and more expensive to be manufactured using a cast acrylic material. On the other hand,

many tests are made using different small boxes in order to figure out the number of ribs and screws needed to hold the high pressure inside the divergent-convergent nozzle and main duct. Warping the divergent-convergent nozzle and main duct with ribs as well as screwing and gluing the sidewalls, increases the pressure, which has a maximum allowable value of 12 kPa inside the system. Figure 3.3 shows the connected adaptor with the divergent-convergent nozzle and the ribs, which are roped around the cross section at different locations toward downstream direction. The divergent convergent nozzle is connected with a main duct, which has a cross section of 11 cm by 5 cm, and a 150 cm total length. The total length for the main duct is divided into two parts with length of 70 cm for the diverging portion and 80 cm for converging portion. Different turbulent grids can be fixed between the two parts in order to generate different turbulence intensities for the mainstream flow.

Afterwards, the main flow enters the test section, which has inlet dimensions of 11 cm in depth by 5 cm in height, which is similar to the dimensions of the main duct. The maximum velocity permitted inside the main duct is 56 m/s and it is calculated by measuring the main flow rate using a 3095 MV air flow meter and the cross section area. Turbulence intensity is an important parameter that affects the heat transfer coefficient and film cooling effectiveness. To generate different turbulence levels for the main flow, a turbulent grid can be fixed inside the duct at a distance of 70 cm from the test section or airfoil leading edge. Two different turbulence grids can be made from steel in order to generate two different values of turbulence intensity for the same flow rate as shown in Fig. 3.4. The coarse grid has dimensions of 0.8 cm in width and 3 cm in pitch to generate high turbulence intensity. In order to generate low turbulence intensity, fine grids can be

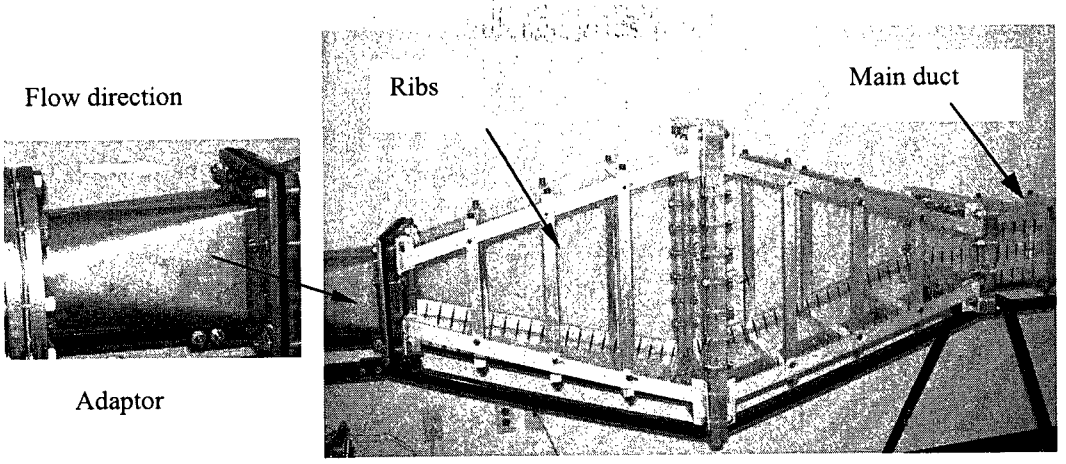

Figure 3.3. Divergent convergent nozzle test section.

used with dimensions of 0.3 cm in width and 1.2 cm in pitch. According to Jungho's design (2004), the turbulence intensity values from the coarse and fine grids will be approximately 8% and 4%, respectively. These two different turbulence grids are not used though the current study, but they are designed as constructed for future turbulence study using the test rig. Through this study, there is no turbulence grids was used and a median turbulence intensity is estimated to be 3.8 %.

Roach (1987) investigated turbulence intensity and found that it decays after turbulence grid by the following relation;

$$T_u = 1.13\left(\frac{x}{d}\right)^{-5/7}, \tag{3.1}$$

where x is the downstream distance from the grid, and d is the width of the bar (0.8 and 0.3 cm).

3.2 Instrumentation and measurements techniques

Air flow meters, pressure transducers and thermocouples are selected, and installed at specific locations along the test rig to measure the flow rate, pressure, and temperature of the main and secondary streams, respectively. Type-T thermocouples with a fine precision are used to measure the temperature in the plenum and Type-E (pipe probe 1/4" NPT) are used to measure the main stream flow temperature. In addition, a type-E thermocouple is used to measure the secondary flow temperature after the air heater. Two 2088G Rosemount pressure transducers (0-5.2 bar) are installed in the main duct and the plenum to measure the pressure of the main and the secondary flows, respectively. A Rosemount multi-variable mass flow transmitter (3095MV) is used to measure the main flow rate. A digital display and analog of 4-20 mA are the two output signals from the

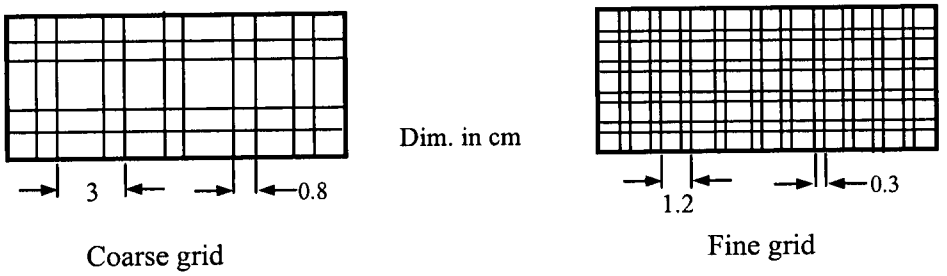

Figure 3.4. Grid construction.

pressure transducers and the multi-variable mass flow transmitter. Additionally, PGH-45L-100 Omega pressure gauges are also placed in each loop in order to monitor the pressure. The output signals from the instruments are connected to an M series National Instruments (NI) data acquisition system (DAQ), and then monitored by using labview software. An in-house labview code is developed in this study in order to monitor and save a variety of signals from pressure, flow and temperature instruments under steady state and transient conditions. The solenoid valves are also controlled through labview software.

Figure 3.5 presents a schematic diagram showing all connections and output signals from the instruments to the data acquisition system. The DAQ system consists of a SCXI-1000 signal-conditioning unit, with appropriate modules, NI PCI-6281 18-bit (analog input resolution), M series DAQ with an output rate of 2.8 MS/s and a SCXI-1160 16-channel SPDT relay model. The instrument output analog signals are mA, and mV, as well as connect and disconnect signals. These signals are transferred to a DAQ card (PCI 6281) through a signal conditioner. Figure 3.6 illustrates the block diagram of the developed labview software. It is built up through this study for the transient measurements of film cooling applications.

3.3 Image acquisition system

A digital 3CCD IK-TF7C Toshiba camera is used to capture the TLC images over the downstream surface area of the film holes at a rate of 10 fps. The acquired simultaneous images are transferred to the computing workstation through a NI PCIE-1340 dual frame grabber, which can work up to two base Camera Link configurations using the Labview program. The image quality depends on the adjustment of the lens, light distribution, and

intensity. The light intensity is adjusted with a variable light source. A color calibration target is used as an objective to adjust the resolution. The captured, Red-Green-Blue (RGB) images are saved in Tagged Image File Format (TIFF) with a size of 1024 X 768 pixels. An in-house image processing code is created using MATLAB software through this study. The RGB images are converted to hue values, then to temperature values, using TLC calibration curves. The calibration curve has a polynomial relationship between the temperature and hue values. The calibration curve is determined by reading thermocouples corresponding to the hue value for each region of interest (ROI).

Flat surface stick thermocouples (SA1XL-T) from Omega, are fixed over the target surface for the TLC calibration process. A Dolan-Jenner PL-800 fiber illuminator model is used to generate light originating with constant light temperature. Internal flitter is holed to absorb the heat generation. The light is directed over the target surface through a dual optic cable which is 1.9 m long. The TLC is protected from the heat generated from light by using light which has an EKE Quartz Halogen lamp with 250 W and a constant voltage of $\pm$ 1.0%. The light beam is generated through a fiber optic illuminator box then the beam passes through a single fiber optic cable, which is later separated, into a duel cable. The light beam from the two duel cables passes across the upper Plexiglas surface and then each branch is focused on the target surface. The two cables and light intensity are adjusted simultaneously over the target area in order to obtain uniform light distribution. Moreover, the beam of light has a specific inclination angle, around 20° - 30°, with the 3 CCD camera. A 1/3" C-Mount (TF8DA-8B) lens is mounted on the 3 CCD color camera and the zoom is adjusted through a focus ring, which has a scale of

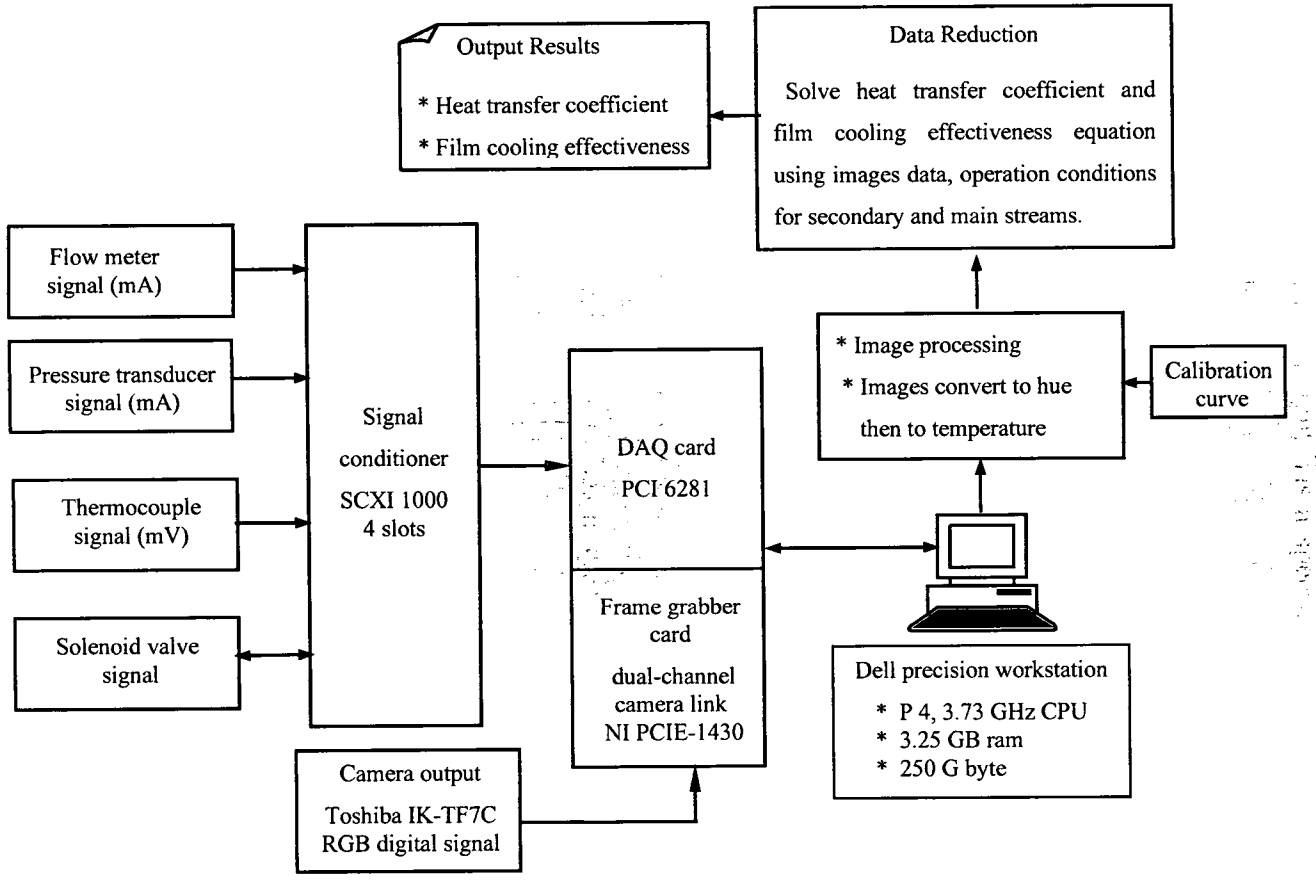

Figure 3.5. Schematic of data acquisitions system (DAQ).

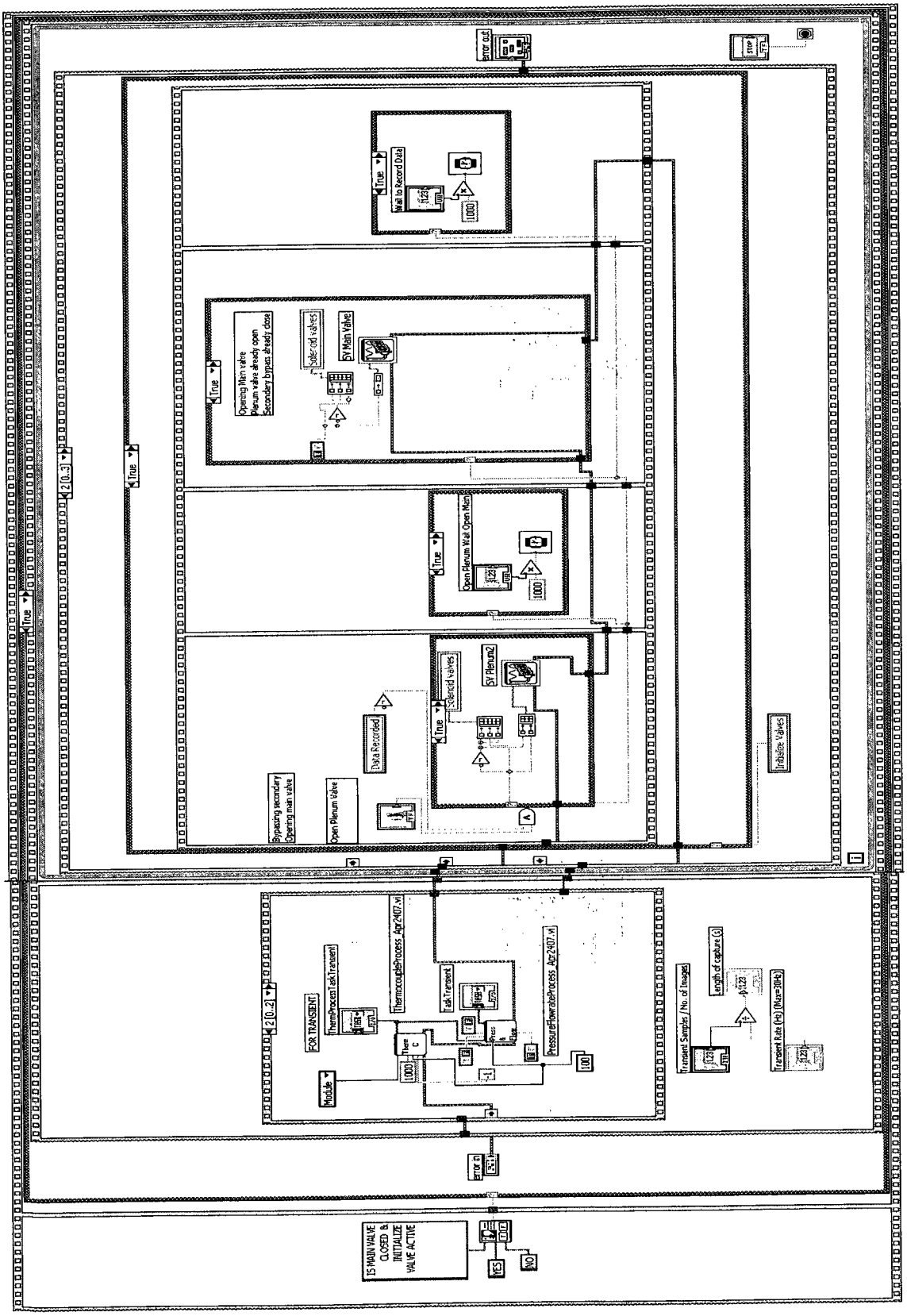

Figure 3.6. Block diagram of the labview program.

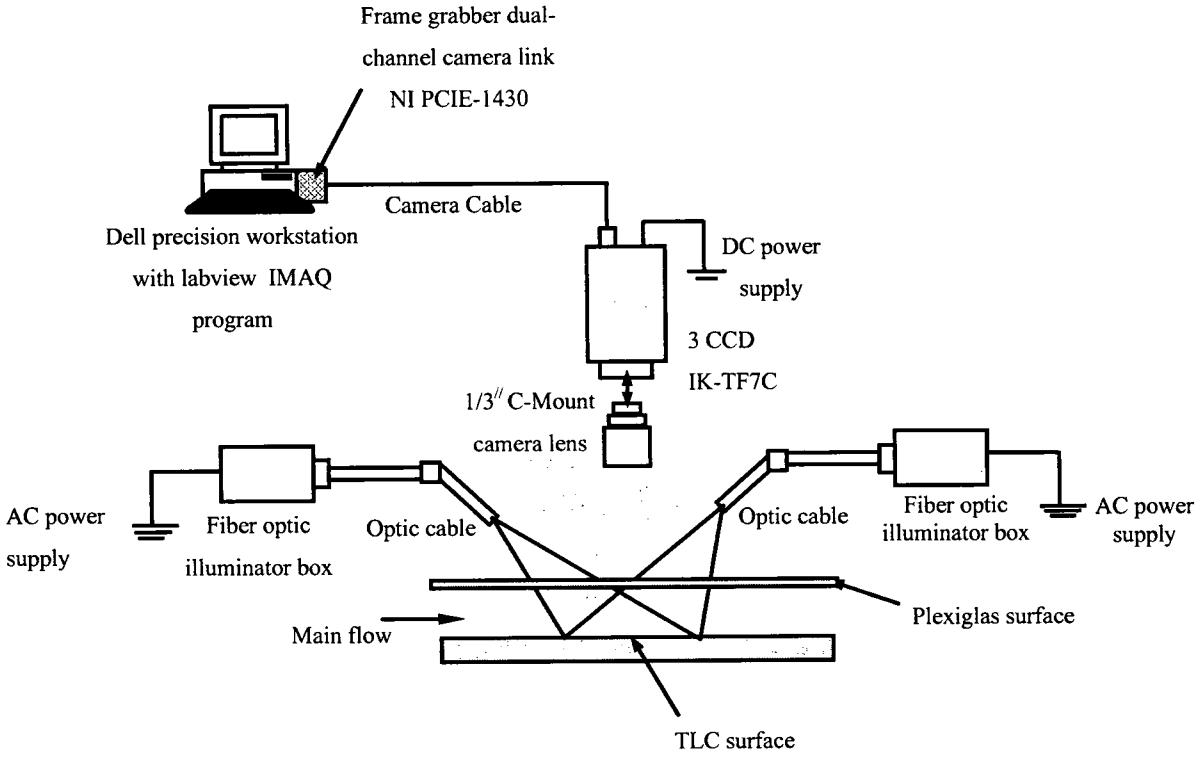

Figure 3.7. Image acquisition system.

1:2.2 / 8 mm.

Figure 3.7 shows a schematic of the image acquisition system. The 3 CCD camera is mounted on a 475 Pro Tripod and it is adjusted to be perpendicular to the target surface.

The camera location is adjusted to cover 15.875 cm by 11.43 cm of the target area with good resolution. A color calibration target is used as a reference to adjust the resolution. The image quality depends on the adjustment of the lens, the light distribution and intensity. The light intensity is adjusted through an illuminator switch, which has a percentage scale from 0 to 100. The acquisition images are transferred to a PC workstation through a NI PCIE-1340 dual frame grabber, which can work up to two base Camera Link configurations using the labview program. The images are captured simultaneously by recoding the measurement signals and saving them on a PC hard drive.

3.4 Thermochromic liquid crystal (TLC)

This section describes the Thermochromic Liquid Crystal (TLC) technique to measure the film cooling surface temperature based on color changes. The image system is developed to provide high performance for the film cooling measurements. Using the TLC technique for film cooling applications can produce a large thermal mapping over the target surface with high resolution and accuracy especially for the transient experiment. TLC has fast response is a popular technique for measuring temperature in thermal gas turbine application studies. From temperature measurements, film cooling effectiveness and the heat transfer coefficient can be calculated under various flow and temperature conditions. In addition, the TLC is repeatable because the color change is reversible. Therefore, the same TLC can be

used for different measurements under different operating conditions, such as varying blowing ratios, turbulence intensity and density ratio.

3.4.1 Liquid crystal fundamentals

The Thermochromic Liquid Crystal is employed as a temperature sensor over the airfoil surface. Liquid crystals are highly anisotropic fluids with a crystal like molecular orientation. When the liquid crystal is subjected to different temperatures, it reflects different colors, and is therefore referred to as thermochromic. It has a helical molecular structure and by changing the temperature, it rotates, expands or shrinks. Due to that change in structure, the liquid crystals reflect the incident white light and expose different colors related to different temperatures. It is provided in bands from 0.5°C to 20°C and it has a working temperature range from -30°C to 120°C. The TLC bands can be classified into narrow and wide bands. The narrow bands have bandwidth less than 5°C, while wide bands have bandwidth greater than 5 °C. Selection of TLC bands and ranges are dependent on the applications and required accuracy. Figure 3.8 presents the reflected wavelength temperature response for TLC material. The Smectic, cholesteric (Chiral nematic), and isotropic are three different regions of TLC color. Smectic are characterised by long axes of the molecules and a layering of the molecular centers of gravity in two dimensions. In the Chiral nematics, the martial are optically active and have a natural twisted structure. Liquid crystals exist between the boundaries of the solid phase and the conventional, isotropic liquid phase and are highly anisotropic fluids. Smectic region occurs at low temperatures, which is less than the red starting temperature, while the isotropic (colorless) region occurs at temperatures greater than the starting blue temperature. The region between red and blue colors is called cholesteric and the width of this region corresponds to the TLC's band.

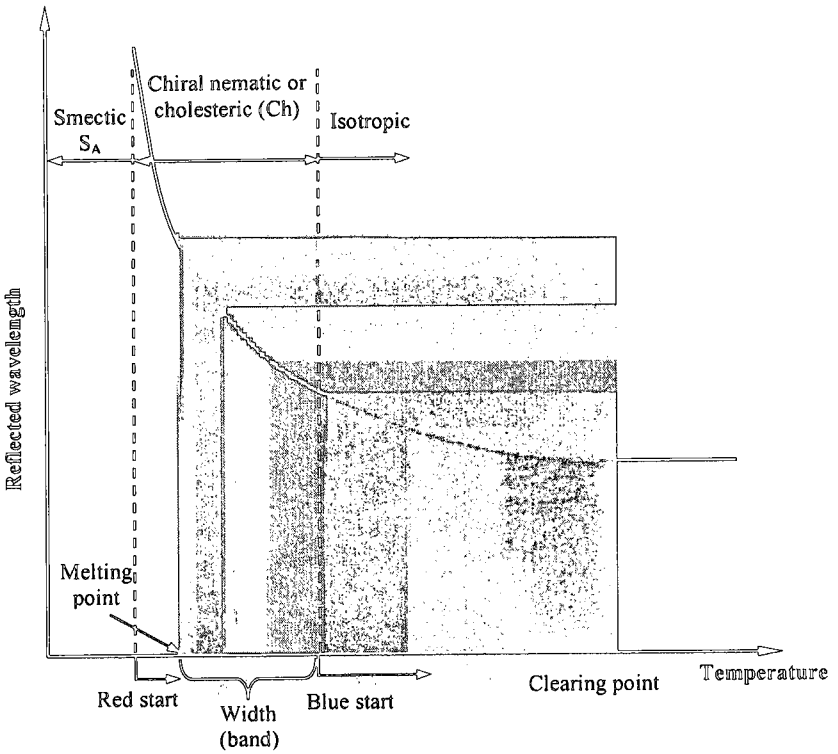

Figure 3.8. Reflected wavelength temperature response of TLC.

When TLC works above melting point, the solid crystal starts to melt. On the other hand, when it works below clearing point, it loses the optical properties associated with solid phase. At low temperatures, the red color is displayed in the color-play interval, then yellow, green, and blue color at higher temperatures. At high temperatures, greater than the blue range, the TLC becomes colorless (isotropic). This is similar to the clear temperature at room condition. The changing color from red to blue depends on the band; larger bands provide more accuracy. In addition, the TLC's response time depends on the material viscosity. The most significant factor when using TLC is preparing a uniform coating, which will produce quiver colors. By increasing the TLC layer thickness, non-negligible temperature gradients will start to be produced. An airbrush is used to apply a uniform coating for encapsulated TLC material. The color vibrancy of the TLC response is improved by coating a black paint over the surface using an airbrush before coating the TLC material. Moreover, by using a black surface, the color sharpness is improved, whereas for other backgrounds, the reflected colors will pass through the crystal coating, producing an undesirable contrast. The maximum operating temperature for TLC is limited to 120 °C and cannot be used at higher temperature as an Infra Red (IR) technique.

TLC material is sensitive to mechanical stress. It is affected when it is used as a pure material under laboratory conditions. The encapsulated liquid crystal material (SPNR24C16W), supplied by LCR Hallcrest, was used as a first try throughout the present study. In fact, the encapsulated material is commonly used for heat transfer applications, especially for external flow when the working fluid passes over the TLC material. The encapsulated chiral-nematic crystal is derived from Greek words, meaning to exhibit the twisted structure of the phase (Licu, 2000). It is easily washed off from the target surface using acetone or water. Data acquisition and interpretation

methods are necessary to obtain quantitative information and there are three broad classes for interpretation methods; human observers, intensity-based image processing systems, and true-color processing systems. The TLC's color quality is dependent on the type of TLC used; coating or sheets.

3.4.2 TLC coating

The quality of the TLC coating has a prominent effect on the TLC image results. There are a few steps for coating the surface with the TLC. The first step is to clean the target surface to remove all the dirt, grease, fingerprints, etc. Common organic solvents such as acetone or petroleum ether can be used for cleaning the target surface before coating. After that, the target surface is coated by using black paint, such as BB-G1 or BB-M1. In order to get a uniform layer of paint on the surface, an air brush was used with compressed air at 20-30 psi. The black paint on the surface needs 20-45 minutes to dry before painting the TLC. The time can be reduced by blowing warm air over the surface. Finally, the TLC material is sprayed using an airbrush with compressed air at 20-30 psig. The airbrush should be perpendicular to the surface and it should be far away from the target surface, at a distance of 15-20 cm. After coating the TLC, the surface takes 30-45 min to dry and blowing warm air over the surface can reduce drying time. The thickness of the TLC layer is very important for TLC quality. For example, 250 grams are sufficient for a coating of 2.5 m^2 (0.01 gram/cm^2). This ratio is proposed by LCR and it has produced good resolution for TLC images. With time, the TLC material properties will deteriorate due to the light and the temperature effects. Therefore, the TLC should be removed and recoated again for future tests. To clean the TLC, soapy water or acetone can be used. The current type of TLC should be stored inside a refrigerator at 5-10°C without freezing.

3.4.3 TLC sheet

The thickness of the TLC coating has an effect on the TLC quality, and hence on the temperature measurement. Many attempts to properly spray the TLC should be carried out until the appropriate quality and experience are achieved. After using the TLC coating for a few tests, a new unencapsulated TLC sheet was proposed by LCR. The TLC sheet has a fine resolution and uniform coating and produces a clear RGB color with minimal uncertainty in the TLC. The TLC sheet consists of a 125 μm clear polyester layer, which is printed black color on one side and coated with micro-unencapsulated TLC. On the other side of the sheet, an adhesive backing (pressure-sensitive adhesive) is used to adhere to desired surface. The R25C5W TLC sheet is used throughout this study. The TLC sheets retain color play characteristics for many months under normal handling conditions. If TLC sheets are stored correctly, a lifetime of one year can be expected.

3.4.4 Preparing the TLC sheet over the surface

The surface is cleaned thoroughly to remove all dirt, grease, etc. using petroleum ether or any similar organic solvent and the surface is left to dry. After that, the TLC sheet is cut to the same sized area as the downstream target surface. The protective backing from the adhesive on the back of TLC sheet is removed and the sheet is placed lightly in position on the surface. The sheet is pressed down firmly with fingers using a smooth paper in the center of the sheet, and is smoothed outwards in each direction to ensure that no air bubbles are trapped between the sheet and the surface. A soft cloth can be used to clean the TLC sheet if needed.

3.4.5 Advantages of using a TLC sheet in the current study

1. TLC sheets are the most stable form and are readily available.

2. TLC sheets are constructed from clear polyester. Therefore, the color change properties of the TLC coating are viewed through the clear over laminate.
3. TLC sheets have a fine resolution and uniform coating, and produce a clear RGB color with minimal uncertainty of the TLC.
4. The sheet has a pressure-sensitive adhesive back to stick easily to surfaces.
5. TLC sheets retain color play characteristics for many months under normal handling conditions.

3.5 Image processing and calibration

RGB images for film-cooling surface are captured using a 3CCD (IK-TF7C) analog Toshiba camera with a progressive scan which has an image size of 1024 X 768 pixels. The images are transferred through a single-channel board that includes a RGB cable with separated lines to a NI PCIE-1340 dual frame grabber. The images are saved in a Tagged Image File Format (TIFF) on the hard drive of a PC workstation. The hue angle method is used to quantify the observed color to the material temperature. The hue is described in Eq.3.2 by Hay and Hollingsworth (1996) and was used as well by Baughn et al (1999).

$$Hue(H) = \frac{1}{2\pi}\arctan\left[\frac{\sqrt{3}(G-B)}{(2R-G-B)}\right]. \tag{3.2}$$

Where RGB are digital values of color signals and the Hue (H) takes a value from 0 to 1 or from 0 to 360 degrees. The color analysis for HSV (hue-saturation-value) is used in image processing and it has a range from 0 to 255 (8-bit scale). TLC colors are dependent on background light spectral characteristics, the distance between the light source and the target area, as well as the camera view angle. The type of TLC formulation and the resolving capability of the optical system limit the highest spatial resolution.

Figure 3.9 presents the color consequence to convert RGB image to HSV, and then to hue value. The RGB are three colored beams, which must be superimposed in order to form a color (Fig.3.9a). The HSV color is described as a cylinder and each point has a color. Every axis of the cylinder has a color range, which corresponds to the range of H, S, and V values, as shown in Fig. 3.9b. First, the hue (H) is related to the angle around the axis (θ direction), and the saturation (S) corresponds to the distance between the point and the cylinder center in radial direction (r). Finally, the value (V) is presented by the distance along the cylinder axis (z direction). Fig. 3.9c presents the range of hue values (0^{o}- 360^{o}) which correspond to a different range of color such as red, blue, green, yellow, etc.

The TLC calibration is a very important step for any test in order to quantify the captured color change (from red to blue) to surface temperature. Figure 3.10 presents the construction of the calibration setup used in this study. An aluminum flat plate, having a 2 mm thickness, is used for the TLC calibration, well as for measuring the heat transfer coefficient without film cooling. Two identical flat electrical heaters (KH 608/2.5-P) are installed underneath the plate. The two heaters are connected to a variable direct current (DC) power supply, which is used to control the input power to the heaters. The TLC sheet is installed on the top of the plate. The bottom surface of the plate is insulated with a 1.27 cm thick polystyrene layer in order to reduce the heat transfer from the heaters to the surrounding. Four flat sticky thermocouples (SA1XL-T) are installed on the flat plate near the TLC sheet from both sides in order to record the surface temperatures during the calibration process. This method preserves the image measurement conditions, such as camera focus and lighting for the actual tests.

The CCD color camera is focused on the measurement area. After adjusting the position for the camera and the light, the power supply is turned on. During the TLC

calibration, steady state conditions for the temperature and TLC color should be achieved. The calibration starts from high temperature and ends with low temperature, which is called the "down calibration method". Temperature and color stability can be achieved more easily by using the down calibration method. In this case, the plate is heated until the TLC color becomes blue at steady state conditions. By reducing the DC electric power supply to the heater, the TLC color changes to green, followed by red. For each calibration point, the image and corresponding temperature values (from the thermocouples) are captured and recorded on the PC's hard drive using the labview program. The first image in the calibration process is blue (around 30°C according to the selected TLC band). The DC power supply is decreased gradually in small steps using fine toning switches. At each step, steady state conditions should be achieved before capturing the image and recoding the thermocouple temperatures. The image and thermocouple temperatures are recorded for every 0.1 or 0.2°C decrease in thermocouple temperature. The last image for calibration is recorded when the target surface has a red color and the thermocouple temperature reaches to the temperature which corresponds to a red color, which is 25°C for the current band of TLC, although it changes from case to case depending on the selected TLC band.

Image processing for the TLC calibration is done to convert the image's color from RGB to hue, and then to temperature. Throughout the current calibration methodology, the target surface area is divided into regions of interest (ROIs) and each region had a size of 5 x 5 pixels (0.81 x 0.81 mm^2), as shown in Fig. 3.11. The hue value for each ROI is calculated as an average with a mean filter. The hue value for each ROI corresponds to the mean temperature of the thermocouples' reading at the same time as the recording of temperatures and capturing images. By using the

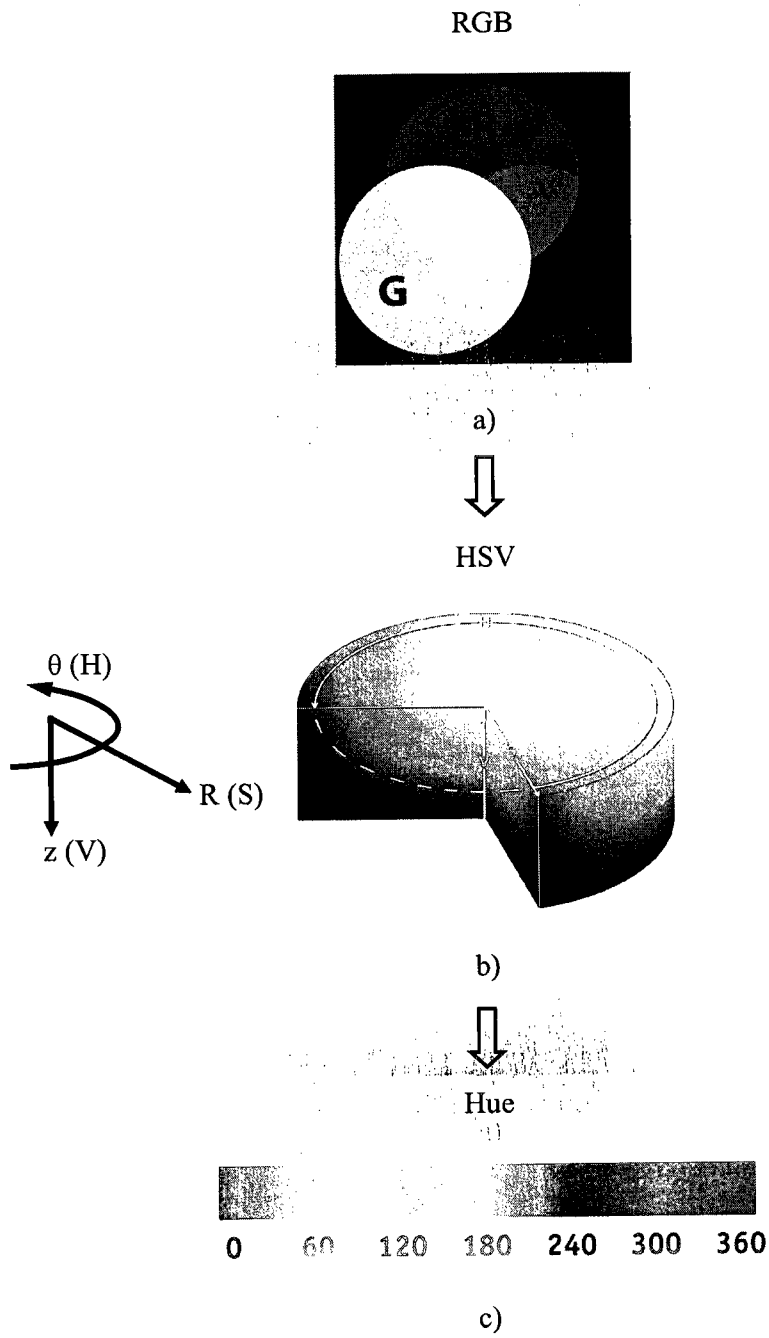

Figure 3.9. Consequent convert color from RBG to hue.

hue values and corresponding temperatures, which yield the curve fit for hue, temperatures can be obtained, whereby each region has a unique calibration curve.

Figure 3.12 illustrates a sample of raw calibration images over the target surface. The first image has blue color, which corresponds to an average temperature of 29.93 °C. By reducing the DC power supply, the TLC color changes to green, then to red, as shown in Fig. 3.12, where each color corresponds to a temperature value. A polynomial fit is used to correlate the temperature and hue values. Calibration is achieved by correlating the thermocouple reading and the corresponding hue values at steady state measurement. A 3rd order polynomial is fit to the calibration data and is appropriate for most ROIs, while a 5th order polynomial fit for other regions of interest. Therefore, combinations of 3 rd and 5th order polynomial fits are used over the target surface. A sample calibration curve for a single ROI is presented in Fig. 3.13. The 3rd order curve fitting appropriately represented this ROI. As a result, by dividing the target area into ROIs, good quality data points are provided covering the entire color range, thus reducing the error obtained from other calibration methods.

3.6 Similarity analysis for the film cooling model in a gas turbine

The working conditions under which a gas turbine operates makes it difficult to measure film cooling with good accuracy. Therefore, film-cooling models are widely used. The analysis of the film cooling geometry is similar to that of the gas turbine, except for the scale of the model arrangement. The ratio of physical parameters such as velocity, pressure, and temperature are the same in order to achieve a similar boundary layer.

Figure 3.14 shows a sketch of the film cooling modeling. The parameters that describe gas turbine film cooling are; gas flow velocity (U_m), mainstream temperature (T_m), cooling flow injection velocity (V_j), and temperature (T_j) through a

characteristic length of d. The total heat flux per unit area is q_w, and the wall surface temperature is T_w. The flow properties such as specific heat (C_p), density (ρ), viscosity (μ), and thermal conductivity (k) are functions of temperature. The pressure variation in the film-cooling model is neglected at low flow velocity. Therefore, the flow density is proportional to 1/T. In the film cooling analysis, the properties of the main stream are used as reference values.

For the adiabatic film-cooling model, the dimensionless parameters can be describes as follows:

For the temperature:

$T^* = \rho_j/\rho_m$, and $\theta = \dfrac{(T_m - T_j)}{(T_m - T_w)}$,

For the velocity:

$V_x^* = u/U_m$, $V_y^* = v/U_m$, and $V_z^* = w/U_m$,

And for the pressure:

$P^* = P / (\rho_m U^2_m)$.

The temperature, velocity and pressure can be presented as a relation as follows:

$$\left(\frac{u}{U_m}, \frac{v}{U_m}, \frac{w}{U_m}, \frac{T}{T_m}, \frac{P}{\rho_m U_m^{\ 2}}\right) = f\left\{\frac{x}{d}, \frac{y}{d}, \frac{z}{d}, \mathrm{Re}_d, \mathrm{Pr}, Br, \frac{\rho}{\rho_m}\right\}. \tag{3.3}$$

$$\text{where, } \mathrm{Re}_d = \frac{\rho U_m d}{\mu},\ \mathrm{Pr} = \frac{C_p \mu}{k}, \text{ and } Br = \frac{\rho_j V_j}{\rho_m V_m}. \tag{3.4}$$

In order to present the downstream adiabatic wall temperature in dimensionless form, film cooling effectiveness is selected.

$$\eta = \frac{T_m - T_{aw}}{T_m - T_j} = f\left\{\frac{x}{d}, \frac{z}{d}, \mathrm{Re}_d, \mathrm{Pr}, Br, \frac{\rho}{\rho_m}\right\}. \tag{3.5}$$

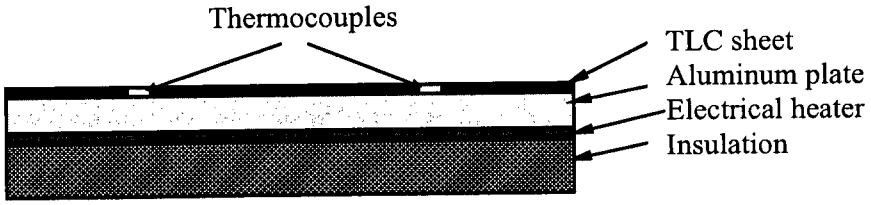

Figure 3.10. TLC calibration setup.

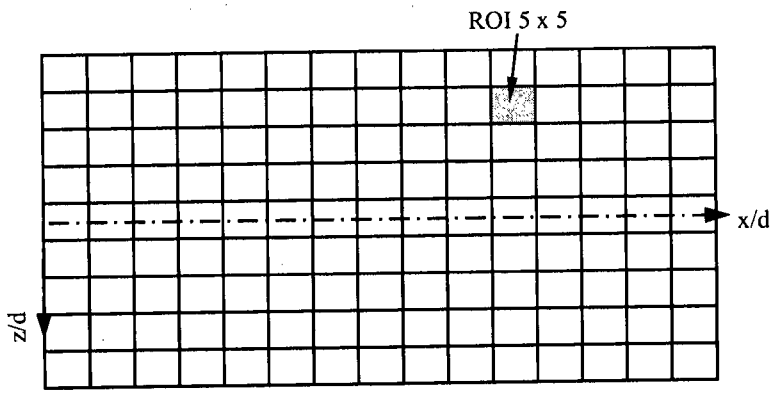

Figure 3.11. Regions of interest (ROIs) for target surface.

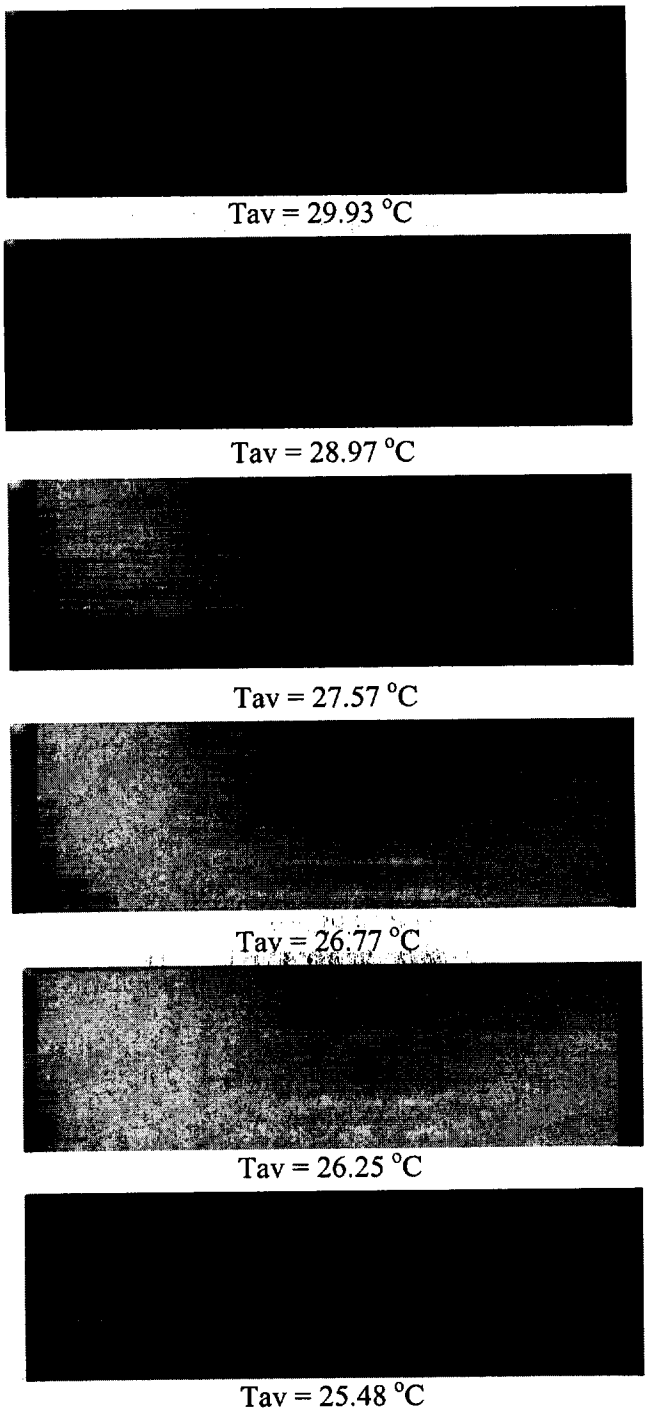

Figure 3.12. Sample raw of TLC images for calibration process.

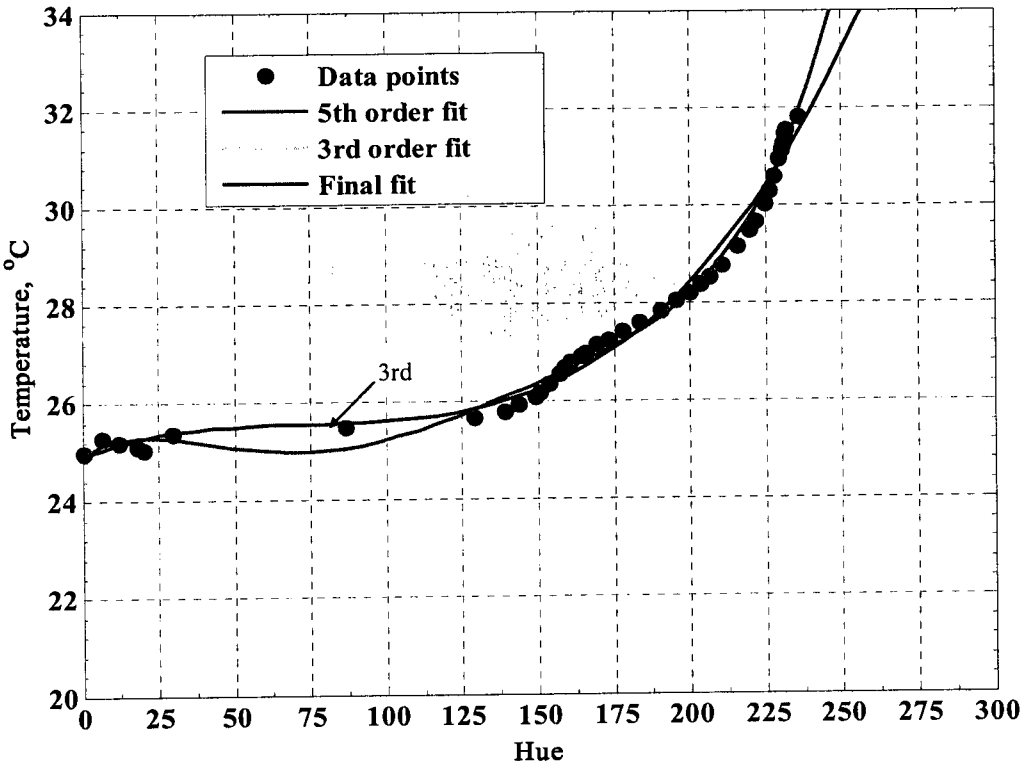

Figure 3.13. TLC calibration curve for a single ROI.

In addition, Nusselt and Frossling numbers are used to present the dimensionless form of the heat transfer coefficient over the film-cooling surface as follows;

$$St = \frac{h}{\rho_m C_p U_m} = f\left\{\frac{x}{d}, \frac{z}{d}, Re_d, Br, \frac{\rho}{\rho_m}\right\}, \tag{3.6}$$

$$F_n = \frac{Nu}{\sqrt{Re}} = f\left\{\frac{x}{d}, \frac{z}{d}, \eta, Br, \frac{\rho}{\rho_m}\right\}. \tag{3.7}$$

The net heat flux reduction is used as a dimensionless combination of the heat transfer coefficient ratio and film cooling effectiveness over the downstream surface as follows:

$$NHFR = 1 - \frac{q_f}{q_o} = f\left\{\frac{x}{d}, \frac{z}{d}, \mathrm{Re}_d, Br, \frac{\rho}{\rho_m}, \eta, \theta\right\}. \tag{3.8}$$

3.7 Heat transfer data reduction

The TLC technique is used to measure the wall temperature as a function of the color and hence, by using the data reduction method, the local heat transfer coefficient (h) and film cooling effectiveness (η) can be determined. The local heat transfer coefficient is determined by assuming one dimensional transient heat conduction over a semi-infinite solid as shown in Fig.3.15. The main flow has a uniform velocity and temperature of U_m and T_m, respectively, and the secondary flow has jet temperature of T_j and velocity of V_j. The flat plate test section is made of a cast acrylic material with a thickness of 3.2 cm to ensure the validity of the one-dimensional semi-infinite assumption.

A brief summary of the data reduction method is follows:

The one dimension unsteady heat conduction equation without heat generation can be written as follows:

$$\rho C_p \frac{\partial T}{\partial t} = \frac{\partial}{\partial y}\left(K \frac{\partial T}{\partial y}\right). \tag{3.9}$$

In order to solve this equation, one initial and two boundary conditions are needed;

$$\left.\begin{array}{lll} 1- \ @\ t = 0, & T = T_i, & \text{Initial condition} \\ 2- \ @\ y = 0, & h\left(T_f - T_w\right) = -K\frac{\partial T}{\partial y}, & \text{Boundary condition} \\ 3- \ @\ y = \infty, & T = T_i. & \text{Boundary condition} \end{array}\right\} \tag{3.10}$$

According to these initial and boundary conditions, Chen et al. (2001) gave the solution for equation (3.9) as follows:

$$\frac{T_w - T_i}{T_f - T_i} = 1 - \exp\left(\frac{h^2 \overline{\alpha} t}{k^2}\right) erfc\left(\frac{h\sqrt{\overline{\alpha} t}}{k}\right), \tag{3.11}$$

where, $erfc(y) = 1 - erf(y) = 1 - \frac{2}{\sqrt{\pi}} \int_0^y \exp\left(-x^2\right) dx$, and $\overline{\alpha}$ is the thermal diffusivity of the cast acrylic = k/ρCp. Thermal conductivity of the cast acrylic is k, and t is the time taken for the images after the test is initiated. In order to keep the semi-infinite solid assumption; the target plate is made from a cast acrylic (Plexiglas) material which had low thermal conductivity (k=0.18737 W/m.K) and low thermal diffusivity ($\overline{\alpha}$ =1.075215x10^{-7} m^2/s), as well as, low the lateral heat conduction. Moreover, the plate thickness was large to insure that Fourier number was small. The duration time for the experiment did not exceed 40 seconds, which is less than τ. As a result, the semi-infinite assumption is valid through the present study since the transient test duration is 30 sec.

$$\text{Fourier number} = \frac{\overline{\alpha}\tau}{s^2}. \tag{3.12}$$

where, s is half of the plate thickness and τ is the time required to transfer the temperature from one side of the plate to the other by conduction.

The initial temperature (T_i) over the target surface and the mainstream temperature (T_m) are measured by using T-type thermocouples, and wall temperatures are measured using the TLC technique. The film temperature (T_f) can be calculated as a function of injection temperature (T_j), mainstream temperature (T_m) and film cooling effectiveness (η) as follows:

$$\eta = \frac{(T_f - T_m)}{(T_j - T_m)} \text{ or, } T_f = \eta T_j + T_m(1-\eta). \tag{3.13}$$

By substituting T_f into Eq. 3.11 from Eq. 3.13., Eq. 3.11 will be a function of two variables; h and η. In order to calculate the two variables, film cooling effectiveness and the heat transfer coefficient (η, h), there are different methods which can be used. The first method is a single event procedure, which was described by Licu (2000). This method allows for the simultaneous determination of the local heat transfer and film cooling effectiveness during one transient test with multi event sampling. If we assumed that the initial temperature is equal to the mainstream temperature ($T_i = T_m$). By applying this method at two different time events (t_1 and t_2), Eq. (3.11) can be written as follows:

$$\frac{T_{w1} - T_i}{\eta(T_j - T_i)} = 1 - \exp\left(\frac{h^2 \overline{\alpha} t_1}{k^2}\right) erfc\left(\frac{h\sqrt{\overline{\alpha} t_1}}{k}\right). \tag{3.14}$$

$$\frac{T_{w2} - T_i}{\eta(T_j - T_i)} = 1 - \exp\left(\frac{h^2 \overline{\alpha} t_2}{k^2}\right) erfc\left(\frac{h\sqrt{\overline{\alpha} t_2}}{k}\right). \tag{3.15}$$

There are two unknowns in Eqs. 3.14 and 3.15. The numerical solution for these two equations is dependent on the measurement error and the method of running the experiment, as well as the selection of the TLC band according to the working fluid temperature. There are many constraints to be considered in order to use this method, such as no variations in injection temperature during the test period and a proper selection of TLC range to produce a good and entirely available surface temperature

(T_w) history over the target surface during one transient test. Therefore, all the previous reasons should be considered in order to have a numerical solution for the film cooling effectiveness and heat transfer coefficient, and to minimize the experimental error. The second method is called the steady state test. This method is performed by running two different steady state tests with different flow temperatures, but fixing the other flow conditions for main and secondary streams. Therefore, there are two sets of experimental results to calculate the two unknowns in Eqs. 3.14 and 3.15. This method is not valid for the current test rig due to the limitation of attaining steady state conditions for the main flow.

Any variation for main and secondary flow temperatures during the experiment should be minimized for the single transient test to minimize the experimental error and calculate the two unknowns (η, h) in Eq. (3.14) or Eq. (3.15). However, experimentally it is difficult to avoid the heat loss in the pipeline or plenum during the test. As a result, the plenum temperature changes during the experimental test, where the secondary flow temperature is higher than room temperature. Therefore, Duhamel's superposition theorem or nonlinear least square regression analysis technique should be used to calculate the two unknown in the case with variation in secondary flow temperatures during running of the test.

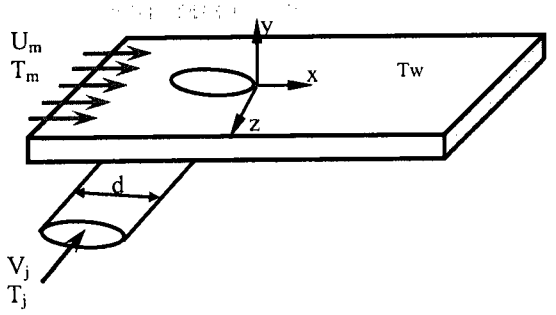

Figure 3.14. Sketch of film cooling modeling.

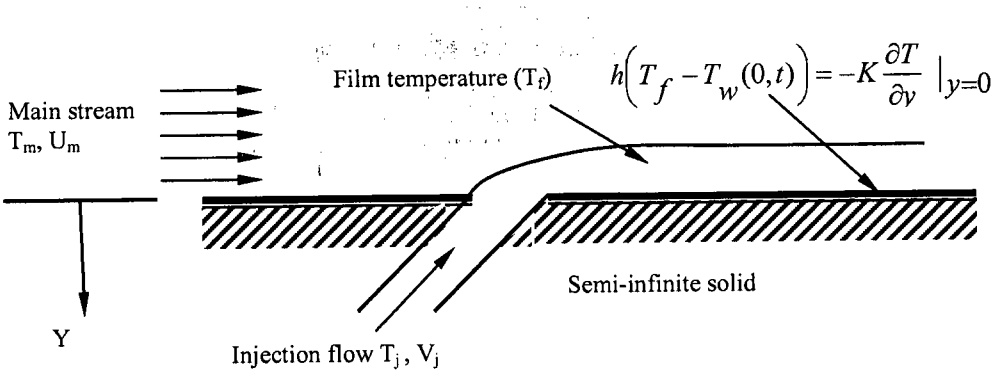

Figure 3.15. Flow and film cooling injection over flat plate.

3.7.1 Duhamel's superposition method

Experimentally, the injection temperature (T_j) is dependent on the time, $T_j = T_j(t)$. Thermocouples are installed inside the plenum, close to the entrance of the film hole to record the variation of secondary flow temperature with time (t). Figure 3.16 presents the discretized response for the secondary temperature. Chen et al. (2001) modified equations (3.14) and (3.15) in order to take in the consideration the variation of the jet temperature by using the superposition principle (Duhamel's theorem). The gradual change of the mean bulk temperature is obtained using a series of time steps. The final solution is calculated as follows:

$$T_{w(t)} - T_i = \sum_{n=1}^{N} \left\{ 1 - exp\left(\frac{h^2 \overline{\alpha}(t-\tau_j)}{k^2} \right) erfc\left(\frac{h\sqrt{\overline{\alpha}(t-\tau_j)}}{k} \right) \right\} * (\Delta T_j). \qquad (3.16)$$

In order to obtain the two unknowns, h and η, equation (3.7) should be applied at two different pairs of times as follows;

$$\frac{T_{w(t1)} - T_i}{T_{w(t2)} - T_i} = \frac{\sum_{n=1}^{N1} \left\{ 1 - \exp\left(\frac{h^2 \overline{\alpha}(t_1 - \tau_n)}{k^2} \right) erfc\left(\frac{h\sqrt{\overline{\alpha}(t_1 - \tau_n)}}{k} \right) \right\} * (\Delta T_j)_{t1}}{\sum_{n=1}^{N2} \left\{ 1 - \exp\left(\frac{h^2 \overline{\alpha}(t_2 - \tau_n)}{k^2} \right) erfc\left(\frac{h\sqrt{\overline{\alpha}(t_2 - \tau_n)}}{k} \right) \right\} * (\Delta T_j)_{t2}}. \qquad (3.17)$$

where, N is the number of time steps, which is the number of the frames, and ΔT_j is the incremental change of jet flow temperature with time. Equation (3.17) can be solved iteratively to determine the local heat transfer coefficient. By calculating the heat transfer coefficient from Eq. (3.17), the film cooling effectiveness can be obtained from one of the following equations at any time; either at t_1 or at t_2, as presented in Eqs. 3.18 or 3.19, respectively:

$$\eta = \frac{(T_{w(t1)} - T_i)}{\sum_{n=1}^{N1} \left\{ 1 - \exp\left(\frac{h^2 \overline{\alpha}(t_1 - \tau_n)}{k^2} \right) erfc\left(\frac{h\sqrt{\overline{\alpha}(t_1 - \tau_n)}}{k} \right) \right\} * (\Delta T_j)_{t1}}, \qquad (3.18)$$

$$\eta = \frac{(T_{w(t2)} - T_j)}{\sum_{n=1}^{N2}\left\{1 - \exp\left(\frac{h^2\overline{\alpha}(t_2 - \tau_n)}{k^2}\right) erfc\left(\frac{h\sqrt{\overline{\alpha}(t_2 - \tau_n)}}{k}\right)\right\} * (\Delta T_j)_{t2}}. \quad (3.19)$$

3.7.2 Regression analysis method

Hoffs (1996) and Lu (2007) used the regression analysis technique to reduce the experimental error for the film cooling application. There were many important parameters that should be considered in data analysis, such as time step, and increment of changing the secondary flow temperature during the experimental test. The regression method is the preferred method for high response of the secondary flow temperature; however, the Duhamel's superposition method is used for slow response of changing secondary flow temperature during the experimental test.

Many parameters are measured using the transient experimental method to determine the heat transfer coefficient (h) and film cooling effectiveness (η), such as the wall surface temperature using TLC technique, secondary flow temperature, and initial and main stream temperatures. The one-dimensional non-linear least-square regression method is used to solve Eq. (3.20) in order to calculate the two unknown parameters; h and η. For every ROI, there is one particular value for the heat transfer coefficient and film cooling effectiveness for each test.

$$T_w - T_i = \left[1 - exp\left(\frac{h^2\overline{\alpha}t}{k^2}\right) erfc\left(\frac{h\sqrt{\overline{\alpha}t}}{k}\right)\right] * \left[\eta(T_j - T_m) + T_m - T_i\right]. \quad (3.20)$$

The surface temperature for each ROI over the target surface is calculated using the TLC technique at each time step during the transient measurement as follows:

$$T_{w(ROI)}(h, \eta)\Big|_{t=\tau} = T_{TLC}\Big|_{t=\tau}, \quad (3.21)$$

Therefore;

$$T_{w(ROI)}(h,\eta)\Big|_{t=\tau} - T_{TLC}\Big|_{t=\tau} = 0 \ , \quad \text{for i = 1 to N.} \tag{3.22}$$

where, N is the total number of images captured during each transient test.

A total of 300 images (N) are captured during each experimental test. In the first few images (n), there is no TLC response over the entire target area. As a result, N-n equations are applied in Eq.(3.20) to calculate the two parameters (h and η) using the non-linear least square regression method. The optimum solution is achieved by minimizing the least square error (ε) for each ROI over the downstream film-cooling surface as follows:

$$\varepsilon(h,\eta) = \frac{1}{2}\sum_{i=n}^{N}\left(T_{w(ROI)}(h,\eta)\Big|_{t=\tau} - T_{TLC}\Big|_{t=\tau}\right)^2 . \tag{3.23}$$

where, ε is the least square error.

Figure 3.17 presents the temperature response data for a single ROI as well as the curve fit solution using the non-linear least square regression method. This method minimizes the residual error for the heat transfer coefficient and film cooling effectiveness and also reduces the experimental error. The number of unused images (n) had an effect on the final solution of h and η. The "n" is dependent on the time response of the secondary flow over the downstream TLC surface. Each ROI, over the surface, had a different value of n, based on the flow conditions. For each experimental test, different regions of interest are selected downstream of the film holes to determine the proper "n" values that could provide the minimum least square error (ε), in Eq.3.23. A linear profile of "n" with x/d is used to calculate the two parameters, h and η, for the entire downstream surface. The "n" value increases in the downstream direction.

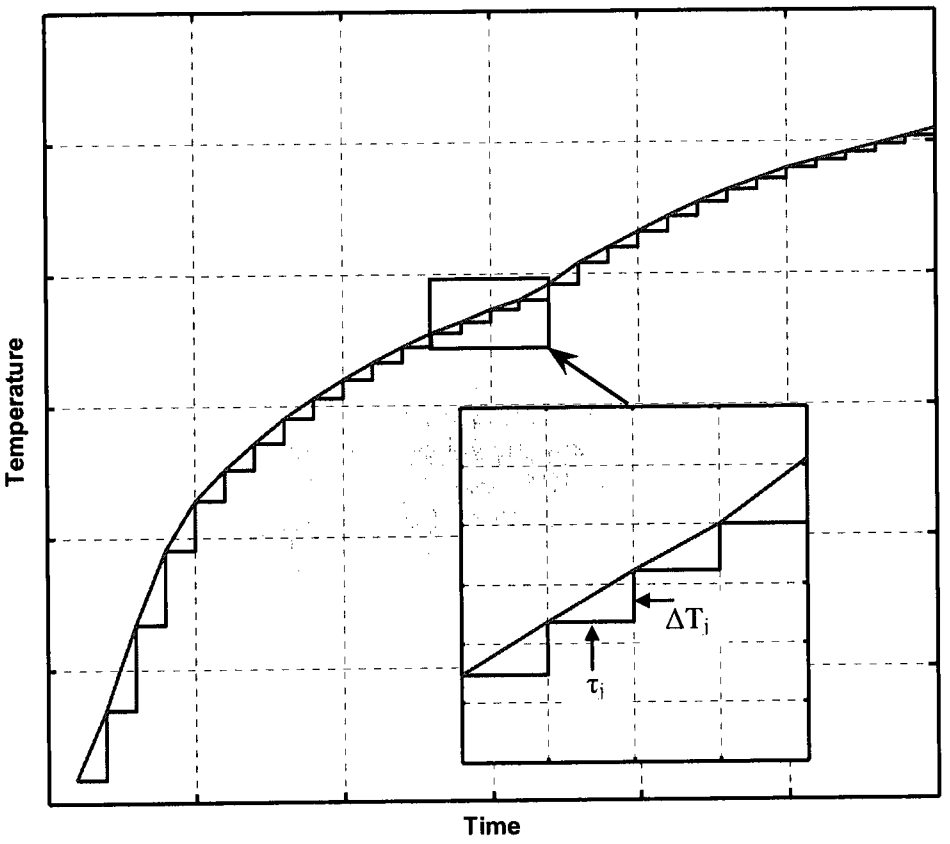

Figure 3.16. Discretized response of the secondary flow temperature.

3.8 Experimental procedure

1. Adjust appropriately all imaging equipment including the cameras and the lights to obtain desired field of view and focus.
2. Initialize the imaging system and Data Acquisition Software, and then run the labview program.
3. Open the main control valves then adjusted according to the required flow rate then close it through solenoid valves until the secondary flow steady state condition is achieved.
4. Open the secondary flow control valve and adjust the secondary flow rate according to the required blowing ratio then start to turn on the air heater. Meanwhile, the secondary flow is routed through the bypass solenoid valve until heating the secondary flow to the target temperature.
5. At that time, all operating conditions are fixed and the test rig is ready to record the data and images for a test period of 30 seconds. By pressing the start button through the labview software, the two main solenoid valves are opened at the same time, and the secondary flow is routed to pass to the plenum. The time delay between main and secondary solenoids valves can be controlled through the labview.
6. Based on the calibration curve, the target surface temperature distributions are determined using image processing MATLAB code.
7. The film cooling effectiveness and the heat transfer coefficient are determined for the entire downstream surface using the regression analysis method.

3.9 Uncertainty analysis

An error analysis is investigated to determine the accuracy in measuring the heat transfer parameters studied and the film cooling effectiveness. There are three types of errors; conservative error, relative uncertainty error for measuring quantities, and an average uncertainty error of the results. The error analysis is preformed using the same methodology of Kline and McClintock (1953). The accuracy for various measurement signals is presented in Table 3.1. The accuracy for the pressure transducer, multivariable flow transmitter, and thermocouples are based on the manufacturer specification. Typical uncertainty in TLC measurement is estimated to be ± 0.5 °C. As well, uncertainty of thermal conductivity and diffusively are estimated to be ± 3 %.

Table 3.1. Instruments accuracy.

Sensor	Accuracy
3095Mv multi-variable mass flow transmitter	Measuring differential pressure and static pressure, and temperature with 1% (for right length before and after the orifice)
Type-T thermocouple	Greater of 0.5°C or 0.4% of the reading
Type-E thermocouple	Greater of 1.0°C or 0.4% of the reading
2088G pressure transducer (0-75 psig)	± 0.2% of the span

The heat transfer coefficient over the flat plate can be presented as follows:

$h = f(T_w, T_m, T_j, T_i, t, \overline{\alpha}, k)$,

Therefore, uncertainty for the heat transfer coefficient is,

$Uh = U(T_w, T_m, T_j, T_i, t, \overline{\alpha}, k)$,

The variation in the parameters T_w, T_m, T_j, T_i, t, $\overline{\alpha}$, and k are δT_w, δT_m, δT_j, δT_i, δt, $\delta \overline{\alpha}$, and δk, respectively, which cause variation in δh.

It follows that:

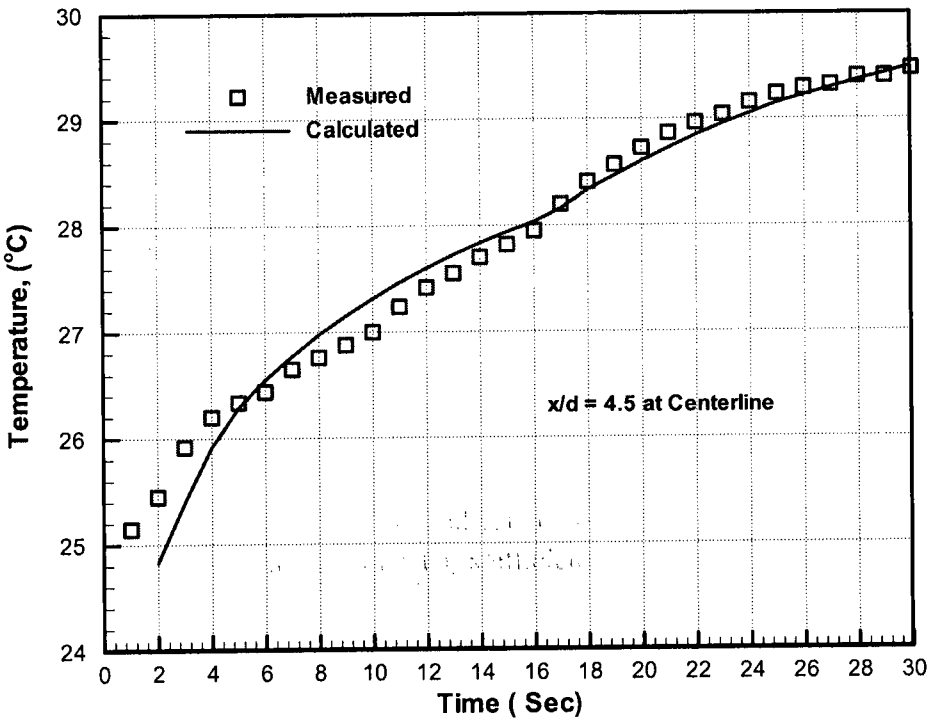

Figure 3.17. Temperature response and data fitting.

$$\delta h = \frac{\partial h}{\partial T_i}\partial T_i = \frac{\partial h}{\partial t}\partial t = \frac{\partial h}{\partial \overline{\alpha}}\partial \overline{\alpha} = \frac{\partial h}{\partial k}\partial k \,. \tag{3.24}$$

The relative variation in h is a function of all other uncertainty parameters;

$$\frac{\delta h}{h} = \frac{1}{h}\frac{\partial h}{\partial T_i}\partial T_i = \frac{T_i}{h}\frac{\partial h}{\partial T_i}\frac{\partial T_i}{T_i} = ,\ldots\ldots\ldots\ldots\ldots\ldots\frac{k}{h}\frac{\partial h}{\partial k}\frac{\partial k}{k} \,. \tag{3.25}$$

So that the heat transfer coefficient uncertainty from a single test can be presented as follows;

$$Uh = \pm\sqrt{\left(\frac{T_w}{h}\frac{\partial h}{\partial T_w}\frac{\partial T_w}{T_w}\right)^2 + \left(\frac{T_m}{h}\frac{\partial h}{\partial T_m}\frac{\partial T_m}{T_m}\right)^2 + \ldots\ldots\ldots\left(\frac{k}{h}\frac{\partial h}{\partial k}\frac{\partial k}{k_i}\right)^2} \,. \tag{3.26}$$

It is difficult to calculate the error for the heat transfer coefficient as in Eq. (3.26), where h is presented in a complex form in Eq. (3.20). Therefore, the above equation is simplified to use only the term of the square root of the summation of the squares of the relative uncertainty for measuring, in order to calculate the accuracy of the heat transfer coefficient, as shown in Eq (3.27).

$$Uh = \pm\sqrt{\left(\frac{\partial T_w}{T_w}\right)^2 + \left(\frac{\partial T_m}{T_m}\right)^2 + \left(\frac{\partial T_j}{T_j}\right)^2 + \left(\frac{\partial T_i}{T_i}\right)^2 + \left(\frac{\partial t}{t}\right)^2 + \left(\frac{\partial \overline{\alpha}}{\alpha}\right)^2 + \left(\frac{\partial k}{k}\right)^2} \,, \tag{3.27}$$

or

$$Uh = \pm\sqrt{(UT_w)^2 + (UT_m)^2 + (UT_j)^2 + (UT_i)^2 + (Ut)^2 + (U\overline{\alpha})^2 + (Uk)^2} \,. \tag{3.28}$$

As a result, the error for each measured variable should be determined in order to calculate the accuracy for the heat transfer coefficient using Eqs. 3.27 or 3.28. Accordingly, the average uncertainty for the heat transfer ratio (h_f/h_o), film cooling effectiveness, Frossling number, net heat flux reduction, and blowing ratio are calculated.

The uncertainty of the heat transfer coefficient is calculated using the root mean square as in Eq. (3.28), and the film cooling effectiveness uncertainty is calculated as the follows:

$$U\eta = \pm\sqrt{(UT_w)^2 + (UT_m)^2 + (UT_j)^2 + (UT_i)^2 + (Ut)^2 + (U\alpha)^2 + (Uk)^2 + (Uh)^2} \quad (3.29)$$

Moreover, the accuracy of measuring the blowing ratio can be calculated as the following:

$$Br = f(P, T_m, T_j, V, A),$$

Therefore, according to the same previous theory,

$$UBr = \pm\sqrt{\left(\frac{P}{Br}\frac{\partial Br}{\partial P}\frac{}{P}\right)^2 + \left(\frac{T_m}{Br}\frac{\partial Br}{\partial T_m}\frac{}{T_m}\right)^2 + \left(\frac{T_j}{Br}\frac{\partial Br}{\partial T_j}\frac{}{T_j}\right)^2 + \left(\frac{V}{Br}\frac{\partial Br}{\partial V}\frac{}{V}\right)^2 + \left(\frac{A}{Br}\frac{\partial Br}{\partial A}\frac{}{A}\right)^2} \quad (3.30)$$

The current results are tested at atmosphere pressure; hence, the error due to pressure is neglected in Eq. (3.30).

As a result, the uncertainty of each calculated parameter varies from one test to another. The uncertainty value for these parameters will be presented in the next chapters.

3.10 Benchmark study

The performance of the film cooling effectiveness and heat transfer coefficient for circular film holes is compared with previous published data in order to validate the current experimental techniques and methodology. The cylindrical film geometry has been selected since it is the most frequently used baseline geometry in previous research. The film hole with a diameter of 1.39 cm, L/d = 4, and p/d = 3 with an inclination angle of 35° and 0° compound angle is used for validation. One row with a single hole is tested. Figures 3.18a and 3.18b present the test section configuration for the circular film hole over flat plate including the main and the secondary streams

directions. The test section for benchmark case is made from Plexiglas material with 3.2 cm thickness.

3.10.1 Benchmark geometry and boundary conditions

A circular film hole is selected to validate the output results of film cooling and heat transfer using current experimental techniques and methodology. Many researchers using various techniques under different laboratory environments investigated the film cooling performance of the circular hole with a 0^{o} compound angle (CA) over a flat plate experimentally. Different techniques were used through literature review to measure surface temperature for instance thermocouples, TLC, Infrared (IR), and pressure sensitive paint (PSP) techniques. The film cooling effectiveness and heat transfer coefficient are calculated based on measured surface temperatures and flow conditions. The bottom part of the main test section is designed to be replaced by different test sections with different film hole geometries or with metal plate for TLC calibration, as well as for measuring heat transfer coefficients without film cooling. After assembling the test section, the plenum is fixed underneath the test section to be at the central of the inlet film cooling holes. In addition, the secondary pipe line is connected to the plenum through a NPT 3/4" fitting. Table 3.2 presents the test matrix for validation study using the circular film hole. The circular film hole is tested for blowing ratios of 0.5 and 1.0. A single transient test is used for each blowing ratio. The secondary flow is heated, but the main flow is kept at air supply temperature. The density ratio between the secondary and main flow is 0.94. The main flow is fixed but the secondary flow is changed in order to achieve the required blowing ratio. The operating secondary flow temperature is adjusted to be greater than main flow temperature by 20-30°C.

Table 3.2. Test matrix for benchmark study.

Br	Dr	I	Re_{Deq} (duct)	Re_d (hole)
0.5	0.94	0.272	1.16×10^5	1.25×10^4
1.0	0.94	1.085	1.16×10^5	2.5×10^4

3.10.2 Film cooling effectiveness

Local centerline film cooling effectiveness for the present circular hole at Br = 0.5 and 1.0 is compared to published data, as shown in Figs. 3.19a and 3.19b. The results show an agreement of more than 90 % of the centerline film cooling effectiveness with published data at Br = 0.5, by Russin et al. (2009) at Br = 0.5, and Ekkad et al. (1997) for x/d > 6, and Br = 0.5, and with Ekkad et al. (1997), Couthard et al. (2006), and Yu et al. (2002) at Br = 1.0, as shown in Figs. 3.19a and 3.19b. However, there is a distinct difference between the present results and published data near the injection hole at low and high blowing ratios, which is expected to be due to 3D flow structure in this region, which subsequently increases the error of image processing. The results for Coulthard et al. (2006) provided the highest value compared to other studies since they calculated film cooling effectiveness based on adiabatic wall conditions ($T_f = T_w$). Figure 3.20 illustrates streamwise variation of laterally averaged film cooling effectiveness results for the present circular hole with published data at blowing ratios of 0.5 and 1.0. The results show that there is a good agreement between the present obtained results and published data by Ekkad et al. (1995) at low and high blowing ratios. The present spanwise average film cooling effectiveness sets between the results of Yu et al. (2002) and Lee et al. (2002) at Br = 0.5, as shown in Fig. 20a. At a high blowing ratio (Br = 1.0), the provided data by Lee et al. (2002) has a higher value of the laterally averaged film cooling effectiveness than the present obtained results near the film hole injection. The spanwise-average film cooling effectiveness

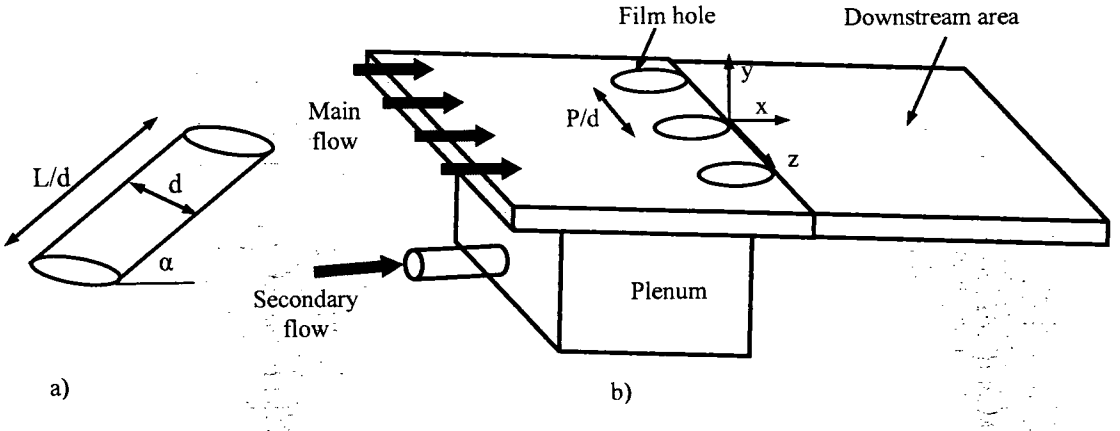

Figure 3.18. Configuration of circular hole over a flat plate.

results for a circular hole by Yu et al. (2002) provides the highest value compare to other results, as shown in Fig. 20b.

3.10.3 Heat transfer

Figure 3.21 presents a comparison of centerline heat transfer coefficient ratio between the present obtained results of the circular hole and published data at blowing ratios of 0.5 and 1.0. From the results, there is a good agreement at $x/d > 3$ between the present obtained results and the provided data for a circular hole by Ekkad et al. (1995), Sen et al. (1996) and Gritsch et al. (1998) at Br = 0.5, as shown in Fig.3.21a. The disparity error between the predicted results and the published data decreases along the downstream direction and it increases near the injection hole, as shown in Fig. 3.21a. At high blowing ratio, the heat transfer coefficient ratio presented a covenant, within experimental uncertainty (± 12%) with Sen et al. (1996), and Gritsch et al. (1998), as shown in Fig.3.21b. Also, there is an agreement of centerline heat transfer ratio between the present result and Sargison et al. (2002) at $x/d > 5$ (Fig.3.21b), but there is disagreement in the region near the exit hole ($x/d < 5$). Moreover, there is a good agreement between the obtained laterally averaged heat transfer coefficient ratio and published data by Yu et al. (2002) and Kim et al. (2001) at Br = 0.5, as shown in Fig. 3.22. As a result, the test rig validation with other published data gave good agreement within the experimental uncertainty, such that the current experimental technique and methodology are deemed reliable.

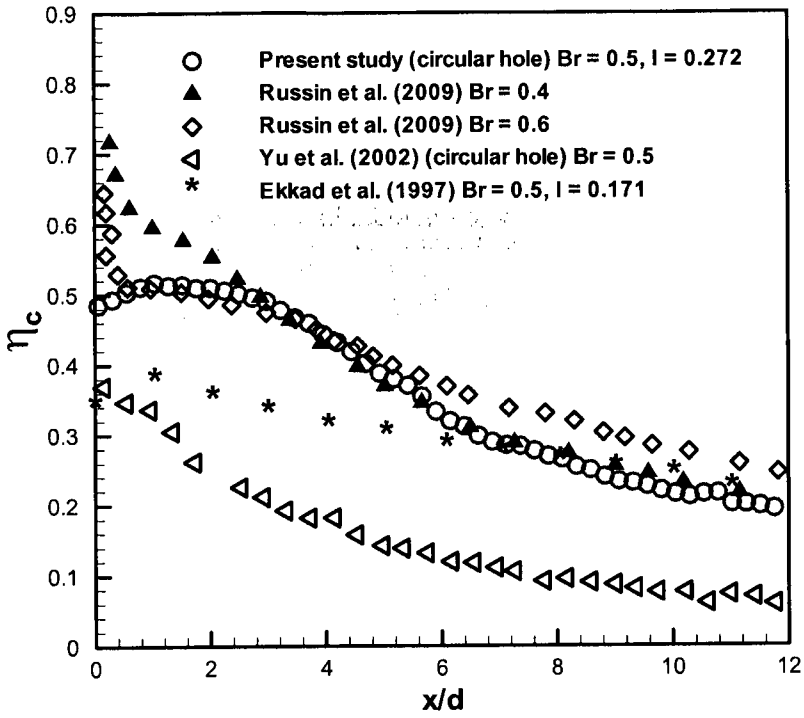

a) Br = 0.5

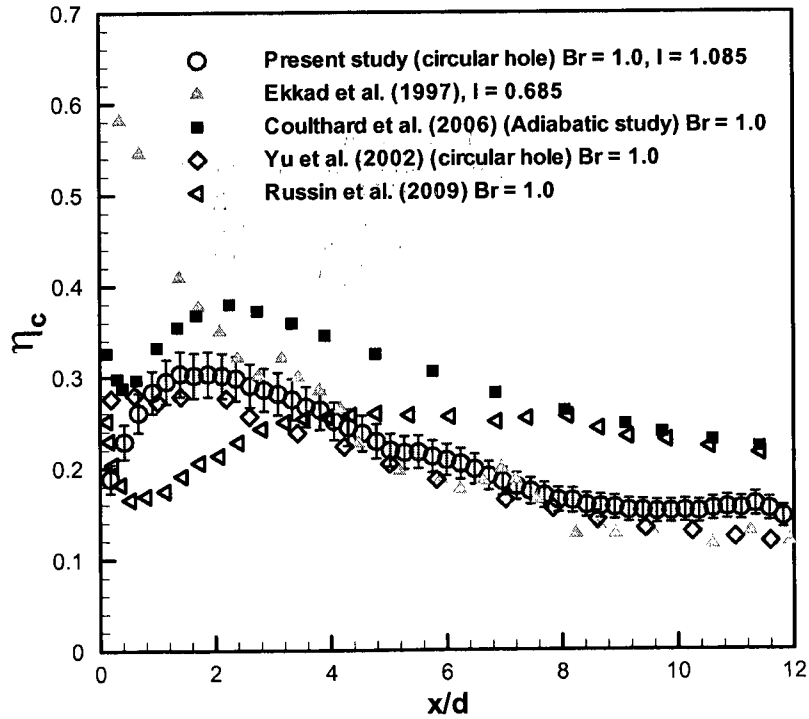

b) Br = 1.0

Figure 3.19. Streamwise comparison of centerline film cooling effectiveness with published data.

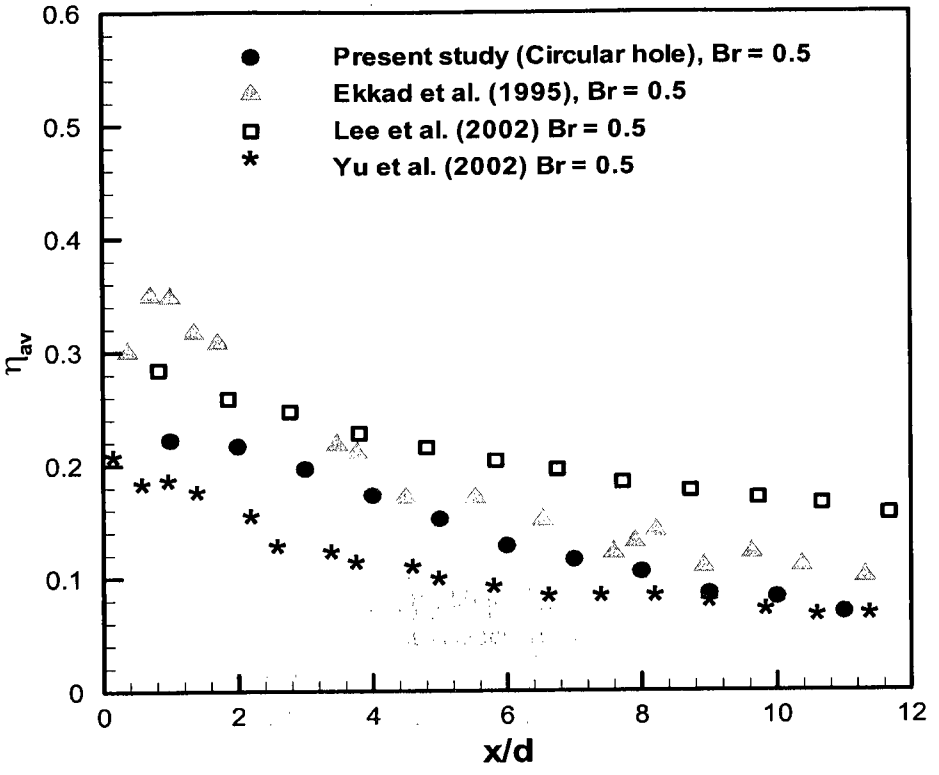

a) Br = 0.5

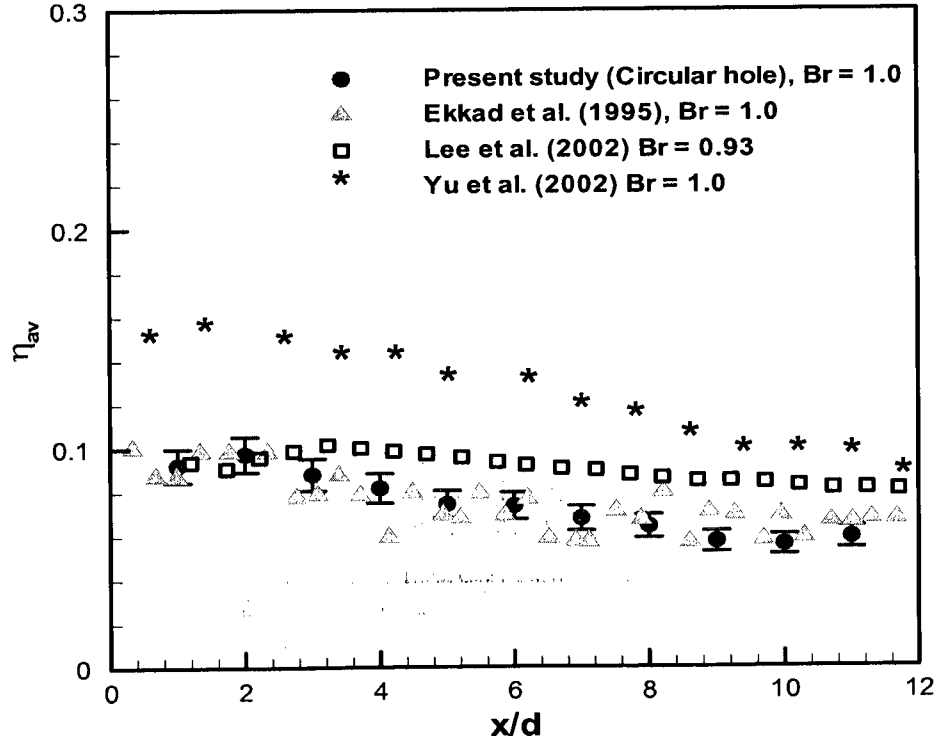

b) Br = 1.0

Figure 3.20. Streamwise comparison laterally averaged film cooling effectiveness of the present result with published data.

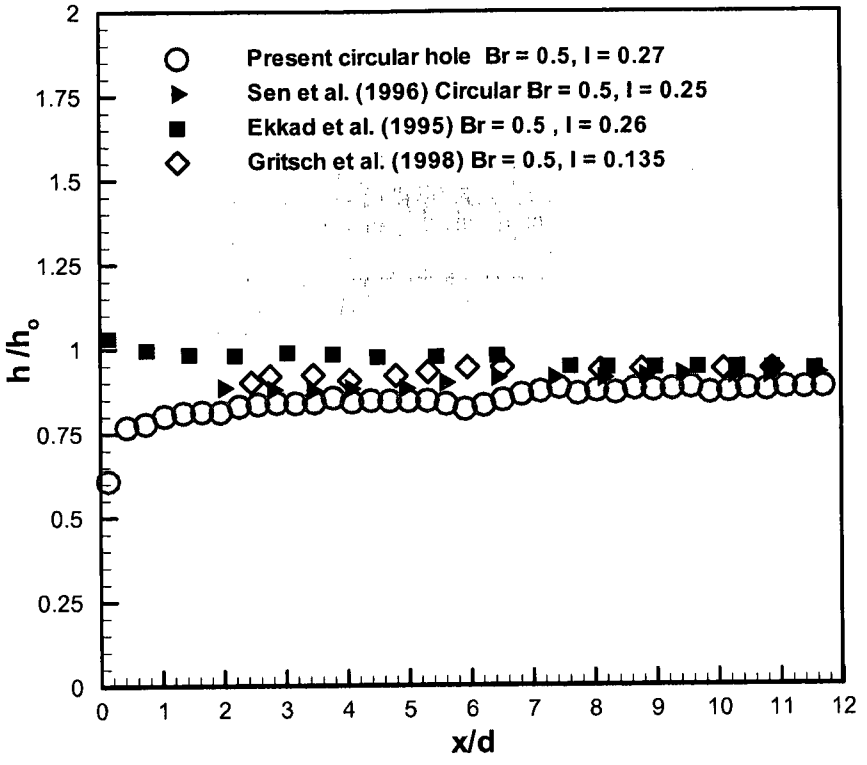

a) Br = 0.5

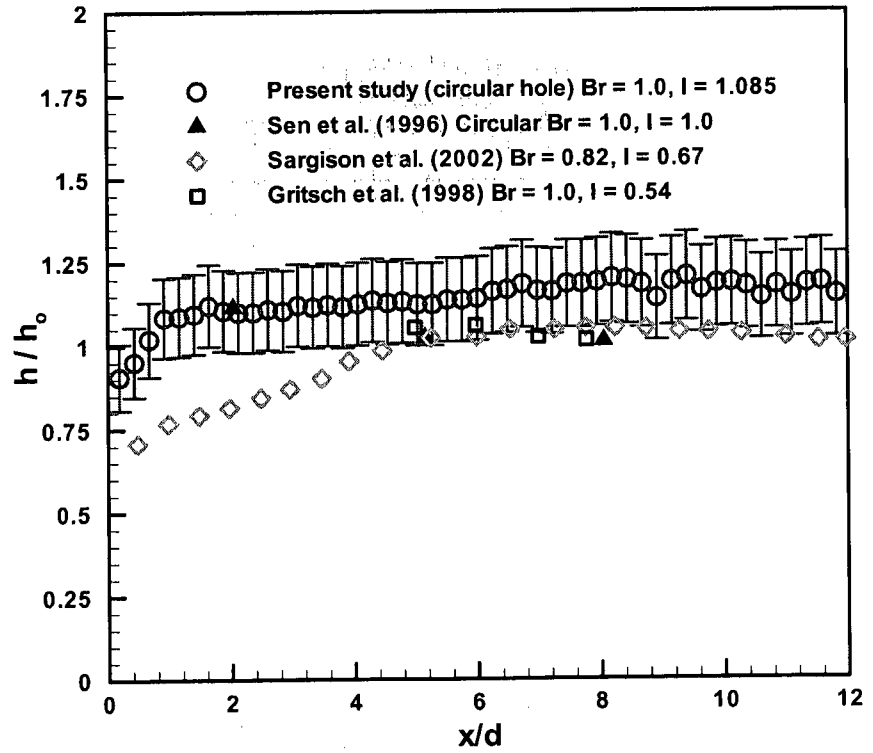

b) Br = 1.0

Figure 3.21. Streamwise comparison of centerline heat transfer ratio of present circular hole with published data.

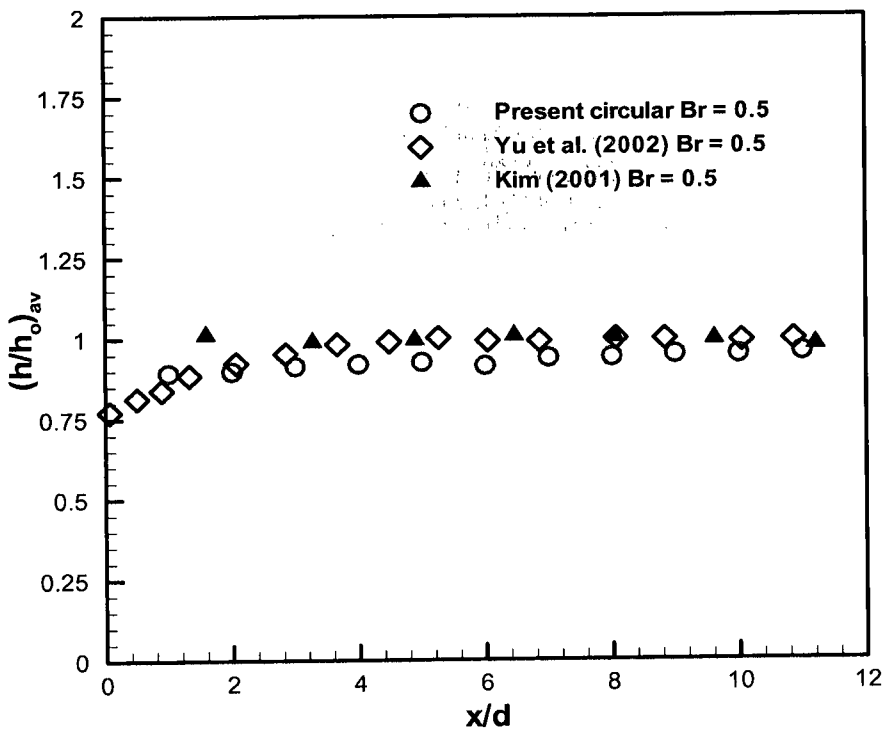

Figure 3.22. Comparison of laterally averaged heat transfer ratio of the present circular hole with other published data.

Chapter 4

Chapter 4 Film Cooling Performance of the Louver Scheme

The film cooling performance for the louver scheme was investigated numerically by Immarigeon and Hassan (2006) then by Zhang and Hassan (2006). They concluded that the louver scheme enhanced film cooling effectiveness and reduced the heat transfer coefficient over the downstream surface area as compared to other published schemes. The scheme was designed to combine the advantages of traditional film cooling and the impingement effect. In this chapter, the film cooling performance for the louver scheme will be tested experimentally over a flat plate using the TLC technique across different blowing ratios using a 0.94 density ratio.

4.1 Louver scheme geometry and operating conditions

Figure 4.1 shows a schematic for utilizing the louver film hole configuration on an airfoil and a simplified sketch for the scheme on a flat plate. The louver scheme combines film cooling and impingement effects. The secondary flow passes through a bend that impacts the inner blade material (impingement effect) then exits to the outer surface of the airfoil through the film cooling holes with less jet lift-off. Table 4.1 lists the test conditions and geometrical parameters for the louver scheme. The main and secondary stream Reynolds numbers are calculated based on the hydraulic diameter of the main duct, and film hole diameter, respectively.

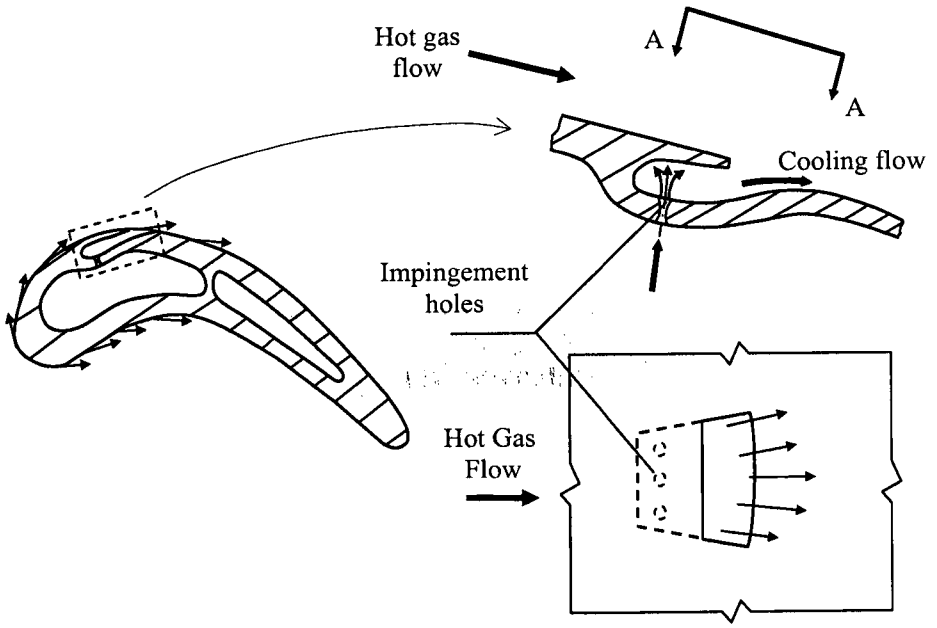

a) On an airfoil

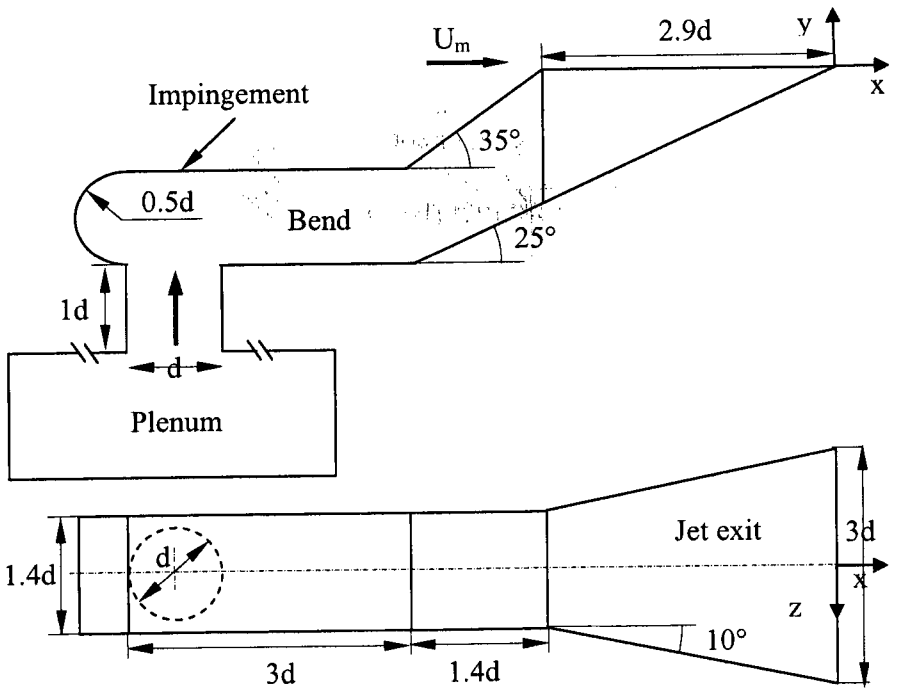

b) over a flat plate

Figure 4.1. Louver film hole geometry.

Table 4.1. Geometrical parameters and measurement conditions of louver scheme.

Parameters	Louver scheme
d (cm)	1.27
p/d	3
Br	0.5, 1.0, 1.5
Dr	0.94
I	0.27, 1.071, 2.385
Re_D (duct)	1.24×10^5
Re_d (hole)	1.23×10^4, 2.47×10^4, 3.68×10^4

4.2 Results and discussion

Figure 4.2 demonstrates historical temperature profile at Br = 1.5, downstream of the trailing edge of the louver scheme at two different span-wise locations: z/d = 0.0 and 1. The secondary flow is heated, while the main flow is kept at supply air temperature. The secondary flow sprays widely over the target surface when it is expelled from the louver hole, consequently changing the TLC colors with the time from black to red then to green followed by blue, as illustrated in Fig. 4.2a. The temperature profiles have a high value at z/d = 0.0 and it diminishes faintly along the downstream and span-wise directions and it increases with time as shown in Fig. 4.2b. The results show that there is no variation in centerline temperature profiles for x/d < 3 with the time after 10 sec where the secondary flow starts to spray more, further downstream as shown in Fig. 4.2b. The temperature profiles increase with time for x/d $\geq$ 3 in the streamwise direction, near the hole center, as well for z/d > 0 in the span-wise direction.

4.2.1 Film cooling effectiveness

Figures 4.3a and 4.3b show the centerline film cooling effectiveness performance at blowing ratios of 0.5 and 1.0 for the louver scheme, compared to

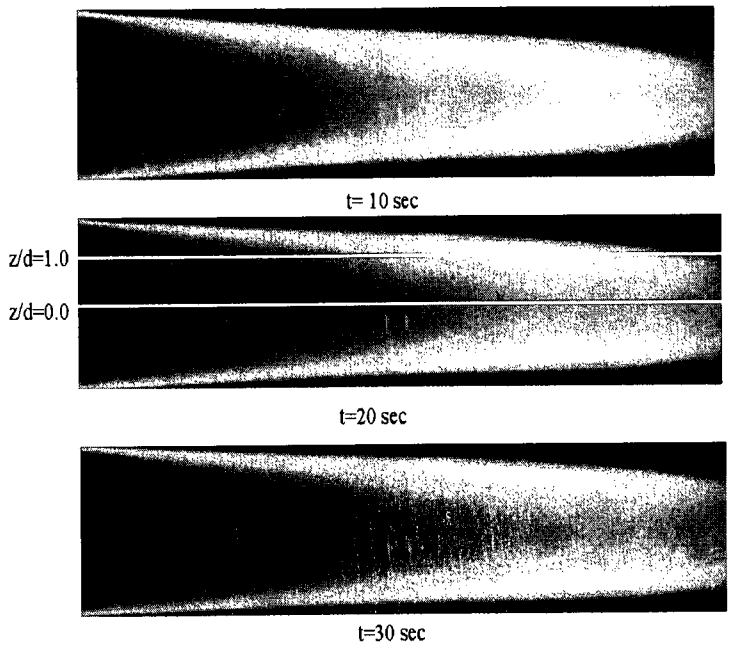

a)

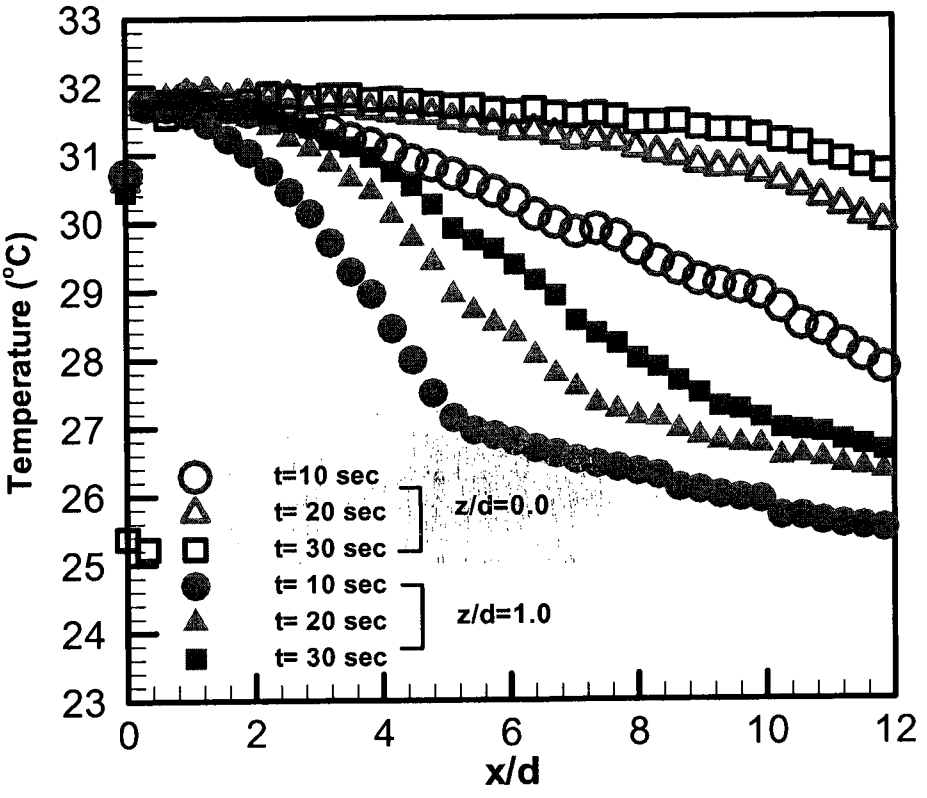

b)

Figure 4.2. Historical downstream TLC images and temperature profiles for louver scheme at different span-wise locations (Br = 1.5).

circular and shaped film holes. At a low blowing ratio (Br = 0.5), the secondary flow exits the circular film hole then sprays over the surface and provides better film cooling performance along the centerline than the shaped hole (Yu et al., 2002). The louver scheme provides enhancement of the film cooling effectiveness over the surface compared to circular and shaped film holes, especially close to the jet holes. The secondary flow jet lifts off and penetrates the main stream at high blowing ratios for a circular hole (Jessen et al. 2007), so it does not attach to the downstream surface after it exits from jet holes. As a result, the film cooling effectiveness is reduced at high blowing ratios, compared to low blowing ratio results. Film cooling holes with large exit areas enhance the film cooling performance (Taslim and Khanicheh, 2005) since there is a reduction in the secondary flow momentum, with more uniformity at the jet exit, which reduces the jet lift-off. Consequently, the film cooling effectiveness performance for the fan shaped holes of Yu et al. (2002), and Goldstein et al. (1974), provide higher performance at high blowing ratios compared to circular holes, as shown in Fig. 4.3b.

The results show that the louver scheme provides the highest film cooling effectiveness performance at high blowing ratios compared to the fan shaped and circular holes. The film cooling effectiveness increases for the louver scheme due to the impingement effect of the secondary flow after it exits from the impingement jet hole, thus the flow momentum is reduced, which reduces the jet lift-off. Moreover, the secondary flow momentum becomes more uniform at the film hole exit (Zhang, X., 2004), so the secondary flow attaches to the downstream surfaces after exiting from the film hole, thereby producing the highest film cooling effectiveness. The film cooling effectiveness decreases gradually in the streamwise direction due to a decrease in the secondary flow momentum.

Figure 4.3b presents a comparison between the film cooling performances of the louver scheme and numerical results by Zhang (2008), at Br = 1.0. The numerical data for the centerline film cooling effectiveness over predicted the obtained experimental data by 10 %. The density ratio used in the numerical study is about 2.13 times that used in the experimental study, and the film cooling effectiveness increases with density ratio (Ekkad et al. 1997). Higher density ratios can be achieved in the laboratory by using gases other than air for the secondary flow. Downstream boundary assumption is the second reason for the differences between experimental and numerical results: it is assumed to be adiabatic in the numerical study while heat losses could not be averted in the experimental test.

The local comparison for film cooling effectiveness is very important, although a global performance is essential in order to evaluate the overall film cooling performance for the film cooling geometries. The laterally averaged film cooling performance for the louver scheme is compared with other traditional and advanced published film hole geometries at blowing ratios of 1.0 and 1.5, as shown in Fig. 4.4. A wider film hole exit area produces higher laterally averaged film cooling effectiveness close to the hole exit. At a high blowing ratio (Br = 1.0), the louver scheme directs the jet flow in the horizontal direction based on the downstream velocity profiles by Zhang (2004, 2008), hence, the film cooling performance increases downstream of the film holes with wider effect (Fig. 4.4a). The results show that the louver scheme provides the highest lateral average film cooling effectiveness with respect to the other film holes such as traditional circular hole, forward and lateral shaped hole (Yu et al., 2002), and console film hole (Sargison et al., 2002) for $x/d > 4$. The jet lift-off increases with blowing ratio for other traditional film holes (Jessen et al. 2007) but the louver scheme is able to adjust the coolant momentum in

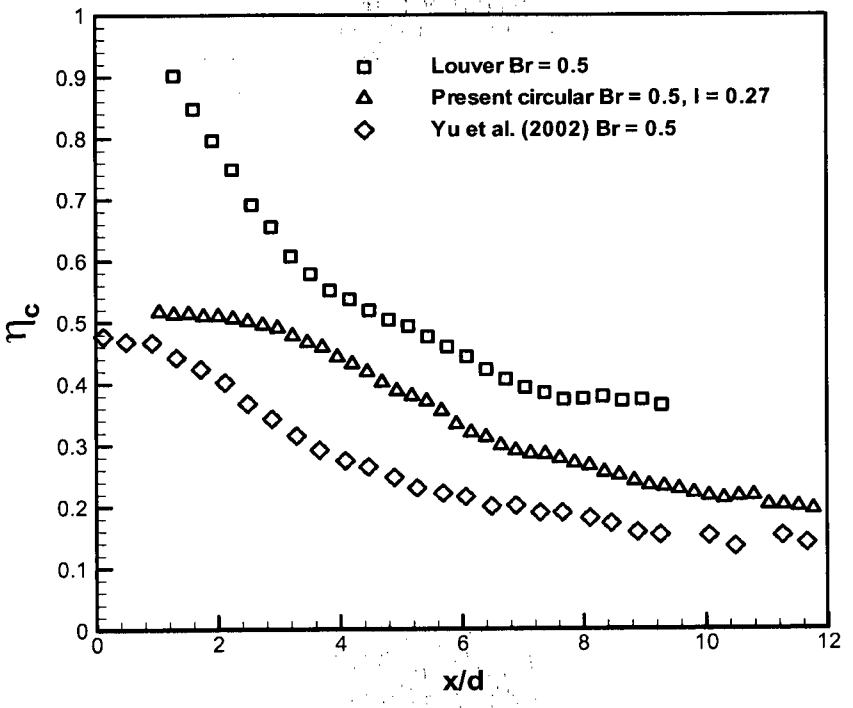

a) Br = 0.5

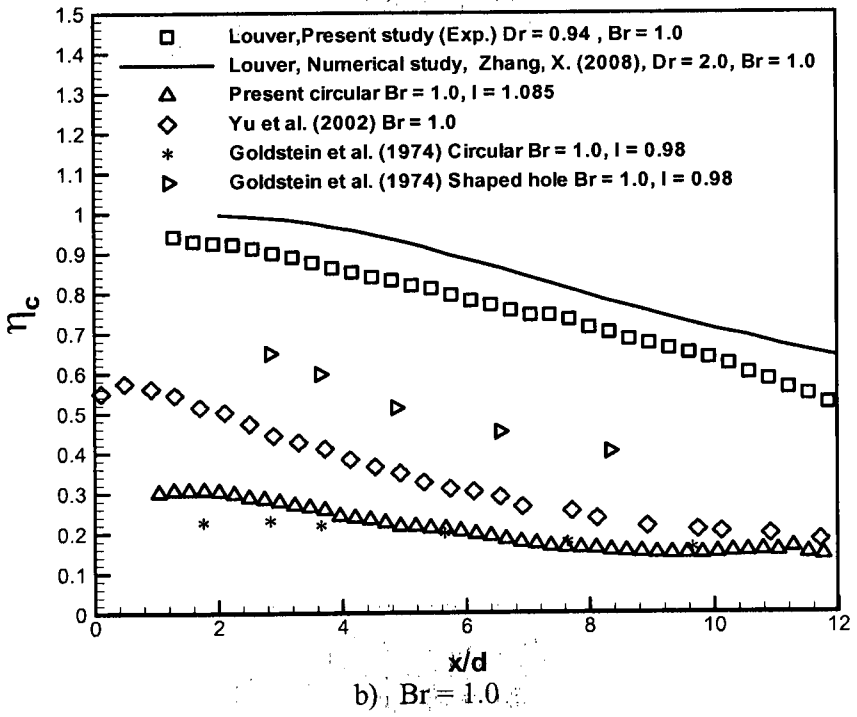

b) Br = 1.0

Figure 4.3. Centerline film cooling effectiveness performance for louver scheme compared to other published data at low and high blowing ratios.

the horizontal direction at high blowing ratios (Zhang and Hassan 2006). Therefore, the louver scheme provides the highest lateral average film cooling effectiveness at Br = 1.5, as shown in Fig. 4.4b, compared to experimental data for the straight fan shaped holes by Dittmar et al.(2003), fan shaped holes by Lu et al. (2009) and numerical data for fan shaped with trench holes by Baheri et al. (2008).

The film cooling effectiveness performance of the louver scheme at Br = 1.0 is presented in Fig. 4.5. The film cooling effectiveness performance has a wider effect in the spanwise direction at $x/d < 2$, which means that the louver scheme enhances the laterally film cooling effectiveness. The louver scheme provides speared peak performance in the spanwise direction, but other film hole geometries produce a peak point. The film cooling performance of the louver scheme has a wider film cooling effectiveness near the centerline along the downstream direction, up to $x/d = 10$. After this point, the scheme provides a pronounced peak of film cooling effectiveness at the centerline with the highest performance compared to the fan shaped hole with trench (Baheri et al. 2008). The film cooling effectiveness gradually decreases along the streamwise direction due to decreasing the secondary flow momentum.

Figure 4.6 presents the effect of blowing ratio on the centerline and lateral film cooling effectiveness, as well the downstream contours at region $-1.5 < z/d < 1.5$ in the spanwise direction and $0 < x/d < 15$ in the streamwise direction. The results show an enhancement of the film cooling effectiveness downstream from the film holes with an increase in blowing ratio. The centerline film cooling effectiveness has the highest value, close to 1.0, at high blowing ratios in the region of $x/d < 3$. At high blowing ratios, the secondary flow is distributed laterally far downstream, which is followed by an increase the lateral film cooling effectiveness performance.

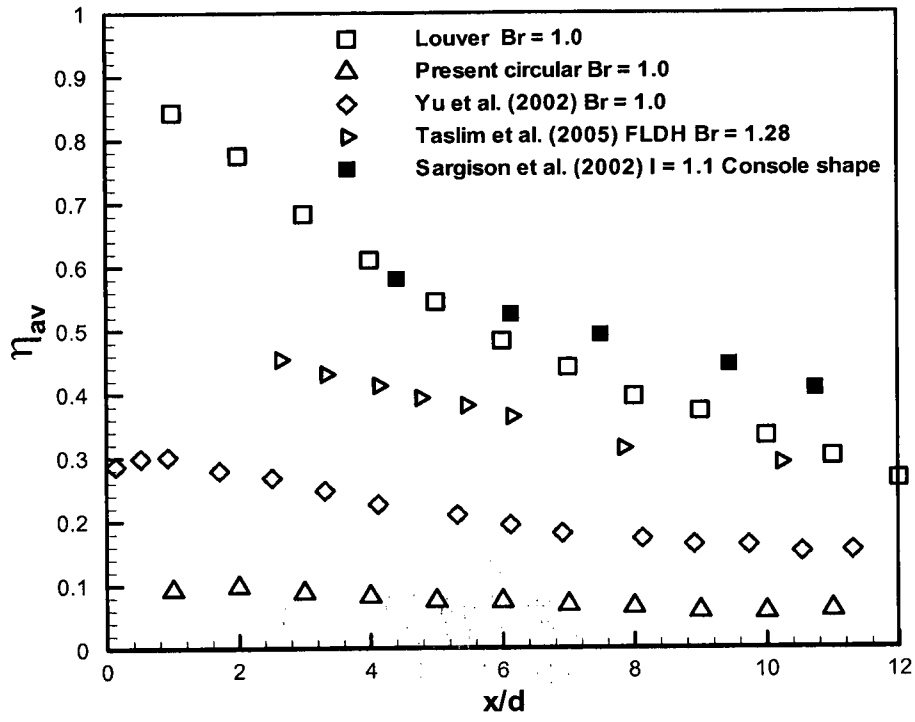

a) Br = 1.0

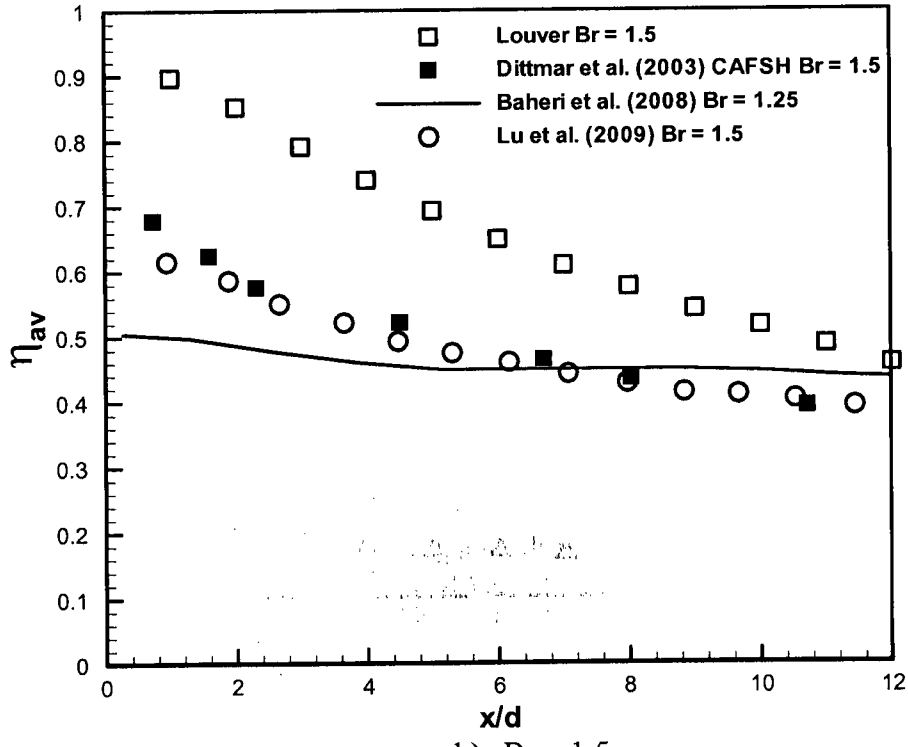

b) Br = 1.5

Figure 4.4. Laterally averaged film cooling effectiveness performance of the louver scheme at a high blowing ratios.

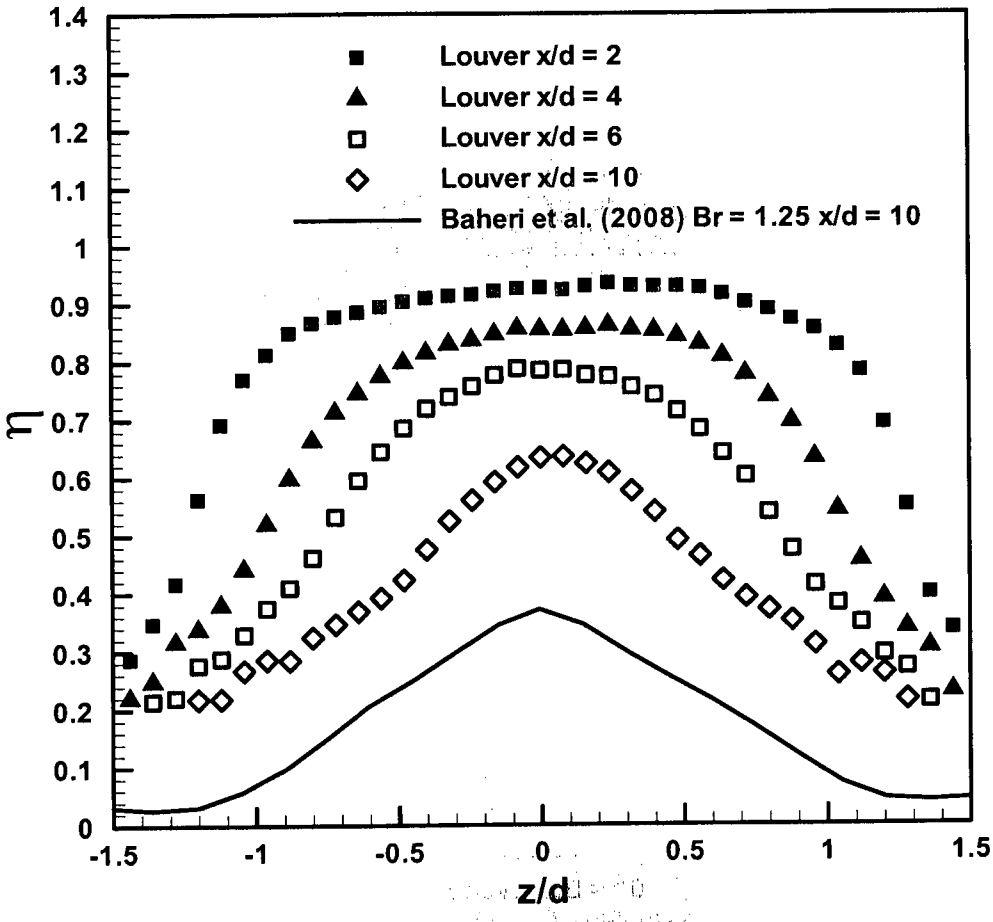

Figure 4.5. Spanwise film cooling effectiveness performance for louver compared to other film hole schemes at Br = 1.0.

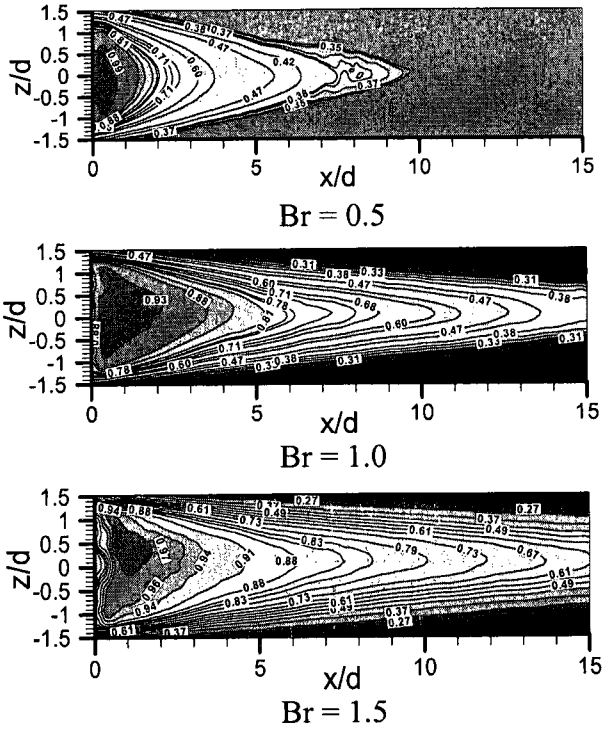

a) Effectiveness contours

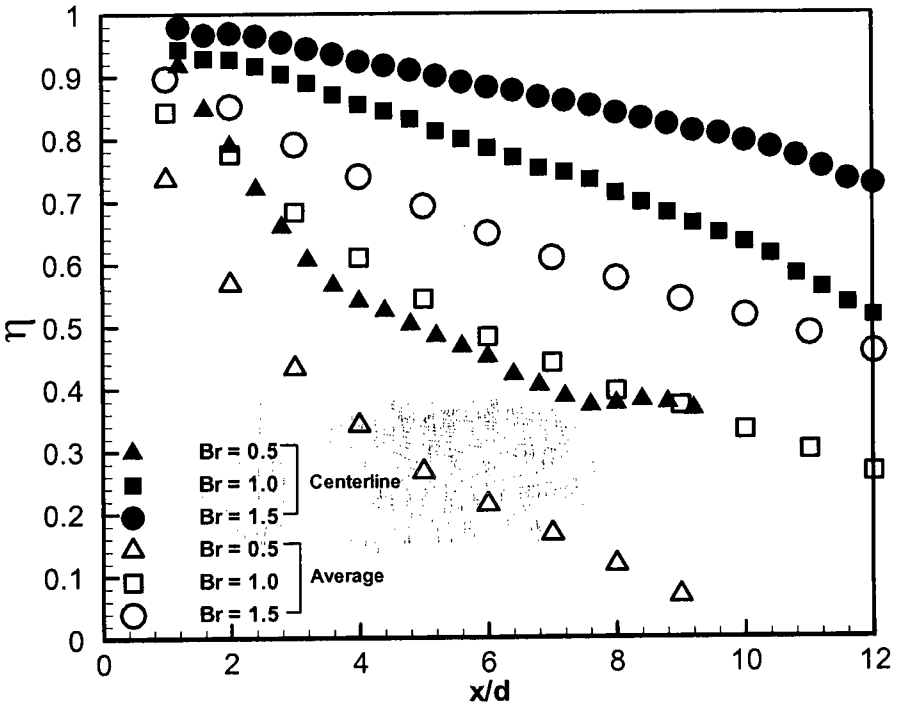

b) Centerline and average film cooling effectiveness

Figure 4.6. Effect of blowing ratio on downstream film cooling effectiveness for louver scheme.

Surface film cooling effectiveness contours for the louver scheme at blowing ratios of 1.0 and 1.5 are presented in Figs. 4.7a and 4.7b, respectively. The contours display an inclusive performance of the louver scheme at high blowing ratios. The maximum value of film cooling effectiveness is achieved at the central line of the film hole and the value is not a pronounced peak point but a line with a length around 2d in the spanwise direction. The maximum lateral film cooling effectiveness has a wide performance near the film hole exit and decreases to a peak point far along the downstream direction. The lateral film cooling performance is further enhanced with increasing blowing ratios. The main reason for that is the large and wide exit area film hole for the louver scheme, which leads the momentum flux of the secondary flow to become more uniform at the exit area, thereby reducing jet lift-off. Therefore, the secondary flow is sprayed widely over the surface. Traditional film holes provide a maximum peak point at z/d = 0.0. As a result, the louver scheme is able to provide better film cooling effectiveness distribution on the downstream surfaces' area.

4.2.2 Heat transfer performance

Streamwise variations of the centerline heat transfer coefficient ratio (h_f/h_o) for the louver scheme and other film holes are illustrated in Figs. 4.8a and 4.8b at 0.5 and 1.0 blowing ratios, respectively. Near the injection hole, at a low blowing ratio, the louver scheme produces variations in the heat transfer ratio similar to the circular hole of the present study and Sen et al. (1996). However, it provides a higher value downstream, as shown in Fig. 4.8a. The heat transfer coefficient ratio increases with blowing ratio for traditional film cooling holes, but it is unvarying for the louver scheme as shown in Fig. 4.8b for Br = 1.0. From the results, the heat transfer coefficient ratio for the present

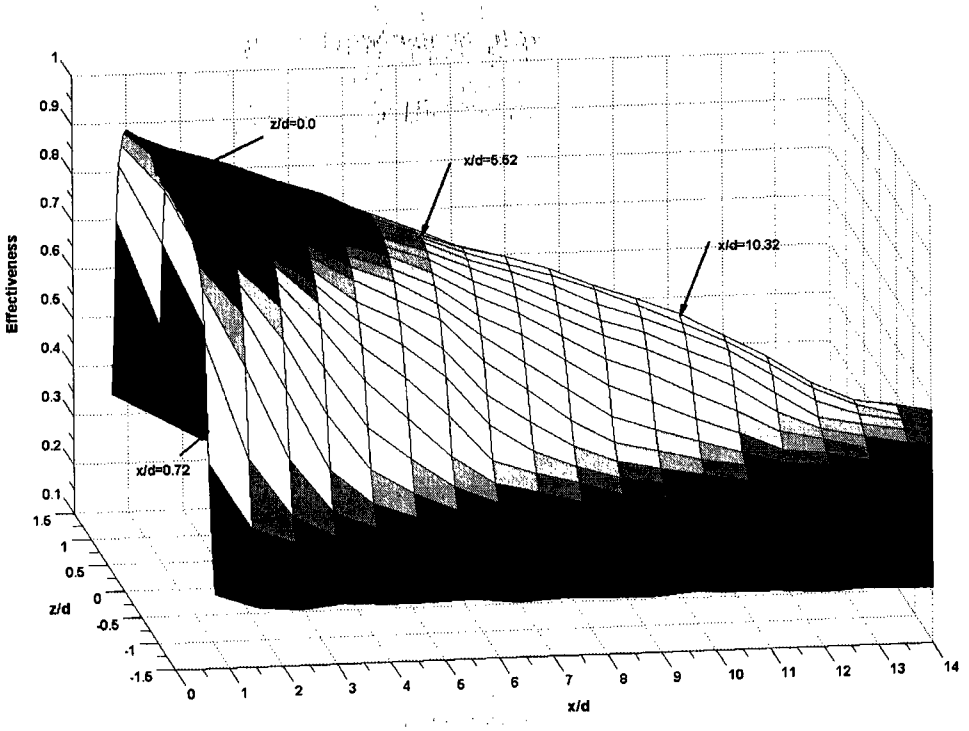

a) Br = 1.0

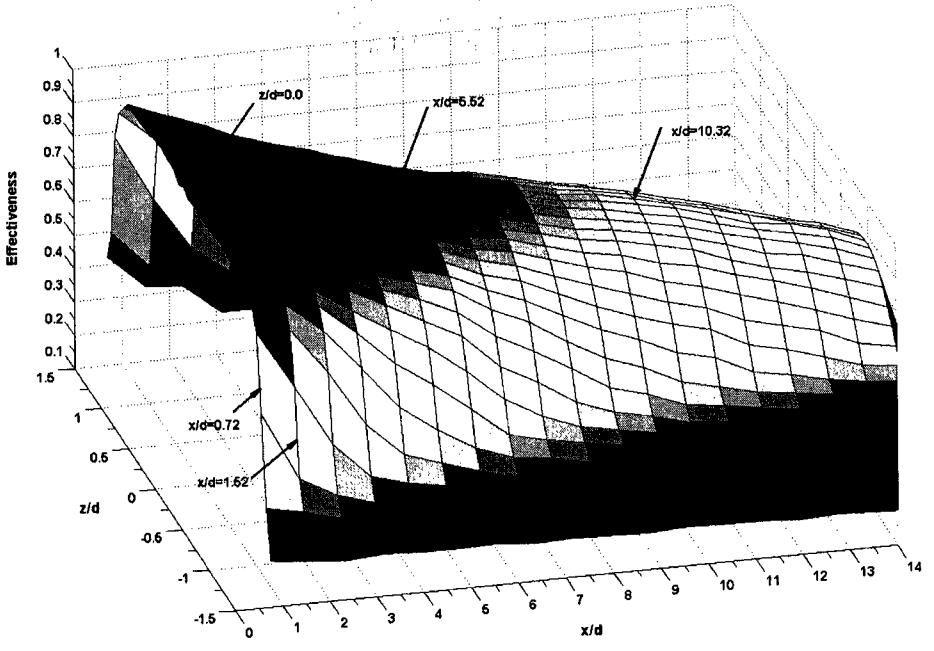

b) Br = 1.5

Figure 4.7. Film cooling effectiveness surface contours for the louver scheme at different blowing ratios.

circular film hole, as well as the holes studied by Sen et al. (1996), Eriksen and Goldstein (1974) and Gritsch et al. (1998), have high values compared to that for the louver scheme, as shown in Fig. 4.8b at a high blowing ratio. The louver scheme is expected to create a thin layer of the secondary flow over the surface, which reduces the turbulent vortices downstream from the film holes, according to results presented by Zhang and Hassan (2006) and Zhang (2004). Therefore the ratio of h_f/h_o is invariable downstream with variations in blowing ratio. At Br = 1.0, the results show a good conformity between the experimental and numerical data (Zhang 2004) of heat transfer coefficient ratio for the louver scheme as displayed in Fig.4.8b.

Laterally averaged heat transfer coefficient ratio (h_f/h_o) profiles in the streamwise direction for the louver scheme and other published film hole geometries, at low and high blowing ratios, are presented in Figs. 4.9a and 4.9b, respectively. The laterally averaged value of h_f/h_o for straight fan shaped holes (Dittmar et al., 2003), is equal to 1.2 at a blowing ratio of 0.5 along the downstream direction. Straight fan shaped holes (Dittmar et al. 2003) produce a higher heat transfer ratio compared to other film hole geometries, such as fan shaped (Yu et al.,2002, and Saumweber et al.,2003), the present circular study, circular holes (Jubran and Maiteh, 1999), for two rows of holes (Ligrani et al., 1994), and the louver holes. The laterally averaged h_f/h_o for the louver scheme is similar to the fan shaped results by Yu et al. (2002). The heat transfer coefficient ratio (h_f/h_o) results for the fan shaped holes (Yuen and Martinez, 2005) produce the highest value close to the hole injection, and provides a similar trend as observed by Dittmar et al. (2003) for x/d > 2.5, as shown in Fig. 4.9a. At Br = 1.0, heat transfer ratio results for the shaped hole (Yuen and Martinez, 2005) have the highest value compared to that of Yu et

al. (2002) and the louver scheme as presented in Fig. 4.9b. The laterally averaged h_f/h_o performance increases more with blowing ratio for the two rows arrangement. The ratio of h_f/h_o for the louver scheme increases gradually along the downstream direction until it reaches unity, since the heat transfer coefficient increases far downstream with less film cooling effectiveness.

The main flow velocity and film hole geometry have significant effects on the heat transfer ratio. The Frossling number is investigated for the louver scheme. The dimensionless number ($Nu/\sqrt{Re}$) combines the effect of the main flow velocity, heat transfer coefficient, and film hole exit area. The Reynolds number is calculated based on main stream velocity and hydraulic diameter for the film hole exit. Figure 4.10 presents the effect of the blowing ratio on the laterally averaged Frossling number at two downstream locations (x/d = 2.0 and 6.0) for the circular hole and the louver scheme. From the results, there is a reduction in Frossling number for the circular film hole with an increase in the blowing ratio due to jet lift-off but there is no significant effect in the downstream direction at low blowing ratio. The Frossling number increases from 0.9 to 1.0 by increasing the blowing ratio from 0.5 to 1.0 for the louver scheme, but decreases again with an increase in blowing ratio since the heat transfer decreases undersized for blowing ratios greater than unity. Moreover, the Frossling number has insignificant effects in the downstream direction, at low and high blowing ratios.

4.2.3 Net heat flux reduction

The film cooling effectiveness and heat transfer coefficient are combined in order to evaluate the film cooling performance for the film hole geometries using the net heat

flux reduction (NHFR). The derivation of the NHFR is presented in Eqs. 4.1 to 4.5, and was presented earlier by Sen et al. (1996) and Gritsch et al. (2000).

The heat flux with and without film cooling can be presented as:

$$q_f = h_f(T_f - T_w), \tag{4.1}$$

$$q_o = h_o(T_m - T_w). \tag{4.2}$$

Therefore, the heat flux ratio is:

$$\frac{q_f}{q_o} = \frac{h_f(T_f - T_w)}{h_o(T_m - T_w)}. \tag{4.3}$$

For $\theta = \dfrac{(T_m - T_j)}{(T_m - T_w)}$, and $\eta = \dfrac{(T_f - T_m)}{(T_j - T_m)}$

Thus

$$\frac{q_f}{q_o} = \frac{h_f}{h_o}(1 - \eta * \theta) \tag{4.4}$$

$$NHFR = 1 - \frac{q_f}{q_o} = 1 - \left(\frac{h_f}{h_o}(1 - \eta * \theta)\right), \text{ and } \theta = 1/\varphi. \tag{4.5}$$

where φ is the overall cooling effectiveness, which has value from 0.5 to 0.7 in a real engine.

$$\phi = \frac{\beta * \eta_{cov} + \eta_f(1 - \eta_{cov})}{1 + \eta_{cov}(\beta - \eta_f)}. \tag{4.6}$$

The convective efficiency and film effectiveness are represented by η_{cov} and η_f, respectively, while β is heat load to the part.

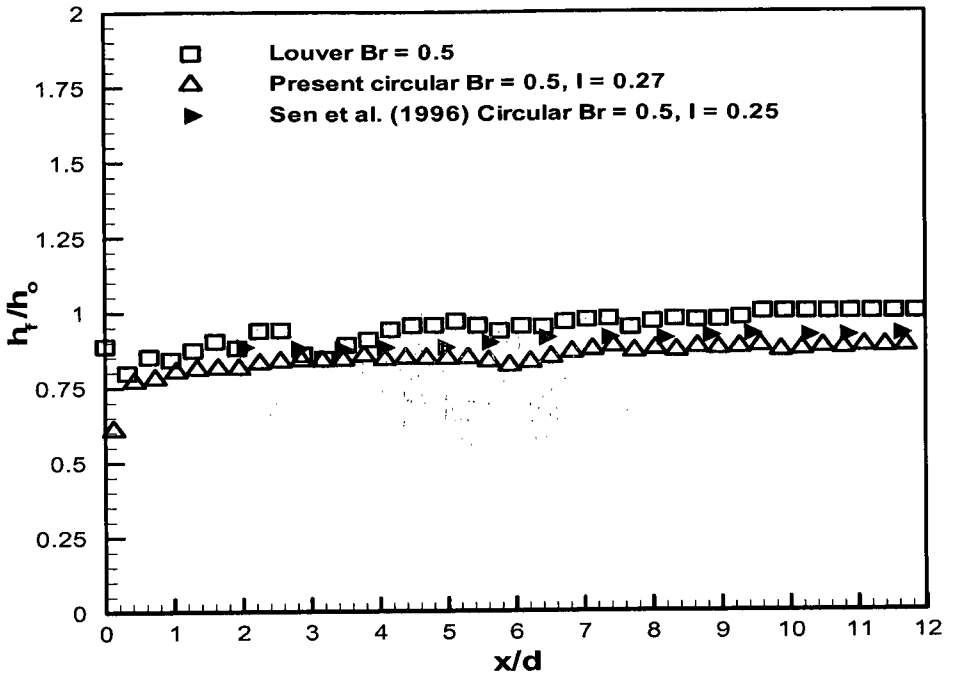

a) Br = 0.5

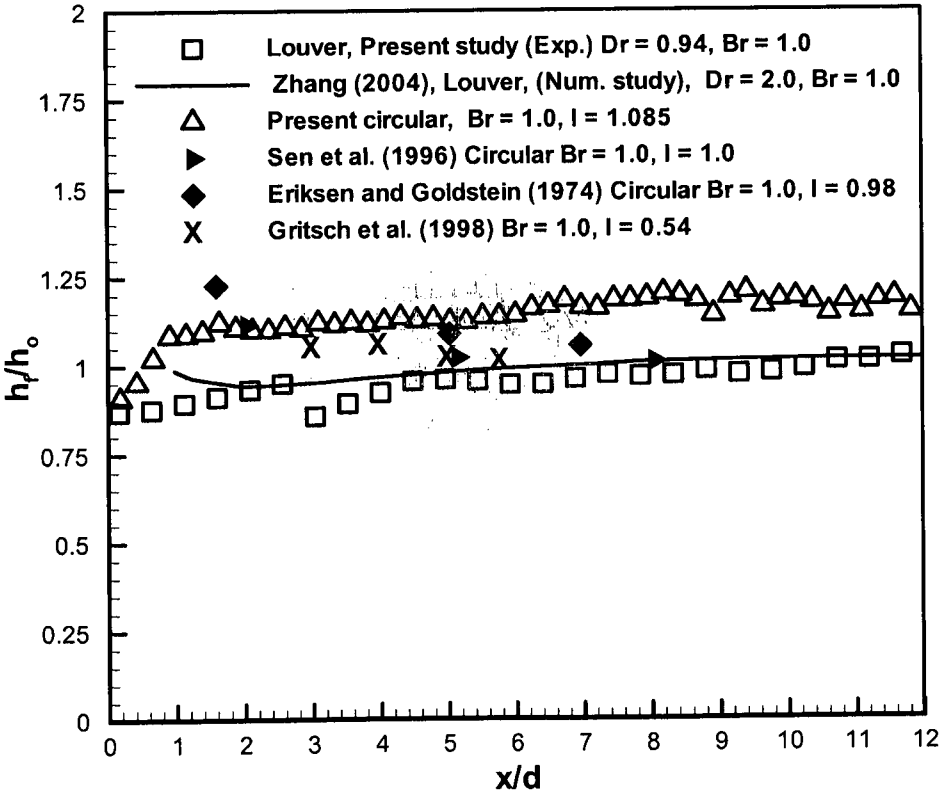

b) Br = 1.0

Figure 4.8. Comparison of centerline heat transfer ratio for the louver scheme with other film holes at different blowing ratios.

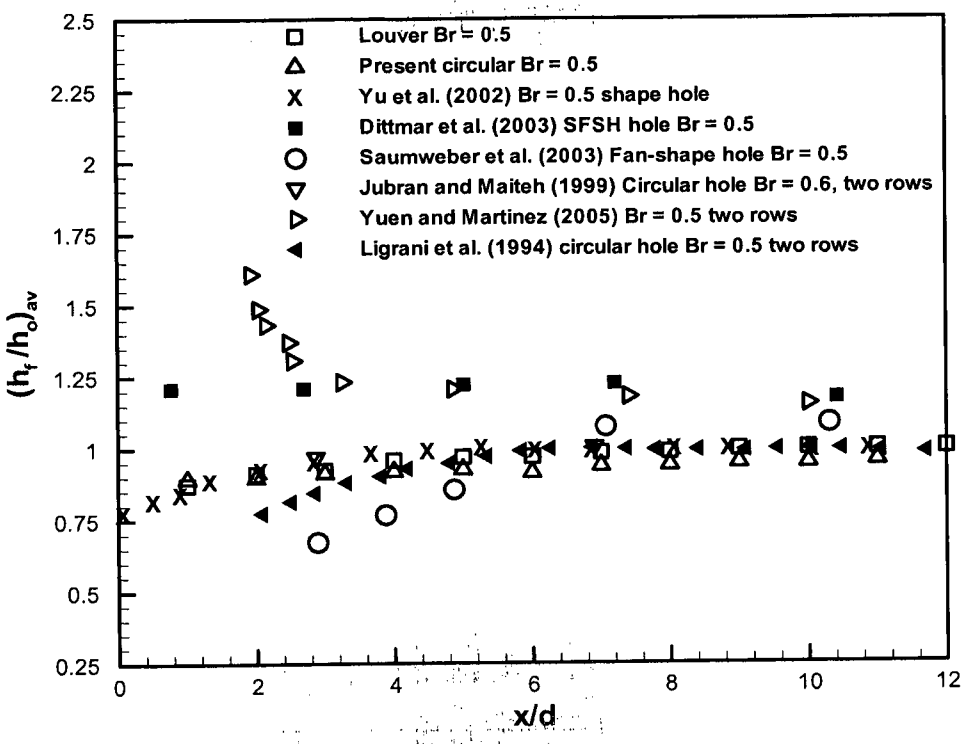

a) Br = 0.5

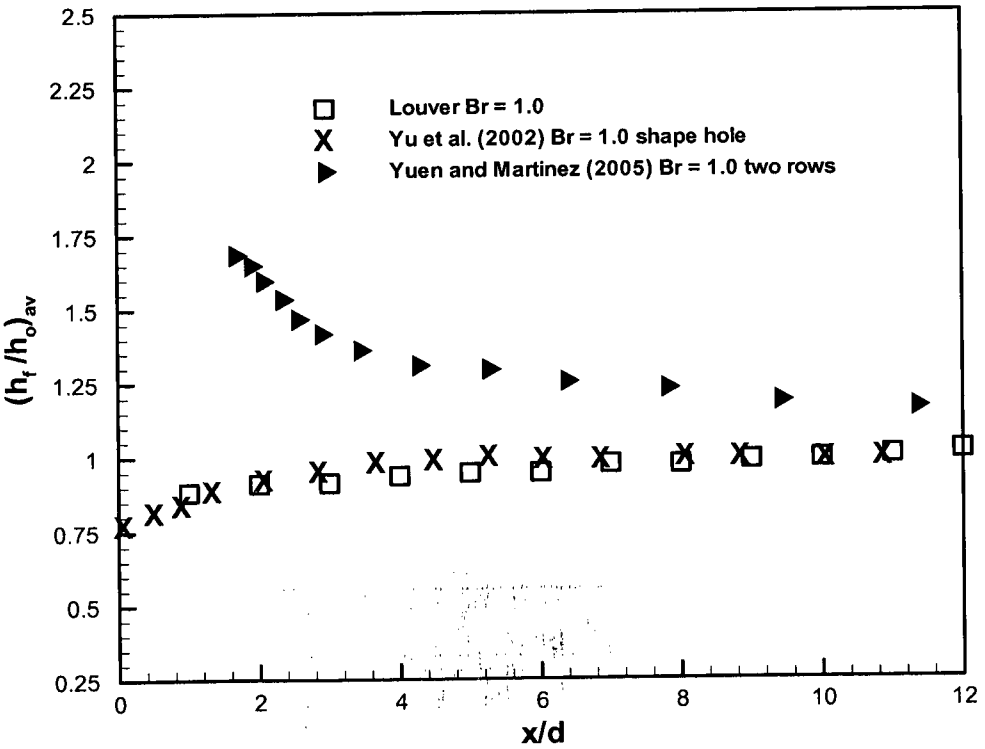

b) Br = 1.0

Figure 4.9. Comparison of lateral average heat transfer ratio of the louver with film hole configurations at low and high blowing ratios.

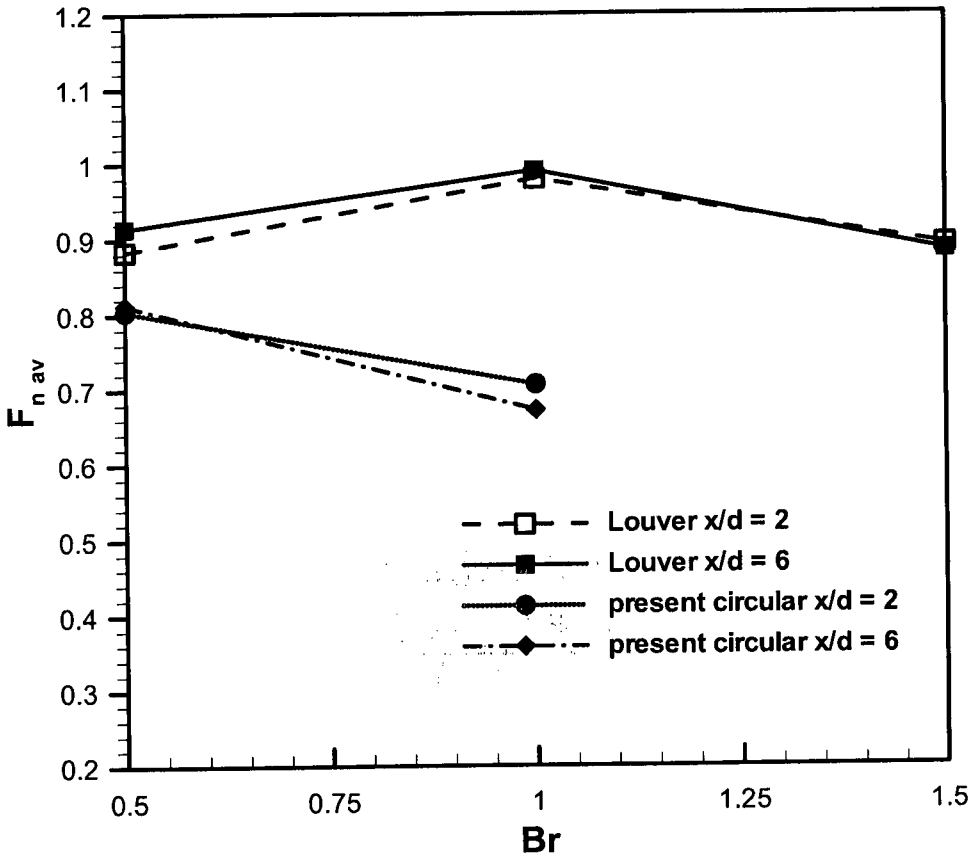

Figure 4.10. Lateral average Frossling number variations of the louver and circular hole with blowing ratio at different downstream locations.

The NHFR can be presented as a map, as shown in Fig. 4.11, for a reference temperature value of $\theta = 1.5$. The map is covers a range of h_f/h_o from 0.5 to 2.0 and from 0.1 to 1.0 for film cooling effectiveness (η). The NHFR can involve a negative effect (NHFR < 0.0) when the film cooling effectiveness is relatively low with high heat transfer coefficient ratio (h_f/h_o), as shown in Fig. 4.11. In this case, a hot spot may occur over the airfoil surface. If the NHFR has a value between 0 and 1.0, the film cooling performance will have a positive effect. Moreover, the NHFR is equal to zero for an uncovered surface with coolant flow ($\eta = 0.0$ and $h_f/h_o = 1.0$), which occurs far downstream of the jet exit holes. As well, the NHFR = 0 when the heat flux with and without film cooling are equal, or at $h_o/h_f = 1 - \eta^* \theta$. When the film cooling effectiveness is equal to a typical overall value of cooling effectiveness for gas turbine ($\eta = \varphi$), the NHFR value is equal to unity for all values of heat transfer ratio, according to Eq.4.5. In addition, for NHFR > 1, the film cooling effectiveness (η) produced by the film hole geometry is greater than the typical overall film cooling effectiveness (φ). As a result, there are three different overall film cooling performance regions for $\theta = 1.5$ ($\theta = 1/\varphi$): negative film cooling (NHFR < 0), positive film cooling (0 < NHFR < 1), and hyper film cooling (NHFR > 1) as shown in Fig. 4.11.

In this study, $\theta = 1.5$ is used to calculate the NHFR, which is a typical value for gas turbine airfoil applications, and was frequently used in previous film cooling research. As a result, according to the NHFR values, the overall film cooling performance for the film hole geometries can be established by using the map in Fig. 4.11.

The NHFR is investigated for the louver scheme in order to further evaluate the overall film cooling performance according to Eq.4.5. Figure 4.12 demonstrates the

centerline NHFR performance of the louver scheme and other film hole geometries at Br = 0.5 and 1.0. From the results, the louver scheme produces a higher NHFR compared to traditional circular and fan-shaped holes (Yu et al., 2002) at a blowing ratio of 0.5, as shown in Fig.4.12a. There is a significant enhancement of NHFR for the louver scheme near the film hole exit compared to other film hole geometries, and the NHFR values decrease gradually along the streamwise direction. For x/d > 4, the NHFR for the louver scheme is higher than the circular hole by ≈ 15 %, and the shaped hole provides the lowest value at a low blowing ratio (Fig. 4.12a). The NHFR performance of the louver scheme at a high blowing ratio (Br = 1.0) is presented in Fig. 4.12b. The louver scheme provides the highest NHFR at a high blowing ratio over the downstream surface with respect to the other film holes. At a high blowing ratio, the jet lift-off increases for the circular hole so it produces a lower NHFR, as shown in Fig. 4.12b. For x/d > 10, the effect of the reattached secondary flow can be detected and the NHFR results for the circular hole are nearly the same as those for the shaped hole.

Figures 4.13a and 4.13b present the lateral average variation of the NHFR for the louver schemes compared to other film holes at blowing ratios of 0.5 and 1.0, respectively. The results show that the louver scheme provides the highest NHFR near the injection hole as compared to the circular hole, fan shaped hole (Yu et al., 2002), and CAFSH (Dittmar et al., 2003) at a low blowing ratio (Br = 0.5). For x/d > 7, the NHFR of all film hole configurations are consistent, as shown in Fig. 4.13a. At a high blowing ratio, the NHFR for the louver scheme is further enhanced near the injection hole, and far downstream, as the secondary flow is widely distributed over a large downstream surface area. Due to jet lift-off, the NHFR of the circular hole decreases near the injection

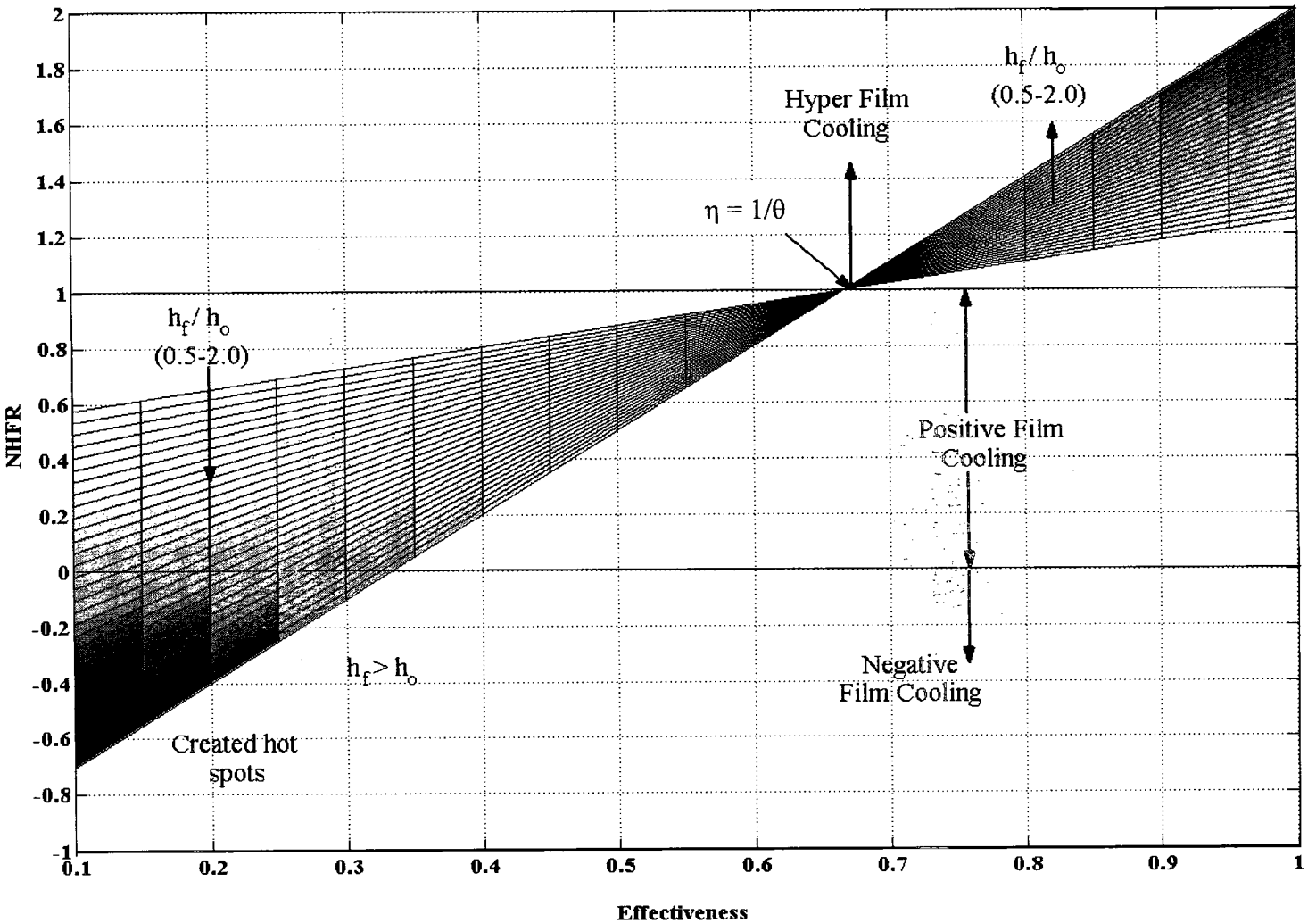

Figure 4.11. Net heat flux reduction map at a temperature references of $\theta = 1.5$.

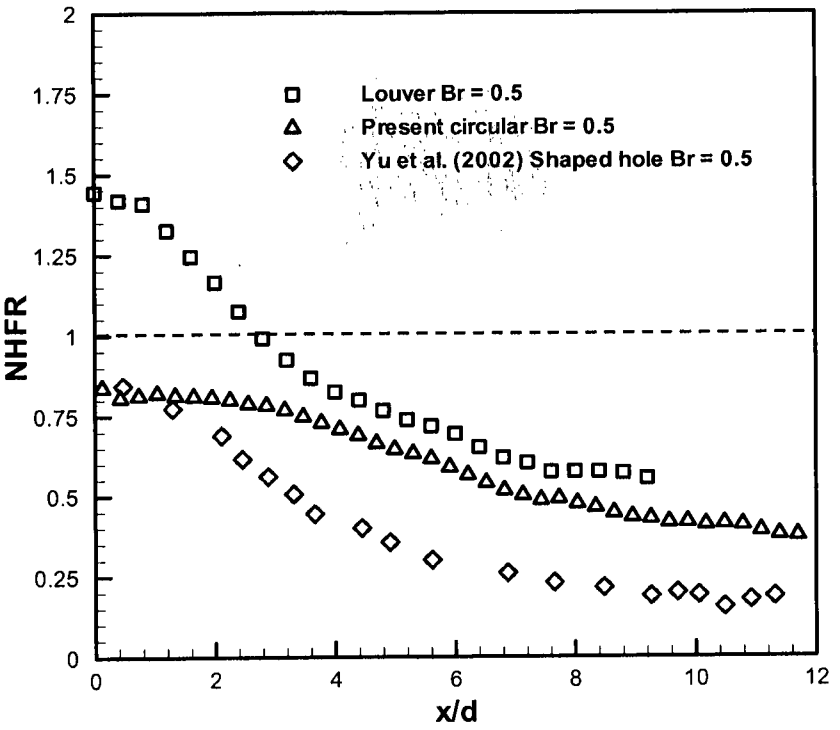

a) Br = 0.5

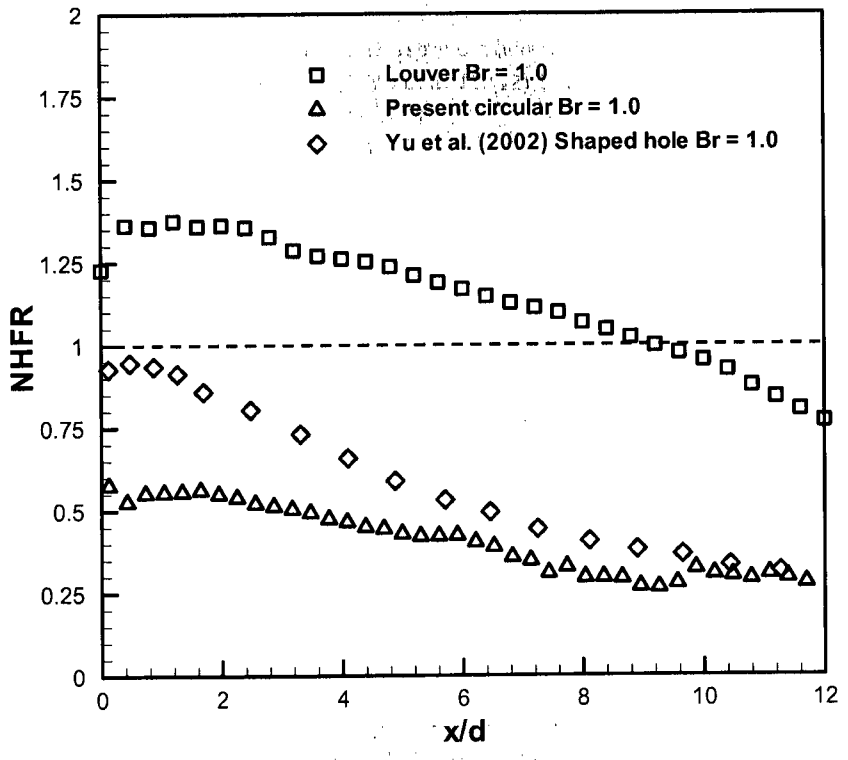

b) Br = 1.0

Figure 4.12. Comparison of centerline NHFR of the louver scheme with other film holes at low and high blowing ratios.

circular film hole (Fig. 4.13b) and it provides the lowest NHFR values compared to the fan shaped hole and the louver scheme.

Spanwise NHFR profiles for the louver scheme and other film hole configurations near the film hole exit (x/d = 2) and far downstream (x/d = 6), at a blowing ratio of 1.0, are presented in Fig. 4.14. From the results, the louver scheme produces higher NHFR in the spanwise direction at x/d = 2, compared to the shaped holes (Cho et al., 2001), as shown in Fig. 4.14. However, for x/d = 6, there is a consistency between the results for the louver scheme and shaped film hole close to centerline in the spanwise direction (-0.5 < z/d < 0.5), but the louver scheme provides a higher value for -0.5 > z/d > 0.5.

Figure 4.15 illustrates the effect of the blowing ratio on the downstream NHFR contours and the centerline NHFR performance for the louver scheme. Near the film hole exit, the NHFR for the louver scheme is enhanced with increasing blowing ratio. The NHFR diminishes in the downstream direction, due to the reduction in the secondary flow momentum. As a result, there is no significant increase in heat flux for the louver scheme, where there are no negative values of NHFR.

Figure 4.16 shows the laterally averaged overall cooling performance for the louver scheme and the circular hole with blowing ratios at different downstream locations. The NHFR performance deteriorates with increasing blowing ratio for the circular hole at locations near the film hole injection. However, far downstream (x/d = 6), the NHFR performance of the circular hole increases gradually for any increase in the blowing ratio since the secondary flow reattaches the surface after jet lift-off. At x/d = 4, the NHFR is nearly independent of the blowing ratio. In contrast, the performance of

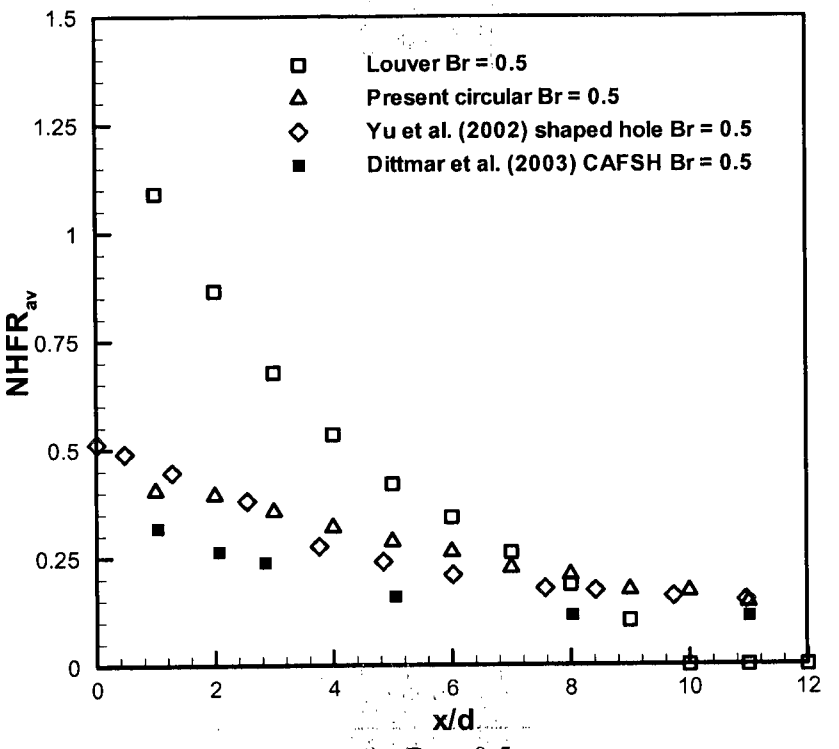

a) Br = 0.5

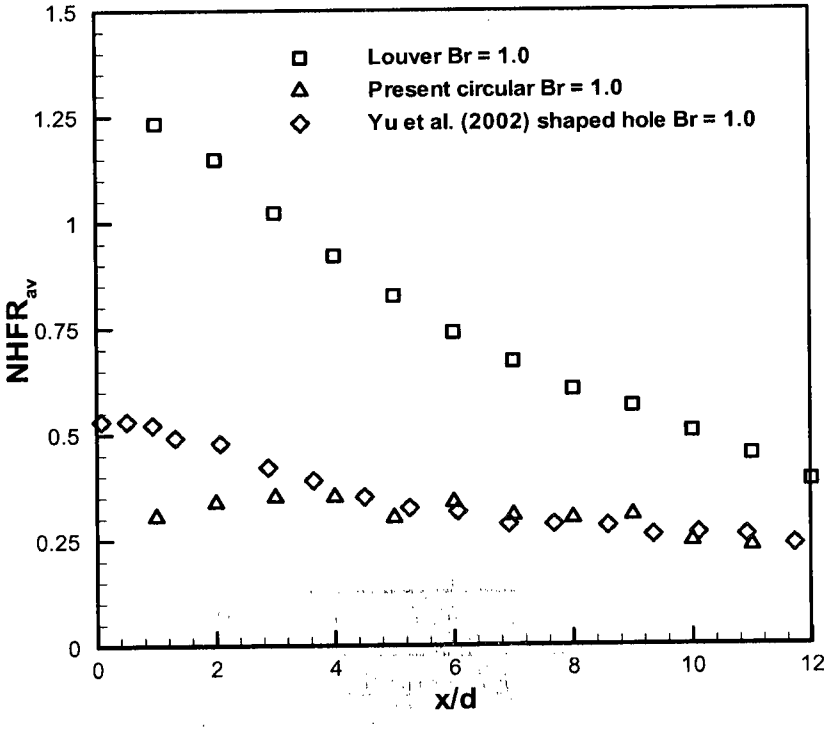

b) Br = 1.0

Figure 4.13. Comparison of lateral average NHFR of the louver scheme with other film holes at low and high blowing ratios.

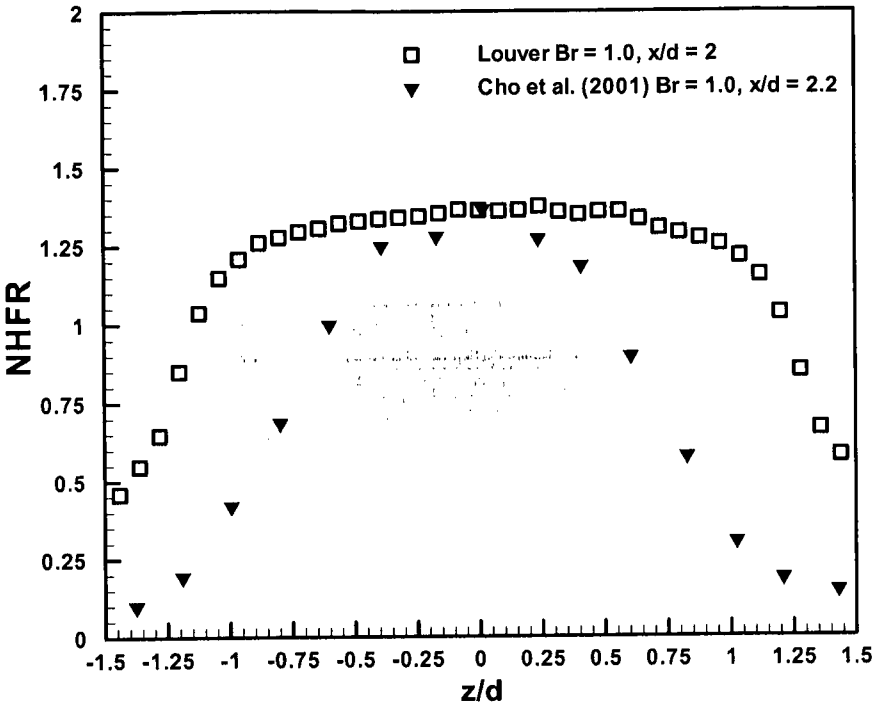

a) x/d = 2.0

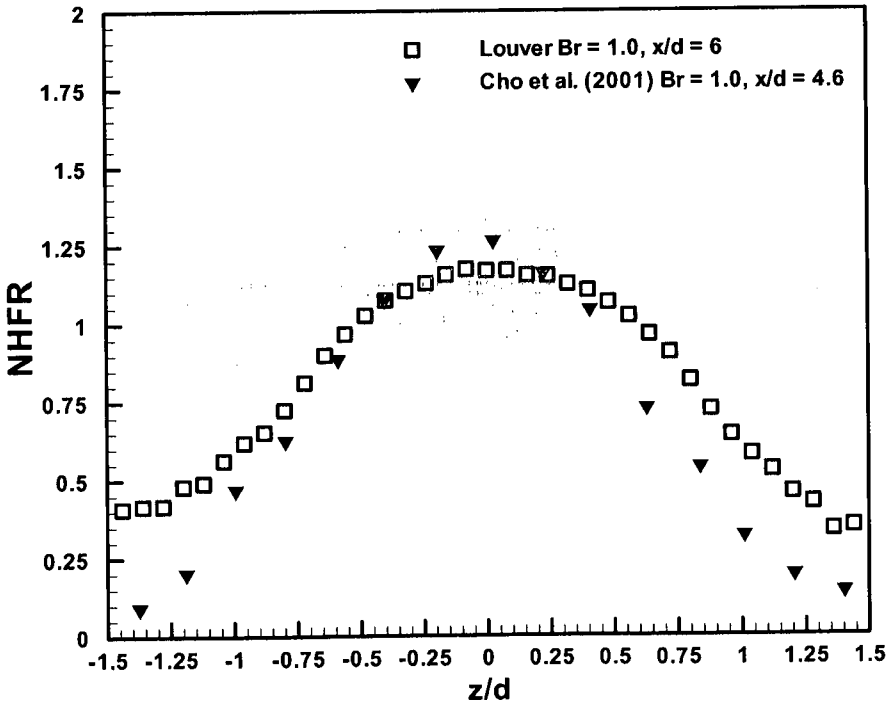

b) x/d = 6.0

Figure 4.14. Comparison of span-wise NHFR of the louver scheme with film holes at Br = 1.0.

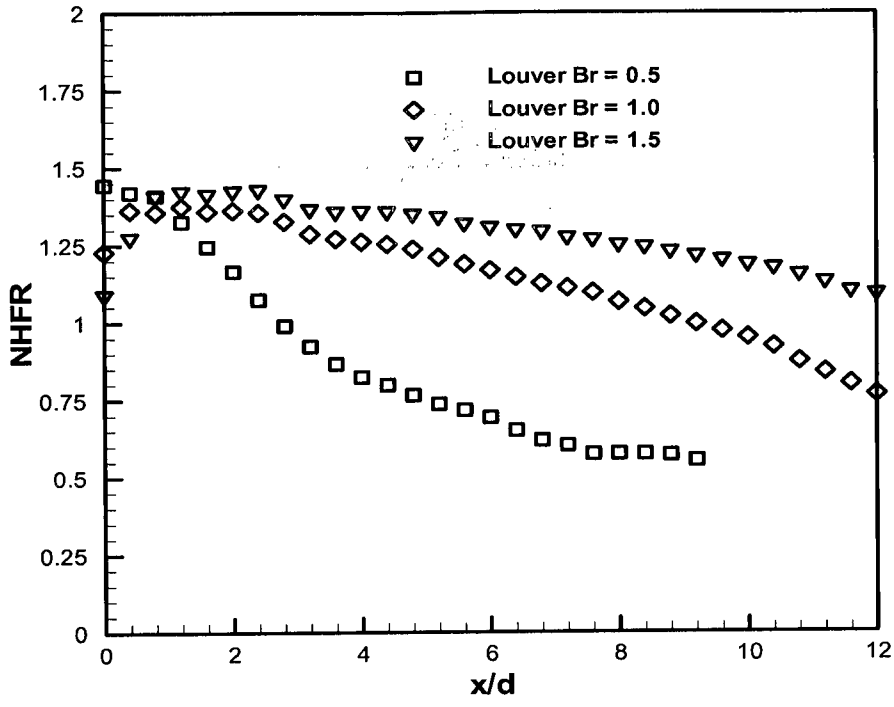

a) centerline

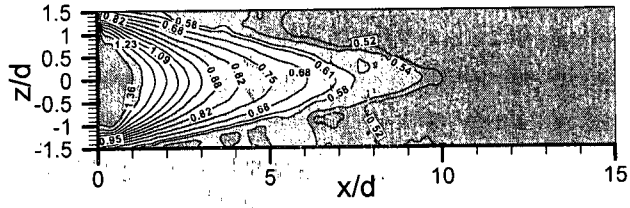

Br = 0.5

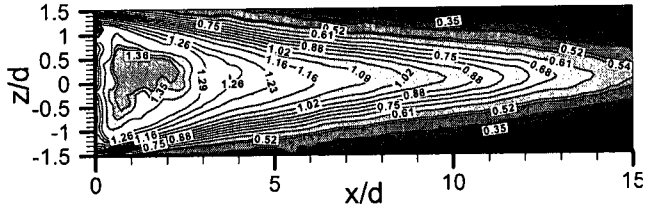

Br = 1.0

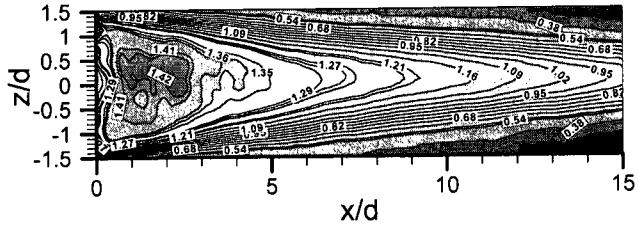

Br = 1.5

b) contours

Figure 4.15. Local centerline NHFR and contours for the louver scheme at different blowing ratios.

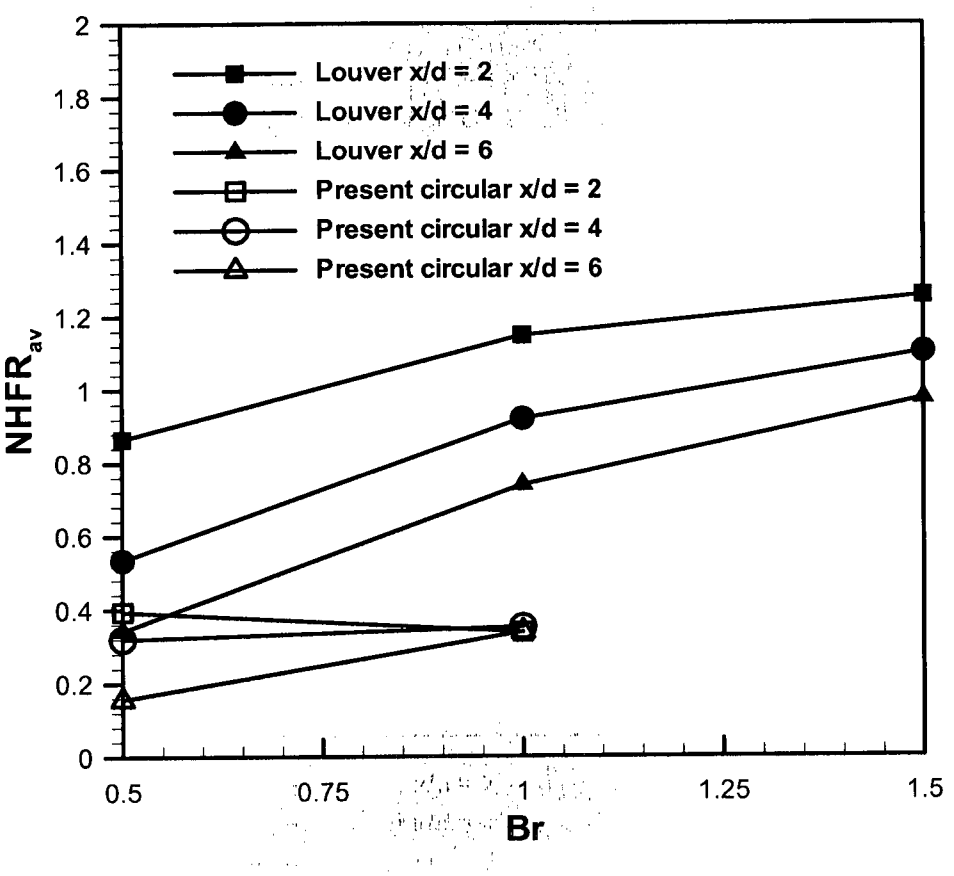

Figure 4.16. Variation of lateral average NHFR with blowing ratio for the louver and the circular film holes.

NHFR for the louver scheme improves with any increase in blowing ratio at all downstream locations (x/d = 2, 4 and 6). The NHFR has a value greater than 1 close to the film hole injection and decreases in the downstream direction for the same blowing ratio. The enhancement in NHFR for the louver scheme with blowing ratio is due to a significant increase in film cooling effectiveness with relatively low heat transfer coefficient ratio values.

Typically the uncertainty in TLC measurement is estimated to be ± 0.5 °C. As well, the uncertainty in thermal conductivity and diffusivity is estimated to be ± 3%. Accordingly, the average uncertainty for the heat transfer ratio, film cooling effectiveness, Frossling number, net heat flux reduction, and blowing ratio were estimated to be ± 11 %, ± 8 %, ± 14 %, ± 15 %, and ± 11 %, respectively.

4.3 Summary

Throughout this chapter, the film cooling effectiveness performance of the louver scheme has been investigated experimentally using TLC technique for a single transient method. The film cooling performance of the louver scheme has been presented and compared with other traditional and advanced published film hole geometries. The film cooling performance of the louver scheme was investigated for blowing ratios from 0.5 to 1.5 and a 0.94 density ratio. The results showed that the louver scheme provided a superior centerline and lateral film cooling effectiveness compared to other published film hole geometries. In addition, the film cooling effectiveness was enhanced with increasing blowing ratio for the louver scheme.

The centerline and laterally averaged heat transfer coefficient for the louver scheme demonstrated lower values over the downstream surface compared to circular

holes but it provided similar results to fan shaped holes. Moreover, there was no significant effect on the heat transfer coefficient ratio with increasing blowing ratios for the louver schemes. The Frossling number performance increased with blowing ratio for the louver schemes until reaching a peak point at which it decreases with any increase in the blowing ratio and remains constant in the downstream direction. The net heat flux reduction was presented to illustrate the overall film cooling performance by combining the film cooling effectiveness and heat transfer coefficient ratio. The dimensionless reference temperature, $\theta = 1.5$, was used to calculate the NHFR. The louver schemes provided a high film cooling effectiveness with relatively low heat transfer coefficient ratio, and therefore demonstrated the highest NHFR in the streamwise and lateral directions compared to the circular and fan shaped holes. As a result, the louver scheme is able to increase the airfoil's lifetime and the inlet gas turbine temperature can be increased, which in turn improves the overall gas turbine efficiency.

Chapter 5

Chapter 5 Film Cooling Performance of Hybrid Scheme

This chapter will present an experimental investigation of the film cooling performance of a New Hybrid Film Cooling Scheme on a flat plate using the Thermochromic Liquid Crystal (TLC) technique for a single transient measurement. The new scheme has been designed to improve the film cooling performance of a gas turbine airfoil. The scheme includes two consecutive film hole configurations with interior bending. The cooling performance of the new scheme will be analyzed across blowing ratios of 0.5 to 1.5, at a density ratio of 0.94. The hybrid film-cooling scheme is expected to provide improved protection on the outer surfaces of gas turbine airfoil, hence increasing the airfoil life expectantly.

5.1 Hybrid scheme geometry and operating conditions

Figure 5.1 shows a schematic view of the new hybrid film hole scheme over a flat plate. The proposed scheme includes two consecutive film hole configurations. The first is a circular hole, having 6.4 mm diameter (d) and an inclination angle of 30°. The second shaped hole configuration starts at a distance of 0.8d from the external surface, and intersects the circular hole. The slot angle of the shaped hole is 10° in the streamwise direction, yielding a lengthwise opening of 3d. The new scheme is designed to combine the advantages of circular and shaped film hole configurations. The hybrid scheme has the ability to reduce the jet lift-off of the secondary flow by directing the secondary flow over the surface in the horizontal direction due to interior scheme bending. The bending

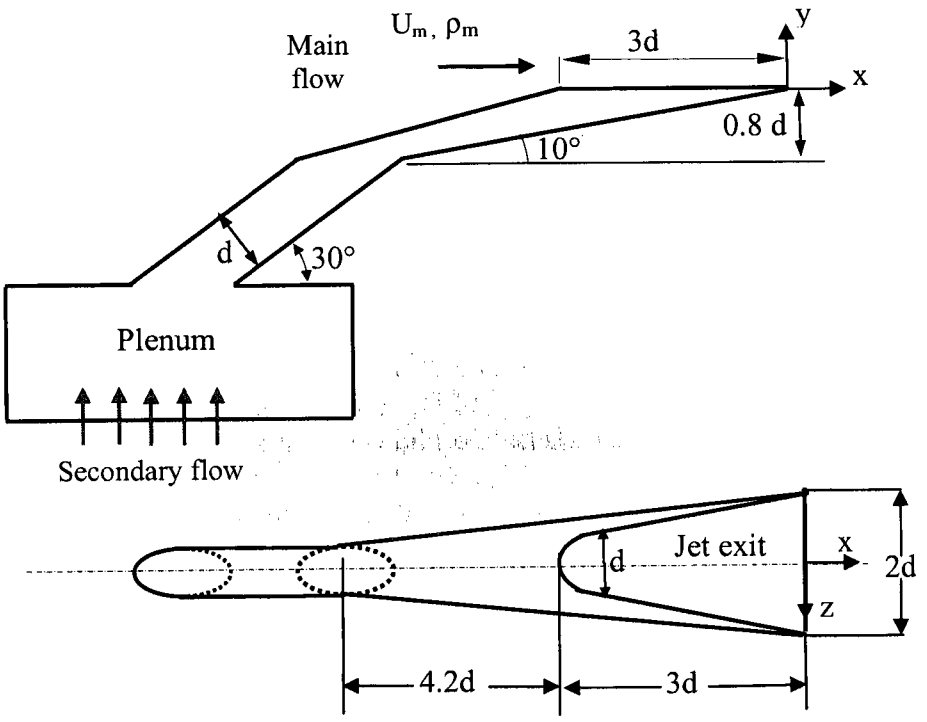

Figure 5.1. Hybrid scheme geometry.

effect of the new scheme throttles the secondary flow causing it to spray widely over the downstream surfaces, enhancing the film cooling performance at low and high blowing ratios. The film cooling performance of the hybrid scheme will be investigated over a flat plate using the TLC technique across different blowing ratios for a 0.94 density ratio. Table 5.1 lists the test conditions and geometry parameters for the circular hole and the hybrid scheme. The main and secondary stream Reynolds numbers are calculated based on the hydraulic diameter of the main duct, and film hole diameter, respectively.

Table 5.1. Geometrical parameters and measurement conditions of the hybrid scheme.

Parameters	Circular hole	Hybrid scheme
d (cm)	1.39	0.64
Br	0.5, 1.0	0.5, 1.0, 1.5
Dr	0.94	0.94
I	0.27, 1.085	0.27, 1.0783, 2.3592
Re_D (duct)	1.14×10^5	1.25×10^5
Re_d (hole)	1.25×10^4, 2.5×10^4	6.26×10^3, 1.25×10^4, 1.85×10^4

5.2 Results and discussion

5.2.1 Film cooling effectiveness

Downstream historical raw TLC surface images, and downstream temperature profiles, at z/d = 0.0 and 0.5 of the hybrid scheme at Br = 1.5 are illustrated in Figs. 5.2a, and 5.2b, respectively. The secondary flow, expelled from the film hole, is sprayed over the target surface downstream. Consequently, the TLC colors change with the time from black to blue, followed by red and green colors, as illustrated the raw TLC images in Fig. 5.2a. Figure 5.2a shows that the secondary flow is sprayed widely at a high blowing ratio to provide superior protection for the downstream surface. The hybrid scheme has been

designed to reduce the vertical jet flow by directing the secondary flow in the horizontal direction while providing a more uniform momentum at the film hole exit (Ghorab et al. 2007). The bending throttles the secondary flow, so it is sprayed more latterly along the streamwise direction. The unsymmetrical distribution of spraying the secondary flow temperature in the downstream region is attributed to errors in the manufacturing process of the hybrid scheme. Figure 5.2b presents the streamwise temperature profiles at z/d = 0.0 and 0.5 for the hybrid scheme. From the results, the hybrid scheme provides a high temperature profile near the injection holes and diminishes faintly along streamwise and spanwise directions, as shown in Fig. 5.2b. Figure 5.2b shows that the downstream temperatures increase with time during the transient test, and after 20 sec, there is no variation of the centerline temperature profiles (at z/d = 0.0) with time for x/d < 2. While for x/d ≥ 2 and z/d ≥ 0.0, the temperature profiles increased with time.

Figures 5.3a and 5.3b present the centerline and the laterally averaged film cooling effectiveness performance of the hybrid scheme at different blowing ratios, respectively. The results show that the hybrid scheme increases the downstream film cooling effectiveness with increasing blowing ratio. The centerline film cooling effectiveness attains a unity value close to the film holes at a high blowing ratio (Br = 1.5), as shown in Fig. 5.3a, and decreases gradually in the streamwise direction. The laterally averaged film cooling effectiveness of the proposed scheme increases with blowing ratio since the secondary flow sprays widely in the streamwise direction, due to the throttling effect. As a result, the highest laterally averaged film cooling effectiveness,

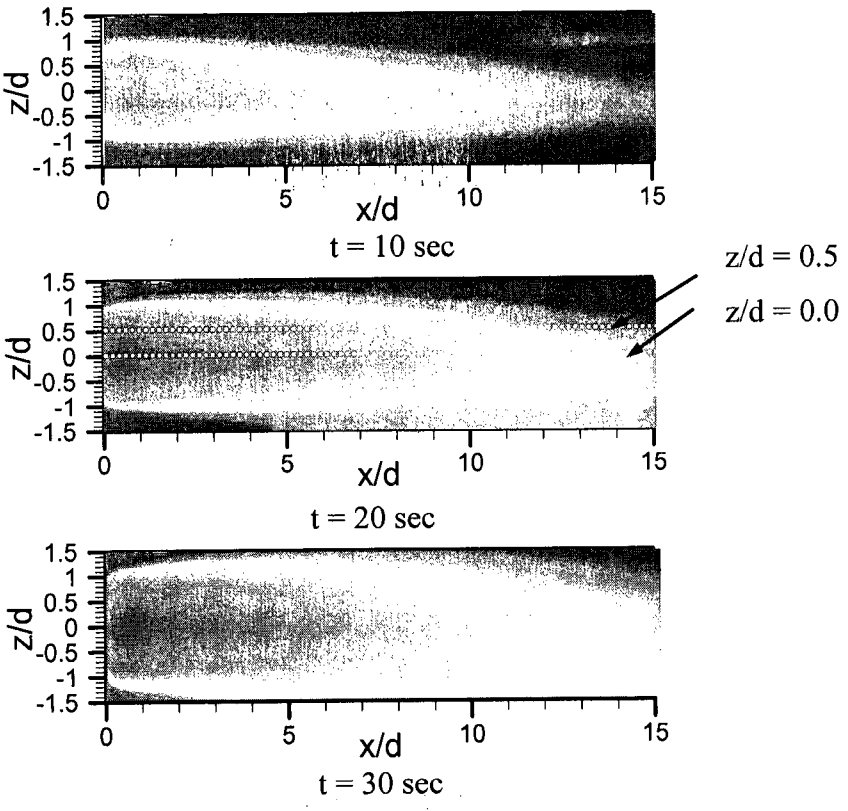

a) Raw TLC images

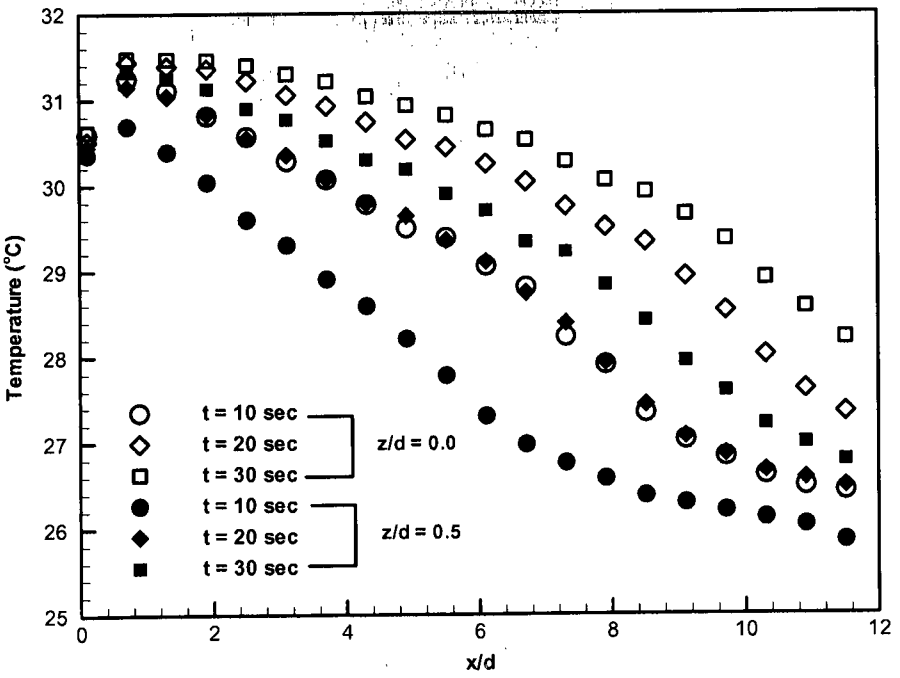

b) Temperature profile at z/d = 0.0 and 0.5

Figure 5.2. Historical TLC response and downstream temperature profiles of the hybrid scheme (Br = 1.5).

with greater enhancement in film cooling effectiveness compared to other blowing ratios, is observed at Br = 1.5, as shown in Fig. 5.3b.

Four downstream locations are selected (x/d = 2, 4, 6 and 10) to present the local film cooling effectiveness performance of the hybrid scheme in the spanwise direction at Br = 1.0 and 1.5 (Figs. 5.4a and 5.4b). The downstream distance (x/d) is measured from the trailing edge of the film hole exit, as illustrated in Fig. 5.1. At Br = 1.0, the hybrid scheme provides a high film cooling effectiveness with a wider effect near the central zone (z/d = 0.0) and it decreases gradually along the streamwise direction. The film cooling effectiveness is further enhanced at high blowing ratio for the hybrid scheme in the downstream and spanwise directions, as shown in Fig. 5.4b. From the results, the film cooling effectiveness performance is greater than 0.9 at x/d = 2, and reduces in the streamwise direction due to the reduction in secondary flow momentum.

Film cooling effectiveness surface contours of the hybrid scheme, at blowing ratios of 1.0 and 1.5, are presented in Fig. 5.5 for the downstream region of $-1.5 < z/d < 1.5$ in the spanwise direction, and $0 < x/d < 14$ in the streamwise direction. The contours displayed an inclusive performance of the hybrid scheme at high blowing ratios over the downstream surfaces. The maximum value of the film cooling effectiveness with a wide spread is achieved at a region near the center of the film hole injection and it decreases gradually in the streamwise direction, as shown in Fig. 5.5a for Br = 1.0. The film cooling effectiveness is further enhanced in the streamwise and spanwise directions at high blowing ratio as shown in Fig. 5.5b. The hybrid scheme is able to direct and to throttle the secondary flow in the horizontal direction; therefore, the secondary flow sprays more over the downstream surface with increasing blowing ratio.

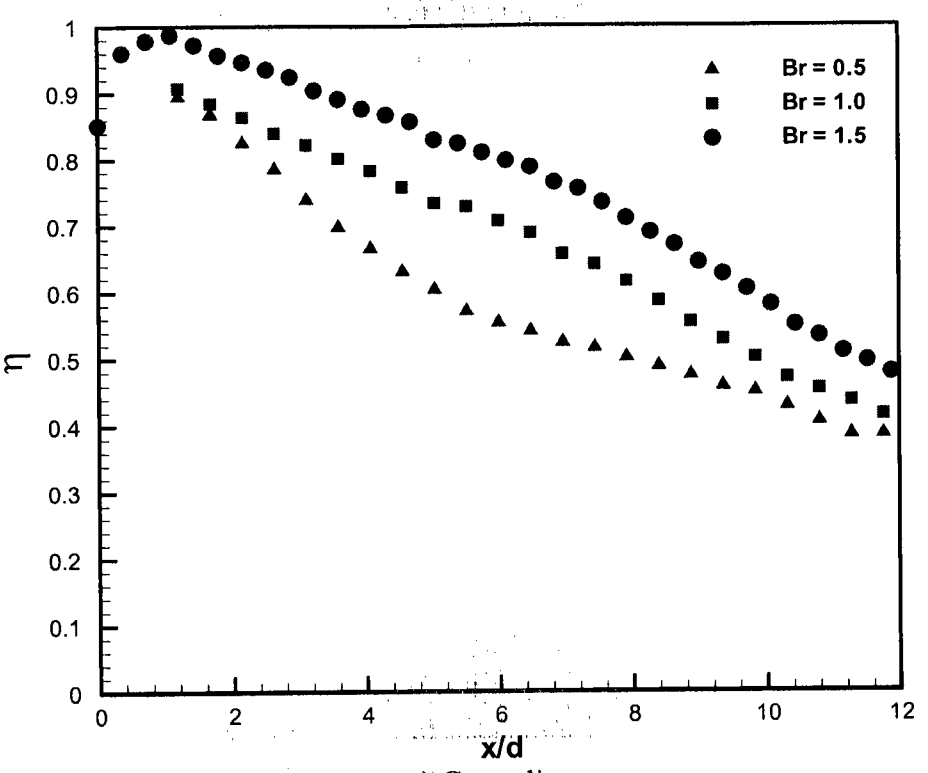

a) Centerline

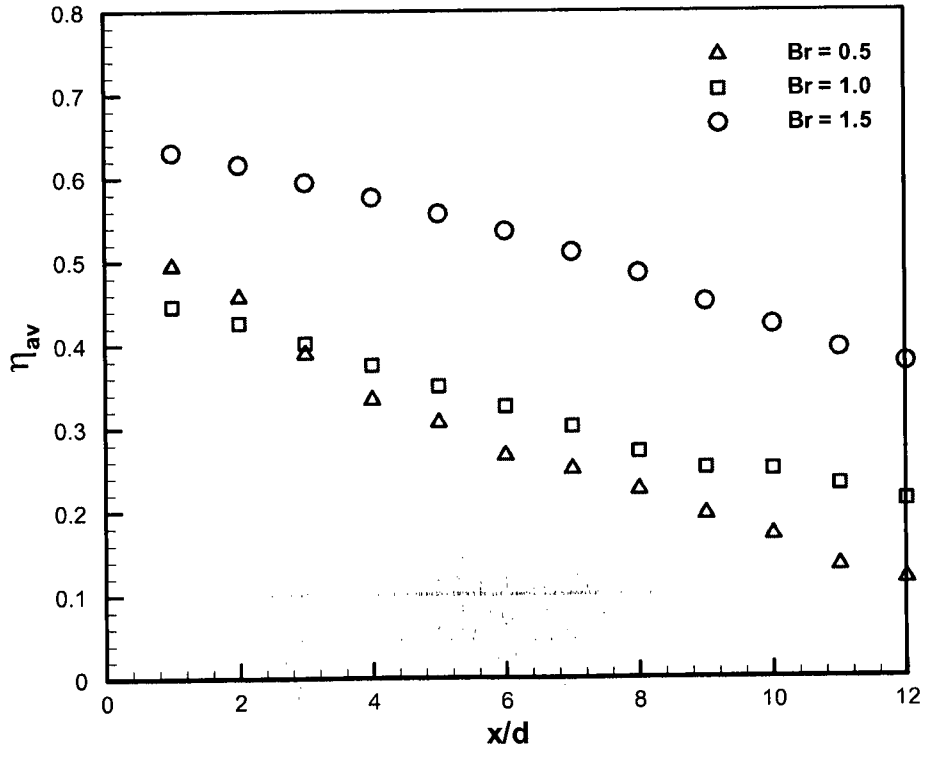

b) Average

Figure 5.3. Film cooling effectiveness performance of the hybrid scheme at different blowing ratios.

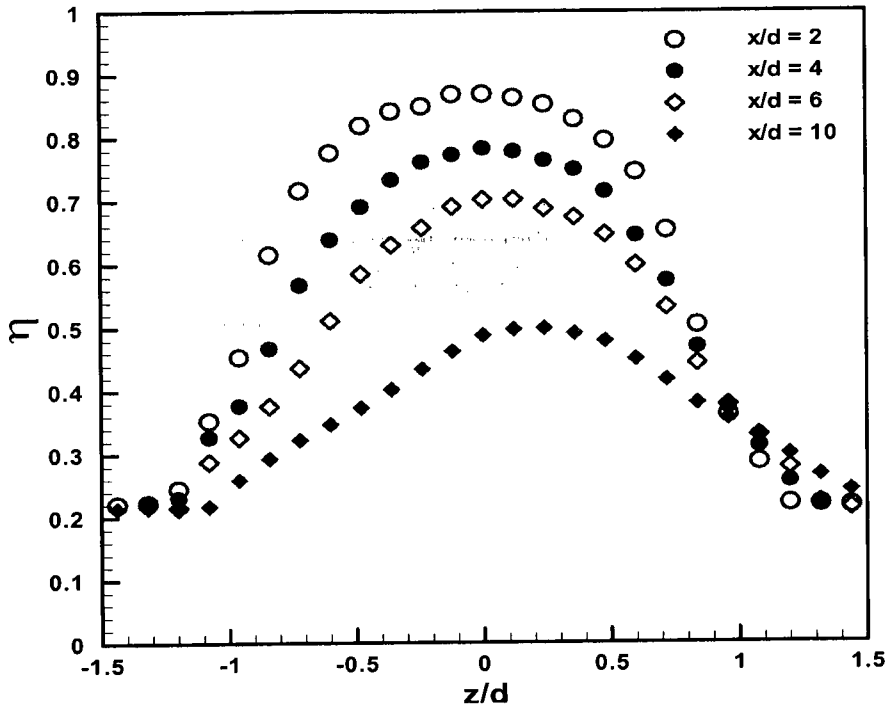

a) Br = 1.0

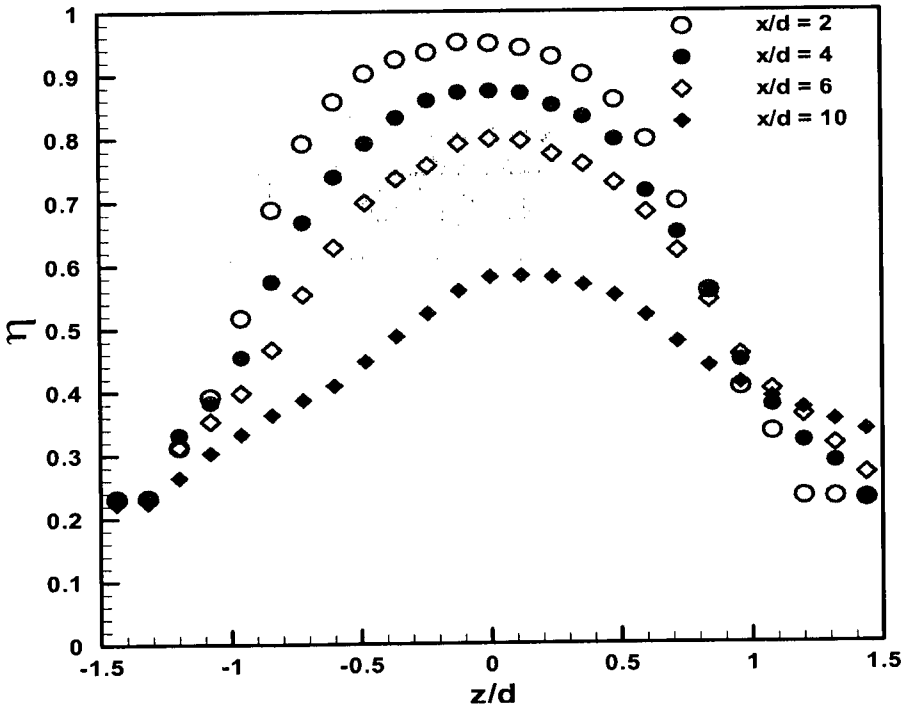

b) Br = 1.5

Figure 5.4. Spanwise film cooling effectiveness of the hybrid scheme at different blowing ratios.

5.2.2 Heat transfer analysis

The central and laterally averaged heat transfer coefficient ratio performances of the hybrid scheme at different blowing ratios are presented in Figs. 5.6a and 5.6b, respectively. The results show that the hybrid scheme provides centerline heat transfer ratio (h_f/h_o) of 1.15 near the film hole exit and it decreases to 1.05 far along the streamwise direction, as shown in Fig. 5.6a. The proposed scheme produces a value of the centerline heat transfer coefficient ratio greater than unity near the trailing edge of the film holes. This is due to high velocity in the boundary layer with three dimensional flow structures, near the film hole. Along the streamwise direction, the velocity decreases and the flow become mainly two dimensional flow structures. The centerline heat transfer coefficient ratio results show also that there is no significant effect of blowing ratio on the centerline heat transfer ratio. The reason for that is the hybrid scheme provides a thin constant boundary layer thickness over the downstream surfaces with increasing the blowing ratios (Ghorab et al. 2007), which will be discussed in chapter 6. Figure 5.6b presents the laterally averaged heat transfer coefficient ratio (h/h_o) of the hybrid scheme at different blowing ratios. The results show that the hybrid scheme provides a small increase in spanwise averaged h_f/h_o performance with increasing blowing ratio, however this is within the range of experimental uncertainty. As a result, the hybrid scheme produces an average heat transfer coefficient ratio near unity without a significant effect of the blowing ratio (Fig. 5.6b).

The main stream velocity and film hole geometry have significant effects on the heat transfer coefficient ratio. Therefore, the Frossling number ($Nu / \sqrt{Re}$) is presented for the hybrid scheme in order to combine the effects of the main flow velocity, heat

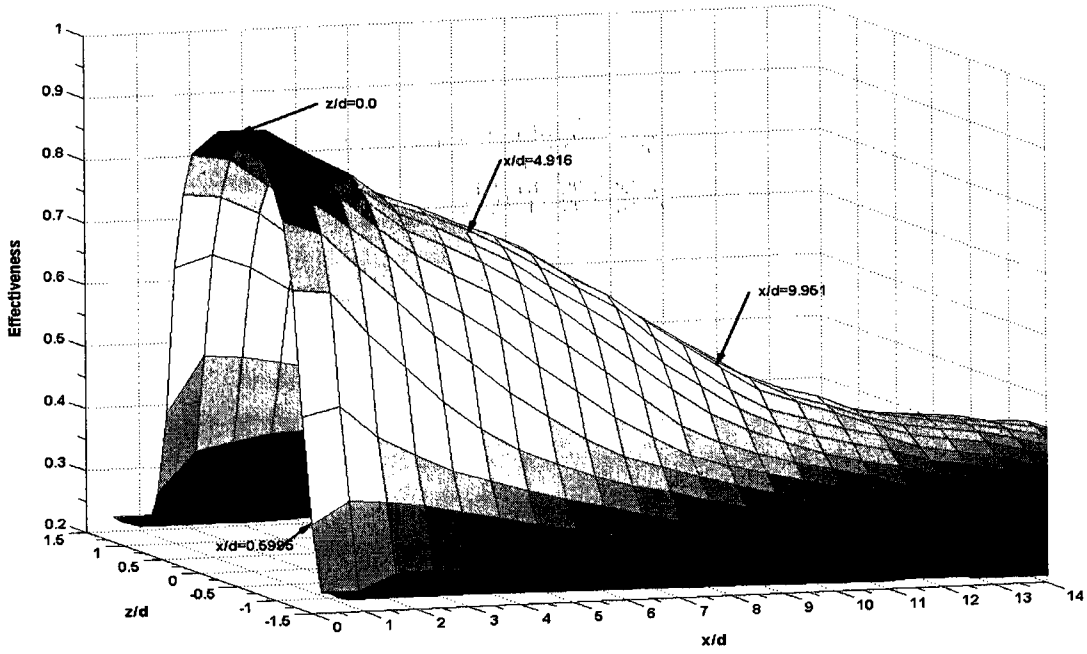

a) Br = 1.0

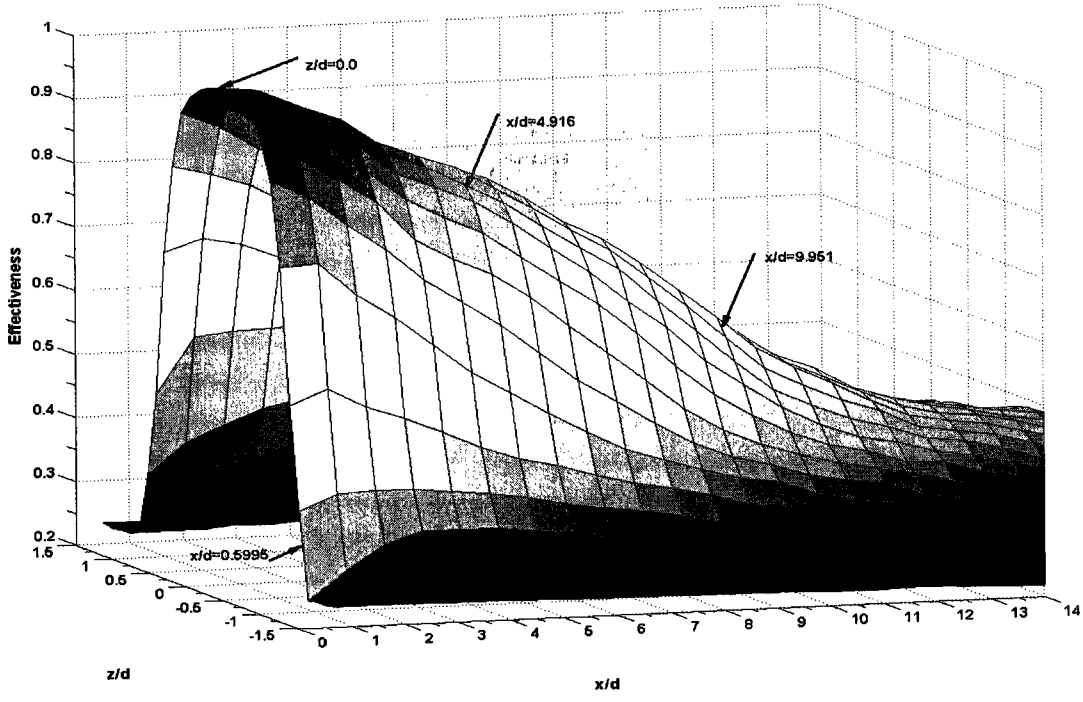

b) Br = 1.5

Figure 5.5. Downstream film cooling effectiveness surface contours of the hybrid scheme at different blowing ratios.

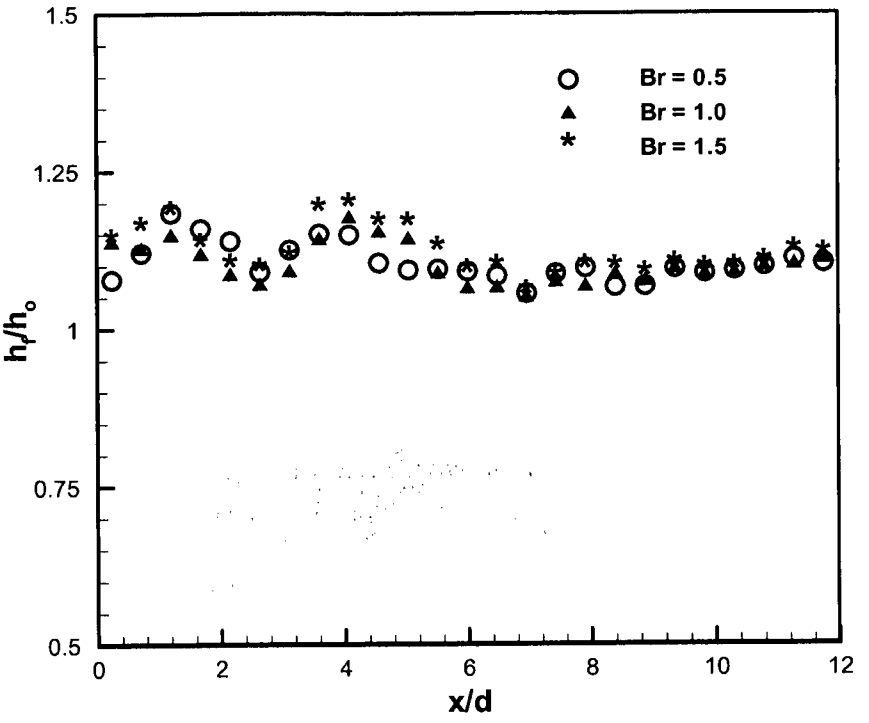

a) Centerline

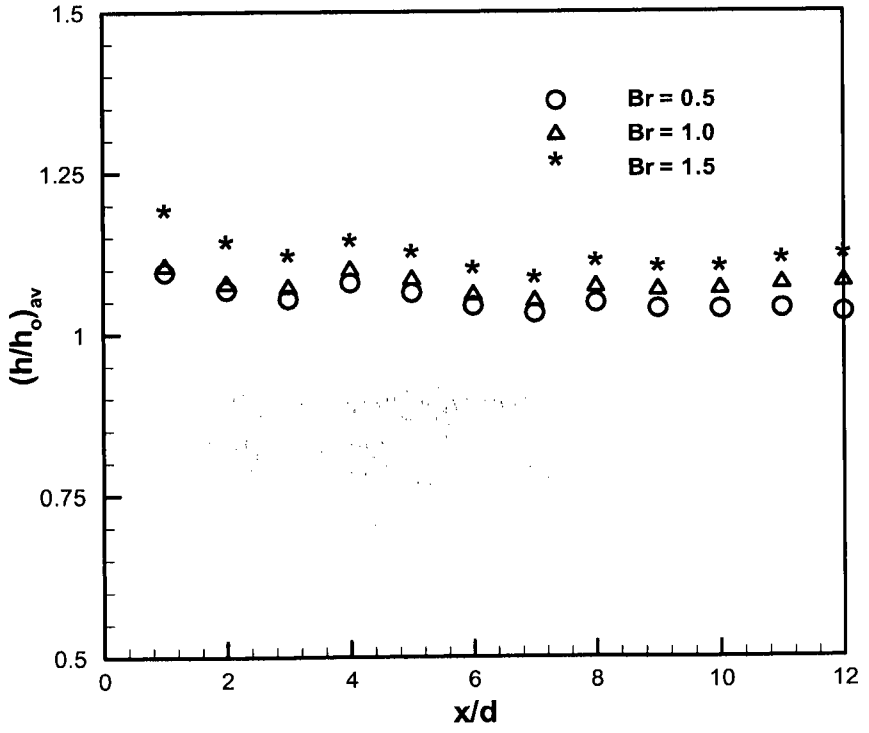

b) Latterly averaged

Figure 5.6. Centerline and latterly averaged heat transfer ratio of the hybrid scheme at different blowing ratios.

transfer coefficient, and film hole exit dimensions. The Reynolds number is calculated based on the main stream velocity and the hydraulic diameter at film hole exit. Figure 5.7 shows the downstream centerline Frossling number performance of the hybrid scheme at different blowing ratios. From the results, the hybrid scheme provides an average Frossling number near 0.6 over the downstream surfaces; there is no significant effect of the blowing ratios on the streamwise Frossling number. The effect of blowing ratios on laterally averaged Frossling number at downstream locations of x/d = 2.0, 4.0 and 6.0 for the hybrid scheme and circular hole are presented in Fig. 5.8. The results show that there is a small increase in Frossling number with blowing ratios with unaffected in streamwise direction for the hybrid scheme. While the Frossling number decreases with blowing ratio due to an increase in the jet lift off in the circular hole, the secondary flow does not attach to the downstream surfaces. Moreover, the Frossling number is affected in the streamwise direction at high blowing ratios due to reattachment of the secondary flow on the surface, as shown in Fig. 5.8.

5.2.3 Net heat flux reduction

In order to evaluate the overall film cooling performance of the hybrid scheme, the NHFR was investigated through this study according to Eq. (5.1). Figure 5.9 presents the downstream centerline NHFR performance of the hybrid scheme at different blowing ratios for $\theta = 1.5$. The results show that the hybrid scheme produces a high NHFR values close to the film hole exit, while values diminish gradually in the streamwise direction at low and high blowing ratios. The NHFR performance also increases with increasing blowing ratio. The hybrid scheme provides NHFR values greater than unity for $\theta = 1.5$ over the most of the downstream region and it increases with blowing ratios. This means

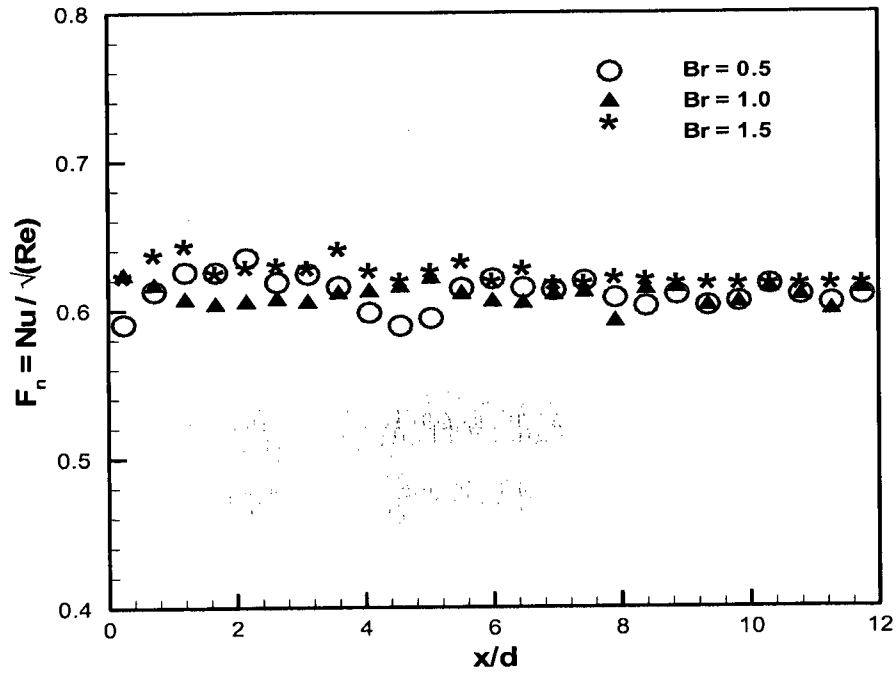

Figure 5.7. Centerline Frossling number of the hybrid scheme at different blowing ratios.

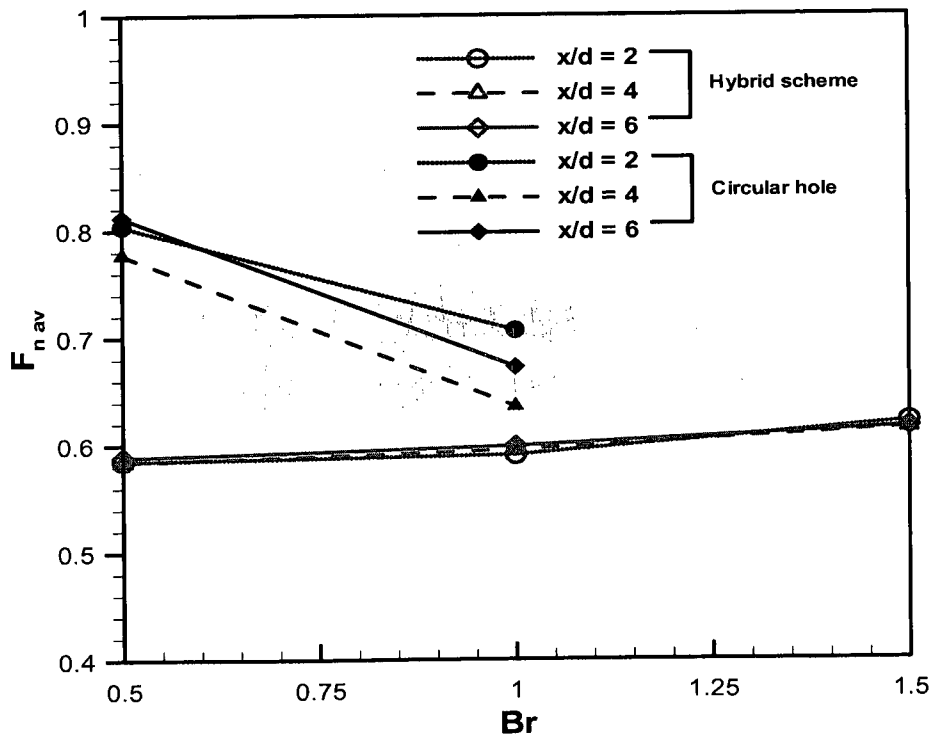

Figure 5.8. Variation of laterally averaged Frossling number of the hybrid scheme and circular hole with blowing ratio.

that the film cooling effectiveness performance provided by the hybrid scheme is greater than the overall cooling effectiveness (φ). The results show that the overall downstream film cooling effectiveness values of the hybrid scheme are positive and hyperactive, without negative values. Therefore, there is no possibility of created hot spots over the downstream surfaces.

$$NHFR = 1 - \frac{q_f}{q_o} = 1 - \left(\frac{h_f}{h_o} \left(1 - \eta * \theta\right) \right) \quad \text{, and } \theta = 1/\varphi. \tag{5.1}$$

Figure 5.10 illustrates the effect of blowing ratio on the downstream NHFR contours of the hybrid scheme. Near the film hole exit, the NHFR enhances with increasing blowing ratio, and diminishes in the spanwise and downstream directions due to a reduction in the secondary flow momentum. The hybrid scheme provides a wider NHFR performance in the spanwise direction at high blowing ratios due to the throttling effect. As a result, the hybrid scheme provides superior protection performance on the downstream surfaces, and it increases with blowing ratio. Thus, there is no significant increase in the heat flux for the hybrid scheme.

Figure 5.11 shows the laterally averaged NHFR, at different downstream locations for the hybrid scheme and the circular hole as function of blowing ratio. The NHFR performance decreases with increasing blowing ratio for the circular hole, at locations near the film hole injection. However, far downstream (x/d = 6) the NHFR performance increases gradually for any increase in the blowing ratio, since the secondary flow reattaches to the surface after jet lift-off. At x/d = 4, the NHFR is nearly independent of the blowing ratio. In contrast, the overall NHFR performance of the hybrid scheme improves with any increase in blowing ratio at all downstream locations (x/d = 2, 4 and 6). The NHFR has a positive value on the downstream surfaces and it is

greater for the hybrid scheme, as compared to the circular film hole. The enhancement in the NHFR for the hybrid scheme with blowing ratio is due to a significant increase in film cooling effectiveness with a relatively low heat transfer coefficient ratio value.

5.2.4 Comparison of film cooling performance between the hybrid scheme and other film cooling geometries

Figures 5.12a and b present the centerline and laterally averaged film cooling effectiveness of the hybrid scheme with other film hole configurations at low and high blowing ratios, respectively. The circular film hole produces jet lift-off (Jessen et al. 2007 and Ghorab et al. 2007), and the secondary flow penetrates into the main stream. As a result, the downstream film cooling effectiveness reduces with blowing ratio, as shown in Fig. 5.12a. Conversely, the film cooling effectiveness for the shaped hole is further enhanced with blowing ratio. The results show that the hybrid scheme produces the highest local centerline film cooling effectiveness compared to circular and fan shaped holes (Yu et al. 2002) in the streamwise direction at a low blowing ratio. At high blowing ratios (Br = 1.0, 1.5), the centerline film cooling effectiveness is further enhanced for the hybrid scheme compared to the shaped hole by Eriksen et al. (1974), the forward and lateral shaped hole by Yu et al. (2002) and trench shaped film hole Baheri et al. (2008) for Br = 1.25. The hybrid scheme causes the secondary flow to inject over and attaches more to the downstream surfaces at high blowing ratios (Ghorab et al. 2007). As a result, film cooling effectiveness is further enhanced more with increasing blowing ratio. Due to a reduction of the secondary flow momentum over the downstream surfaces, film cooling effectiveness declines gradually in the streamwise direction.

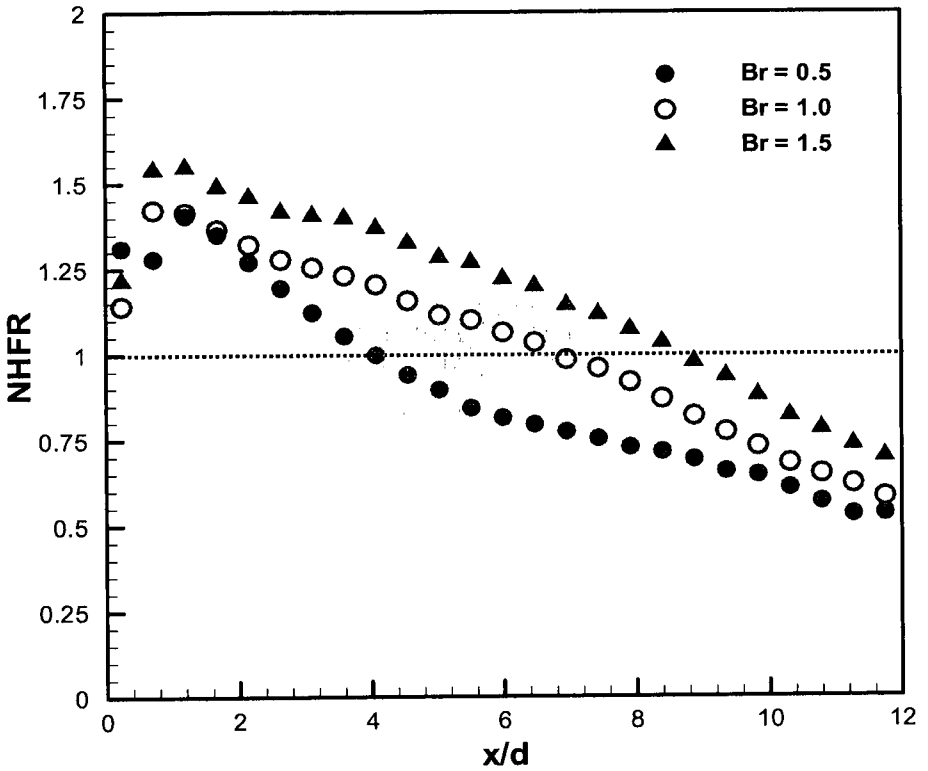

Figure 5.9. Centerline NHFR performance of the hybrid scheme at different blowing ratios.

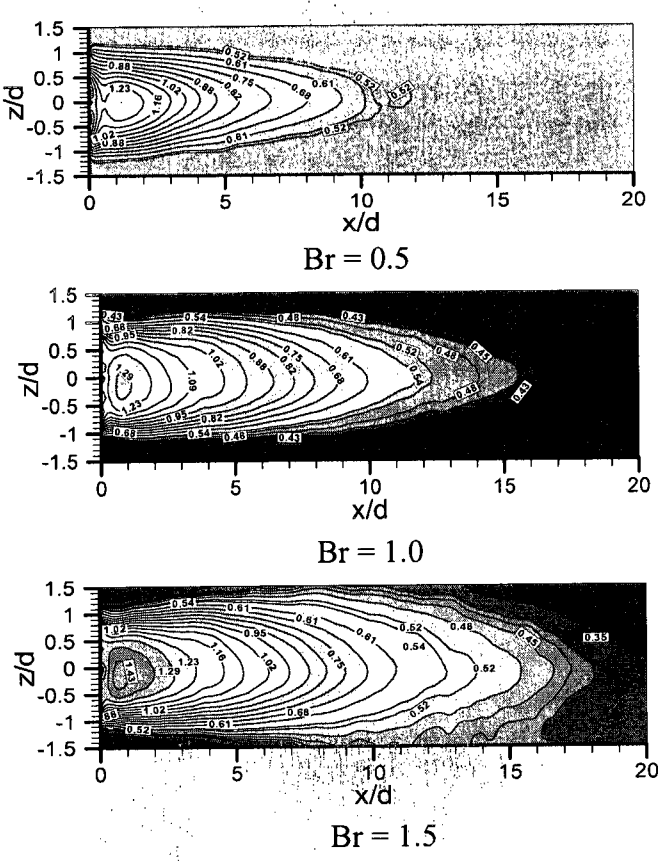

Figure 5.10. NHFR contours of the hybrid scheme with blowing ratio.

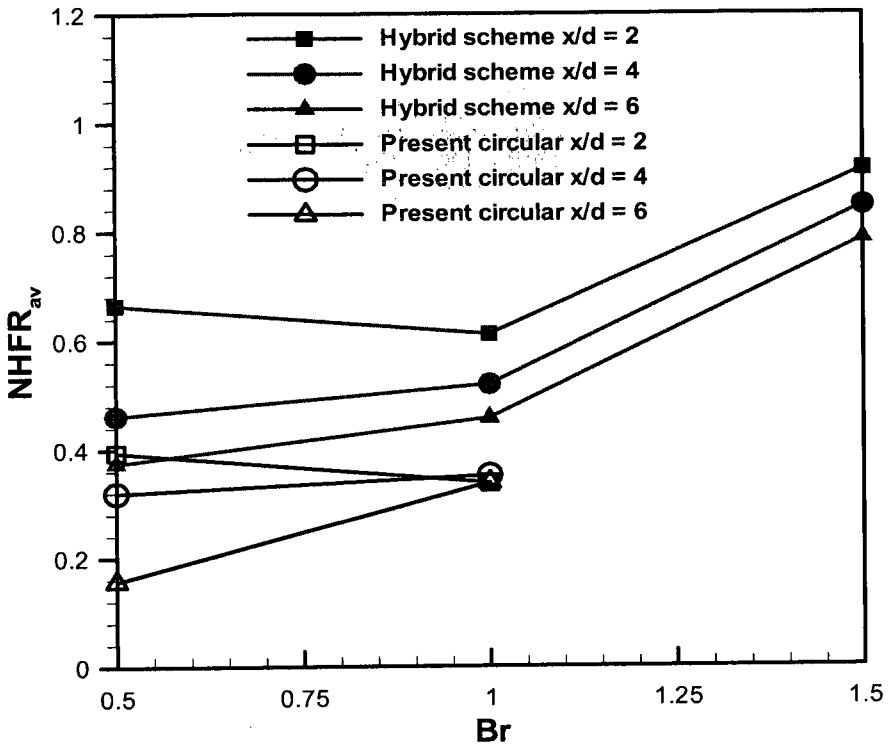

Figure 5.11. Variation of lateral average NHFR with blowing ratio for the hybrid scheme and the circular film hole.

Although the local comparison of film cooling effectiveness is very important, the average performance is most essential in order to evaluate overall film cooling performance for film hole geometries. The laterally averaged film cooling performances for the hybrid scheme are compared with other film hole configurations at low and high blowing ratios, as shown in Fig. 5.12b. The results show that the hybrid scheme provides the highest laterally averaged film cooling performance downstream of the injection film holes compared to fan shaped holes (Yu et al. 2002), circular holes and trench shaped film hole Baheri et al. (2008) at Br = 1.25. In addition, it produces higher performance at $x/d < 5$ than fan shaped holes (Saumweber et al. 2003) at low blowing ratio, but for $x/d \geq 5$, the film cooling effectiveness performance for both schemes are similar. The hybrid scheme has the ability to direct the secondary flow horizontally at high blowing ratios through the bending effect within the film hole. Consequently, the laterally averaged film cooling performance for the hybrid scheme is further enhanced far along streamwise direction at high blowing ratios compared to low blowing ratios. As a result, the new scheme produces the highest laterally averaged film cooling effectiveness at low and high blowing ratios compared to published data for different film hole configurations.

Figure 5.13a presents the centerline film cooling effectiveness performance for the louver and the hybrid schemes at low and high blowing ratios. The results show that, the hybrid scheme provides higher film cooling effectiveness with elongated downstream performance compared to the louver scheme at a low blowing ratio (Br = 0.5). The bending effect inside the film hole has the ability to direct the secondary flow horizontally over the target surface. At a high blowing ratio (Br = 1.0), film cooling effectiveness is enhanced, but it increases more for the louver scheme than the hybrid

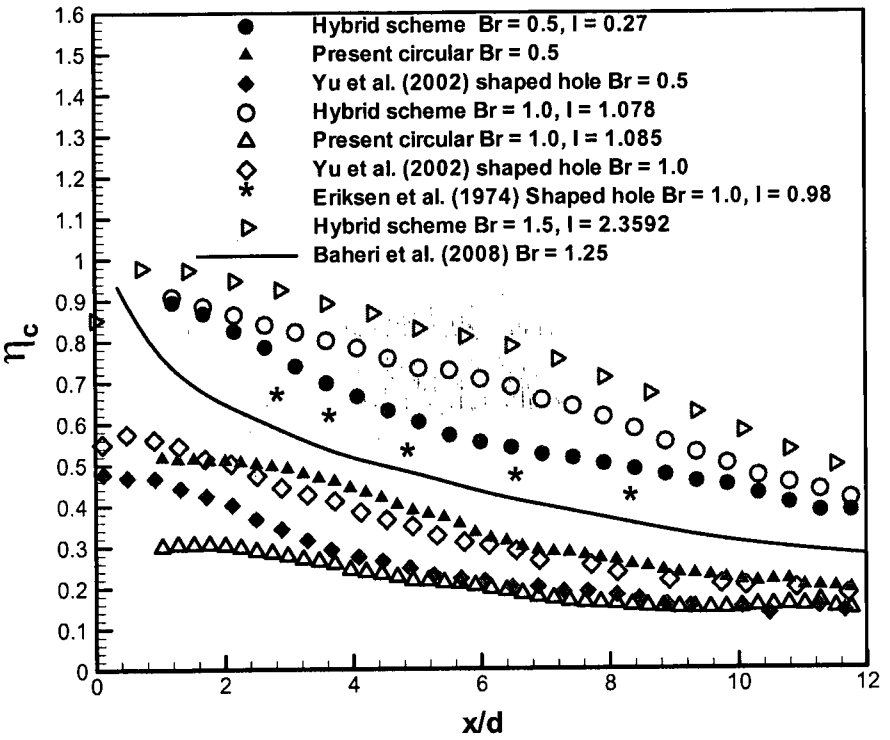

a) Centerline

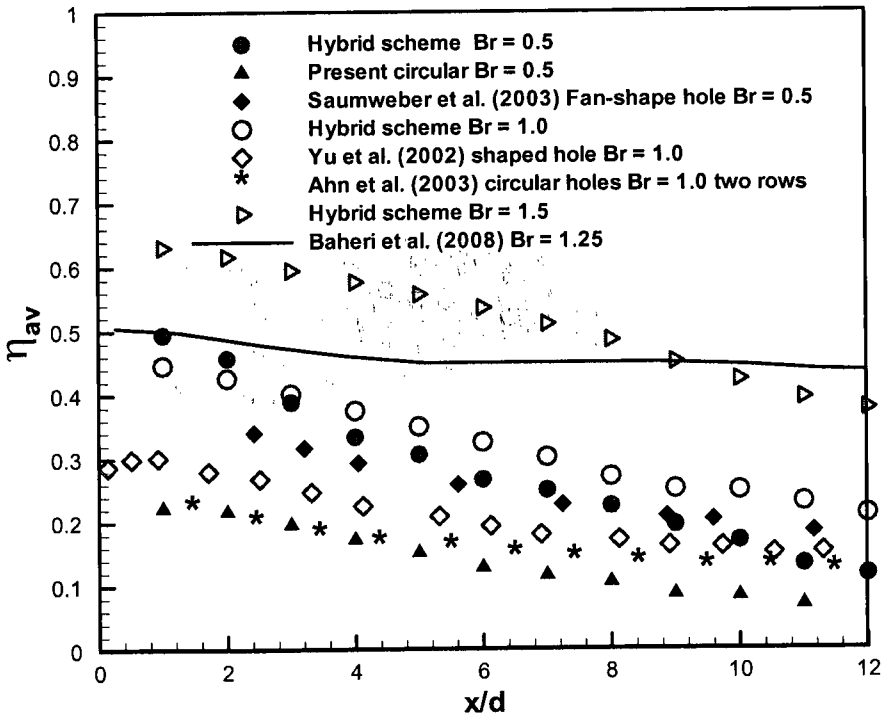

b) Laterally averaged

Figure 5.12. Film cooling effectiveness performance of the hybrid scheme with other published data at low and high blowing ratios.

scheme, as shown in Fig. 5.13a. Increasing the film hole exit area provides uniform momentum of the secondary flow, reducing penetration with the main flow, thereby increasing downstream film cooling effectiveness. The comparison of laterally averaged film cooling effectiveness for the two novel schemes is presented in Fig. 5.13b. The louver scheme has a wider exit area, so the laterally averaged film cooling effectiveness is higher than that for the hybrid scheme. However, the laterally averaged film cooling effectiveness provided by the hybrid scheme is further enhanced far downstream and the results are close to the louver scheme. This is because the interior bending of the hybrid scheme throttles and diffuses the secondary flow over the downstream surface so that the film cooling effectiveness performance increases and is further enhanced with increasing blowing ratio.

The streamwise laterally averaged heat transfer coefficient ratio of the hybrid scheme is compared with other film hole configurations at low and high blowing ratios, as presented in Fig. 5.14. The laterally averaged value of h_f/h_o for straight fan shaped holes (Dittmar et al., 2003) and two rows arrangement (Yuan and Martinez, 2005) has the highest heat transfer coefficient ratio compared to the hybrid scheme at low and high blowing ratios. The fan shaped hole (Yu et al., 2002), and circular hole provide a low value of the heat transfer coefficient ratio close to the film hole exit and increase close to unity far downstream. The hybrid scheme provides a laterally averaged h_f/h_o value of 1.1 close to the film hole exit and it decreases gradually to unity far downstream. There is no significant effect of the blowing ratio on the downstream laterally averaged ratio of h_f/h_o for the hybrid scheme. As a result, the hybrid scheme provides an average heat transfer coefficient ratio near unity and is unaffected by blowing ratio.

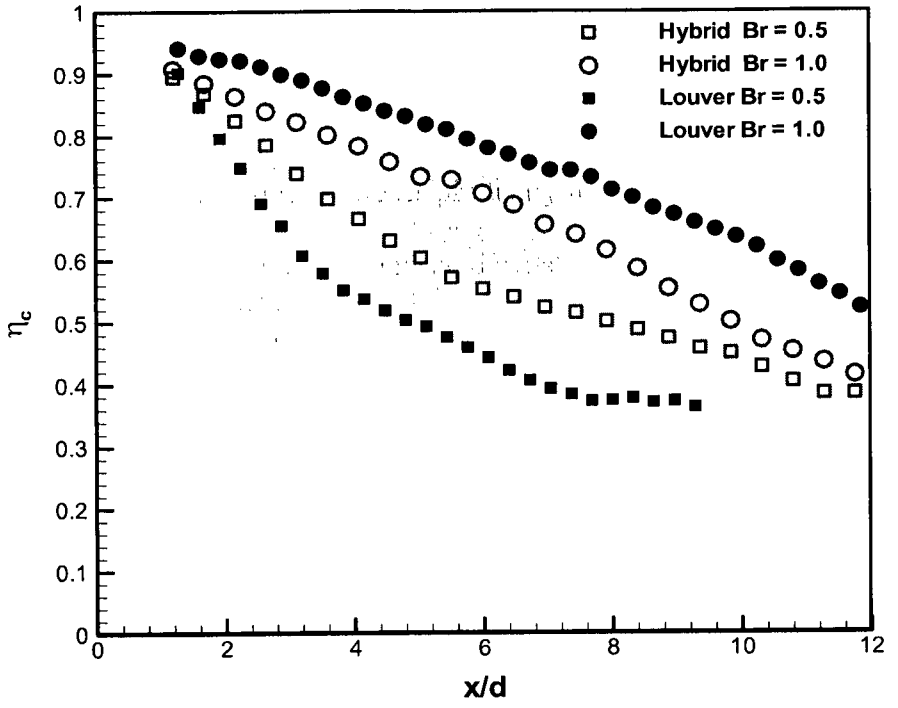

a) Centerline

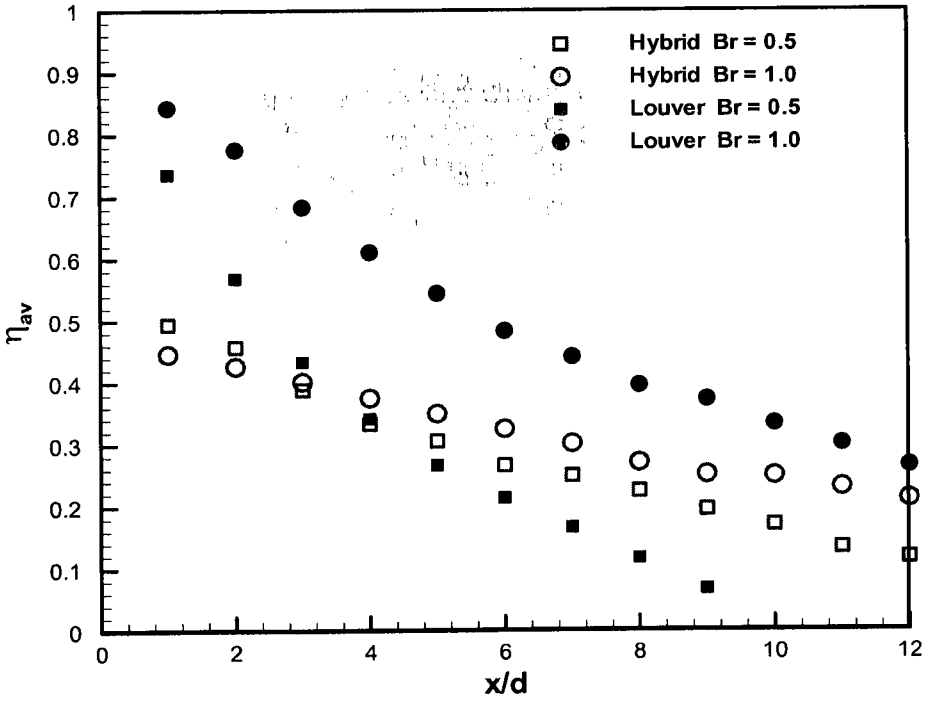

b) Laterally averaged

Figure 5.13. Film cooling effectiveness performance of the louver and the hybrid schemes.

The heat transfer coefficient must be minimized in order to reduce heat flux over the cooling surface. Consequently, hot spots may not be created over the cooling surfaces. Figure 5.15 shows the laterally averaged heat transfer coefficient ratio for the louver and the hybrid schemes at low and high blowing ratios. The laterally averaged heat transfer coefficient ratio increases gradually for the louver scheme until it reaches a unity downstream where the film cooling effectiveness is diminished. Meanwhile the hybrid scheme provides an average heat transfer coefficient ratio near unity over the downstream surfaces. The effect of the blowing ratio on the heat transfer ratio for both schemes is not significant since both the louver and the hybrid schemes create a thin boundary layer. The sub layer thickness does not vary with blowing ratio for both schemes. Creating uniform secondary flow at the film hole exit reduces the downstream turbulent boundary, such that the heat transfer ratio is relatively low.

Figure 5.16 presents the NHFR performance of the hybrid scheme compared to other film hole configurations at low and high blowing ratios using $\theta = 1.5$. The results show that the hybrid scheme produces a higher NHFR compared to traditional circular holes and fan-shaped holes (Yu et al., 2002) at blowing ratios of 0.5 and 1.0. The NHFR performance of the hybrid scheme increases the hyperactive film cooling region (NHFR > 1) in the region close to the trailing edge of the exit hole compared to other film hole configurations. The NHFR values decrease in the streamwise direction due to a reduction in the secondary flow momentum. At a high blowing ratio the jet lift-off increases for the circular holes (Jessen et al. 2007), thereby producing a lower NHFR than the fan shaped holes (Yu et al. 2002). The NHFR results for both film hole configurations are similar far downstream. As a result, the hybrid scheme enhances NHFR performance due to

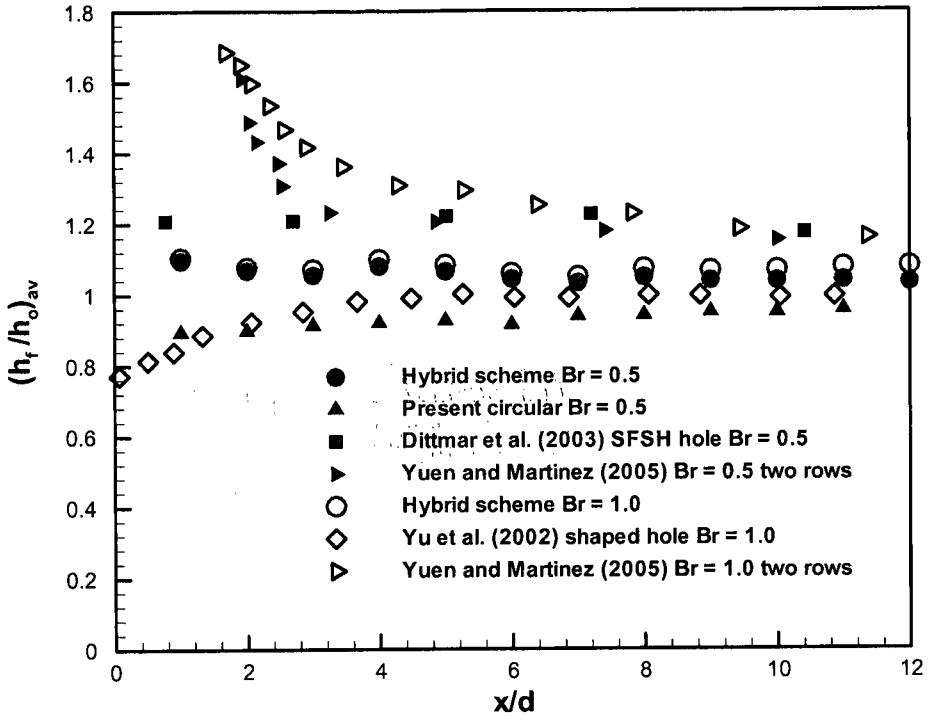

Figure 5.14. Comparison of laterally averaged heat transfer ratio of the hybrid scheme with other film hole configurations at low and high blowing ratios.

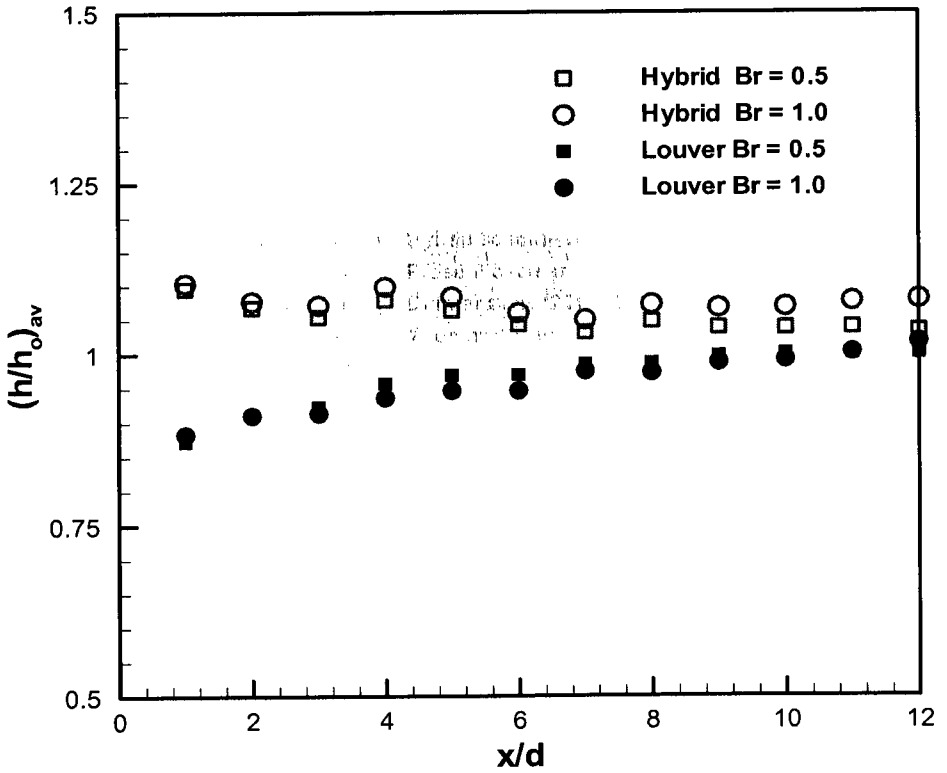

Figure 5.15. Laterally averaged heat transfer ratio for the louver and the hybrid schemes.

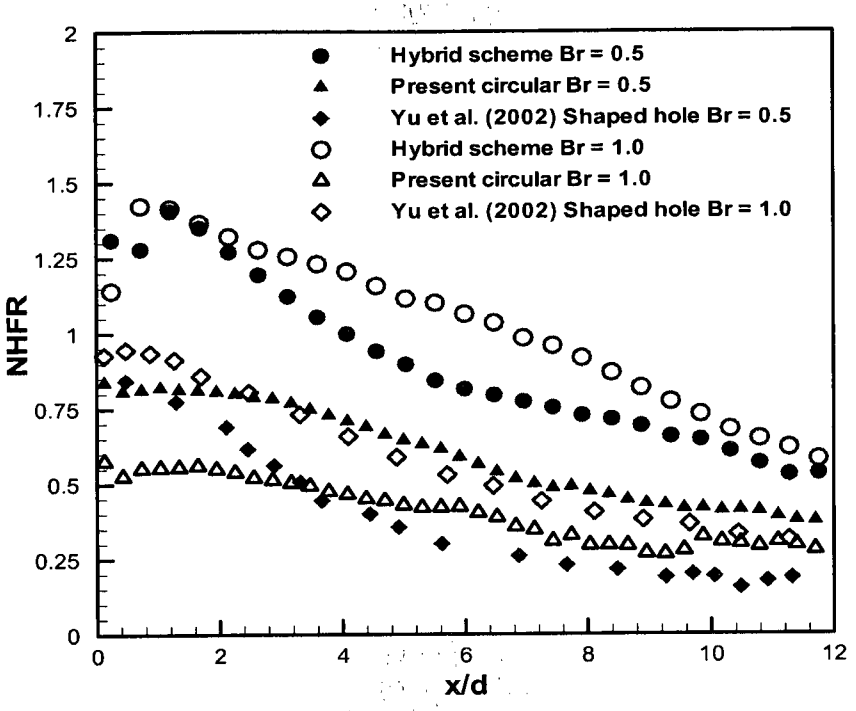

Figure 5.16. Comparison of centerline NHFR of the hybrid scheme with other film holes at low and high blowing ratio for $\theta = 1.5$.

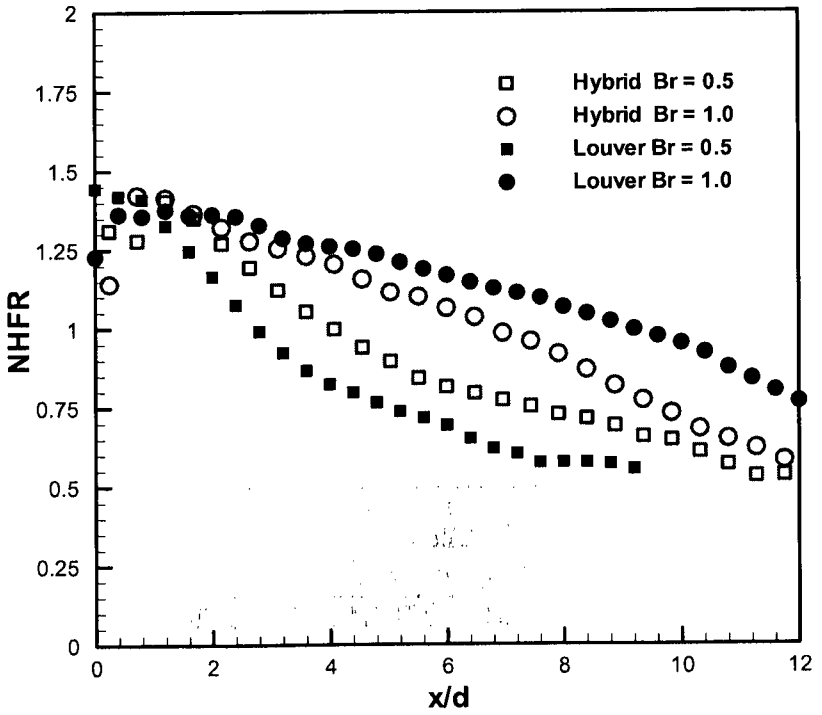

Figure 5.17. Centerline NHFR for the louver and the hybrid schemes at different blowing ratios.

a significant increase in the film cooling effectiveness with relatively low heat transfer coefficient ratio and increases with blowing ratio.

Figure 5.17 presents a comparison of the centerline NHFR for the louver and hybrid schemes at different blowing ratios. From the local centerline results, the hybrid provides a higher NHFR compared to the louver scheme at low blowing ratio (Br = 0.5), since the hybrid scheme provides high film cooling effectiveness with relatively low heat transfer ratio. The NHFR performance of the louver scheme is enhanced at high blowing ratios and it has similar NHFR performance as the hybrid scheme for $x/d < 4$. However, for $x/d \geq 4$, the NHFR for the louver scheme is higher than that for the hybrid scheme, as shown in Fig. 5.17, where the heat transfer coefficient ratio is lower for the louver scheme.

The uncertainty in TLC measurement is estimated to be $\pm$ 0.5°C. The uncertainty of thermal conductivity and diffusivity are estimated to be $\pm$ 3 %. Accordingly, the average uncertainty for the heat transfer ratio, film cooling effectiveness, Frossling number, net heat flux reduction, and blowing ratio are estimated to be $\pm$ 10 %, $\pm$ 8 %, $\pm$ 14 %, $\pm$ 10 %, and $\pm$ 12 %, respectively.

5.3 Summary

The film cooling performance of the hybrid scheme has been investigated for blowing ratios from 0.5 to 1.5 and a 0.94 density ratio using the TLC technique through this chapter. The results of the hybrid scheme are presented in terms of film cooling effectiveness, heat transfer coefficient ratio, Frossling number and NHFR, at low and high blowing ratios. Subsequently, the film cooling performances of the hybrid scheme have been compared with other traditional and advanced published film hole geometries,

as well as with the louver scheme. From the results, the hybrid scheme augments centerline and laterally averaged film cooling effectiveness with respect to other film holes at different blowing ratios. In addition, the film cooling effectiveness is enhanced with increasing blowing ratio for the hybrid scheme.

The centerline and lateral average heat transfer coefficient ratio of the hybrid scheme demonstrate an average near unity over the downstream surface and there is not a significant effect of h_f/h_o with increasing blowing ratio. Moreover, the hybrid scheme provided similar results of heat transfer coefficient ratio as the circular and fan shaped holes at high blowing ratios. The proposed scheme also produced lower values of Frossling number compared to circular holes and it is unfaltering with blowing ratio. The net heat flux reduction was presented to illustrate the overall film cooling performance by combining film cooling effectiveness and the heat transfer coefficient ratio. The dimensionless reference temperature, $\theta = 1.5$, was used to calculate the NHFR. The hybrid scheme provided a high film cooling effectiveness with a relatively low heat transfer coefficient ratio, and therefore demonstrates the highest NHFR in the streamwise and lateral average directions compared to other film hole geometries. As a result, the hybrid scheme is able to increase the airfoil's lifetime and the inlet gas turbine temperature can be increased, which in turn improves the overall gas turbine efficiency without any possibility of creating hot spots on the downstream surfaces.

Chapter 6

Chapter 6 Adiabatic and Conjugate Heat Transfer Analysis of Hybrid Scheme

Throughout this chapter, the adiabatic film cooling and flow structures of the hybrid scheme will be investigated numerically. The flow field and film cooling effectiveness at different locations of the computational domain will be presented in order to understand the physics of the hybrid scheme cooling performance throughout the flow structures at different blowing ratios. The film cooling performance of the hybrid scheme will be evaluated with respect to the circular hole. Subsequently, the film cooling and conjugate heat transfer will be combined to investigate the cooling performance of the hybrid scheme with different flow arrangements, specifically, parallel flow and jet impingement with different gap heights, at different blowing ratios.

6.1 Adiabatic film cooling effectiveness and flow structure analysis of the hybrid scheme

This section will present the adiabatic film cooling effectiveness performance and flow structure of the hybrid scheme and the circular hole numerically. The local and average downstream adiabatic film cooling effectiveness and the heat transfer coefficient ratio in lateral and downstream directions will be illustrated at low and high blowing ratios. As well, the downstream boundary layer and velocity contours at different planes will be presented in order to understand the film cooling physics of the hybrid scheme compared to that of the circular film hole geometry.

6.1.1 Geometry and boundary conditions

The hybrid scheme was simulated based on the finite volume technique. The computational domain included the main duct, the hybrid scheme, and supply plenum, as shown in Fig. 6.1a. The main duct dimension was 85d long, 15d height, and 3d width. The hybrid scheme included two consecutive film hole configurations. The new scheme was designed to combine the advantages of circular and film hole shaped configurations. The first hole of the hybrid scheme was circular, having 6.4 mm diameter (d) and an inclination angle of 30°. The second shaped hole configuration started at a distance of 0.8d from the external surface, and intersected the circular hole, as shown in Fig. 6.1b. The slot angle of the hole shape was 10° in the streamwise direction, yielding a lengthwise opening of 3d. Fig. 6.1b also illustrates all hybrid scheme dimensions based on diameter. The main flow had a uniform inlet velocity and temperature of 10 m/s and 300 K, respectively. The turbulent intensity of the secondary and mainstream flow was 3%. The turbulent length scales for main and secondary flows were 0.001m and 0.0015m, respectively. The secondary flow with temperature of 320 K passes through a plenum, and then moves through the hybrid scheme to spray over the downstream surface.

The main and secondary flows were considered as incompressible-ideal-gas flows with constant inlet properties. The inlet velocity and temperature profiles for both streams were uniform. A single hole was simulated with symmetry boundary conditions at $z = \pm$ 1.5d in the spanwise direction. External walls for the duct, plenum, downstream and upstream bottom surfaces of the duct were considered adiabatic walls with no slip condition. The exit flow from the duct was considered a pressure outlet with zero gauge pressure (P_{abs} = 1.01325 bar).

Structured and unstructured grids with a multi-block were employed throughout the numerical study to provide the highest grid quality. The grids were generated using Gambit 2.4 software. Figure 6.2 demonstrates the center plane computational grids of the circular hole and the hybrid scheme. The grids near the target surface were adapted to investigate the results with different y^+ values for the grid independence study. Moreover, the grids were designed to be intensive, with high quality close to the inlet and exit of the hybrid scheme to capture the interaction and jet characteristics of the flow. In order to resolve the viscosity effects near the wall, the turbulence model with enhanced wall treatment was used in this study. The mesh was designed to give an average y^+ value less than unity. Many researchers have used y^+ less than unity or of order unity near the target wall for their simulation studies such as Jia et al. (2005), who used a y^+ less than unity to investigate numerically the effect of different jet angles on film cooling. Li et al. (2005) investigated the effect of different model schemes on mist film cooling by using y^+ at the order of unity. Moreover, Immarigeon and Hassan (2006) used y^+ equal unity to study the louver scheme on film cooling effectiveness.

The adiabatic film cooling effectiveness performance for the circular and the hybrid film hole configurations, as well as the flow characteristics over a flat surface were investigated throughout this study at different blowing ratios. Table 6.1 lists different adiabatic cases studied for the circular hole and the hybrid scheme. Figure 6.2 shows the center plane view of the grids used, which consists of both structured and unstructured meshes for the circular hole and the hybrid schemes.

Table 6.1. Adiabatic study test matrix.

	Circular	Hybrid
Br	0.5 , 1.0, 2.0	0.5 , 1.0, 2.0
Dr	0.95	0.95

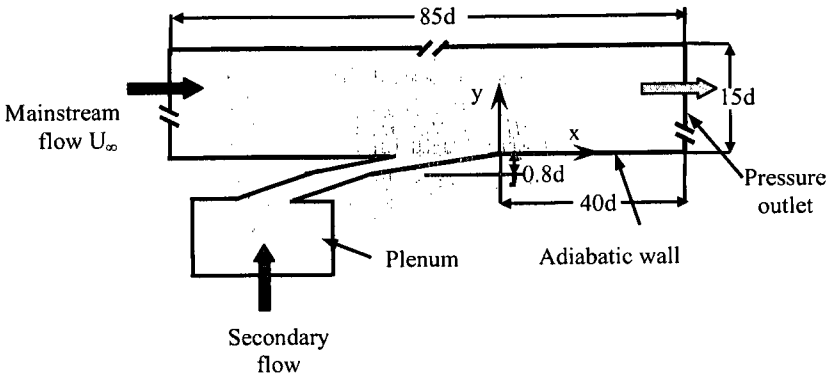

a) Computational domain

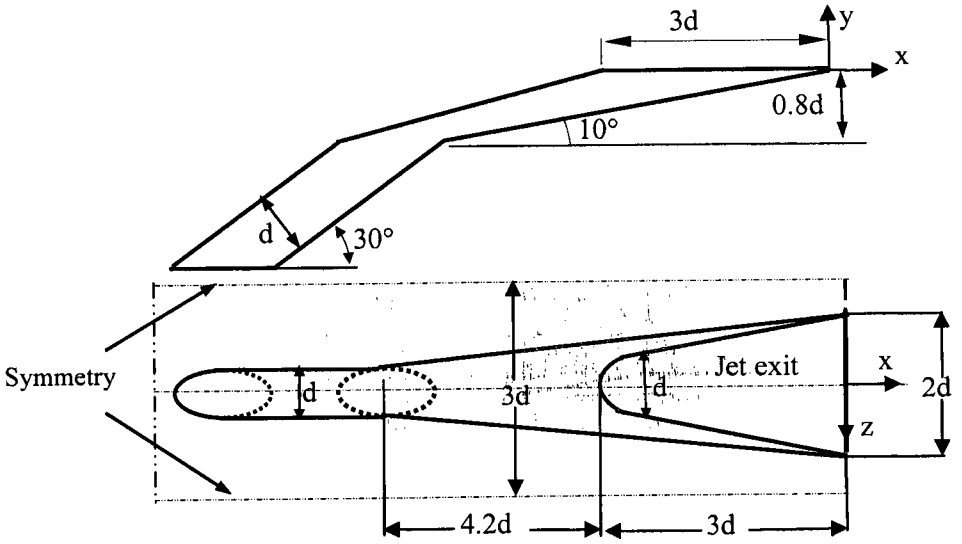

b) Hybrid scheme

Figure 6.1. Schematic of the computational domain and the hybrid scheme.

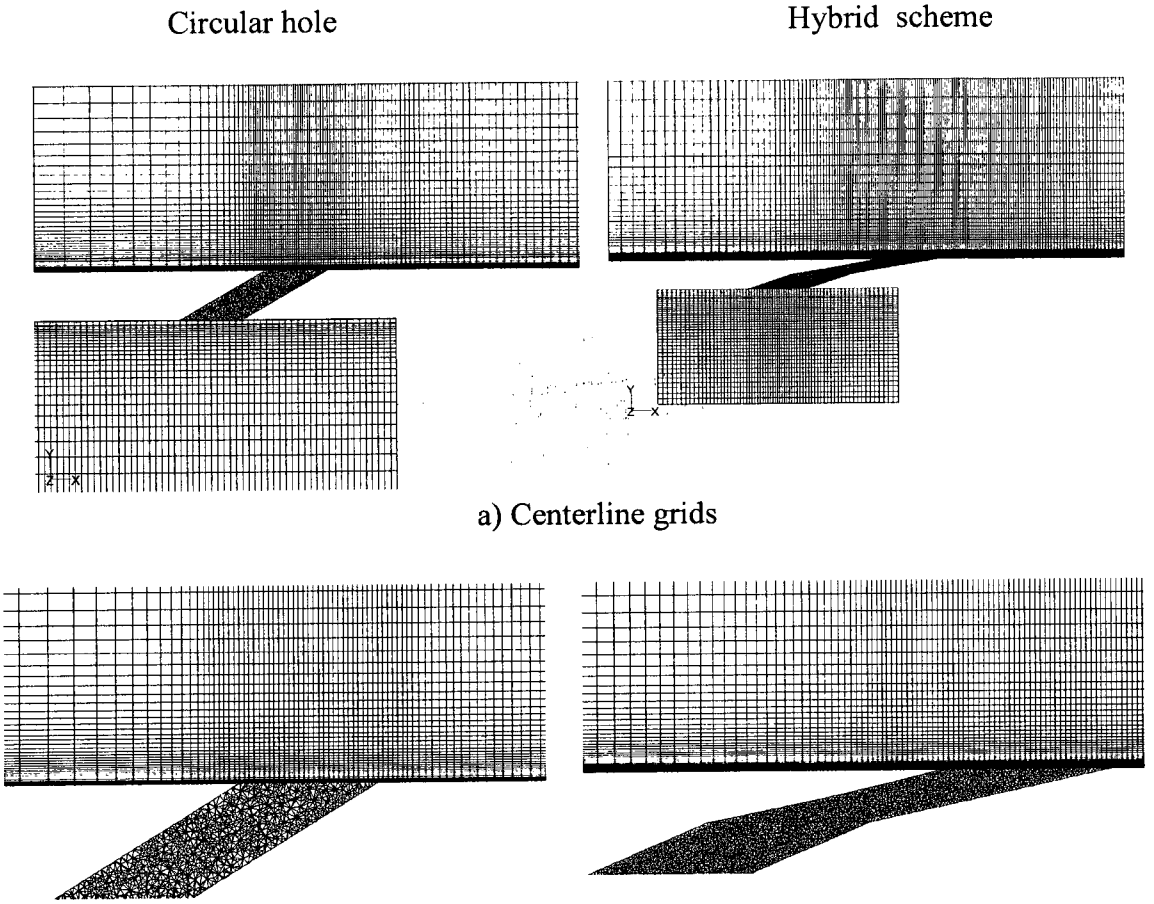

a) Centerline grids

b) Close view grids

Figure 6.2. Computational domain grids of circular hole and hybrid scheme.

6.1.2 Grid test and validation

In order to validate the present numerical methodology, the hybrid scheme experimental results were used. The film hole scheme was experimentally studied in chapter 5.

The grids were designed to be fine close to the target surface and film holes, in order to capture the flow separation as well as the jet lift-off. Each layer of turbulent boundary layers required different treatment for accurate simulation. In the numerical simulations, the grids were designed to provide an average y^+ value over the target surfaces less than unity, which has been recommended and used by Jia et al. (2005), Li and Wang (2005) and Immarigeon and Hassan (2006).

Figure 6.3 demonstrates the film cooling performance of the hybrid scheme using a different grid design of y^+ value less than unity. The discrepancy of film cooling effectiveness between a fine grid of 1.35 M cells and an even finer grid of 1.5 M cells is very small. As a result, the gridded system with a total number of 1.35 M cells was used in the present simulations. Different turbulence models, Realizable k-ε, Standard k-ω, and Spalart Allmaras were examined to accurately simulate film-cooling flow. Figure 6.4 presents the effect of the different turbulence models on the film cooling effectiveness for the hybrid scheme. From the results, the film cooling effectiveness obtained using the Realized k-ε model matched well with the experimental data. The best prediction for the film cooling effectiveness was also obtained using the Realizable k-ε model among the several available turbulent models (Zhang and Hassan, 2006). As a result, Realizable k-ε model with enhanced wall treatment was used as the turbulence model within this study.

6.1.3 Adiabatic film cooling results and discussion

This section will illustrate the film cooling performance and flow characteristics of the hybrid scheme and the circular hole at blowing ratios from 0.5 to 2.0. The results will present the local and average film cooling performance over the downstream surface and will then analyze the physical flow structures.

6.1.3.1 Film cooling effectiveness and flow field

Figure 6.5 illustrates the downstream velocity ratio boundary layer for the hybrid scheme and the circular film hole at different downstream locations and blowing ratios. The secondary flow provided by the hybrid scheme was usually attached to the downstream surfaces with small boundary layer thickness. Moreover, the secondary flow was attached and sprayed over the entire downstream surfaces at high blowing ratios. On the other hand, the boundary layer profiles for the circular hole were relatively high at low blowing ratios compared to the hybrid scheme. Secondary flow jet lift-off was detected for the circular hole at high blowing ratios; it increased with increasing blowing ratios, as shown in Figs. 6.5b and 6.5c. Moreover, the boundary layer thickness increased along the streamwise direction at high blowing ratios (Fig.6.5c). As a result, the secondary flow penetrated the main flow and reduced film cooling effectiveness for the circular hole at high blowing ratios.

Figure 6.6 demonstrates the center plane velocity contours for the circular hole and the hybrid scheme at different blowing ratios. The contours are presented to provide a physical understanding of the secondary and main flow structures for the two film hole geometries at different blowing ratios. Figure 6.6a shows that the secondary flow attaches to the downstream surface with less penetration with the main flow for the

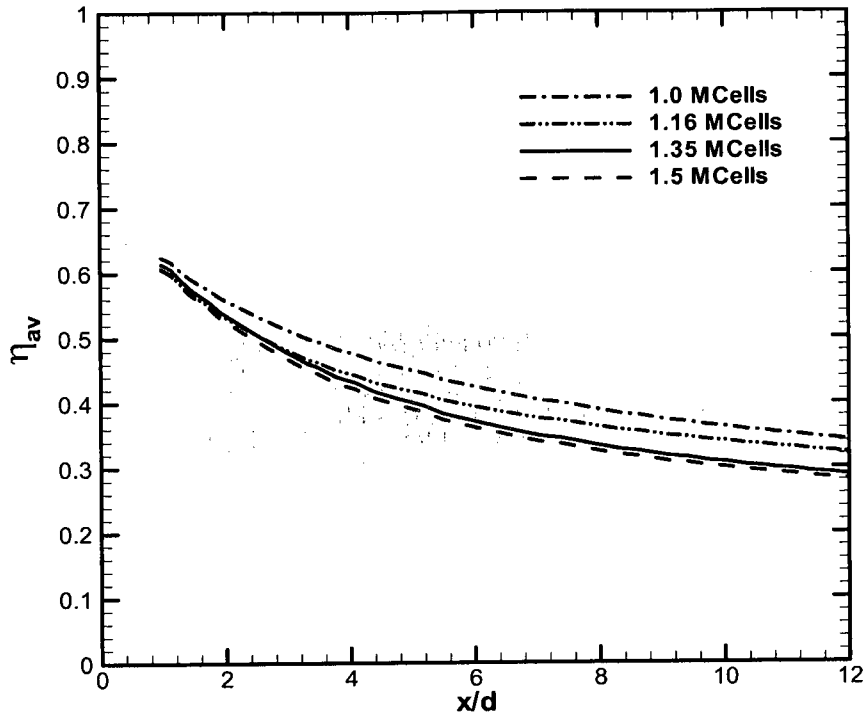

Figure.6.3. Laterally averaged film cooling effectiveness of different grids for the hybrid scheme.

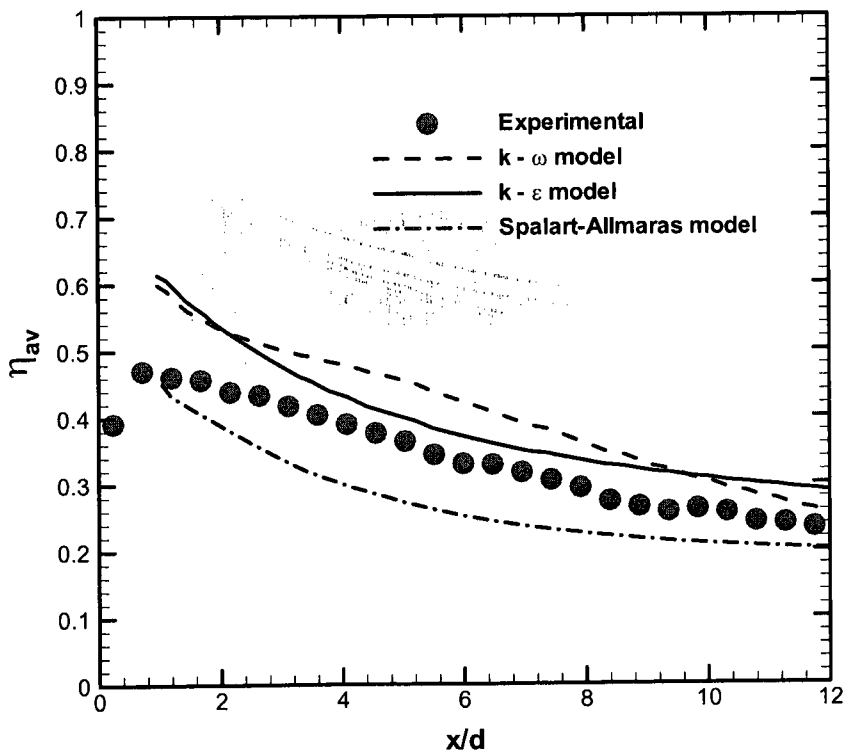

Figure 6.4. Film cooling effectiveness of the hybrid scheme with different turbulence models.

circular hole at low blowing ratio (Br = 0.5). For the same blowing ratio, the hybrid scheme directed the exit secondary flow velocity in the horizontal direction due to interior scheme bending. The advantage of the bending effect increased with increased blowing ratios by reducing the infiltration of the secondary flow with mainstream flow, as shown in Figs. 6.6b and 6.6c for the hybrid scheme. Consequently, the downstream film cooling effectiveness will be enhanced with blowing ratios compared to the circular hole. On the other hand, the jet lift-off increased with blowing ratio for the circular hole (Figs. 6.6b and 6.6c), hence the film cooling effectiveness diminishes at high blowing ratios.

Figures 6.7a and b demonstrates the local downstream centerline film cooling performance of the hybrid scheme and the circular hole at low and high blowing ratios, respectively. From the results, the hybrid scheme provided a higher film cooling effectiveness performance compared to the circular hole at low blowing ratio (Br = 0.5). The film cooling effectiveness values were high close to the film hole exit and where reduced along the streamwise direction due to a decrease in the secondary flow momentum over the downstream surfaces. The secondary flow jet lift-off increased at high blowing ratios for the circular hole, hence downstream film cooling effectiveness was reduced. The reduction in film cooling effectiveness increasing with increased blowing ratio for circular holes, as shown in Fig. 6.7b. However, the hybrid scheme directed the secondary flow in the horizontal direction thereby diminishing the jet lift-off of the secondary flow. Consequently, downstream film cooling performance for the hybrid scheme enhanced with increased blowing ratios (Fig. 6.7b). As a result, the hybrid scheme provided superior film cooling effectiveness at high blowing ratios.

Figures 6.8 illustrates a comparison of laterally averaged film cooling performance between the hybrid scheme and the circular hole at low and high blowing ratios, respectively. The results show that the latterly averaged film cooling effectiveness over the downstream surfaces is enhanced for the hybrid scheme compared to the circular hole, as shown in Fig. 6.8a. The hybrid scheme sprayed the secondary flow intensively in the spanwise direction. Thus, the laterally averaged film cooling performance increased, and further increased at high blowing ratios. However, the laterally averaged film cooling effectiveness performance decreased for the circular hole and reached near zero at high blowing ratios for $3.0 < x/d < 10$ due to the jet lift-off, as shown in Fig. 6.8b.

Local laterally averaged film cooling effectiveness performances for the circular hole and the hybrid scheme are presented in Fig. 6.9 for different downstream locations and blowing ratios. The results show that, at $x/d = 3.0$, the film cooling effectiveness performance provided by the hybrid scheme was superlative compared to the circular hole. The difference in film cooling performance between the two film hole configurations increased more with increasing blowing ratios, as shown in Fig. 6.9. The downstream film cooling effectiveness decreased along the streamwise direction for both configurations, due to a reduction in secondary flow momentum. The laterally averaged film cooling effectiveness performance of the hybrid scheme was still higher than that produced by the circular hole at $x/d = 9.0$, as shown in Fig. 6.9. At a high blowing ratio ($Br = 2.0$), the circular film hole provided a lateral film cooling performance near zero, as shown in Fig. 6.9c.

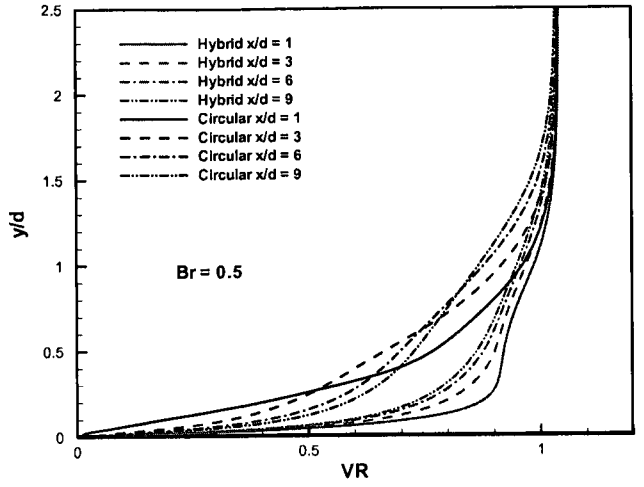

a) Br = 0.5

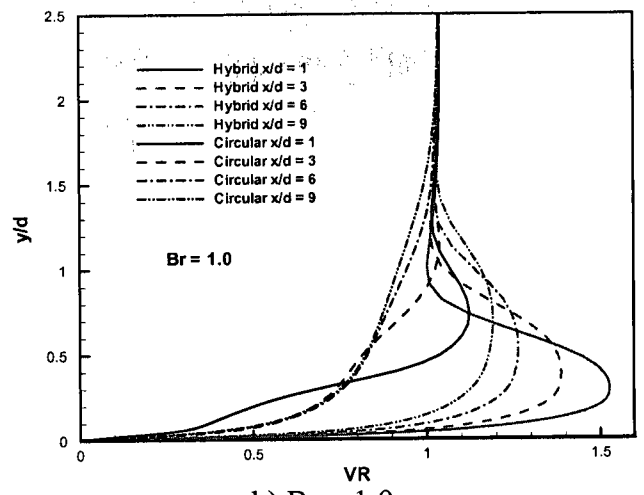

b) Br = 1.0

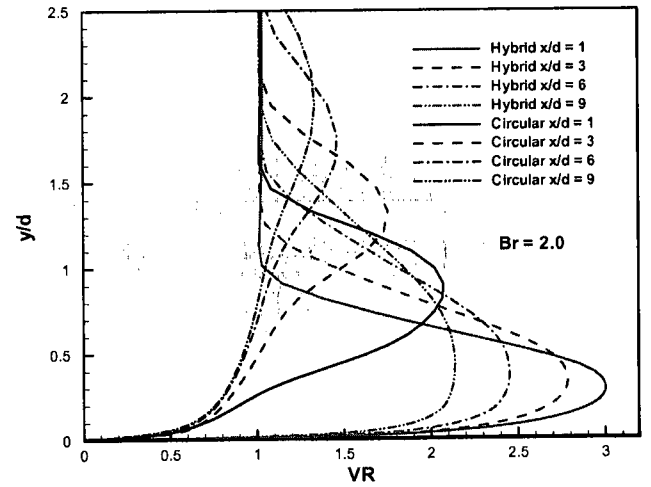

c) Br = 2.0

Figure 6.5. Boundary layer profiles of circular hole and hybrid scheme at different blowing ratios and downstream locations.

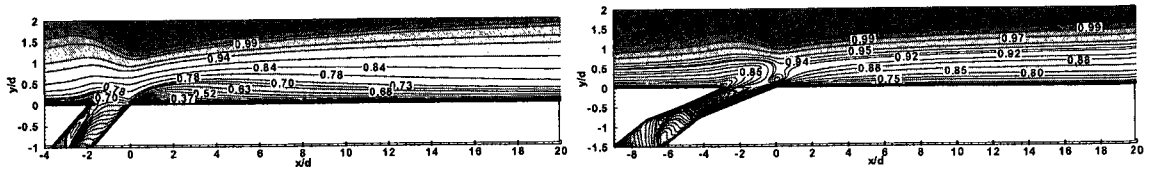

a) Br = 0.5

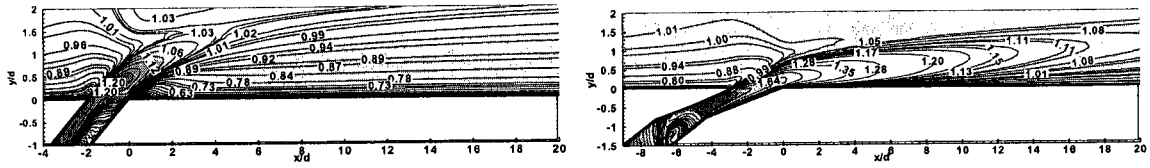

b) Br = 1.0

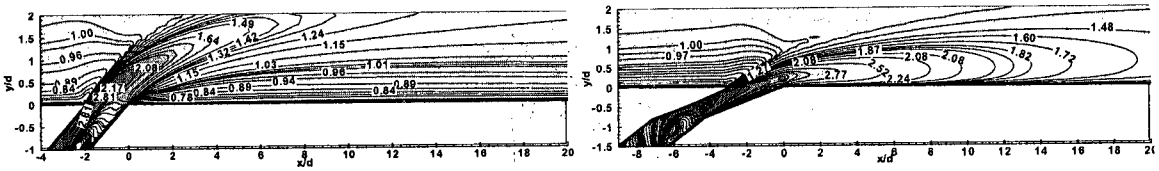

c) Br = 2.0

Figure 6.6. Center plane velocity ratio contours of circular hole and hybrid scheme at different blowing ratios.

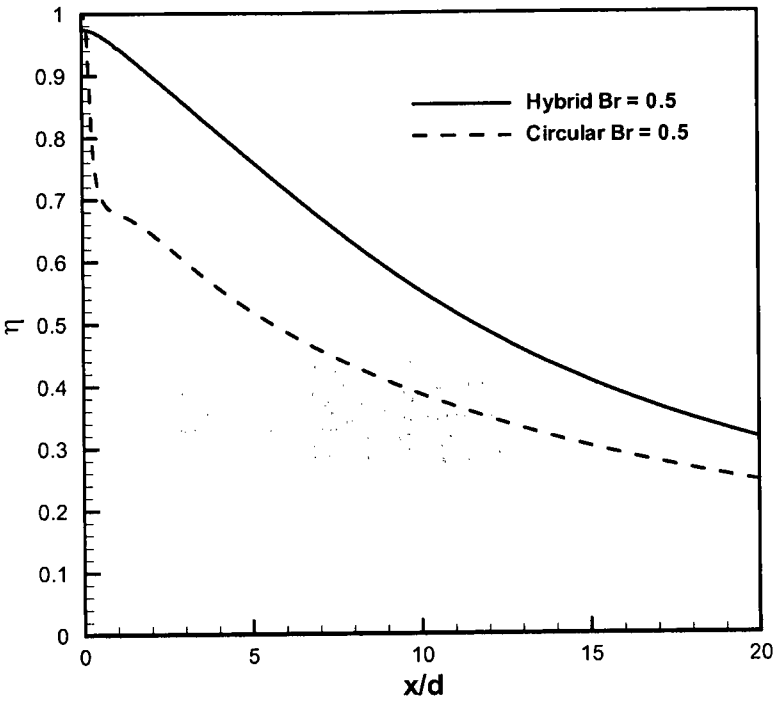

a) low blowing ratio

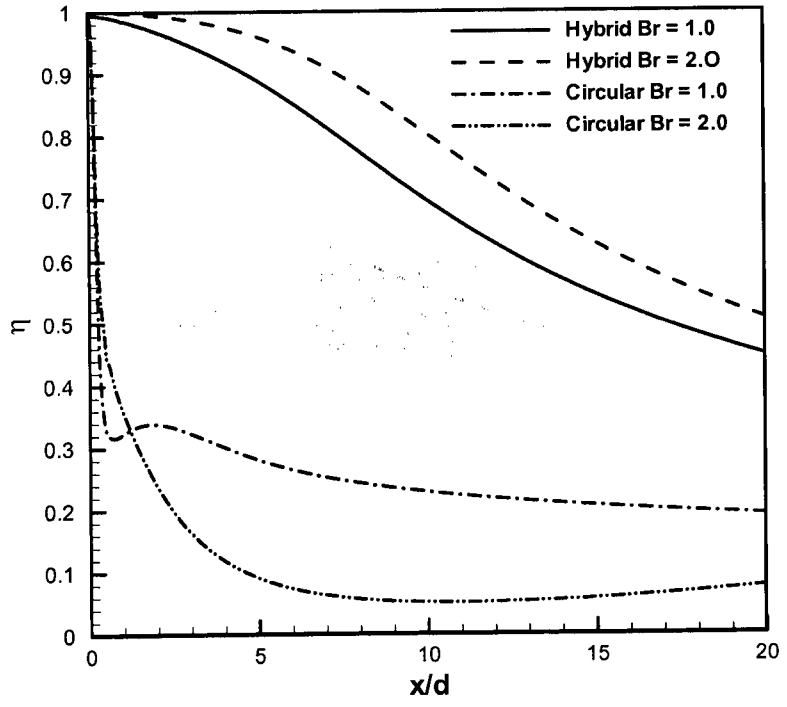

b) high blowing ratio

Figure 6.7. Downstream centerline local film cooling effectiveness performance of circular hole and hybrid scheme at different blowing ratios.

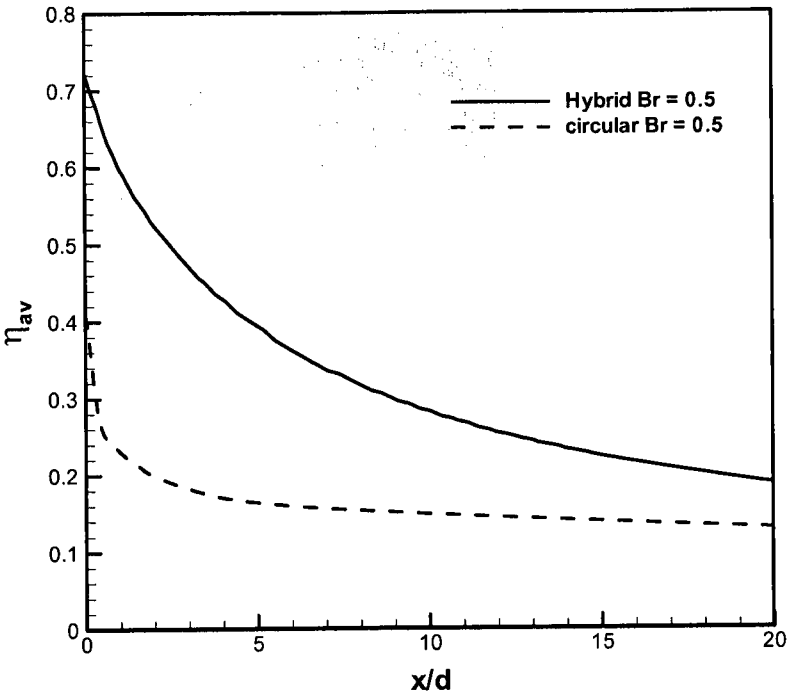

a) low blowing ratio

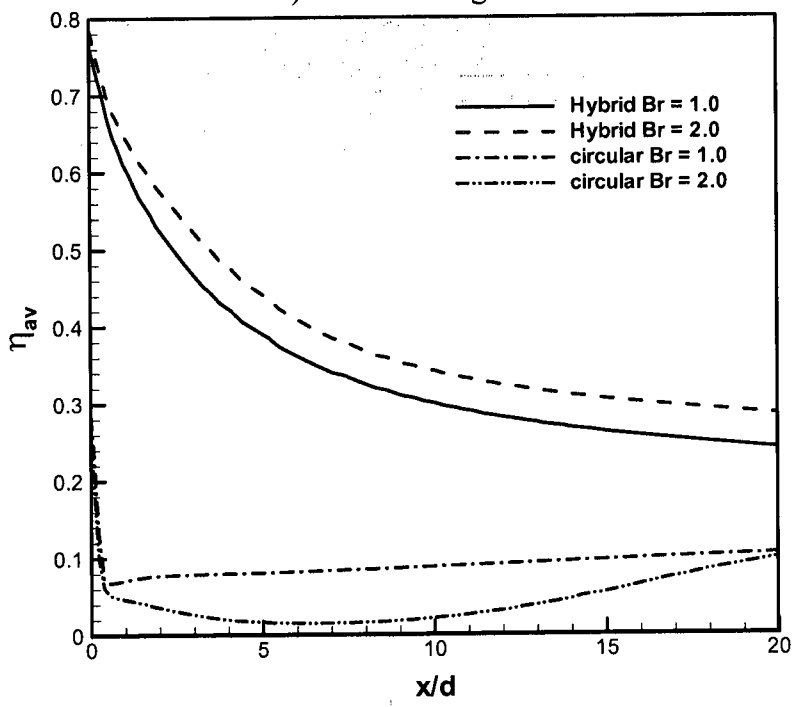

b) high blowing ratio

Figure 6.8. Downstream laterally averaged film cooling effectiveness performance of circular hole and hybrid scheme at different blowing ratios.

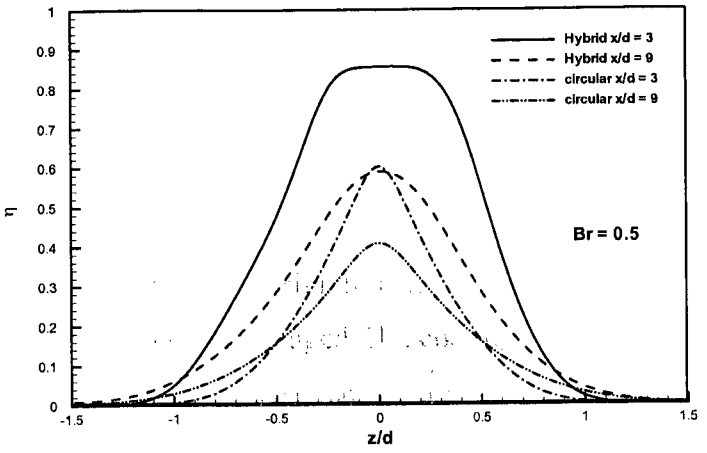

a) Br = 0.5

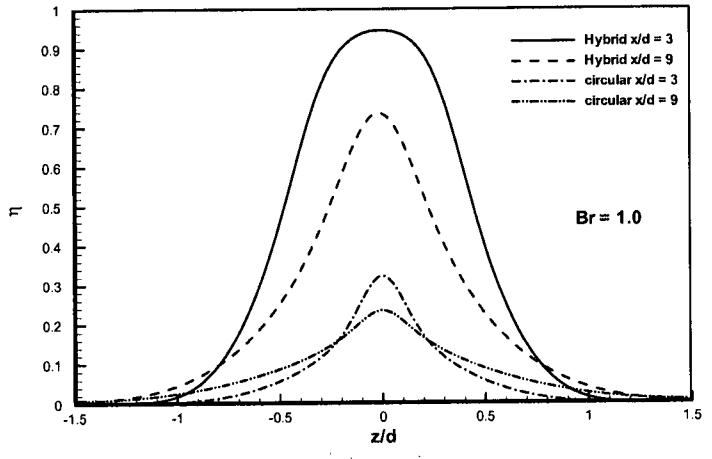

b) Br = 1.0

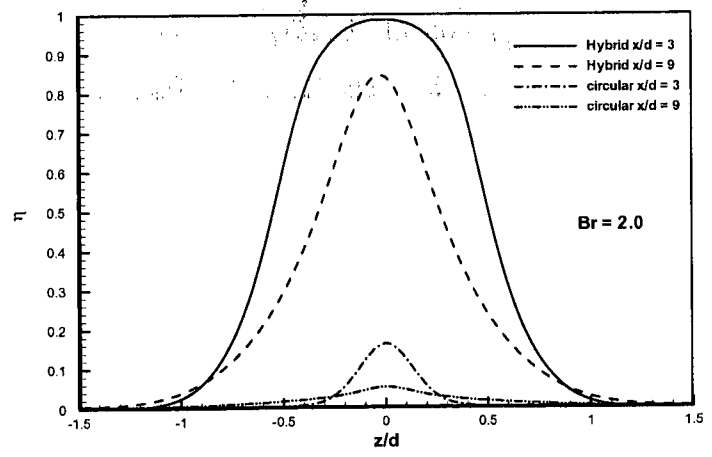

c) Br = 2.0

Figure 6.9. Lateral film cooling effectiveness performance of circular hole and hybrid scheme at different blowing ratios and downstream locations.

Figure 6.10 demonstrates the downstream centerline plane of the film cooling effectiveness contours for the circular hole and the hybrid scheme at different blowing ratios. At a low blowing ratio, the circular film hole provided less jet lift-off, hence the film cooling performance improved for the circular hole. However, the hybrid scheme provided a higher performance compared to the circular hole, as shown in Fig. 6.10a. The reason for this is because the hybrid scheme directed the secondary flow in the horizontal direction, reducing the vertical flow. Consequently, the film cooling effectiveness for the hybrid scheme was enhanced with increasing blowing ratio, but decreased for the circular hole due to an increase in the jet lift-off, as shown in Figs.6.10b and 6.10c.

Downstream film cooling effectiveness contours for the circular hole and the hybrid scheme at blowing ratios of 0.5, 1.0, and 2.0 are presented in Fig. 6.11. The contours illustrate the performance of each film hole configuration at different blowing ratios to cover the downstream surface areas with the secondary flow, therefore, protecting the outside airfoil from extreme main stream temperatures. The results showed that the circular hole provided downstream film cooling effectiveness with a maximum value of ≈ 0.63 near the trailing film hole edge at a low blowing ratio (Br = 0.5). Due to a reduction in the secondary flow momentum, the film cooling effectiveness performance decreased along the streamwise and spanwise directions. The hybrid scheme enhanced the film cooling effectiveness, and it reached a value near unity close to the film hole exit, and reduced gradually along the downstream and spanwise directions, as shown in Fig. 6.11a. The effect of the secondary flow jet lift-off on the downstream film cooling effectiveness for the circular hole can be seen at high blowing ratios, as shown in Figs. 6.11b and 6.11c. In contrast, the downstream film cooling effectiveness increased for the

hybrid scheme with increasing blowing ratio. The hybrid scheme was designed to direct the secondary flow in the horizontal direction. The horizontal jet velocity component was dominant at high blowing ratios compared to the vertical velocity component. As a result, the hybrid scheme provided superior film cooling effectiveness over the downstream surface at high blowing ratios, as shown in Figs. 6.11b and 6.11c.

Vertical downstream planes in the spanwise direction at x/d = 1.0, 3.0, and 9.0 present the film cooling effectiveness and velocity ratio contours for the circular hole and the hybrid scheme at blowing ratios of 0.5 and 2.0, as shown in Figs. 6.12 and 6.13 respectively. From the results, the secondary flow attached to the downstream surfaces at x/d = 1.0 and provided a wider film cooling effectiveness in the spanwise direction for the circular hole, as shown in Fig. 6.12a. Further downstream, the secondary flow sprayed far away from the target surface in the vertical direction, hence reducing the film cooling effectiveness along the streamwise directions (x/d = 3.0 and 9), as shown in Fig.6.12a. In addition, the secondary flow circulation was created over the downstream surface with a high value near the film hole exit, and decreased along the streamwise direction. However, the hybrid scheme provided a uniform velocity ratio at the downstream location with a little damping for the velocity ratio profile near the trailing film hole due to the shape of the exit film hole. Therefore, the film cooling effectiveness provided a wider positive effect on the hybrid scheme along the downstream locations, as shown in Fig. 6.12b for low blowing ratio (Br = 0.5). At high blowing ratio (Br = 2.0), the secondary flow sprayed far away from the downstream surface. The velocity ratio profile had a crescent shape and became more concave far downstream, as shown in Fig. 6.13a. On the other hand, the secondary flow vortex began with kidney shape in the

region, close to the film hole exit and grew along the streamwise direction into a horse shoe shaped vortex. As a result, the film cooling effectiveness for the circular hole was reduced at high blowing ratios. Conversely, the hybrid scheme produced an extensive film cooling effectiveness in the spanwise direction along the downstream locations, as shown in Fig. 6.13b. Furthermore, the secondary flow velocity ratio for the hybrid scheme sustained attachment to the downstream surface with less flow circulation compared to the circular hole at high blowing ratios.

6.1.3.2 Heat transfer coefficient performance of the hybrid scheme

Figure 6.14 illustrates the centerline and laterally averaged performance of the heat transfer coefficient ratio (HTCR) for the hybrid scheme at Br = 0.5 and 1.0. The hybrid scheme produced local laterally averaged values near unity at low blowing ratios. At a high blowing ratio, the laterally averaged HTCR increased by 20% above unity due to an increase in the velocity ratio in the boundary layer region. Figure 6.14 presents the experimental laterally averaged HTCR of the hybrid scheme at Br = 0.5 and 1.0. From the experimental results, the effect of the blowing ratio on the HTCR was small. The difference between the predicted results and the experimental data was within experimental uncertainty. The lateral performance HTCR of the hybrid scheme for Br = 0.5 and 1.0, at different downstream locations are illustrated in Fig. 6.15. The hybrid scheme provided a lower HTCR near the film hole center along the downstream direction at a low blowing ratio. The HTCR profiles increased for Br = 1.0 and produced a dimple around the center, near the film hole exit due to the leading shape of the film hole exit. Moreover, the HTCR performance decreased in the streamwise and spanwise directions, as shown in Fig. 6.15.

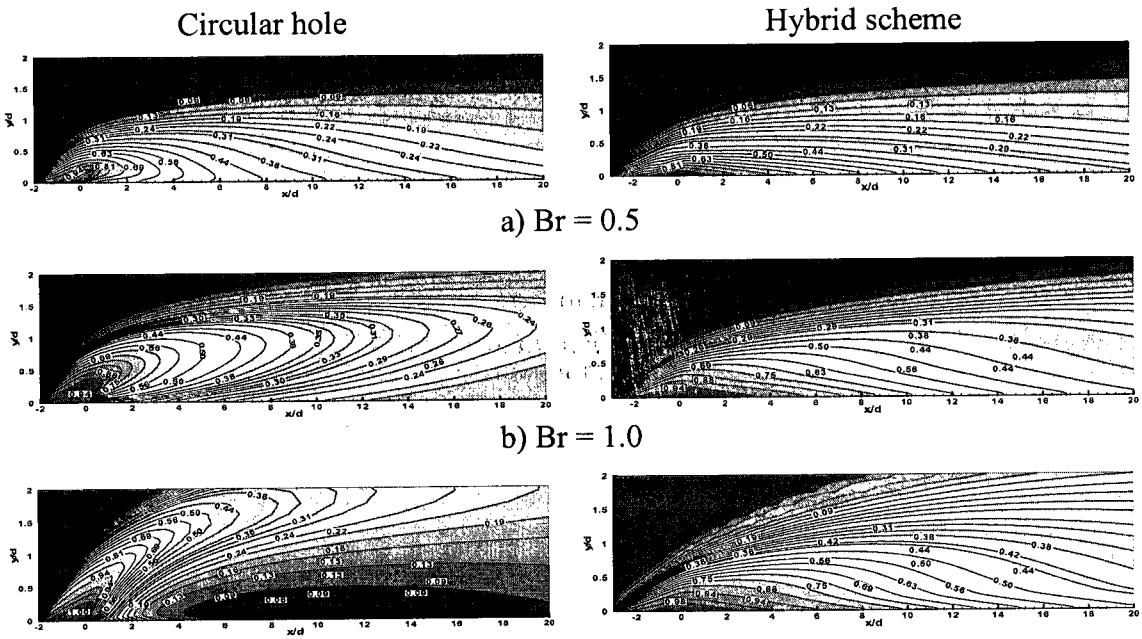

Figure 6.10. Centerline film cooling effectiveness contours for circular hole and hybrid schemes at different blowing ratios.

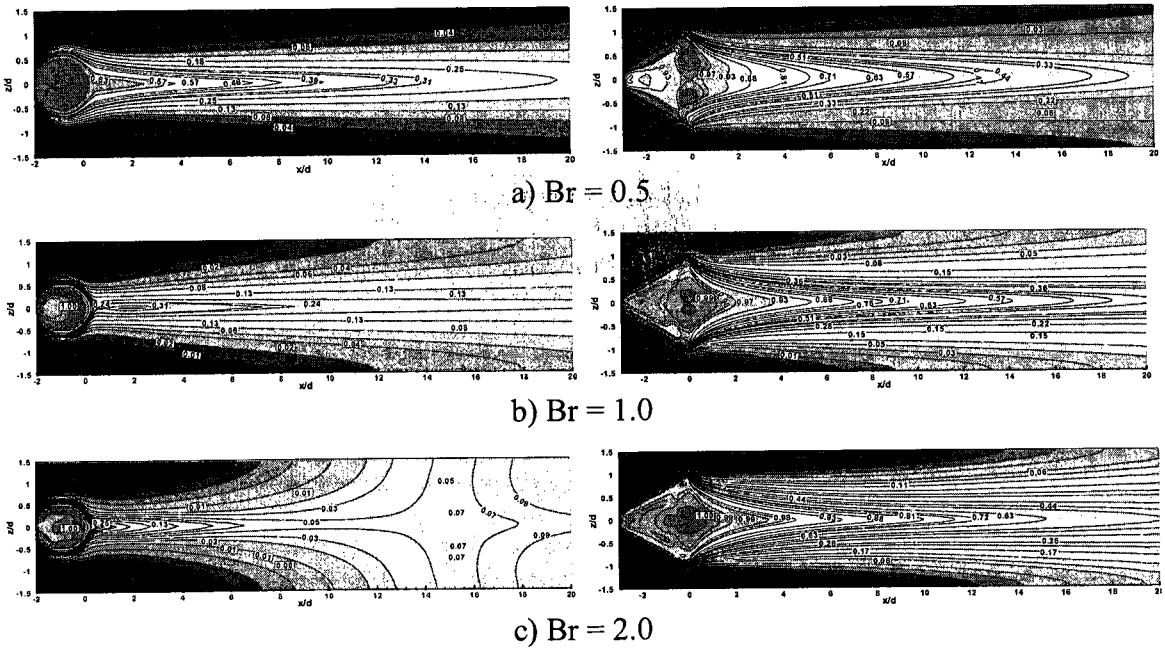

Figure 6.11. Downstream film cooling effectiveness contours for circular hole and hybrid schemes at different blowing ratios.

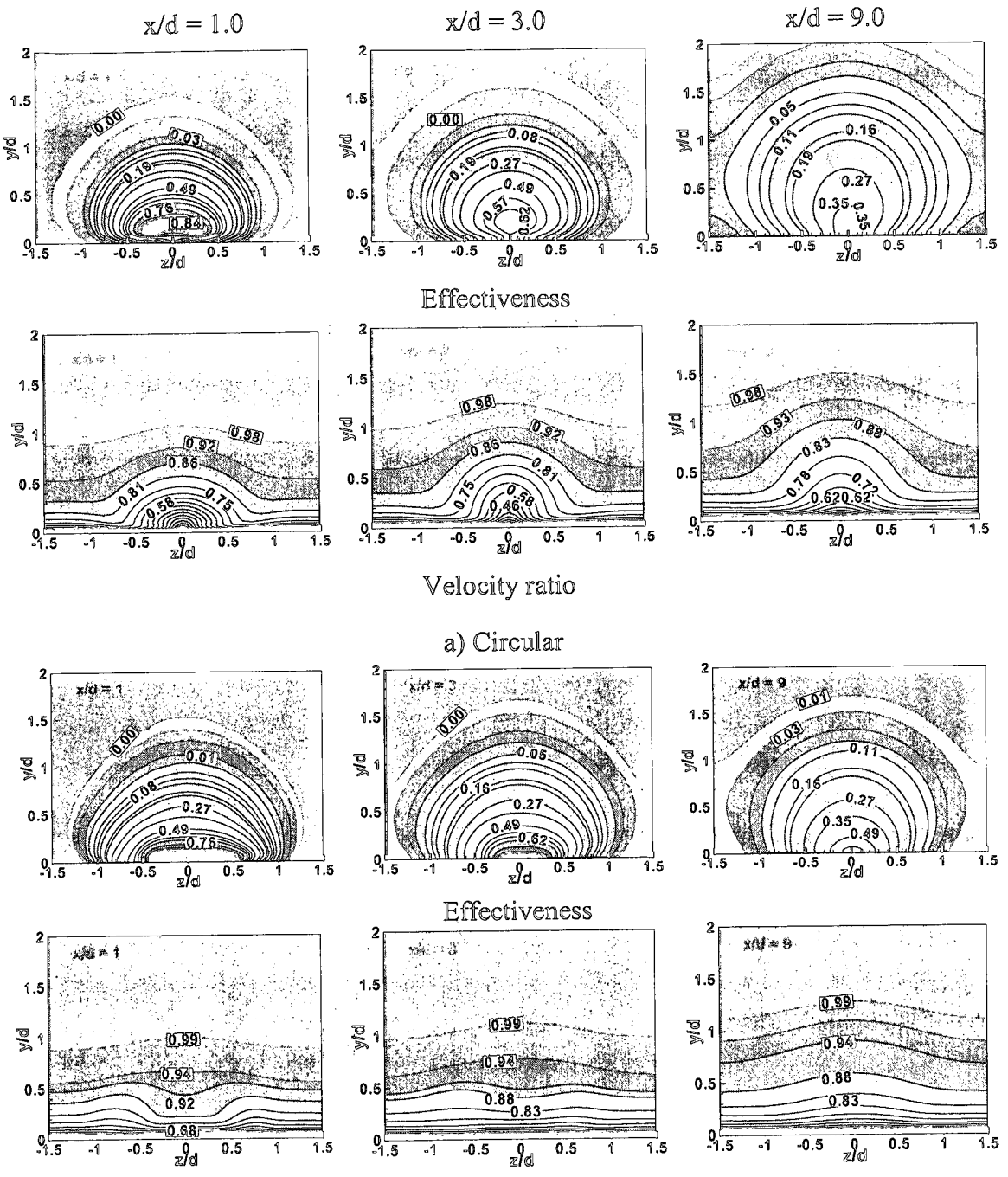

Figure 6.12. Downstream vertical plane effectiveness and velocity ratio contours of circular hole and hybrid scheme at Br = 0.5.

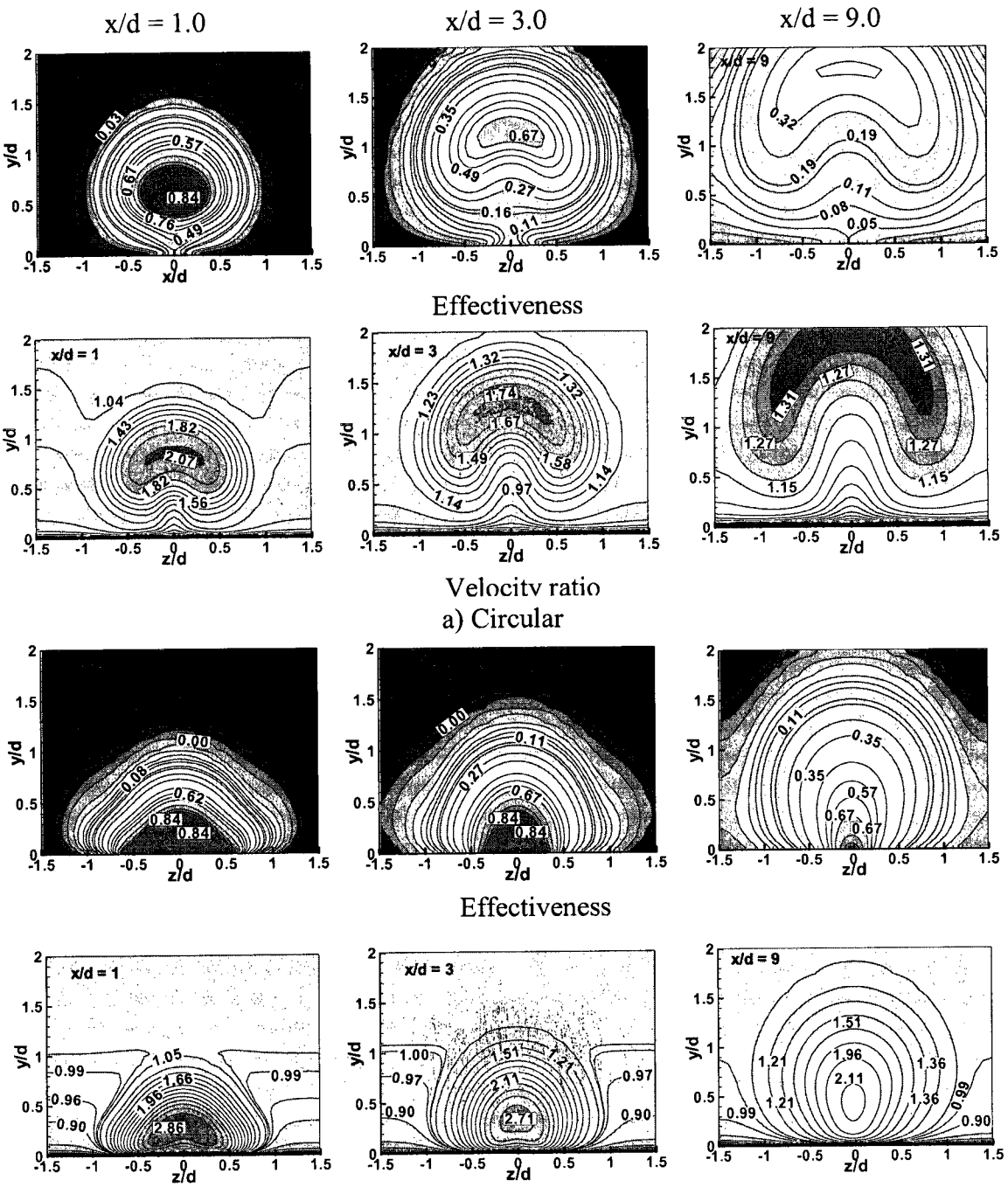

Figure 6.13. Downstream vertical plane effectiveness and velocity ratio contours of circular hole and hybrid scheme at Br = 2.0.

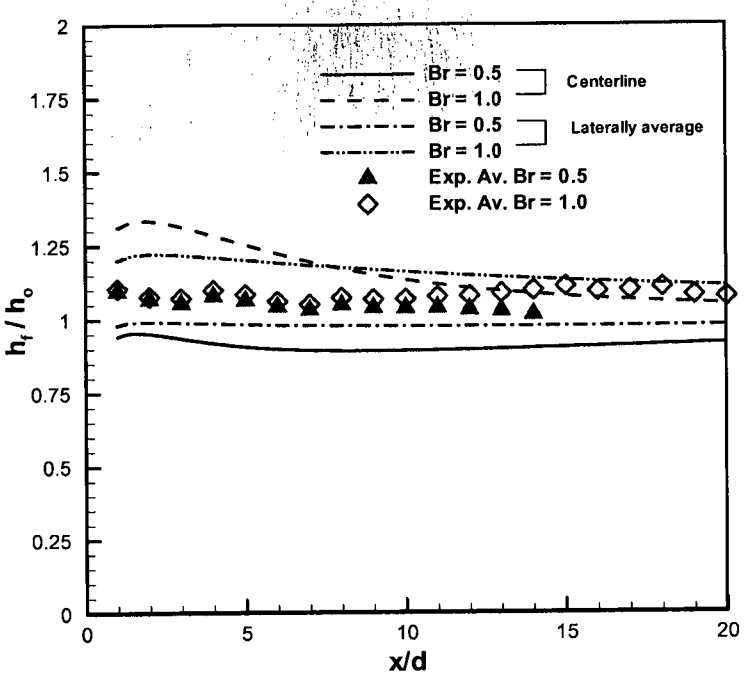

Figure 6.14. Centerline and laterally averaged HTCR of the hybrid scheme at different blowing ratios.

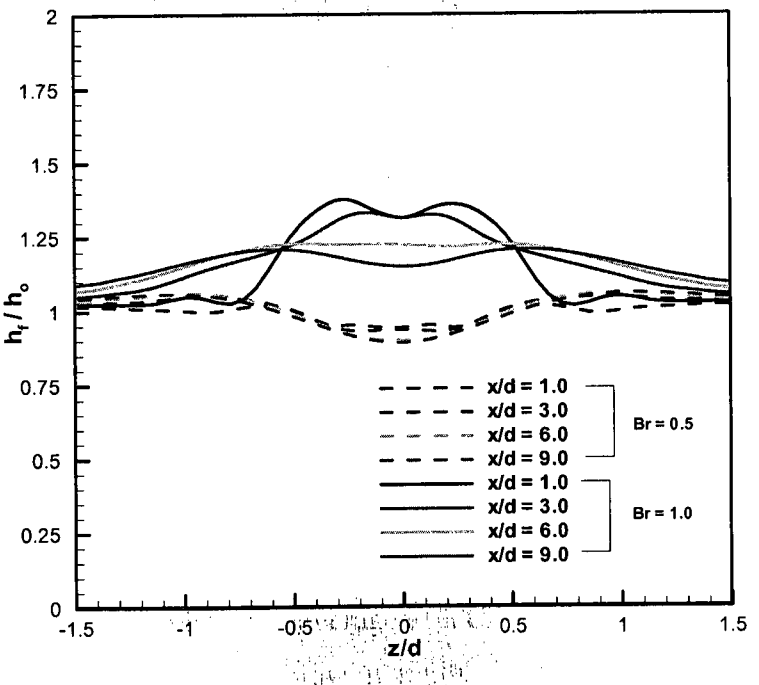

Figure 6.15. Lateral heat transfer coefficient ratio of the hybrid scheme at different blowing ratios.

The downstream HTCR contours of the hybrid scheme are presented in Fig. 6.16. The hybrid scheme provided low HTCR values near the centerline over the downstream surface at Br = 0.5. Furthermore, the HTCR values decreased gradually in the streamwise direction as secondary flow momentum decreased, as shown in Fig. 6.16.

6.2 Film cooling and conjugate heat transfer analysis of the hybrid scheme

Combining the conjugate heat transfer (CHT) with film cooling is essential for developing and improving the thermal design of gas turbine airfoils. Parallel, cross and jet impingement flows are effective methods for internal cooling. In the gas turbine engine, it is preferable to cool the critical region, which has the highest thermal load. Usually, internal cooling methods are appropriate for airfoil cooling near the leading edge, where the airfoil material is thick. Therefore, there will be enough solid material to create internal passes. The secondary flow exiting the plenum passes through internal holes with different flow configurations, and then exits from the film hole for external airfoil cooling. The internal cooling can be affected by different designs and flow conditions such as the number of jets, jet to target plate spacing, jet shape, jet arrangement (inline or staggered), effect of flow directions, and jet inclination angle. The main objective of this study is to investigate the film cooling performance along the upstream and downstream surfaces of the hybrid scheme by combing internal and film cooling for different flow configurations, gap height and operating conditions.

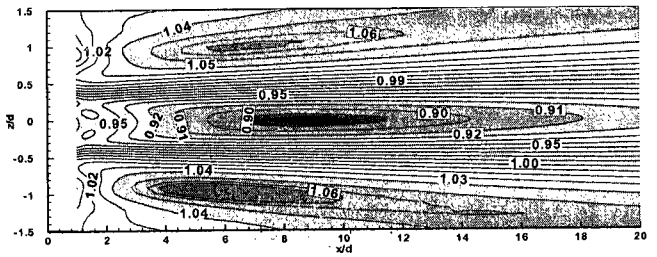

a) Br = 0.5

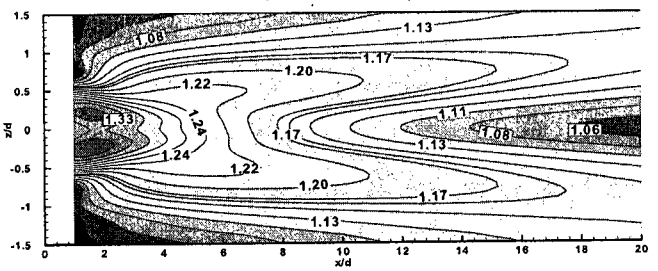

b) Br = 1.0

Figure 6.16. HTCR contours of the hybrid scheme at different blowing ratios.

6.2.1 Geometry configurations and boundary conditions

Different geometries were simulated to study the cooling performance of the hybrid scheme by combing the CHT and film cooling at different blowing ratios. Figure 6.17 demonstrates different conjugate geometries studied: cross flow, parallel flow and jet impingement flow. The cross flow case with a circular hole, which was studied by Lu et al. (2005), is used as a benchmark conjugate case study. One film hole was simulated for all case studies with symmetry boundary conditions. The inlet secondary flow was fixed for all flow configurations studied and blowing ratios were changed by varying the outflow of the secondary flow. For the hybrid scheme study, the main flow stream was simulated with a uniform inlet velocity and temperature of 10 m/s and 300 K, respectively. An inlet secondary flow of 0.0191 m^3/s was used with a 320 K inlet temperature. This amount for the secondary flow rate was equivalent to a blowing ratio of 1.46 without outlet flow. A median turbulent intensity of 3% was used for the injection and the main flows. The main and secondary flow turbulence lengths were 0.0015 and 0.001, respectively. The conjugate plate material was the same used by Lu et al. (2005), with constant physical property values of 1180 kg/m^3, 0.3315 W/m K and 1730 J/Kg K for density, thermal conductivity, and specific heat, respectively. Table 6.2 illustrates simulated cases for the conjugate heat transfer study.

Table 6.2. Conjugate study test matrix.

Case no	Plate Condition	Flow Directions	Gap height (H/d)	Blowing ratio	Film hole
1	Conjugate	Cross	2	0.764	Circular
2	Adiabatic	n/a	n/a	0.5 , 1.0	Hybrid
3	Conjugate	Parallel	0.8	0.5 , 1.0	Hybrid
4	Conjugate	Impingement	0.8	0.5 , 1.0	Hybrid
5	Conjugate	Impingement	1.2	0.5 , 1.0	Hybrid

6.2.2 Benchmark case study

The grid independence and turbulence models were studied to simulate the conjugate heat transfer. The conjugate heat transfer for the circular hole with cross flow configuration, which presented by Lu X. et al (2005), was used for the conjugate validation study. Figure 6.17a illustrates the computational domain of the conjugate heat transfer validation study. Lu X. et al (2005) investigated conjugate heat transfer over a flat plate. The cross section of the main duct was 240 mm wide by 300 mm high, with a length of 600 mm. The dimensions of the secondary flow duct were 240 mm wide and 10 mm high. The two ducts were separated with a 20 mm thick plate. One of five circular film holes was simulated on the plate with a 5 mm diameter and a 30° inclination angle. The hole length and the pitch to diameter ratio were 40.3 mm and 8.06, respectively. The inlet and exit boundary conditions were the same as those used by Lu et al. (2005) for the validation study.

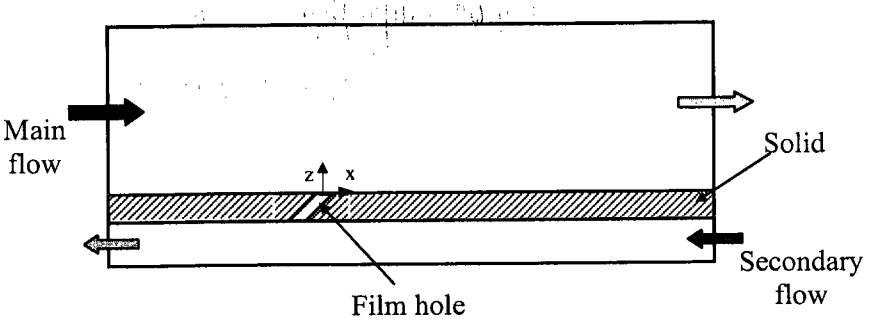

a) Cross flow and film cooling validation case (circular hole)

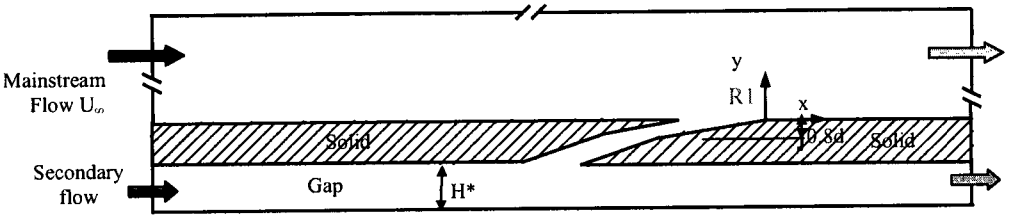

b) Parallel flow and film cooling (hybrid scheme)

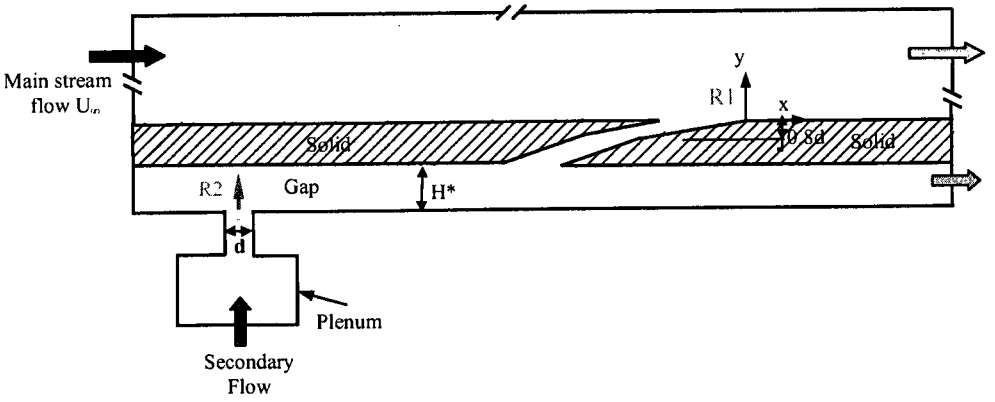

c) Impingement and film cooling (hybrid scheme)

Figure 6.17. Different configurations of the conjugate heat transfer study.

Figure 6.18a presents the local centerline surface temperatures for different grid studies, which achieved different average y^+ values over the surface at a 0.764 blowing ratio. From the results, the difference in the temperature profiles between a fine and a finer mesh (y^+ = 0.85 and 0.6) was negligible. Furthermore, there was a difference in temperature profile results obtained for y^+ = 90 and y^+ values less than unity. Lu et al. (2005) noticed that accurate results from the simulation were obtained by designing y^+ less than unity.

Figure 6.18b shows the effect of different turbulence models on the output surface temperature profiles for the validation case study. The k-ε, k-ω SST and Spalart-Allmaras (SA) turbulence models were examined for turbulence model tests. The output temperature profiles compared with the infrared (IR) experimental data obtained by Lu et al. (2005) are shown in Fig. 6.18b. From the results, there was a good agreement between the experimental data and the predicted results obtained by using k- ε turbulence model with enhanced wall treatment. The k-ε turbulence model predicted the flow characteristics and physics near the wall more accurately, compared to other two turbulence models: k-ω SST and Spalart-Allmaras. As a result, the grids, which provided an average y+ of 0.6 and k- ε model with enhanced wall treatment, will be used throughout this study.

6.2.3 Computational grid of the hybrid scheme

Figure 6.19 illustrates the centerline grid plans used to simulate the conjugate heat transfer of the hybrid scheme. Three different grids were designed for an average y^+ value less than unity to examine grid independence for the hybrid scheme. Grids that provided an average y+ value of 0.6 over the surface were used to simulate the CHT for the hybrid

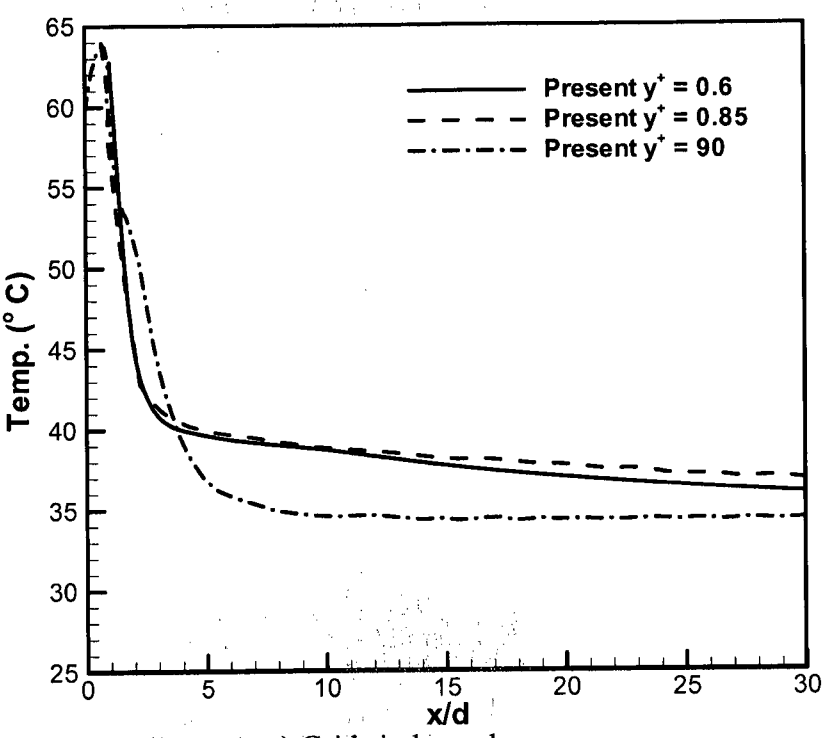

a) Grids independence

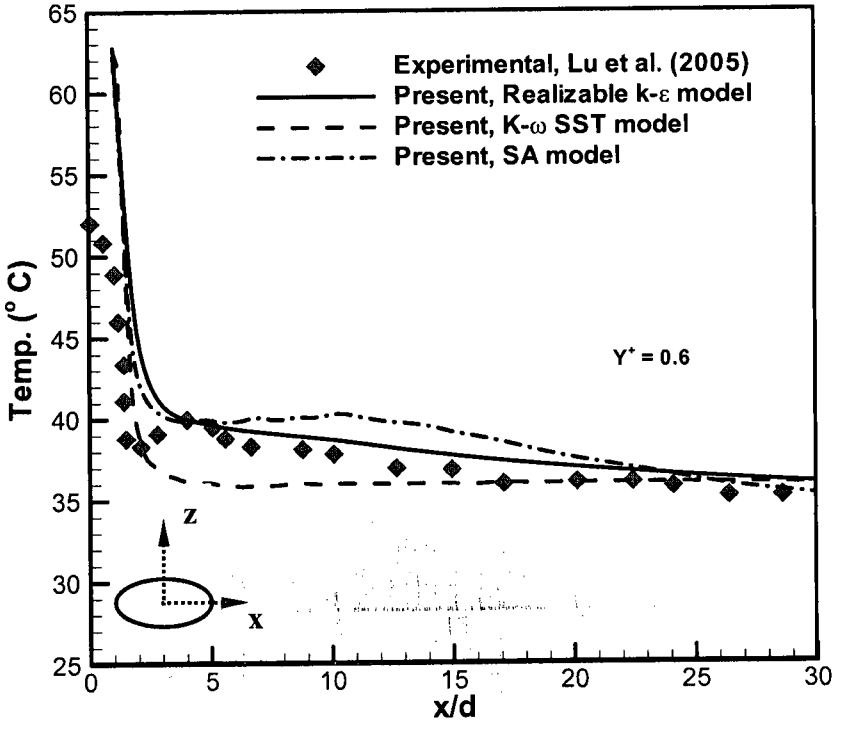

b) Turbulence model test

Figure 6.18. Conjugate heat transfer validation with Lu et al. (2005), Br = 0.764.

scheme. Structured and unstructured grids with multi-block numerical grids were employed throughout the CHT study to provide enhance grid quality. Clustered grids were designed near the walls, inlet and exit of the hybrid scheme, as shown in Fig. 6.19. A close view of the mesh near the hybrid scheme and the first hole (circular hole) are presented in Figs. 6.19a and 6.19b.

6.2.3 Film cooling and conjugate heat transfer results and discussion of the hybrid scheme

Figure 6.20 presents the centerline downstream film cooling effectiveness for case studies 2, 3, 4, and 5 (in Table 6.2) at blowing ratio of 0.5 and 1.0. At a low blowing ratio (Br = 0.5), the adiabatic film cooling effectiveness of the hybrid scheme provided the highest performance compared to other conjugate cases studied for $x/d < 5$, as shown in Fig. 6.20a. Since the parallel flow and jet impingement configurations had the same gap height and the same secondary inlet flow rate, there was no significant effect on the downstream film cooling effectiveness performance. The impingement configuration with $H/d = 1.2$ (case 5) produced the highest film cooling performance compared to other conjugate heat transfer cases studied for all downstream locations as well as the adiabatic case study for $x/d > 5$. The downstream film cooling effectiveness of the hybrid scheme was affected by gap height. A large gap height provided smoothing inlet flow to the hybrid scheme with less interior flow circulation. The film cooling effectiveness enhanced with increasing blowing ratio compared to other conjugate cases, as shown in Fig. 6.20b. Case (5) produced the highest film cooling effectiveness compared to other conjugate cases, but it provided a lower performance than the adiabatic case for $x/d < 7.5$. Moreover, the outlet flow enhanced the downstream cooling effectiveness due to

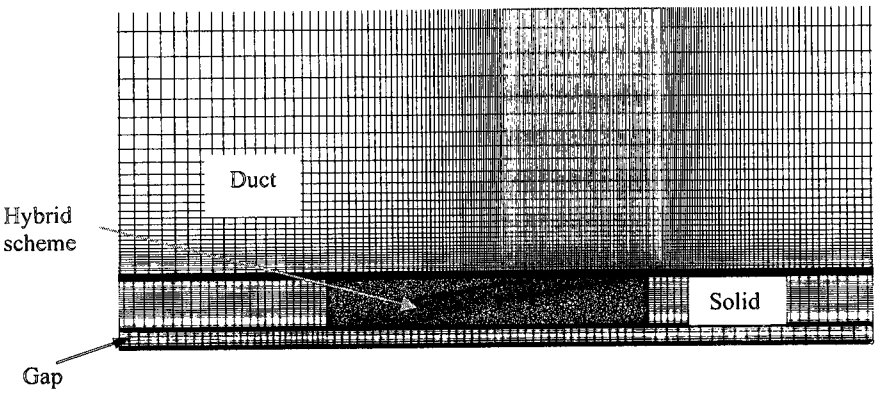

a) Close view of the mesh near the hybrid scheme

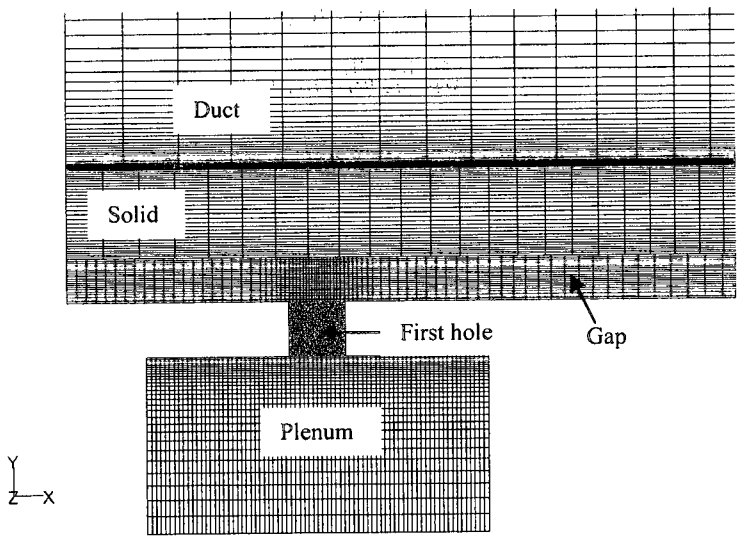

b) Close view of the mesh near the first hole

Figure 6.19. Computational grids of the hybrid scheme with impingement configuration.

downstream conjugate heat transfer. The effect of the downstream CHT on cooling effectiveness can be observed further in the spanwise direction ($z/d > 0.5$).

Figure 6.21 demonstrates the lateral film cooling effectiveness at different downstream locations of $x/d = 1$, 3, and 9 for the hybrid scheme cases studied at Br = 0.5 and 1.0. The results show that the adiabatic case study enhanced the film cooling effectiveness compared to the conjugate cases, near the film hole center until the downstream distance of $x/d < 9.0$. For $x/d = 9$, the adiabatic case provides lower film cooling effectiveness values compared to the jet impingement (case 5) near the film hole centerline. Moreover, it provides the lowest value of film cooling effectiveness further in the spanwise direction with respect to other conjugate case studies. Since there was CHT for the downstream surface from the outlet secondary flow, the film cooling effectiveness increased further in the spanwise direction, as shown in Fig.6.21. Moreover, the parallel flow configuration produced the lowest film cooling effectiveness near the hole center, but it provided the highest values further in the spanwise direction. Further downstream ($x/d > 9$), the film cooling effectiveness performance was similar for all conjugate case studies, as shown in Fig. 6.21.

Figure 6.22 illustrates the downstream film cooling effectiveness contours for the different case studies at Br = 0.5 and 1.0. At Br = 0.5, the adiabatic case produced the highest film cooling effectiveness performance near the film hole center compared to other conjugate case studies as shown the left side contours in Fig. 6.22. The conjugate heat transfer enhanced the film cooling effectiveness far in the streamwise direction compared to the adiabatic case study. The jet impingement with large gap height provided the highest film cooling effectiveness compared to other case studies.

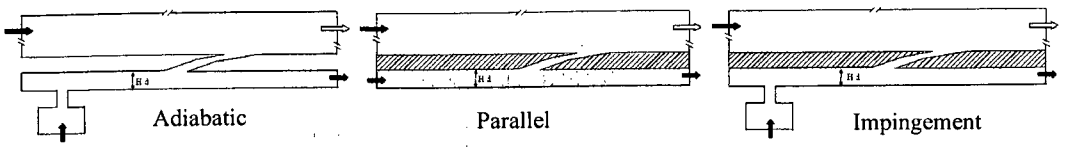

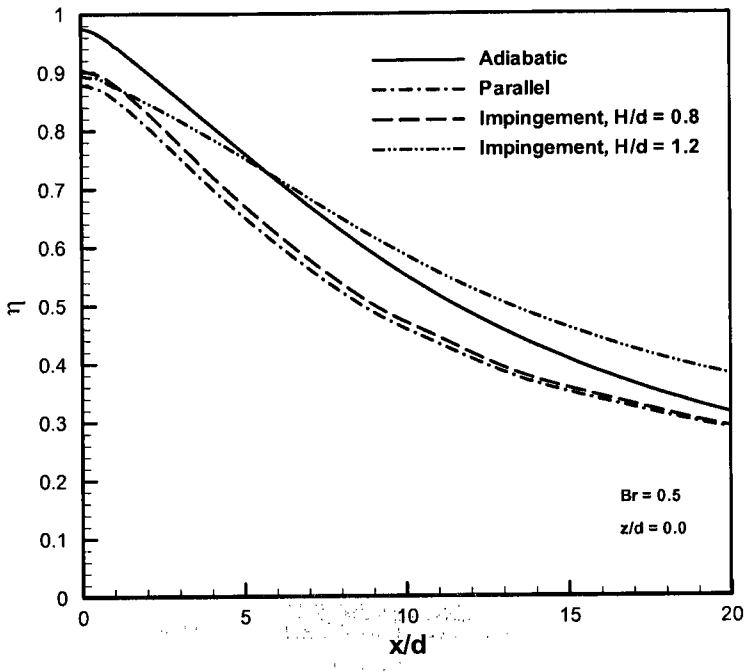

a) Br = 0.5

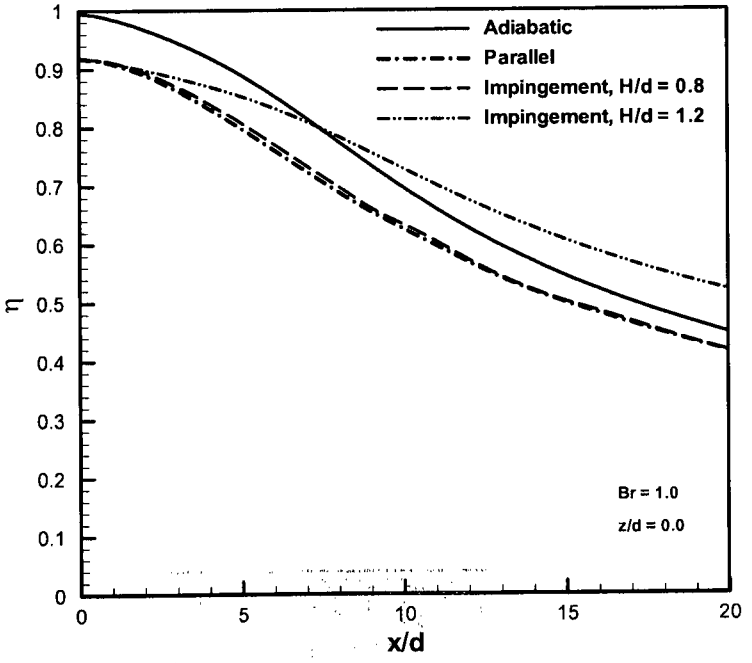

b) Br = 1.0

Figure 6.20. Downstream centerline film cooling effectiveness performance of the hybrid scheme for different case studies at Br = 0.5 and 1.0.

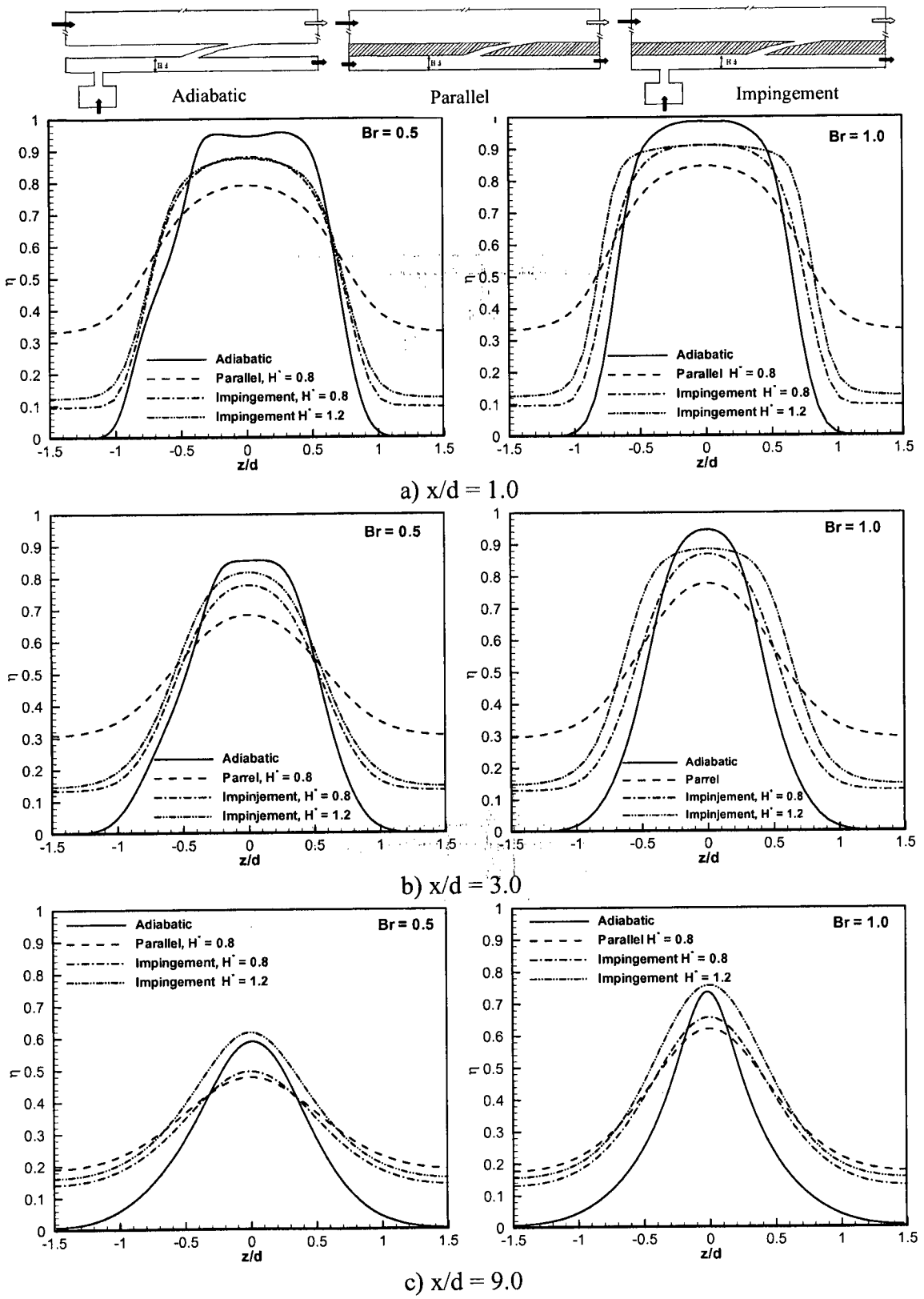

Figure 6.21. Lateral film cooling effectiveness performance of the hybrid scheme for different case studies at Br = 0.5 and 1.0.

Br = 0.5 Br = 1.0

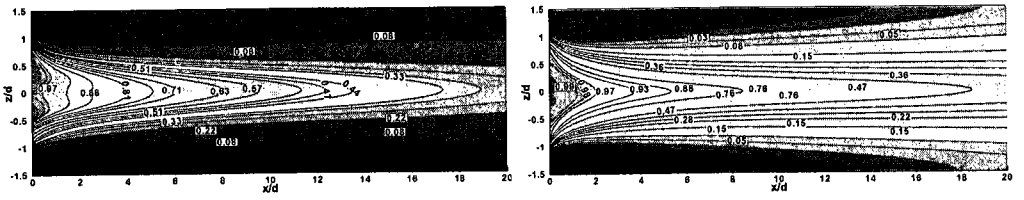

a) Adiabatic (case 2)

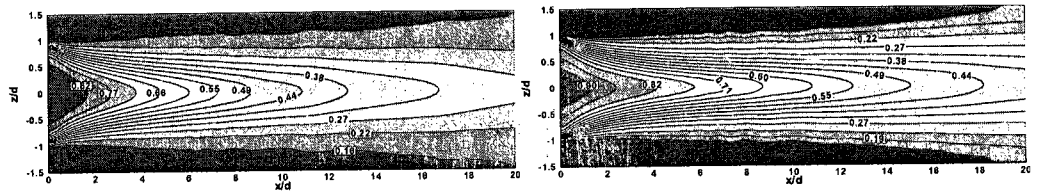

b) Parallel (case 3)

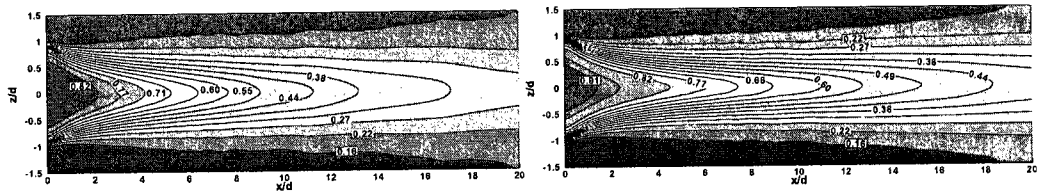

c) Impingement H/d = 0.8 (case 4)

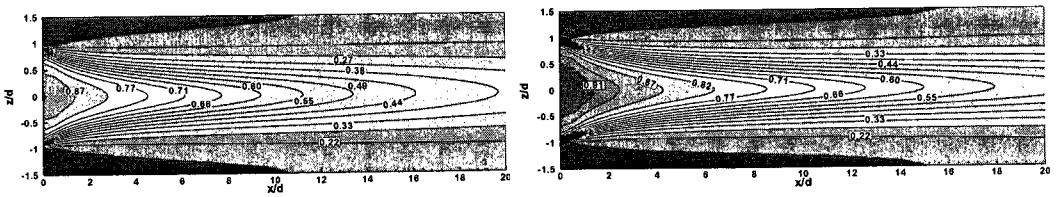

d) Impingement H/d = 1.2 (case 5)

Figure 6.22. Downstream film cooling effectiveness contours of the hybrid scheme for different configurations.

The hybrid scheme is able to spray the secondary flow widely and intensively over the downstream surface in the spanwise direction at high blowing ratios. As a result, the downstream film cooling effectiveness is enhanced at a high blowing ratio (Br = 1.0), as shown in Fig. 6.22. The jet impingement configuration with large gap height provides the highest downstream cooling performance among other flow configuration studies. In addition, Fig. 6.23 illustrates the laterally average downstream cooling performance of the hybrid scheme for different flow configurations at Br = 0.5 and 1.0. The results show that the adiabatic case study provides the highest cooling performance near the film hole exit (x/d <1.5). While, the conjugate case with large gap height enhances the downstream laterally cooling performance for x/d > 1.5 among other configuration cases studied. For the same gap height (H/d = 0.8), there is a significant effect of flow configuration (parallel or impingement) on downstream laterally film cooling performance at Br = 0.5 and 1.0.

Figure 6.24 illustrates centerline velocity ratio contours near the hybrid scheme entrance for different conjugate case studies at a blowing ratio of 1.0. From the results, the parallel flow and jet impingement configurations with gap height of H/d = 0.8 provided the same flow structure at the entrance region. A large gap height provided a more uniform inlet flow to the hybrid scheme compared to small gap height cases. In addition, the inlet velocity ratio for the hybrid scheme was less for large gap heights, reducing the circulation flow inside the hybrid scheme. As a result, the secondary flow sprayed effectively over the downstream surface.

Figure 6.25 illustrates velocity ratio component contours at the inlet and exit area of the hybrid scheme for different conjugate case studies at a blowing ratio of 1.0. The

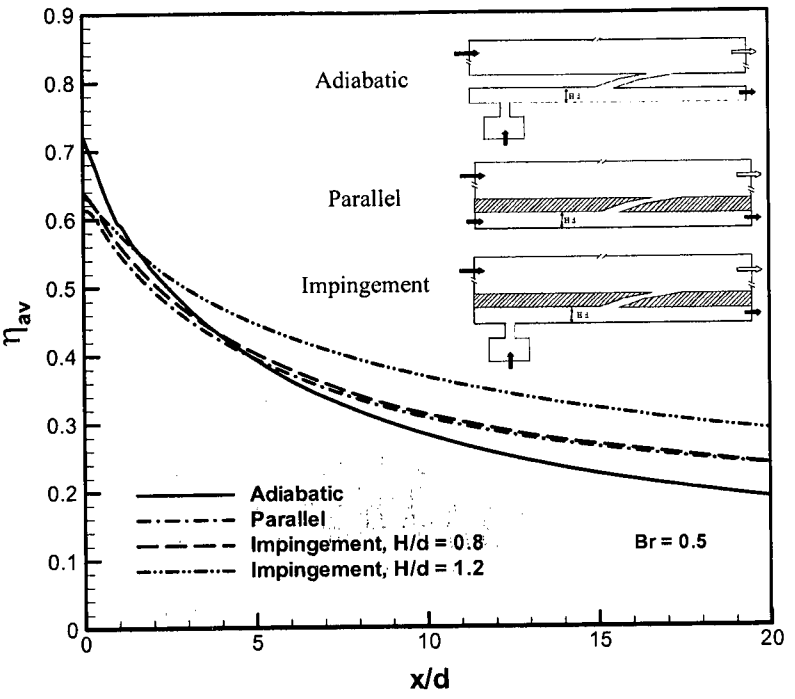

a) Br = 0.5

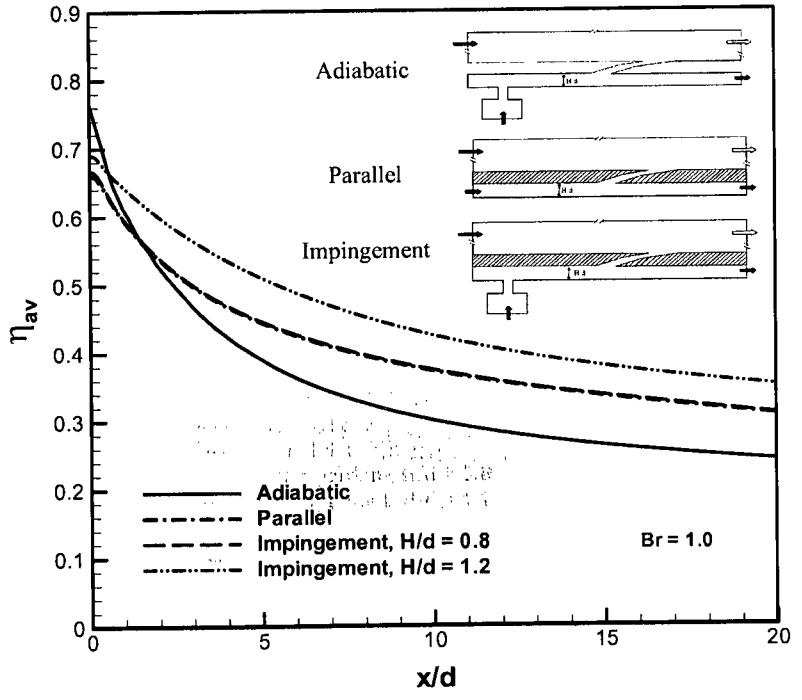

b) Br = 1.0

Figure 6.23. Laterally averaged downstream cooling performance of the hybrid scheme for different configurations.

results showed that the gap height affected the inlet velocity of the hybrid scheme. Large gap height produced uniform velocity ratio contours with less flow disturbance at the entrance cross section, as shown the left side velocity ratio contours in Fig. 6.25. The velocity component U was dominant with respect to the V component at the entrance area of film hole scheme. At the inlet cross-section, the vortex flow generated due to the change in flow direction was decreased for large gap heights. Therefore, the inlet flow structure was affected by the flow at the exit area of the scheme. The results showed that the horizontal velocity component for the hybrid scheme was dominant since the internal bending directed the flow in the streamwise direction with less jet lift-off as shown in Fig. 6.25. The U velocity for the exit scheme had the highest value near the leading edge and decreased gradually in the streamwise direction. The horizontal velocity component sprayed more toward the trailing edge for large gap heights. Consequently, the secondary flow sprayed entirely over the downstream surface to enhance the film cooling effectiveness.

Figure 6.26 demonstrates centerline cooling performance of CHT and film cooling of the hybrid scheme for different flow configurations at Br = 1.0. In addition, the results presented the cooling gradient inside the conjugate plate and boundary layer over the bottom surface of the duct. The downstream cooling performance for parallel flow and jet impingement cases studied with the same gap height is almost similar. However, the impingement configuration provides higher upstream cooling performance compared to the parallel configuration. The upstream and downstream cooling performance were enhanced for the jet impingement configuration with large gap height. The secondary flow is circulated more around the X-axis for a large gap height as shown in Fig.6.27).

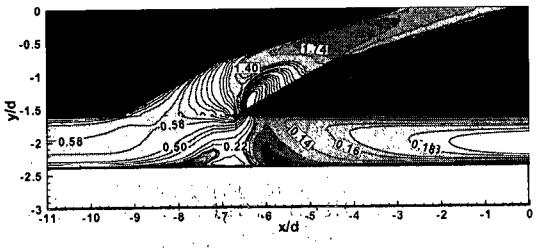

a) Parallel, (case 3)

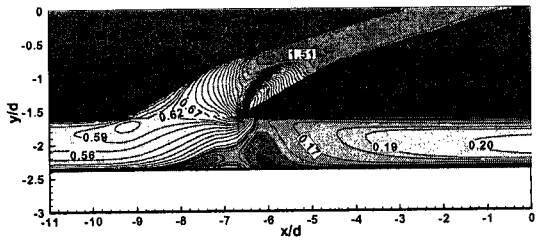

b) Impingement, H/d = 0.8 (case 4)

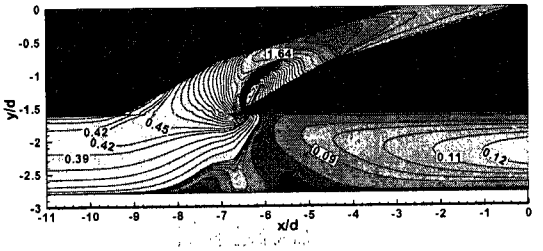

c) Impingement, H/d = 1.2 (case 5)

Figure 6.24. Velocity ratio contours at the inlet of the hybrid scheme for different configurations.

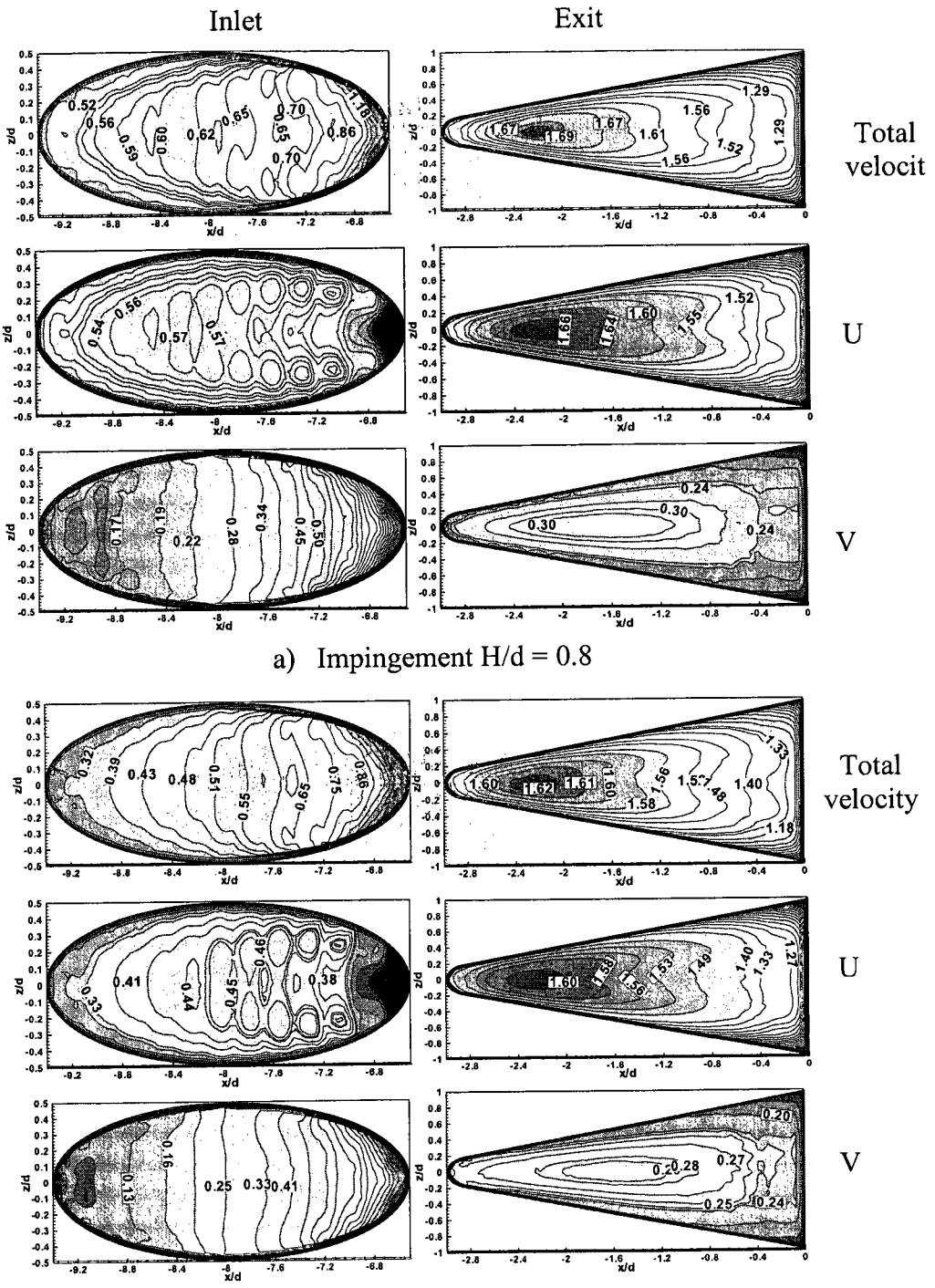

Figure 6.25. Velocity ratio component contours at inlet and exit area of the hybrid scheme for different configurations (Br = 1.0).

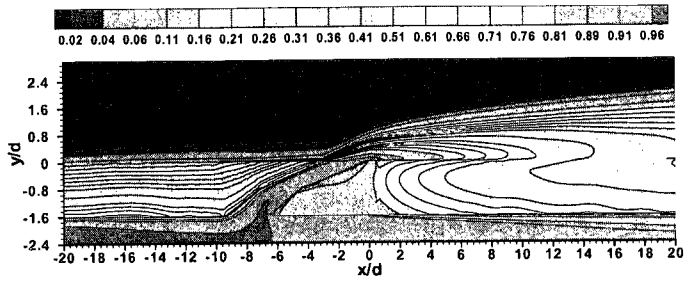

a) Parallel flow

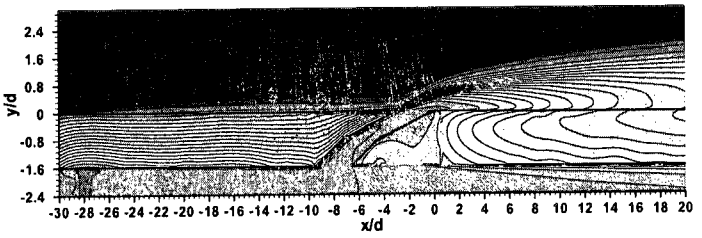

b) Impingement H/d = 0.8

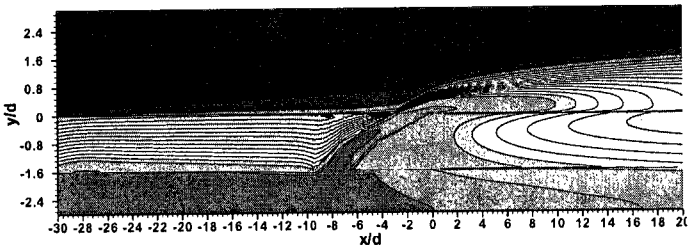

c) Impingement H/d = 1.2

Figure 6.26. Centerline cooling performance contours of different flow configuration cases studied (Br = 1.0).

Therefore, the upstream cooling performance is further enhanced with respect to small gap heights.

Figure 6.27 illustrates vertical-spanwise planes of velocity ratio contours inside the gap for different flow configurations at different locations of x/d = 1, 6, and 15 measured from the centerline of the first hole (R2 In Fig. 6.17c). Near the conjugate plate, the secondary velocity values were lower for parallel flow (Fig. 6.27a) compared with the jet impingement configuration. As a result, the convective heat transfer between the secondary flow and the conjugate plate was reduced. The secondary flow circulation inside the gap increased for the jet impingement cases near the first hole and reduced along the streamwise direction, as shown in Figs. 6.27b and c. Less flow circulation was observed, for jet impingement cases with smaller gap height, in the region far from the conjugate surface and x/d > 1 (Fig. 6.27b), while the secondary flow was further circulated in large domains for jet impingement with a large gap height (in Fig. 6.27c), improving the convective heat transfer inside the gap. Therefore, the upstream cooling performance was affected by the flow structure inside the gap. Furthermore, increased vorticity of the flow enhanced the cooling performance.

The upstream cooling performances of the parallel flow and the jet impingement with small and large gap heights at Br = 1.0 were presented in Fig. 6.28. Since the secondary inlet flow rate was fixed, there was no significant effect of blowing ratio on the upstream cooling performance for each flow configuration. The jet impingement improved the cooling performance due to the impact of the secondary flow on the conjugate plate bottom surface, and created vortex flow inside the gap. As a result, the convective heat transfer increased subsequently, and the cooling performance was

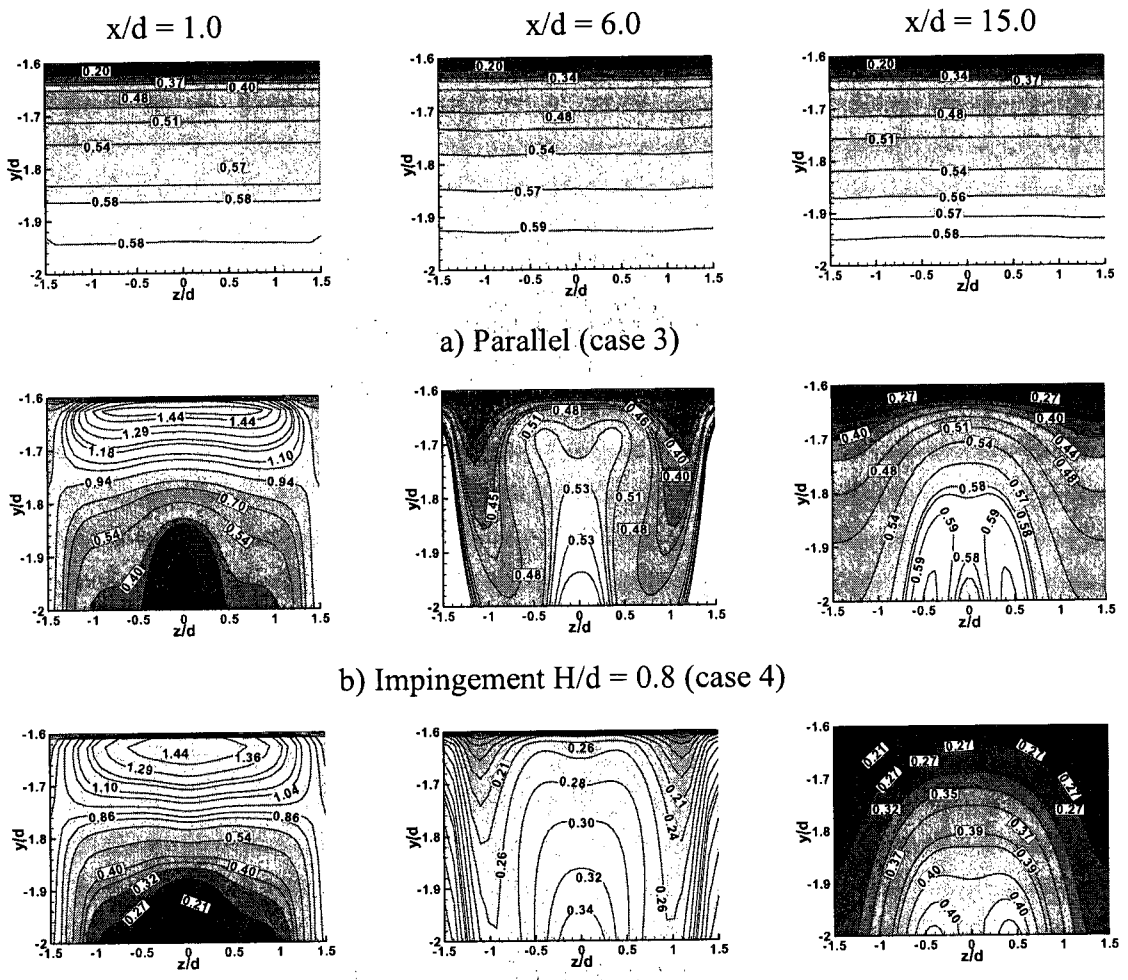

Figure 6.27. Velocity ratio contours inside the gap at x/d = 1, 6 and 9 (from R2) for different configurations (Br = 1.0).

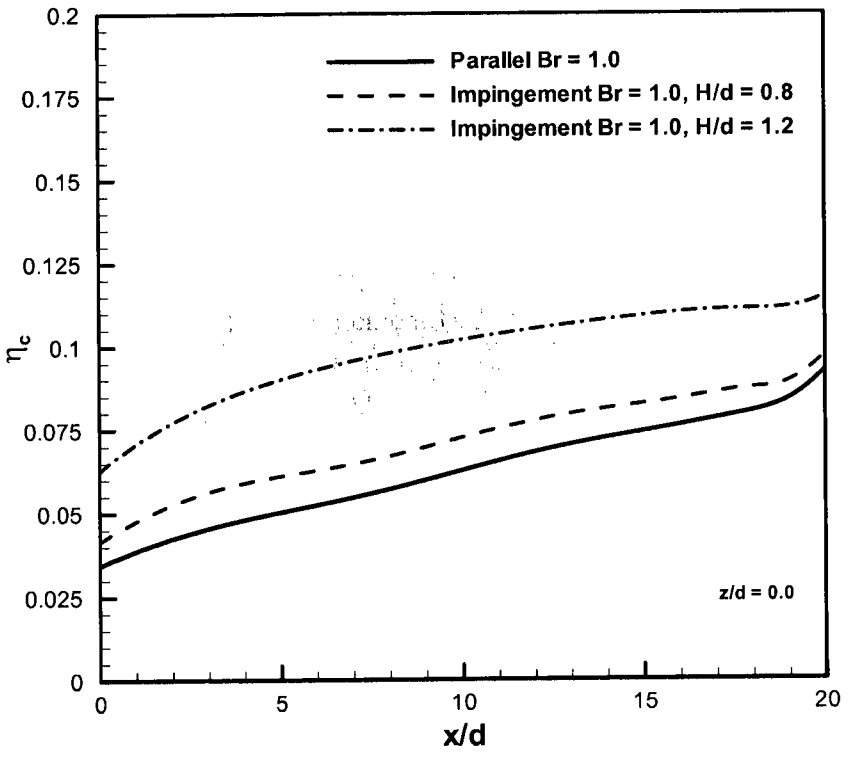

Figure 6.28. Upstream cooling performance for different conjugate cases studied (Br = 1.0).

enhanced compared to the case of the parallel flow configuration. The vortex flow increased with increasing gap height, thereby improving the cooling performance, as shown in Fig. 6.28.

6.3 Summary

The adiabatic film cooling effectiveness performance and flow characteristics of the circular film hole and the hybrid scheme were investigated numerically at blowing ratios of 0.5 and 1.0. The results showed that the secondary flow jet lift-off was reduced for the hybrid scheme since the secondary flow injected mainly in the horizontal direction over the surfaces due to interior bending effect. Consequently, the downstream film cooling effectiveness was enhanced and increased with increasing blowing ratio. Conversely, the film cooling effectiveness was reduced for the circular hole at high blowing ratios due to increasing jet lift-off.

Moreover, the conjugate heat transfer and film cooling were combined to evaluate the cooling performance of the hybrid scheme for different flow configurations at Br = 0.5 and 1.0. Parallel flow and jet impingement with two different gap heights have been simulated to study the hybrid scheme cooling performance including CHT. The secondary flow rate for the three cases studied was fixed and the outlet flow was changed to obtain the required blowing ratio. The results showed that there was no significant effect of blowing ratio on upstream cooling performance for each case study. Jet impingement configurations enhanced the upstream film cooling performance and increased for large gap height. Moreover, the jet impingement with a large gap height provided improvement in the downstream film cooling effectiveness. The outflow

enhanced downstream film cooling effectiveness due to the downstream conjugate heat transfer and increased further, especially in the spanwise direction.

Chapter 7

Chapter 7 Conclusion and Recommendation

7.1 Conclusion

A new test facility was designed and constructed to investigate film-cooling performance of advanced film cooling schemes over a flat plate and airfoil surfaces. Software codes, including Labview and image processing using Matlab, for transient film cooling tests, were developed through the current experimental work. The Thermochromic liquid crystal (TLC) technique was used to measure the wall surface temperature. A circular film hole over the flat plate was used to validate the current experimental technique and methodology through a comparison between the obtained results and published data. The validation results showed a good agreement, such that the current experimental technique and methodology are deemed reliable.

The film cooling performance of the louver scheme was investigated and compared with other traditional and advanced published film hole geometries. The film cooling performance of the louver scheme was tested for blowing ratios of 0.5, 1.0, and 1.5 and a density ratio of 0.94. The results show that the louver schemes provided superior centerline and lateral film cooling effectiveness compared to other published film hole geometries. In addition, the film cooling effectiveness was enhanced with increasing blowing ratio for the louver scheme. The centerline and lateral average heat transfer coefficient for the louver scheme had lower values over the downstream surface with respect to the circular hole scheme, but it provided similar results to the shaped hole. Moreover, there was an insignificant effect on the heat transfer coefficient ratio with

increasing blowing ratio for the louver scheme. In addition, the Frossling number was introduced to evaluate the heat transfer performance of the louver scheme by combining the heat transfer coefficient, Reynolds number, and exit area of the film hole. From the results, the Frossling number performance of the louver scheme increased with increasing blowing ratio until it reached a peak point, for which it then decreased with any further increase in the blowing ratio. However, it provided a constant value along the downstream jet holes. The net heat flux reduction (NHFR) was determined to present the overall film cooling performance by combining the film cooling effectiveness and heat transfer coefficient ratio. The dimensionless reference temperature, $\theta = 1.5$, was used to calculate the NHFR. The louver schemes provided a high film cooling effectiveness with a relatively low heat transfer coefficient ratio, therefore providing the highest NHFR in the streamwise and laterally averaged directions compared to circular and fan shaped holes.

The film cooling performance of the hybrid scheme was presented in terms of film cooling effectiveness, heat transfer coefficient ratio, Frossling number and NHFR, at low and high blowing ratios. Subsequently, the film cooling performances of the hybrid scheme were compared with other traditional and advanced published film hole geometries. The film cooling performance of the hybrid scheme was investigated for blowing ratios from 0.5 to 1.5 and a 0.94 density ratio. From the results, the hybrid scheme augmented the centerline and the laterally averaged film cooling effectiveness with respect to other film holes at different blowing ratios. In addition, the film cooling effectiveness was enhanced with increasing blowing ratio for the hybrid scheme. The centerline and laterally averaged heat transfer coefficient ratio of the hybrid scheme

demonstrated an average value near to unity, over the downstream surface. In addition there was no significant effect of h_f/h_o with increasing blowing ratio. The hybrid scheme provided similar results for the heat transfer coefficient ratio as the circular and fan shaped holes at high blowing ratio. The proposed scheme provided lower values of Frossling number compared to the circular hole scheme, which was unaffected by the blowing ratio. The net heat flux reduction was presented to illustrate the overall film cooling performance by combining the film cooling effectiveness and heat transfer coefficient ratio. The dimensionless reference temperature, $\theta = 1.5$, was used to calculate the NHFR. The hybrid scheme provided a high film cooling effectiveness with a relatively low heat transfer coefficient ratio. Therefore, it demonstrated the highest NHFR in the streamwise and laterally averaged directions compared to that of the circular and fan shaped holes.

As a result, the louver and the hybrid schemes are able to increase the airfoil's lifetime. Furthermore, the inlet gas turbine temperature can be increased, which in turn improves the overall gas turbine efficiency without any possibility of creating hot spots on the downstream surfaces.

The adiabatic film cooling effectiveness performance and flow structures for the hybrid and circular hole schemes were investigated numerically, at different blowing ratios. The results showed that the hybrid scheme spewed the secondary flow in the horizontal direction with less jet lift-off. Consequently, the downstream film cooling effectiveness was enhanced, and increased with increasing blowing ratios. However, the film cooling effectiveness was reduced for the circular hole scheme with increasing blowing ratios due to increased jet lift-off.

Different flow configurations were simulated to study the conjugate heat and film cooling performance of the hybrid scheme at blowing ratios of 0.5 and 1.0. Parallel flow and jet impingement configurations with gap heights of 0.8d and 1.2d have been simulated. For the three cases studied, the inlet secondary flow rate was fixed, and the outlet flow was varied to obtain the required blowing ratio. The results showed that the upstream cooling performance for each case studied was constant for variable blowing ratio. The jet impingement configuration enhanced the upstream film cooling performance with respect to the parallel flow. Moreover, a large gap height with jet impingement provided improvement on the downstream film cooling effectiveness and enhanced the upstream performance.

7.2 Recommendation

The film cooling performance of the louver and hybrid schemes were tested experimentally on a flat plate. It was found that both schemes enhanced the film cooling effectiveness at different blowing ratios. Future studies are recommended to investigate the performance of the schemes on an airfoil. This could include optimizing their locations on the pressure and suction sides of the airfoil for peak film cooling performance. The louver scheme was designed to include jet impingement, and was found to significantly effect on the conjugate heat transfer (CHT). Future experimental and numerical studies are therefore recommended to combine CHT and film cooling on an airfoil.

The CHT and film cooling analysis of the hybrid scheme were investigated over a flat plate through this study. Future numerical and experimental studies could include CHT and film cooling of the hybrid scheme on airfoil with multi-row configurations.

New designs that incorporate internal cooling, including swirling flow, are recommended to improve the hybrid scheme's overall cooling performance for gas turbine airfoils. The evaporative cooling for the inlet cooling air has significant effect on overall film cooling effectiveness, hence on overall thermal efficiency of the engine, therefore it is recommended for future studies with advanced film cooling schemes.

References

[1] Ahn, Joon , Jung, Sung In, and Lee, Joon Sik, "Film cooling from two rows of holes with opposite orientation angles: Heat transfer", JSME International Journal, Series B: Fluids and Thermal Engineering, Vol. 43, No.4, 2000, pp. 706-711.

[2] Ames, F.E., and Plesniak, M.W., "The influence of large-scale high-intensity turbulence on vane aerodynamic losses, wake growth, and the exit turbulence parameters" ASME Journal of Turbomachinery, vol. 119, 1997, pp. 182-192.

[3] Ammari, H.D., Hay, N., and Lampard, D. "Effect of density ratio on the heat transfer coefficient from a film-cooled flat plate", Journal of Turbomachinery, Vol. 112, No.3, 1990, pp. 444-450.

[4] Baheri, S., Tabrizi, S. P. Alavi, and Jubran, B.A., "Film cooling effectiveness from trenched shaped and compound holes", International journal of Heat and Mass Transfer, vol 44, n 8, 2008, pp. 989-998.

[5] Baines, N.C., Oldfield, M.L.G., Jones, T.V., Schultz, D.L., King, P.J., and Daniels, L.C., "A short-duration blowdown tunnel for aerodynamic studies on gas turbine blade" ASME Turbo Expo 1982, GT1982-312.

[6] Baldauf, S., Schulz, A., and Wittig, S., "High-Resolution measurements of local heat transfer coefficients from discrete hole film cooling" Journal of Turbomachinery, Vol.123, Oct. 2001, pp.749-757.

[7] Barlow, Douglas N., and Kim, Yong W., "Effect of surface roughness on local heat transfer and film cooling effectiveness", American Society of Mechanical Engineers (Paper), 1995, 10pp.

[8] Baskharone E. A., "Principles of turbomachinery in air-breathing engine", Cambridge, 2006.

[9] Baughn, J.W., Anderson, M.R., Mayhew, J.E., and Wolf, J.D., "Hysteresis of thermochromic liquid crystal temperature measurement based on hue", Transactions of the ASME. Journal of Heat Transfer, vol. 12, n 4, 1999, pp. 1067-72.

[10] Bell, C.M., Hamakawa, H., and Ligrani, P.M., "Film cooling from shaped holes", Journal of Heat Transfer, Vol. 122, 2000, pp.224-232.

[11] Bergeles, G., Gosman, A.D., and Launder, B.E., "Near-field character of a jet discharged through a wall at 30° to a mainstream", AIAA Journal, Vol. 15, No.4, 1977, pp. 499-504.

[12] Blair, M.F., Dring, R. P., and Joslyn, H.D., "The effects of turbulence and stator/rotor interaction on turbine heat transfer part I : design operating Conditions . Part II effect of reynolds number and incidence", ASME, Journal of Turbomachinery, Vol. 111, 1989, pp. 87-103.

[13] Bohn, D., Ren, J., and Kusterer, K., "Systematic investigation on conjugate heat transfer rates of film cooling configurations", International Journal of Rotating Machinery, Vol. 3, 2005, pp. 211–220.

[14] Bons, J. P., MacArthur, C. D., and Rivir, R. B., "Effect of high freestream turbulence on film cooling effectiveness", American Society of Mechanical Engineers (Paper), 1994, pp. 1-14.

[15] Bons, J.P., Taylor, R.P., McClain, S.T., and Rivir, R.B., "The many faces of turbine surface roughness", Journal of Turbomachinery, Vol. 123, No. 4, 2001, pp. 739-748.

[16] Cardwell, N.D., Sundaram, N., and Thole, K.A., "Effect of midpassage gap, endwall misalignment, and roughness on endwall film-cooling", Transactions of the ASME. The Journal of Turbomachinery, Vol. 128, No. 1, 2006, pp. 62-70.

[17] Chen, P.-H., Ai, D., and Ding, P.-P., "Selection criterion of injection temperature pair for transient liquid crystal thermography on film cooling measurements", International Journal of Heat and Mass Transfer, Vol. 44, n 7, Apr 2001, pp. 1389-1399.

[18] Cho, H., Rhee, D., Kim, B., "Enhancement of film cooling performance using a shaped film cooling hole with compound angle injection", JSME international journal Fluid and thermal Engineering, vol.44,n.1, 2001, pp.99-110.

[19] Coulthard, Sarah M., Volino, R. J., and Flack, K. A., "Effect of unheated starting lengths on film cooling experiments", Journal of Turbomachinery, vol. 128, n 3, 2006, pp. 579-588.

[20] Dhungel, A., Lu, Y., Phillips, W., Ekkad, S. V., and Heidmann, J. "Film cooling from a row of holes supplemented with anti vortex holes", ASME Turbo Expo, 2007, pp. 375-384.

[21] Dittmar, J., Schulz, A., and Wittig, S., "Assessment of various film-cooling configurations including shaped and compound angle holes based on large-scale experiments", Journal of Turbomachinery, vol. 125, 2003, pp. 57-64.

[22] Drost, U., Bolcs, A, and Hoffs, A.," Utilization of the transient liquid crystal technique for film cooling effectiveness and heat transfer investigations on a flat

plate and a turbine airfoil ", American Society of Mechanical Engineers (ASME), 1997, 9p.

[23] Ekkad, S. V., Zapata, D., and Han, J. C., "Film effectiveness over a flat surface with air and CO2 injection through compound angle holes using a transient liquid crystal image method", Journal of Turbomachinery, vol. 119, n 3, 1997, pp. 587-593.

[24] Ekkad, S. V., Zapata, D., Han, J. C., "Heat transfer coefficients over a flat surface with air and CO2 injection through compound angle holes using a transient liquid crystal image method", American Society of Mechanical Engineers (Paper), 1995, 9pp.

[25] Eriksen,E.R.G., and Goldstein, R.J. "Effects of hole geometry and density on three-dimensional film cooling", International Journal of Heat and Mass Transfer, vol. 17, n 5, 1974, pp. 595-607.

[26] FLUENT 6.3, Fluent Inc., 2006.

[27] Garg, V.K., and Gaugler, R.E., "Effect of coolant temperature and mass flow on film cooling of turbine blades", International Journal of Heat and Mass Transfer, Vol. 40, No. 2, 1997, pp. 435-45.

[28] Garg, Vijay K., and Rigby, David L., "Heat transfer on a film-cooled blade - effect of hole physics", American Society of Mechanical Engineers (Paper), n GT, 1998.

[29] Ghorab, M, Hassan, I., and Beauchamp, M., "Simulation of a multi-stage cooling scheme for gas turbine engines: part I", ASME Turbo Expo 2007, GT2007-28036.

[30] Goldstein, R.J. and Jin, P., "Film cooling downstream of a row of discrete holes with compound angle", Journal of Turbomachinery, Vol. 123, 2001, No. 2, pp.222-230.

[31] Goldstein, R.J., Eckert, E.R.G., and Burggraf, F., "Effect of hole geometry and density on three-dimensional film cooling", International Journal Heat and Mass Transfer, Vol. 17, 1974, pp. 595-607.

[32] Goldstein, R.J.; Taylor, J.R., "Mass transfer in the neighborhood of jets entering a crossflow", Journal Heat Transfer Trans ASME, Vol. 104, 1982, N 4, pp.715-721.

[33] Gritsch, M., Schulz, A., and Wittig, S., "Adiabatic wall effectiveness measurements of film-cooling holes with expanded exits", Journal of Turbomachinery, vol. 120, 1998, pp. 549-556.

[34] Gritsch, M., Schulz, A., and Wittig, S., "Film-cooling holes with expanded exits: Near-hole heat transfer coefficients", International Journal of Heat and Fluid Flow, vol. 21, n 2, 2000, pp. 146-155.

[35] Hay, H.L., and Hollingsworth, D.K., "A comparison of trichromic systems for use in the calibration of polymer-dispersed thermochromic liquid crystals", Experimental Thermal and Fluid Science, vol. 12, 1996, No. 1, pp. 1-12.

[36] Hay, N., Lampard, D., and Saluja, C.L., "Effects of the condition of the approach boundary layer and of mainstream pressure gradients on the heat transfer coefficient on film-cooled surfaces", Transactions of the ASME. Journal of Engineering for Gas Turbines and Power, Vol. 107, No.1, 1985, pp. 99-104.

[37] Heidmann, J., D., and Ekkad, S., "A Novel antivortex turbine film-cooling hole concept", Journal of Turbomachinery, July, Vol. 130, 2008, pp. 031020-1: 031020-9.

[38] Heidmann, J., Kassab, A., Divo, E., Rodriguez, F., and Steinthorsson, E., "Conjugate Heat Transfer Effects On A Realistic Film-Cooled Turbine Vane", ASME Turbo Expo 2003, pp. 1-11.

[39] Hoffs, Alexander, "Experimental investigations of heat transfer and film cooling effectiveness using the transient liquid crystal technique", PhD. Thesis, Technische Hochschule Aachen, Germany, 1996.

[40] Immarigeon, A. and Hassan, I., "An advanced impingement/film cooling scheme for gas turbines –numerical study", International Journal of Numerical Methods for Heat and Fluid Flow, Vol. 16, 2006, No. 4, pp. 470-493.

[41] Jackson, D.J., Lee, K.L., Ligrani, P.M., and Johnson, P.D., "Transonic aerodynamic losses due to turbine airfoil, suction surface film cooling", Journal of Turbomachinery, Transactions of the ASME, Vol. 122, 2000, No 2, pp. 317-326.

[42] Jenkins, S., Varadarajan, K., and Bogard, D.G., "The effects of high mainstream turbulence and turbine vane film cooling on the dispersion of a simulated hot streak", Transactions of the ASME. The Journal of Turbomachinery, Vol. 126, No. 1, 2004, pp. 203-11.

[43] Jessen, W., Schröder, W., and Klaas, M., "Evolution of jets effusing from inclined holes into crossflow", International Journal of Heat and Fluid Flow, vol. 28, 2007, pp. 1312-1326.

[44] Jia, R., Sunden, B., Miron, P., and Leger, B., "A numerical and experimental investigation of the slot film-cooling jet with various angles", Journal of Turbomachinery, Vol. 127, 2005, No. 3, pp. 635-645.

[45] Jubran, B.A. and Maiteh, B.Y., "Film cooling and heat transfer from a combination of two rows of simple and/or compound angle holes in inline and/or staggered configuration", Heat and Mass Transfer, vol. 34, n 6, April 1999, pp. 495-502.

[46] Jumper, G.W., Elrod, W.C., and Rivir, R.B., "Film cooling effectiveness in high-turbulence flow", Journal of Turbomachinery, Vol. 113, No. 3, 1991, pp. 479-483.

[47] Jungho C. "An experimental investigation of blade heat transfer and turbine blade trailing edge cooling", Ph D thesis, 2004, Texas A&M University.

[48] Kim Y., Engels G., and Peck R. E.; "Investigation of a quasi-steady liquid crystal technique for film cooling heat transfer measurements", Journal of Experimental Heat Transfer; Vol.14, 2001, pp. 181-198.

[49] Kim, Y. J., and Kim, S. M., "Influence of shaped injection holes on turbine blade leading edge film cooling", International Journal of Heat and Mass Transfer, Vol. 47, No. 2, 2004, pp. 245–256.

[50] Kline, S. J., and McClintock, F. A., "Describing uncertainties in single sample experiments", Mech. Eng. Am. Soc., vol. 75, 1953, pp. 3–8.

[51] Knost, D. G., and Thole, K. A., "Heat transfer and film-cooling for the endwall of a first stage turbine vane", International Journal of Heat and Mass Transfer, Vol 48, 2005, No. 25-26, pp. 5255-5269.

[52] Koc, I., "Experimental and numerical investigation of film cooling effectiveness for rectangular injection holes", International Journal of Aircraft Engineering and Aerospace Technology, 79/6, 2007, pp.621–627

[53] Kohli, A., and Bogard, D. G., "Effects of hole shape on film cooling with large angle injection", ASME Paper 99- GT-165, 1999.

[54] Kusterer, K., Bohn, D., Sugimoto, T., and Tanaka, R., "Double-Jet ejection of cooling air for improved film cooling", Journal of Turbomachinery, Vol. 129, 2007, pp. 809-815.

[55] Kusterer, K., Hagedorn, T., Bohn, D., Sugimoto, T., and Tanaka, R., "Improvement of a film-cooled blade by application of the conjugate calculation technique", Journal of Turbomachinery, Vol. 128, No.3, 2006, pp. 572-578.

[56] Lakshminarayana, B., "Fluid Dynamics and Heat Transfer of Turbomachinery", Wiley-Interscience, December, 1995.

[57] Lee, J. S., "Effects of orientation angles on film cooling over a flat plate: boundary layer temperature distributions and adiabatic film cooling effectiveness", Journal of Turbomachinery, Transactions of the ASME, Vol. 122, 2000, No 1, pp. 153-160.

[58] Lee, Joon Sik, Jung, Ho Gyung, and Kang, and Sae Byul, "Effect of embedded vortices on film cooling performance on a flat plate", Experimental Thermal and Fluid Science, 5th World Conference on Experimental Heat Transfer, Fluid Mechanics and Thermodynamics, Vol. 26, No. 2-4, 2002, pp. 197-204.

[59] Li, X. and Wang, T., "Effects of various modeling schemes on mist film cooling simulation", ASME International Mechanical Engineering Congress, Proceedings of the ASME Heat Transfer Division, 2005, pp. 513-523.

[60] Li, X., and Wang, T., "Simulation of film cooling enhancement with mist injection", Transactions of the ASME. Journal of Heat Transfer, Vol. 128, No. 6, 2006, pp. 509-19.

[61] Licu D.N., Findlay M.J., Gartshore I.S., and Salcudean M.S., "Transient heat transfer measurements using a single wide-band liquid crystal test", Journal of Turbomachinery, Transactions of the ASME, Vol. 122, No. 3, 2000, pp. 546-552.

[62] Ligrani, P.M., Ciriello, S., and Bishop, D.T., "Heat transfer, adiabatic effectiveness, and injectant distributions downstream of a single row and two staggered rows of

compound angle film-cooling holes", Transactions of the ASME, The Journal of Turbomachinery, Vol. 114, No.4, 1992 pp. 687-700.

[63] Ligrani, P.M., Wigle, J.M, Ciriello, S, and Jackson, S.M., "Film-cooling from holes with compound angle orientations. Part 1. Results downstream of two staggered rows of holes with 3d spanwise spacing", Journal of Heat Transfer, vol. 116, No. 2, 1994, p 341-352.

[64] Ling, J. P.C.W. , Ireland, P. T. and Turner, L."A technique for processing transient heat transfer, liquid crystal experiments in the presence of lateral conduction", Journal of turbo machinery Vol. 126, 2004, pp. 247-258.

[65] Liu, C., Zhu, H., Bai, J. and Xu, D., "Film cooling performance of converging-slot holes with different exit-entry area ratios", ASME Turbo Expo, GT2009-59002.

[66] Liu, G., "Endwall heat transfer and film cooling measurement in a turbine cascade with injection upstream of leading edge", Transactions of the ASME, 2004.

[67] Lu, X., Jiang, P., Sugishita, H., Uechi, H., and Suenaga, K., "Conjugate heat transfer analysis of film cooling flows", Journal of Thermal Science, Vol.15, 2005, No.1 pp. 85-91.

[68] Lu, Y., "Effect of hole configurations on film cooling from cylindrical inclined holes for the application to gas turbine blades", Ph.D. Thesis, Louisiana State University, 2007.

[69] Lu, Y., Dhungel,A., Ekkad, S.,and Bunker, R., "Effect of trench width and depth on film cooling from cylindrical holes embedded in trenches", Journal of Turbomachinery, vol. 131, n 1, 2009, pp. 011003 (13 pp.),

[70] Makki, Y. H., and Jakubowski, G. S., "An experimental study of film cooling from diffused trapezoidal shaped holes", AIAA Paper AIAA-86-1326, 1986.

[71] Martin N. "Film-Cooled turbine endwall in a transonic flow field: part ii- heat transfer and film-cooling effectiveness", Journal of Turbomachinery, Vol. 123, 2001, pp. 720-729.

[72] Martinez-Botas, R.F., Lock, G.D., and Jones, T.V., "Heat transfer measurements in an annular cascade of transonic gas turbine blades using the transient liquid crystal technique", ASME Journal of Turbomachinery, vol. 117 , 1995, pp. 425-431.

[73] Martini, P., Schulz, A., Whitney, C.F., and Lutum, E., "Experimental and numerical investigation of trailing edge film cooling downstream of a slot with internal rib arrays", Institution of Mechanical Engineers, Part A: Journal of Power and Energy, Vol. 217, 2003, No. 4, pp. 393-402.

[74] Mayhew, J. E., Baughn, J. W., and Byerley, A. R., "The effects of free-stream turbulence on film cooling adiabtaic effectiveness", International Journal of Heat and Fluid Flow, Vol. 24, No. 5, 2003, pp. 669–679.

[75] Mazur, Z., Hernandez-Rossette, A., Garcı´a-Illescas, R., and Luna-Ramı´rez, A., "Analysis of conjugate heat transfer of a gas turbine first stage nozzle", Applied Thermal Engineering, Vol. 26, 2006, pp. 1796–1806.

[76] Miao, Jr-M. and Wu, C.-Y., "Numerical approach to hole shape effect on film cooling effectiveness over flat plate including internal impingement cooling chamber", International Journal of Heat and Mass Transfer, Vol. 49, 2006, pp. 919-938.

[77] Nearly, D.A., Mihelc, M.S., Hylton, L.D., and Gladden, H.J., "Measurements of heat transfer distribution over the surfaces of highly loaded turbine nozzle guide vanes", ASME Journal of Engineering for gas turbine and power, Vol.106, 1985, pp. 149-158.

[78] Okita, Y., and Nishiura, M., "Film effectiveness performance of an arrowhead-shaped film-cooling hole geometry", Journal of Turbomachinery, Vol. 129, 2007, pp.331-339.

[79] Ou, S. , and Rivir, R.B., "Leading edge film cooling heat transfer with high free stream turbulence using a transient liquid crystal image method", International Journal of Heat and Fluid Flow, Vol. 22, No. 6, 2001, pp. 614-623.

[80] Rhee, Dong Ho , Nam, Yong Woo , and Cho, Hyung Hee, "Local heat/mass transfer with various rib arrangements in impingement/effusion cooling system with crossflow", Journal of Turbomachinery, Vol. 126, 2004, Issue 4, PP. 615-626.

[81] Roach, P.E. "Generation of nearly isotropic turbulence by means of grids", International Journal of Heat and Fluid Flow, Vol. 8, 1987, No.2, pp.82-92 .

[82] Russin, Rebekah A., Alfred, Daniel, and Wright, Lesley M., "Measurement of detailed heat transfer coefficient and film cooling effectiveness distributions using PSP and TSP", ASME, Turbo Expo 2009, GT2009- 59975.

[83] Sargison, J. E., Guo, S. M., Oldfield, M. L. G., Lock, G. D., and Rawlinson, A. J., "A converging slot-hole film-cooling geometry – part 1: low-speed flat-plate heat transfer and loss", Journal of Turbomachinery, vol. 124, 2002, pp. 453-460.

[84] Saumweber, C., Schulz, A., and Wittig, S., "Free-stream turbulence effects on film cooling with shaped holes", Journal of Turbomachinery, Vol. 125, 2003, pp. 65-73.

[85] Schmidt, D. L., Sen, B., and Bogard, D. G., "Film cooling with compound angle holes: adiabatic effectiveness", Journal of Turbomachinery, Vol. 118, 1996, pp. 807-813.

[86] Sen, B., and Bogard, D.G., "Effects of surface roughness on film cooling", International Gas Turbine and Aeroengine Congress & Exhibition, Birmingham, UK, 1996, Jun 10-13, 7pp..

[87] Sinha, A. K., Bogard, D. G., and Crawford, M. E., "Film- Cooling effectiveness downstream of a single row of holes with variable density ratio", Journal of Turbomachinery, Vol. 113, 1991, pp. 442–449.

[88] Taslim, M.E. and Khanicheh, A., "Film effectiveness downstream of a row of compound angle film holes", Journal of Heat Transfer, Vol. 127, 2005, pp. 434-440.

[89] Vogel, G., Grat, A.B.A., Von Wolfersdorf, J., and Weigand, B., "A novel transient heater-foil technique for liquid crystal experiments on film-cooled surfaces", Journal of Turbomachinery, Vol. 125, 2003, No. 3, pp.529-537.

[90] Weigand, B., Von Wolfersdorf, J., and Semmler, K., "Film cooling on a convex surface with zero pressure gradient flow" , International Journal of Heat and Mass Transfer, Vol. 43, 2000, No. 16, pp. 2973-2987.

[91] Wu, C.-Y. and Miao, Jr-M., "Numerical visualization of conjugate heat transfer of a fan-shaped film-cooling concave composite plate", Journal of Flow Visualization and Image Processing, Vol. 13, 2006, pp. 377-391.

[92] Yu, Y., Yen, C.-H., Shih, T. I.-P., Chyu, M. K., Gogineni, S., "Film cooling effectiveness and heat transfer coefficient distributions around diffusion shaped holes", Journal of Heat Transfer, Vol. 124, No. 5, 2002, pp. 820-827.

[93] Yuen, C.H.N., and Martinez-Botas, R.F., "Film cooling characteristics of rows of round holes at various streamwise angles in a crossflow: part I. effectiveness", International Journal of Heat and Mass Transfer, Vol. 48, No. 23-24, 2005, pp. 4995-5016.

[94] Zhang, X. Z., and Hassan, I., "Film cooling effectiveness of an advanced-louver cooling scheme for gas turbines", Journal of Thermophysicis and Heat Transfer, Vol. 20, No. 4, 2006, pp. 754-763.

[95] Zhang, X-Z, "An advanced-louver cooling scheme for gas turbine – adiabatic effectiveness and heat transfer performance", MSc. Thesis, Concordia University, 2004.

[96] Zhang, X-Z, "Numerical study of louver cooling scheme on gas turbine airfoil", PhD. Thesis, Concordia University, 2008.

Appendix A: Different Methods to Calculate h and η

A.1 Comparison between three different methods to calculate h and η

This section presents a comparison of three different methods used to solve heat transfer coefficient and film cooling effectiveness. The flow-chart in Fig.A.1 shows the three methods: two points, Nonlinear Least Square Regression, and Duhamel's Superposition methods. The method selected is highly dependent on test rig design as well as the procedure used to run the experimental where it will affect thermally changing flow conditions. Thermal flow conditions are very difficult to keep constant during transient tests due to heat transfer losses either from the working fluid to test rig material or to the surroundings.

The first method to solve film cooling effectiveness and heat transfer coefficient is called the two points method. Two pairs of time should be selected in order to solve Eq. A1. The transient time is 30 sec and there is a different value of jet, main, and wall temperatures for each corresponding time. For the selected two pairs of time, heat transfer coefficient can be calculated can be determined from Eq. A.4, then the film cooling effectiveness from Eqs. A.2 and A.3. From the results, there is more than one solution of film cooling effectiveness for every two pairs of time as shown in Table A.1. Each solution is obtained by Eq. A.1 with a specific error. Moreover, there are many solutions of heat transfer coefficient for the same two pairs of time, as presented in Table A.2. As a result this method cannot be used in the present study to calculate film cooling effectiveness and heat transfer coefficient for the transient test.

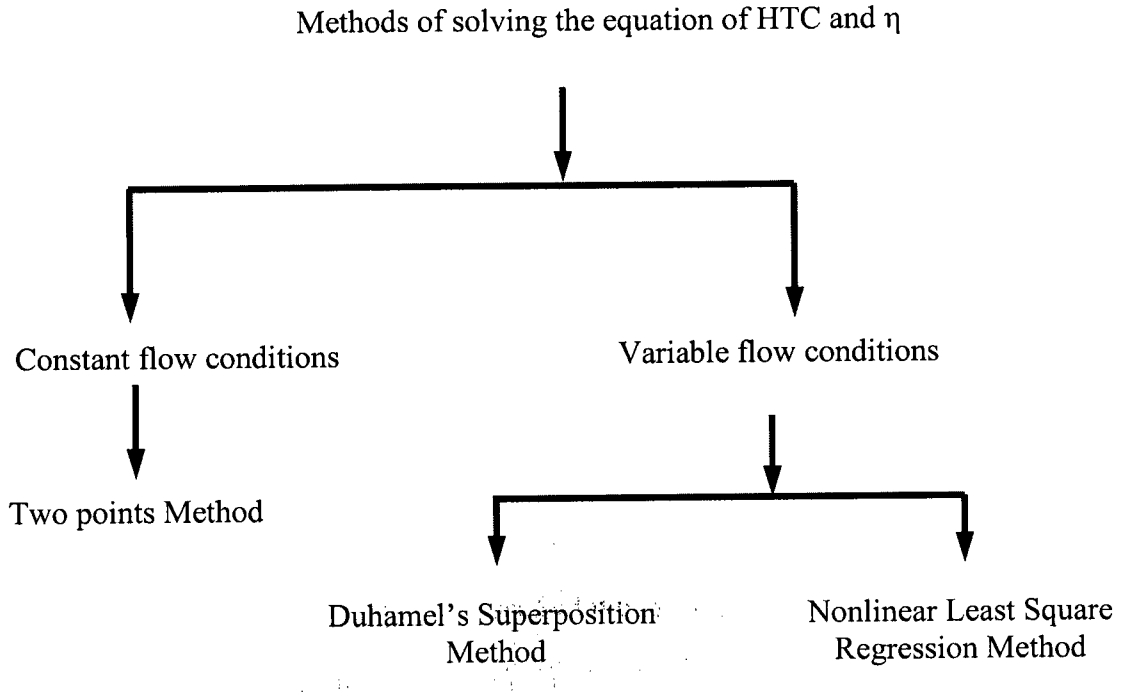

Figure A.1. Flow chart for different methods to solve heat transfer coefficient and film cooling effectiveness.

A.1.1 Two points methods

$$T_{w1} - T_i = \left[1 - \exp\left(\beta_1^2\right) erfc(\beta_1)\right] * \left[\eta\left(T_{j1} - T_{m1}\right) + T_{m1} - T_i\right] \quad \text{(A.1)}$$

where $\beta = \dfrac{h\sqrt{\alpha t}}{k}$

$$\eta_1 = \left(\frac{T_{w1} - T_i}{\left[1 - \exp\left(\beta_1^2\right) \mathrm{erfc}\left(\beta_1\right)\right]} + \left(T_i - T_{m1}\right) \right) * \frac{1}{\left(T_{j1} - T_{m1}\right)} \quad \text{(A.2)}$$

$$\eta_2 = \left(\frac{T_{w2} - T_i}{\left[1 - \exp\left(\beta_2^2\right) erfc\left(\beta_2\right)\right]} + \left(T_i - T_{m2}\right) \right) * \frac{1}{\left(T_{j2} - T_{m2}\right)} \quad \text{(A.3)}$$

$$T_{w2} - T_i = \left[1 - \exp\left(\beta_2^2\right) erfc(\beta_2)\right] * \left[\left(\frac{T_{w1} - T_i}{\left[1 - \exp\left(\beta_1^2\right) erfc(\beta_1)\right]} + \left(T_i - T_{m1}\right) \right) * \frac{\left(T_{j2} - T_{m2}\right)}{\left(T_{j1} - T_{m1}\right)} + T_{m2} - T_i \right] \quad \text{(A.4)}$$

Table A.1. h and η at different time steps for two points method.

t_1	t_2	h	η_1	η_2
4	30	295	0.786207	0.0707
6	30	471.95	0.768279	0.070178
8	30	379.2	0.775509	0.070389
10	30	315.5	0.783051	0.07061
12	30	255.2	0.793861	0.070927
14	30	164.1	0.826463	0.071881
16	30	129.8	0.851664	0.072619
20	30	191.2	0.780798	0.071496
24	30	144.5	0.789914	0.072257
Average		260.7167	0.795083	

Table A.2. h and η at one pairs of time for two-point method.

t_1	t_2	h	η_1	η_2
12	30	93.3	0.972655	0.074058
		104.05	0.941972	0.073521
		116.75	0.913453	0.073022
		132.15	0.886689	0.072555
		151.25	0.861553	0.072116
		175.8	0.837779	0.071699
		208.65	0.815262	0.071304
		255.2	0.793861	0.070927
		327.05	0.773408	0.070563
		453.7	0.753802	0.070212
		740.5	0.734923	0.06987

A.1.2 Nonlinear least square method

The second method is called nonlinear least square regression. This method is used to further reduce experimental error for film cooling applications. It is preferable to use the regression method with high response of the secondary flow temperature during the experimental test. Many parameters are measured using the transient experimental method to determine the heat transfer coefficient (h) and film cooling effectiveness (η), such as wall surface temperature using TLC technique, secondary flow temperature, and initial and mainstream temperatures. All these parameters are changeable during the transient test except the initial temperature. The non-linear least-square regression method is used to solve Eq. (A.5) in order to calculate the two unknown parameters: h and η. For every ROI, the surface wall temperatures values for each transient test (during 30 sec) are related to one particular value for heat transfer coefficient and film cooling effectiveness.

$$T_w - T_i = \left[1 - \exp\left(\frac{h^2 \overline{\alpha} t}{k^2}\right) erfc\left(\frac{h\sqrt{\overline{\alpha} t}}{k}\right)\right] * \left[\eta\left(T_j - T_m\right) + T_m - T_i\right] \qquad \text{(A.5)}$$

The downstream wall surface temperature for each ROI over the target surface is measured using the TLC technique at each time step during the transient measurement according the following equation:

$$\mathrm{T}_{\mathrm{w\,(ROI)}}(\mathrm{h}, \eta)\Big|_{t=\tau} - T_{TLC}\Big|_{t=\tau} = 0 \qquad \text{for i = 1 to N.} \qquad \text{(A.6)}$$

where N is total number of images captured during each transient test.

To obtain the optimum solution for solving the two unknown parameters (h and η), N-N_b equations should have minimum values in the error function for each ROI over the target area as follows:

$$\frac{1}{2}\sum_{i=N_b}^{N}\left(\mathrm{T}_{\mathrm{w\,(ROI)}}(\mathrm{h}, \eta)\Big|_{t=\tau} - T_{TLC}\Big|_{t=\tau}\right)^2 = \varepsilon(h, \eta) \qquad \text{(A.7)}$$

Where N_b is the number of black images (without cooling effect) and ε is the least square error (LSE).

Figure A.2 presents the temperature response data for a single ROI as well as the curve fit solution using the non-linear least square regression method. The residual error of heat transfer coefficient and film cooling effectiveness is minimized by using the LSQ method, such that the experimental error will also be reduced.

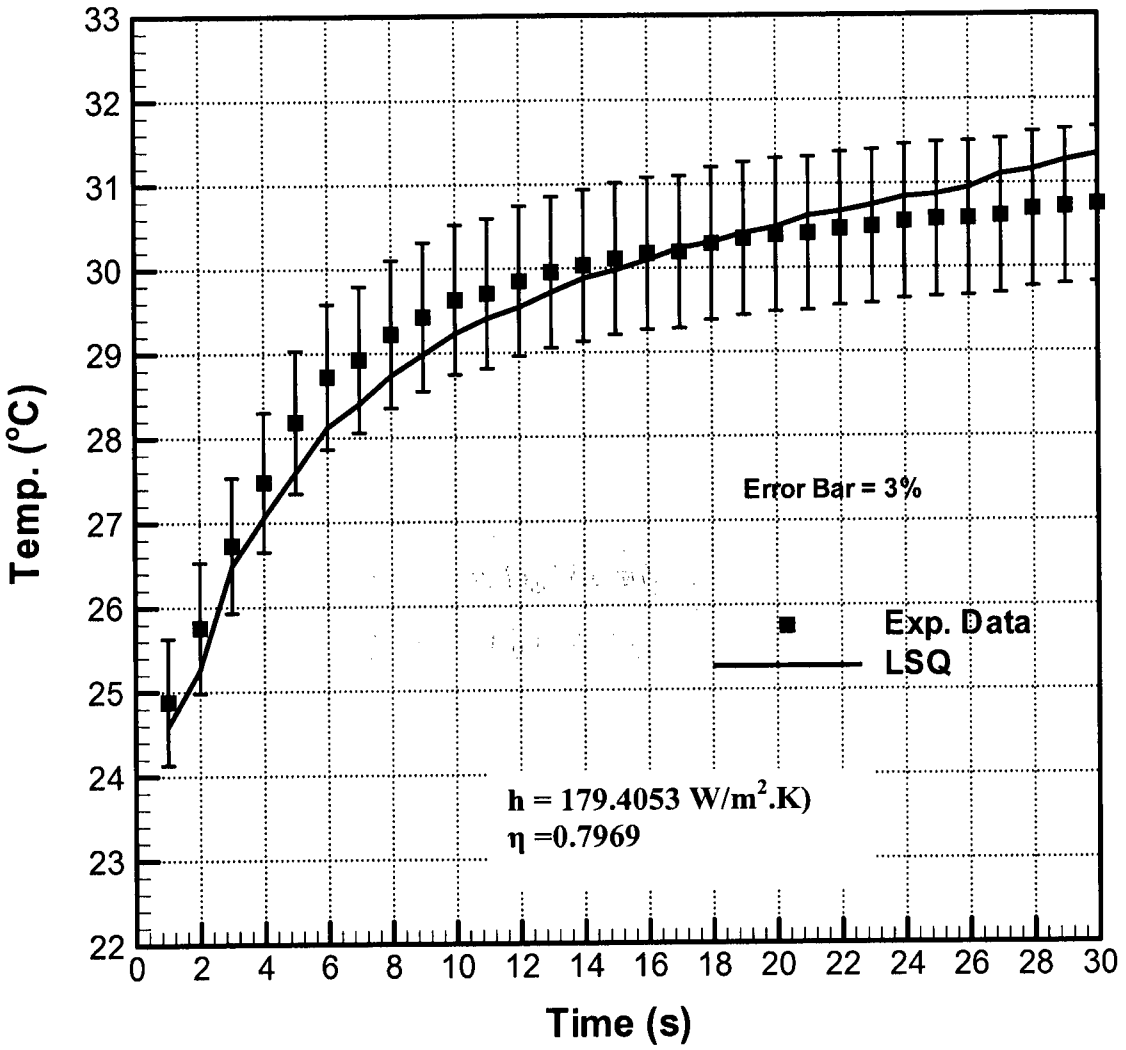

Figure A.2. Measured and calculated temperature profiles using LSQ.

A.1.3 Duhamel's superposition method (DSM)

Duhamel's superposition method is used for slow response of changing secondary flow temperature during the experimental test. The following results present the solution of the heat transfer coefficient and film cooling effectiveness using Duhamel's superposition method considering the variation of the secondary flow. Two time steps are selected and applied to Eq. A.8 to calculate the two unknowns (h and η). The second time step is selected to be 30 sec while the first time step is changed in order to study the effect of the first time on the final value of h and η, as shown in Table A.3. Firstly, the heat transfer coefficient is calculated from Eq. A.8, and then the film cooling effectiveness can be calculated from either Eq. A.9 or Eq. A.10. Theoretically, η_1 and η_2 should be the same however in reality, there is a difference, as shown in Table A.3. Each value of η has an error according to Eq. A.11, as shown in Table A.3. From these results, there is no solution for the two variables if t_1<14 sec. When the two times steps become very close, the heat transfer coefficient has low value. As a result, h and η have different values according to the selection of t_1. Therefore, the final values of h and η are considered as an average value.

$$\frac{T_{w(t1)}-T_i}{T_{w(t2)}-T_i}=\frac{\sum_{n=1}^{N1}\left\{1-\exp\left(\frac{h^2\overline{\alpha}(t_1-\tau_n)}{k^2}\right)erfc\left(\frac{h\sqrt{\overline{\alpha}(t_1-\tau_n)}}{k}\right)\right\}*(\Delta T_j)_n}{\sum_{n=1}^{N2}\left\{1-\exp\left(\frac{h^2\overline{\alpha}(t_2-\tau_n)}{k^2}\right)erfc\left(\frac{h\sqrt{\overline{\alpha}(t_2-\tau_n)}}{k}\right)\right\}*(\Delta T_j)_n} \tag{A.8}$$

$$\eta_1=\frac{(T_{w(t1)}-T_i)}{\sum_{n=1}^{N1}\left\{1-\exp\left(\frac{h^2\overline{\alpha}(t_1-\tau_n)}{k^2}\right)erfc\left(\frac{h\sqrt{\overline{\alpha}(t_1-\tau_n)}}{k}\right)\right\}*(\Delta T_j)_n} \tag{A.9}$$

$$\eta_2 = \frac{(T_{w(t2)} - T_i)}{\sum_{n=1}^{N2}\left\{1-\exp\left(\frac{h^2\overline{\alpha}(t_2-\tau_n)}{k^2}\right)erfc\left(\frac{h\sqrt{\overline{\alpha}(t_2-\tau_n)}}{k}\right)\right\}*(\Delta T_j)_n} \quad \text{(A.10)}$$

where ΔT_j is the incremental change in jet temperature.

$$\varepsilon_{1,2} = \frac{T_{TLC} - Tw_{1,2}}{T_{TLC}} * 100 \quad \text{(A.11)}$$

where 1 and 2 in ε are biased on η_1 and η_2, respectively. In T_w, 1 and 2 refer to the first and second selected time.

Table A.3. h and η at different time steps for Duhamel's superposition method.

t_1 (N1)	t_2 (N2)	h (W/m2.K)	η_1	ε_1	η_2	ε_2
4	30	No solution found				
6	30					
8	30					
10	30					
12	30					
14	30	196.1	0.8702	3.3749	0.825	5.1779
15	30	196	0.8664	3.5202	0.82	5.3583
17	30	195.4	0.842	4.3207	0.7944	6.3167
19	30	195.3	0.838	4.5297	0.7908	6.4577
21	30	183.1	0.8267	4.9431	0.7802	6.8777
23	30	125.2	0.8695	3.5703	0.8202	5.3497
25	30	77.7	0.9583	1.0443	0.9041	2.5909
Average values		**166.9714**	**0.8673**	**3.614743**	**0.819243**	**5.446985714**

A.1.4 Summary

The method selected to calculate h and η values is affected by the main and secondary flow conditions during the experimental measurement. The two points method is used for constant temperature of the two flows, as well as for two different steady state experimental runs. If the secondary flow temperature response is slow, the Duhamel's superposition method must be used at two different pairs of times, and the final results of heat transfer coefficient and film cooling effectiveness is considered as an average value of output results of each two pairs of times. Conversely, the nonlinear least square regression method is used if the secondary flow temperature response is high. Table A.4 presents the percentage difference between the three methods (two points, Duhamel's superposition, nonlinear least square method), using Eq. A.12.

$$\varepsilon_{h,\eta}=\frac{(h,\eta)_{Duhamel,Two...points}-(h,\eta)_{LSQ}}{(h,\eta)_{LSQ}}*100. \qquad (A.12)$$

Table A.4. Comparison of h and η for different solved methods.

Two points		Duhamel's superposition method		
ε h %	ε η%	ε h %	ε η_1%	ε η_2%
45.3227 %	0.22801%	6.7 %	8.83%	2.8%

The nonlinear least square method requires an initial guess for h and η , which has a significant effect on the final result of the heat transfer coefficient, film cooling effectiveness, as well on LSQ error. Therefore, different downstream selected points are tested with scanning a range of heat transfer coefficient and film cooling effectiveness as an initial guess to investigate the acceptable initial guess value of h and η to be used for all downstream surfaces with a minimum LSQ error. Figure A.3 presents the output

values of the heat transfer coefficient ratio (h/h_o), film cooling effectiveness and the LSQ error for different initial guess values of heat transfer coefficient and film cooling effectiveness. These results are obtained for a single ROI located at x/d = 2 on the centerline. From the results, the initial guess values for $h < 400$ ($W/m^{2o}C$) has a significant effect on the output stability values of h/h_o, η and the LSQ error, as shown in Fig.A.3. The final output values are stable with minimum LSQ error value of 5 for an initial guess value of $h > 450$ ($W/m^{2o}C$) with any value of η. Other ROIs are tested at different downstream locations. For example, Fig.A.4 presents the effect of initial values on the output results for different ROIs, located at x/d = 10. The results show that the minimum LSQ error has a stability value of 0.44 for an initial guess $h_{IG} > 500$, which corresponds to the stability of η with a small variation of 2-3% for h/h_o values, as shown in Fig.A.4. As a result, according the two ROIs tested, the initial guess value for heat transfer coefficient should be > 500 ($W/m^{2o}C$) with any initial value of film cooling effectiveness in order to achieve stability of the solution with a minimum LSQ error. The LSQ error over the downstream surfaces has a maximum value near the film hole exit and decreases along the streamwise direction.

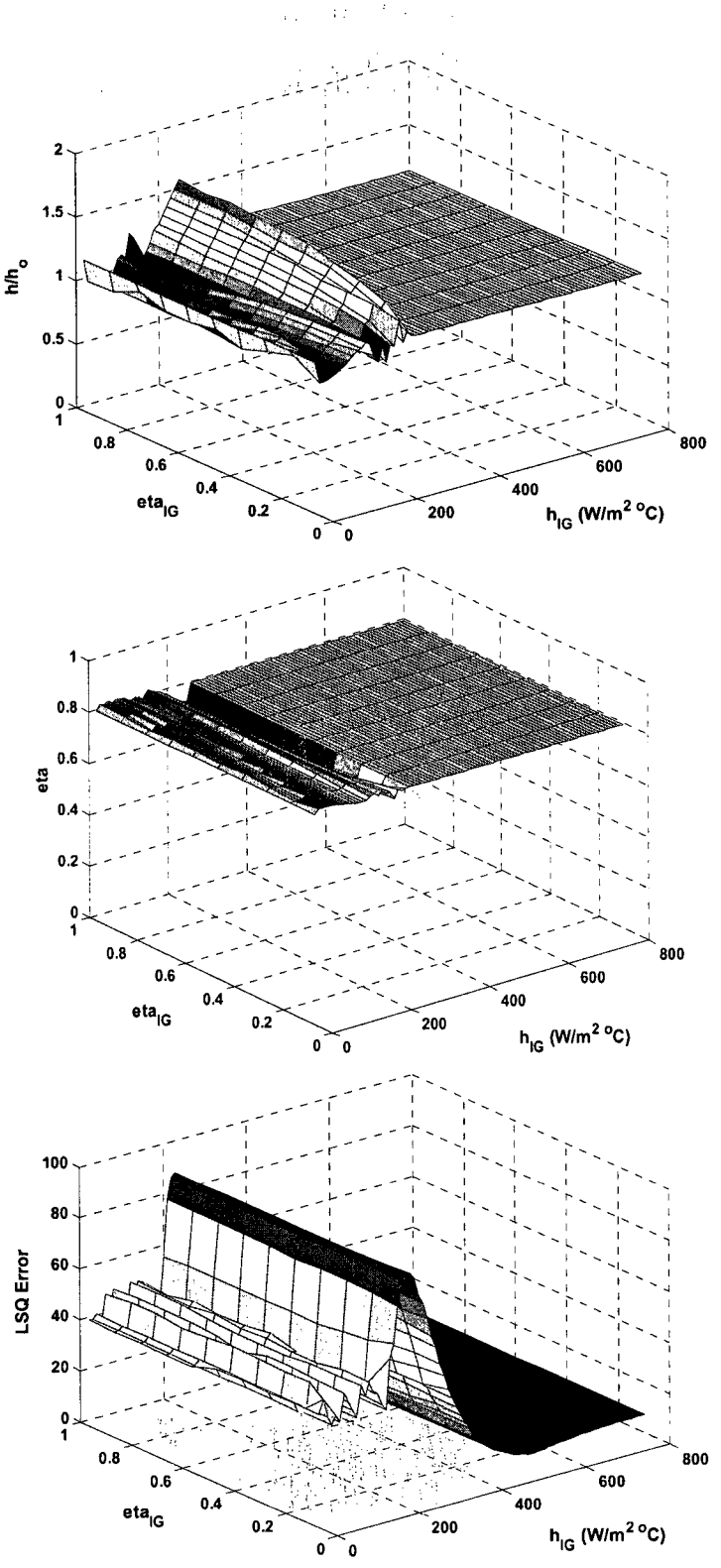

Figure A.3. Output results for different initial guess values for a single ROI at the centerline and x/d = 2 (Br = 1.0) (min error around 5).

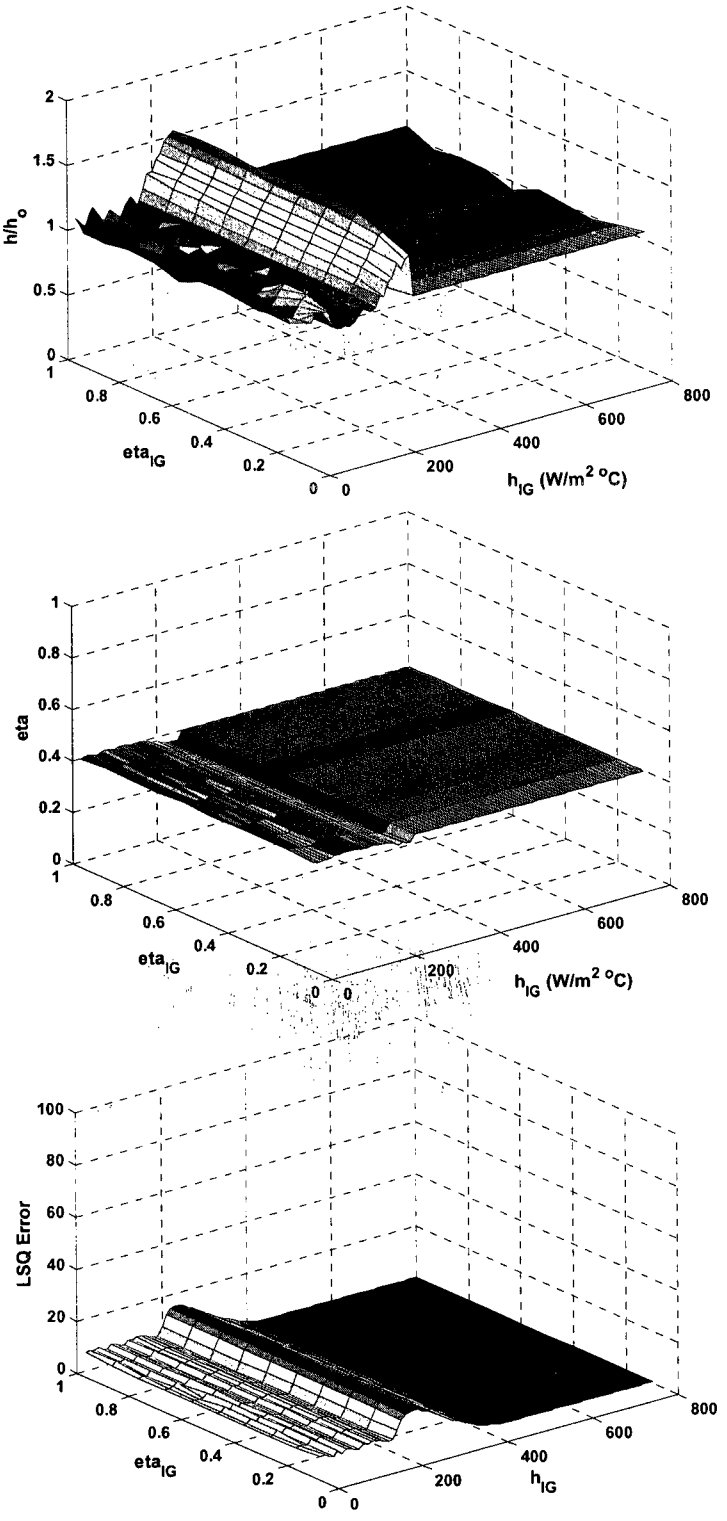

Figure A.4. Output results for different initial guess values for a single ROI at the centerline and x/d = 10 (Br = 1.0) (min error around 0.44).

Appendix B: Local and average experimental data

Table B.1. Centerline downstream cooling data of circular film hole Br = 0.5.

x/d	η	HTCR	Fn	NHFR	x/d	η	HTCR	Fn	NHFR	x/d	η	HTCR	Fn	NHFR
0	0.481	0.6	0.718	0.833	1.949	0.508	0.813	0.718	0.807	3.898	0.445	0.85	0.717	0.718
0.061	0.485	0.585	0.719	0.841	2.01	0.51	0.816	0.718	0.808	3.959	0.443	0.851	0.717	0.714
0.122	0.488	0.608	0.719	0.837	2.071	0.508	0.824	0.718	0.803	4.02	0.437	0.846	0.717	0.709
0.183	0.491	0.692	0.719	0.818	2.132	0.507	0.834	0.718	0.801	4.081	0.436	0.842	0.718	0.708
0.244	0.492	0.748	0.718	0.805	2.193	0.508	0.835	0.718	0.801	4.142	0.435	0.849	0.717	0.705
0.305	0.493	0.754	0.719	0.804	2.254	0.505	0.83	0.718	0.799	4.203	0.432	0.854	0.718	0.699
0.365	0.494	0.77	0.718	0.8	2.315	0.506	0.84	0.719	0.798	4.264	0.426	0.851	0.715	0.692
0.426	0.498	0.769	0.718	0.806	2.376	0.505	0.828	0.718	0.799	4.325	0.42	0.845	0.718	0.688
0.487	0.5	0.781	0.718	0.804	2.437	0.504	0.842	0.719	0.794	4.386	0.422	0.846	0.716	0.689
0.548	0.503	0.789	0.718	0.807	2.497	0.501	0.836	0.718	0.792	4.447	0.418	0.852	0.717	0.683
0.609	0.502	0.777	0.719	0.808	2.558	0.497	0.836	0.718	0.787	4.508	0.415	0.857	0.715	0.677
0.67	0.504	0.78	0.718	0.81	2.619	0.497	0.831	0.719	0.788	4.569	0.409	0.847	0.718	0.673
0.731	0.506	0.779	0.718	0.813	2.68	0.496	0.838	0.718	0.786	4.629	0.409	0.851	0.718	0.671
0.792	0.511	0.776	0.718	0.819	2.741	0.495	0.844	0.719	0.783	4.69	0.401	0.845	0.718	0.664
0.853	0.512	0.786	0.718	0.818	2.802	0.494	0.841	0.718	0.782	4.751	0.402	0.851	0.717	0.662
0.914	0.511	0.789	0.718	0.816	2.863	0.494	0.84	0.718	0.783	4.812	0.397	0.867	0.715	0.649
0.975	0.512	0.789	0.718	0.816	2.924	0.492	0.83	0.718	0.782	4.873	0.391	0.857	0.714	0.645
1.036	0.517	0.802	0.719	0.82	2.985	0.49	0.846	0.718	0.776	4.934	0.387	0.849	0.71	0.644
1.096	0.515	0.798	0.718	0.818	3.046	0.486	0.842	0.718	0.772	4.995	0.387	0.844	0.716	0.645
1.157	0.513	0.807	0.719	0.814	3.107	0.484	0.833	0.718	0.772	5.056	0.387	0.849	0.717	0.644
1.218	0.51	0.805	0.718	0.811	3.168	0.482	0.838	0.718	0.768	5.117	0.385	0.86	0.717	0.637
1.279	0.513	0.806	0.718	0.814	3.228	0.477	0.843	0.718	0.761	5.178	0.379	0.855	0.717	0.631
1.34	0.512	0.81	0.719	0.812	3.289	0.475	0.833	0.718	0.76	5.239	0.376	0.845	0.718	0.632
1.401	0.516	0.809	0.718	0.817	3.35	0.47	0.836	0.719	0.754	5.299	0.376	0.845	0.717	0.632
1.462	0.514	0.811	0.718	0.814	3.411	0.47	0.842	0.719	0.752	5.36	0.373	0.855	0.716	0.623
1.523	0.514	0.812	0.718	0.814	3.472	0.467	0.841	0.719	0.748	5.421	0.37	0.849	0.715	0.622
1.584	0.513	0.819	0.719	0.812	3.533	0.466	0.849	0.718	0.744	5.482	0.366	0.844	0.716	0.619
1.645	0.511	0.814	0.718	0.81	3.594	0.463	0.843	0.718	0.742	5.543	0.363	0.829	0.71	0.622
1.706	0.509	0.817	0.719	0.807	3.655	0.461	0.853	0.718	0.737	5.604	0.36	0.835	0.717	0.616
1.766	0.509	0.827	0.719	0.805	3.716	0.459	0.855	0.719	0.733	5.665	0.355	0.826	0.717	0.614
1.827	0.509	0.825	0.718	0.805	3.777	0.455	0.854	0.718	0.728	5.726	0.349	0.834	0.716	0.602
1.888	0.509	0.82	0.718	0.806	3.838	0.45	0.853	0.718	0.723	5.787	0.343	0.829	0.715	0.598

Table B.1. (Continue).

x/d	η	HTCR	Fn	NHFR	x/d	η	HTCR	Fn	NHFR	x/d	η	HTCR	Fn	NHFR
5.848	0.337	0.83	0.716	0.59	7.797	0.273	0.863	0.719	0.49	9.746	0.223	0.87	0.719	0.421
5.909	0.333	0.82	0.711	0.59	7.858	0.27	0.872	0.722	0.481	9.807	0.221	0.863	0.719	0.423
5.97	0.332	0.82	0.716	0.588	7.919	0.266	0.877	0.722	0.473	9.868	0.22	0.868	0.721	0.418
6.03	0.328	0.826	0.716	0.581	7.98	0.27	0.875	0.719	0.479	9.929	0.216	0.869	0.726	0.412
6.091	0.325	0.816	0.716	0.582	8.041	0.267	0.874	0.72	0.475	9.99	0.215	0.866	0.721	0.414
6.152	0.32	0.824	0.716	0.571	8.102	0.266	0.877	0.719	0.473	10.05	0.216	0.864	0.718	0.416
6.213	0.318	0.832	0.716	0.565	8.162	0.262	0.87	0.72	0.472	10.11	0.218	0.873	0.718	0.412
6.274	0.315	0.839	0.715	0.558	8.223	0.256	0.852	0.718	0.475	10.17	0.215	0.872	0.719	0.41
6.335	0.313	0.843	0.717	0.553	8.284	0.255	0.856	0.718	0.471	10.23	0.216	0.88	0.718	0.405
6.396	0.312	0.846	0.714	0.55	8.345	0.255	0.868	0.72	0.464	10.29	0.212	0.874	0.718	0.404
6.457	0.31	0.847	0.714	0.546	8.406	0.252	0.866	0.719	0.462	10.36	0.215	0.875	0.719	0.407
6.518	0.305	0.847	0.717	0.54	8.467	0.25	0.866	0.72	0.46	10.42	0.22	0.873	0.718	0.415
6.579	0.302	0.847	0.715	0.536	8.528	0.255	0.868	0.719	0.464	10.48	0.222	0.88	0.72	0.413
6.64	0.299	0.847	0.716	0.532	8.589	0.25	0.87	0.718	0.456	10.54	0.215	0.874	0.719	0.409
6.701	0.299	0.85	0.717	0.531	8.65	0.247	0.88	0.72	0.446	10.6	0.211	0.874	0.716	0.403
6.761	0.298	0.855	0.718	0.527	8.711	0.246	0.868	0.72	0.452	10.66	0.214	0.879	0.72	0.403
6.822	0.293	0.863	0.717	0.517	8.772	0.243	0.875	0.722	0.444	10.72	0.216	0.866	0.717	0.414
6.883	0.29	0.853	0.713	0.518	8.832	0.241	0.869	0.719	0.445	10.78	0.217	0.877	0.72	0.408
6.944	0.29	0.86	0.712	0.515	8.893	0.239	0.882	0.724	0.434	10.84	0.215	0.875	0.715	0.407
7.005	0.285	0.868	0.719	0.503	8.954	0.236	0.876	0.72	0.434	10.9	0.213	0.874	0.718	0.405
7.066	0.287	0.862	0.717	0.509	9.015	0.234	0.875	0.72	0.433	10.96	0.21	0.883	0.719	0.395
7.127	0.285	0.872	0.717	0.501	9.076	0.234	0.879	0.721	0.429	11.03	0.201	0.877	0.72	0.388
7.188	0.284	0.877	0.717	0.497	9.137	0.234	0.879	0.727	0.43	11.09	0.206	0.884	0.722	0.39
7.249	0.285	0.888	0.718	0.492	9.198	0.234	0.87	0.719	0.436	11.15	0.206	0.888	0.722	0.387
7.31	0.282	0.877	0.717	0.495	9.259	0.234	0.88	0.718	0.429	11.21	0.202	0.881	0.717	0.386
7.371	0.284	0.887	0.717	0.491	9.32	0.232	0.877	0.719	0.428	11.27	0.201	0.882	0.717	0.383
7.431	0.279	0.883	0.718	0.486	9.381	0.226	0.875	0.725	0.422	11.33	0.201	0.867	0.712	0.394
7.492	0.278	0.867	0.718	0.495	9.442	0.228	0.884	0.719	0.418	11.39	0.197	0.882	0.718	0.378
7.553	0.275	0.861	0.717	0.494	9.503	0.228	0.885	0.72	0.418	11.45	0.193	0.883	0.718	0.373
7.614	0.277	0.86	0.72	0.498	9.563	0.227	0.884	0.719	0.417	11.51	0.198	0.881	0.714	0.381
7.675	0.275	0.859	0.721	0.495	9.624	0.223	0.878	0.721	0.416	11.57	0.199	0.893	0.715	0.373
7.736	0.275	0.866	0.72	0.491	9.685	0.224	0.875	0.722	0.419	11.63	0.193	0.88	0.717	0.375

Table B.2. Centerline downstream cooling data of circular film hole Br = 1.0.

x/d	η	HTCR	Fn	NHFR	x/d	η	HTCR	Fn	NHFR	x/d	η	HTCR	Fn	NHFR
0	0.193	0.608	0.74	0.569	2.01	0.303	0.82	0.734	0.552	4.02	0.243	0.847	0.731	0.461
0.061	0.202	0.591	0.739	0.588	2.071	0.302	0.827	0.733	0.548	4.081	0.243	0.842	0.73	0.465
0.122	0.207	0.616	0.74	0.576	2.132	0.3	0.837	0.733	0.541	4.142	0.239	0.851	0.731	0.455
0.183	0.219	0.693	0.732	0.535	2.193	0.298	0.844	0.738	0.534	4.203	0.238	0.858	0.734	0.448
0.244	0.227	0.756	0.738	0.502	2.254	0.297	0.833	0.734	0.538	4.264	0.237	0.854	0.729	0.45
0.305	0.239	0.755	0.733	0.516	2.315	0.296	0.843	0.734	0.531	4.325	0.236	0.851	0.736	0.45
0.365	0.248	0.768	0.729	0.518	2.376	0.295	0.833	0.735	0.536	4.386	0.234	0.847	0.73	0.45
0.426	0.255	0.769	0.731	0.525	2.437	0.291	0.849	0.738	0.522	4.447	0.233	0.86	0.737	0.441
0.487	0.262	0.786	0.736	0.523	2.497	0.289	0.839	0.733	0.524	4.508	0.232	0.857	0.727	0.442
0.548	0.268	0.795	0.736	0.525	2.558	0.285	0.839	0.733	0.52	4.569	0.229	0.843	0.727	0.446
0.609	0.276	0.786	0.74	0.539	2.619	0.285	0.838	0.738	0.52	4.629	0.228	0.854	0.733	0.437
0.67	0.283	0.787	0.737	0.546	2.68	0.284	0.838	0.731	0.519	4.69	0.225	0.84	0.726	0.444
0.731	0.286	0.786	0.737	0.551	2.741	0.284	0.851	0.737	0.512	4.751	0.222	0.86	0.738	0.426
0.792	0.29	0.791	0.745	0.553	2.802	0.283	0.853	0.741	0.509	4.812	0.219	0.871	0.731	0.414
0.853	0.293	0.799	0.743	0.552	2.863	0.282	0.846	0.736	0.512	4.873	0.218	0.866	0.734	0.417
0.914	0.297	0.792	0.733	0.561	2.924	0.28	0.836	0.735	0.515	4.934	0.217	0.858	0.73	0.421
0.975	0.299	0.799	0.74	0.559	2.985	0.277	0.848	0.732	0.505	4.995	0.218	0.849	0.732	0.429
1.036	0.3	0.813	0.741	0.553	3.046	0.276	0.846	0.735	0.504	5.056	0.216	0.856	0.735	0.421
1.096	0.301	0.807	0.739	0.557	3.107	0.274	0.834	0.731	0.508	5.117	0.216	0.858	0.728	0.419
1.157	0.304	0.818	0.742	0.555	3.168	0.273	0.84	0.732	0.504	5.178	0.216	0.859	0.734	0.419
1.218	0.306	0.812	0.737	0.56	3.228	0.27	0.847	0.734	0.496	5.239	0.213	0.848	0.732	0.422
1.279	0.305	0.819	0.743	0.555	3.289	0.269	0.833	0.73	0.503	5.299	0.212	0.85	0.733	0.421
1.34	0.304	0.819	0.739	0.555	3.35	0.267	0.84	0.735	0.497	5.36	0.212	0.855	0.729	0.417
1.401	0.306	0.821	0.742	0.556	3.411	0.264	0.846	0.734	0.488	5.421	0.212	0.861	0.737	0.413
1.462	0.307	0.816	0.734	0.56	3.472	0.265	0.84	0.731	0.493	5.482	0.213	0.858	0.74	0.417
1.523	0.305	0.828	0.745	0.551	3.533	0.264	0.852	0.734	0.485	5.543	0.211	0.844	0.735	0.424
1.584	0.305	0.837	0.748	0.546	3.594	0.262	0.843	0.73	0.488	5.604	0.21	0.845	0.737	0.422
1.645	0.307	0.816	0.733	0.56	3.655	0.26	0.858	0.735	0.477	5.665	0.21	0.824	0.727	0.435
1.706	0.306	0.836	0.748	0.548	3.716	0.258	0.852	0.728	0.478	5.726	0.209	0.83	0.725	0.43
1.766	0.306	0.841	0.744	0.545	3.777	0.256	0.853	0.73	0.475	5.787	0.208	0.836	0.734	0.424
1.827	0.306	0.843	0.746	0.545	3.838	0.25	0.858	0.735	0.464	5.848	0.206	0.839	0.736	0.42
1.888	0.306	0.825	0.734	0.554	3.898	0.247	0.854	0.733	0.462	5.909	0.204	0.83	0.732	0.424
1.949	0.304	0.829	0.746	0.549	3.959	0.243	0.853	0.731	0.458	5.97	0.205	0.816	0.724	0.435

Table B.2. (Continue).

x/d	η	HTCR	Fn	NHFR	x/d	η	HTCR	Fn	NHFR	x/d	η	HTCR	Fn	NHFR
6.03	0.203	0.821	0.725	0.428	8.041	0.156	0.92	0.771	0.295	10.05	0.15	0.886	0.75	0.313
6.091	0.199	0.829	0.74	0.419	8.102	0.16	0.883	0.736	0.329	10.11	0.151	0.894	0.748	0.308
6.152	0.197	0.84	0.742	0.408	8.162	0.158	0.896	0.754	0.317	10.17	0.151	0.897	0.753	0.305
6.213	0.196	0.845	0.741	0.403	8.223	0.159	0.882	0.755	0.329	10.23	0.152	0.919	0.763	0.29
6.274	0.193	0.84	0.729	0.404	8.284	0.156	0.922	0.787	0.294	10.29	0.153	0.907	0.757	0.301
6.335	0.191	0.843	0.729	0.398	8.345	0.155	0.918	0.775	0.296	10.36	0.157	0.89	0.744	0.319
6.396	0.192	0.862	0.74	0.386	8.406	0.155	0.9	0.76	0.309	10.42	0.155	0.897	0.751	0.311
6.457	0.189	0.845	0.725	0.395	8.467	0.152	0.89	0.753	0.313	10.48	0.154	0.911	0.757	0.3
6.518	0.186	0.849	0.731	0.388	8.528	0.154	0.884	0.745	0.32	10.54	0.154	0.9	0.753	0.308
6.579	0.184	0.864	0.742	0.375	8.589	0.153	0.915	0.769	0.295	10.6	0.153	0.905	0.755	0.303
6.64	0.184	0.867	0.745	0.372	8.65	0.152	0.916	0.762	0.293	10.66	0.154	0.898	0.748	0.309
6.701	0.181	0.871	0.747	0.366	8.711	0.151	0.917	0.773	0.291	10.72	0.154	0.895	0.754	0.313
6.761	0.18	0.878	0.75	0.359	8.772	0.152	0.879	0.738	0.321	10.78	0.156	0.925	0.774	0.291
6.822	0.176	0.874	0.739	0.357	8.832	0.151	0.921	0.775	0.288	10.84	0.155	0.936	0.778	0.281
6.883	0.176	0.883	0.751	0.35	8.893	0.15	0.893	0.746	0.308	10.9	0.155	0.922	0.77	0.292
6.944	0.175	0.884	0.744	0.349	8.954	0.149	0.943	0.788	0.268	10.96	0.155	0.917	0.76	0.295
7.005	0.176	0.877	0.738	0.354	9.015	0.149	0.888	0.743	0.311	11.03	0.154	0.92	0.768	0.293
7.066	0.173	0.878	0.743	0.35	9.076	0.149	0.937	0.781	0.272	11.09	0.159	0.911	0.758	0.306
7.127	0.172	0.88	0.736	0.347	9.137	0.15	0.918	0.771	0.289	11.15	0.154	0.932	0.77	0.284
7.188	0.172	0.909	0.756	0.326	9.198	0.147	0.929	0.781	0.276	11.21	0.159	0.935	0.774	0.288
7.249	0.17	0.912	0.75	0.321	9.259	0.148	0.946	0.786	0.264	11.27	0.163	0.958	0.792	0.277
7.31	0.165	0.921	0.766	0.307	9.32	0.148	0.94	0.784	0.268	11.33	0.163	0.916	0.766	0.308
7.371	0.166	0.899	0.74	0.324	9.381	0.149	0.907	0.765	0.295	11.39	0.151	0.913	0.756	0.294
7.431	0.162	0.914	0.756	0.309	9.442	0.152	0.889	0.735	0.313	11.45	0.147	0.907	0.751	0.293
7.492	0.163	0.9	0.759	0.32	9.503	0.15	0.951	0.786	0.263	11.51	0.148	0.922	0.761	0.283
7.553	0.161	0.91	0.771	0.309	9.563	0.148	0.929	0.768	0.277	11.57	0.148	0.947	0.771	0.262
7.614	0.163	0.862	0.735	0.348	9.624	0.148	0.93	0.777	0.277	11.63	0.149	0.913	0.757	0.291
7.675	0.162	0.891	0.761	0.325	9.685	0.149	0.871	0.731	0.323	11.7	0.146	0.923	0.757	0.278
7.736	0.161	0.887	0.751	0.327	9.746	0.147	0.921	0.774	0.282	11.76	0.144	0.928	0.766	0.272
7.797	0.16	0.903	0.764	0.313	9.807	0.148	0.938	0.795	0.269	11.82	0.139	0.952	0.768	0.247
7.858	0.161	0.886	0.746	0.329	9.868	0.151	0.877	0.741	0.322	11.88	0.133	0.907	0.736	0.274
7.919	0.16	0.905	0.758	0.312	9.929	0.151	0.927	0.788	0.284	11.94	0.136	0.967	0.77	0.23
7.98	0.158	0.922	0.77	0.296	9.99	0.151	0.884	0.749	0.316					

Table B.3. Laterally average downstream cooling data of circular film hole.

Br = 0.5					Br = 1.0				
x/d	η	HTCR	Fn	NHFR	x/d	η	HTCR	Fn	NHFR
1	0.222	0.893	0.825	0.404	1	0.092	0.807	0.758	0.305
2	0.217	0.898	0.804	0.394	2	0.097	0.775	0.706	0.338
3	0.196	0.913	0.788	0.356	3	0.088	0.748	0.657	0.351
4	0.173	0.919	0.777	0.319	4	0.082	0.739	0.636	0.352
5	0.152	0.925	0.791	0.286	5	0.075	0.785	0.684	0.302
6	0.128	0.914	0.812	0.262	6	0.074	0.744	0.672	0.338
7	0.116	0.938	0.794	0.225	7	0.068	0.773	0.665	0.306
8	0.105	0.94	0.779	0.208	8	0.064	0.776	0.654	0.299
9	0.085	0.948	0.777	0.173	9	0.057	0.76	0.633	0.306
10	0.083	0.948	0.775	0.17	10	0.056	0.825	0.686	0.244
11	0.069	0.955	0.78	0.144	11	0.059	0.842	0.7	0.232

Table B.4. Centerline downstream cooling data of Louver scheme Br = 0.5.

x/d	η	HTCR	Fn	NHFR	x/d	η	HTCR	Fn	NHFR
0	1	0.888	0.867	1.444	2.56	0.69	0.94	0.875	1.033
0.08	1	0.85	0.88	1.425	2.64	0.686	0.931	0.866	1.027
0.16	1	0.854	0.877	1.427	2.72	0.679	0.898	0.864	1.017
0.24	1	0.825	0.864	1.413	2.8	0.66	0.913	0.88	0.991
0.32	1	0.799	0.839	1.399	2.88	0.655	0.859	0.871	0.985
0.4	1	0.839	0.874	1.42	2.96	0.648	0.848	0.878	0.976
0.48	1	0.846	0.876	1.423	3.04	0.626	0.853	0.877	0.948
0.56	0.999	0.845	0.86	1.422	3.12	0.613	0.871	0.873	0.93
0.64	1	0.853	0.861	1.426	3.2	0.607	0.845	0.871	0.924
0.72	1	0.854	0.857	1.427	3.28	0.597	0.881	0.877	0.908
0.8	0.979	0.875	0.869	1.409	3.36	0.587	0.881	0.877	0.894
0.88	0.975	0.861	0.871	1.398	3.44	0.584	0.889	0.875	0.89
0.96	0.961	0.842	0.857	1.372	3.52	0.578	0.891	0.875	0.881
1.04	0.941	0.864	0.864	1.355	3.6	0.566	0.877	0.878	0.867
1.12	0.926	0.88	0.868	1.343	3.68	0.562	0.865	0.879	0.864
1.2	0.918	0.866	0.852	1.326	3.76	0.556	0.898	0.88	0.851
1.28	0.902	0.873	0.871	1.308	3.84	0.551	0.908	0.88	0.843
1.36	0.887	0.823	0.833	1.272	3.92	0.545	0.914	0.881	0.834
1.44	0.871	0.883	0.878	1.271	4	0.541	0.928	0.881	0.824
1.52	0.854	0.875	0.875	1.246	4.08	0.537	0.933	0.881	0.819
1.6	0.848	0.904	0.876	1.245	4.16	0.537	0.941	0.878	0.817
1.68	0.84	0.881	0.86	1.229	4.24	0.533	0.934	0.879	0.813
1.76	0.825	0.893	0.876	1.213	4.32	0.528	0.938	0.881	0.804
1.84	0.808	0.877	0.875	1.186	4.4	0.525	0.947	0.88	0.799
1.92	0.796	0.881	0.871	1.171	4.48	0.519	0.954	0.881	0.788
2	0.789	0.9	0.86	1.165	4.56	0.514	0.948	0.881	0.783
2.08	0.773	0.906	0.86	1.145	4.64	0.51	0.95	0.881	0.777
2.16	0.758	0.927	0.876	1.127	4.72	0.506	0.955	0.881	0.769
2.24	0.748	0.938	0.875	1.115	4.8	0.503	0.955	0.88	0.766
2.32	0.736	0.946	0.879	1.099	4.88	0.501	0.958	0.881	0.761
2.4	0.72	0.928	0.858	1.074	4.96	0.501	0.961	0.881	0.762
2.48	0.7	0.939	0.865	1.047	5.04	0.494	0.959	0.881	0.752

Table B.4. (Continue).

x/d	η	HTCR	Fn	NHFR	x/d	η	HTCR	Fn	NHFR
5.12	0.493	0.968	0.881	0.747	7.68	0.373	0.948	0.884	0.583
5.2	0.484	0.961	0.88	0.737	7.76	0.376	0.962	0.881	0.581
5.28	0.482	0.951	0.88	0.737	7.84	0.379	0.975	0.884	0.579
5.36	0.479	0.956	0.88	0.731	7.92	0.374	0.968	0.883	0.576
5.44	0.476	0.954	0.88	0.726	8	0.375	0.967	0.882	0.577
5.52	0.471	0.947	0.88	0.723	8.08	0.374	0.969	0.882	0.574
5.6	0.468	0.946	0.879	0.718	8.16	0.379	0.968	0.88	0.582
5.68	0.465	0.942	0.879	0.715	8.24	0.381	0.974	0.88	0.582
5.76	0.459	0.937	0.88	0.708	8.32	0.378	0.976	0.881	0.578
5.84	0.457	0.942	0.879	0.704	8.4	0.38	0.987	0.882	0.576
5.92	0.456	0.951	0.879	0.699	8.48	0.377	0.982	0.873	0.573
6	0.451	0.946	0.877	0.694	8.56	0.373	0.977	0.88	0.57
6.08	0.443	0.953	0.881	0.68	8.64	0.371	0.972	0.874	0.569
6.16	0.438	0.949	0.879	0.675	8.72	0.373	0.969	0.875	0.573
6.24	0.433	0.948	0.876	0.668	8.8	0.376	0.982	0.875	0.572
6.32	0.429	0.947	0.881	0.663	8.88	0.376	0.987	0.878	0.569
6.4	0.422	0.95	0.881	0.652	8.96	0.373	0.974	0.865	0.572
6.48	0.417	0.956	0.88	0.642	9.04	0.374	0.986	0.881	0.567
6.56	0.415	0.96	0.881	0.638	9.12	0.364	0.976	0.881	0.556
6.64	0.413	0.959	0.866	0.634	9.2	0.366	0.986	0.873	0.555
6.72	0.406	0.967	0.88	0.623	9.28	0.364	0.981	0.878	0.554
6.8	0.405	0.968	0.872	0.62	9.36	0.362	0.985	0.881	0.55
6.88	0.399	0.958	0.876	0.615	9.44	0.355	0.984	0.879	0.54
6.96	0.397	0.969	0.881	0.608	9.52	0.357	0.99	0.876	0.54
7.04	0.393	0.974	0.878	0.6					
7.12	0.388	0.97	0.881	0.595					
7.2	0.386	0.943	0.88	0.603					
7.28	0.385	0.964	0.881	0.593					
7.36	0.384	0.978	0.881	0.586					
7.44	0.381	0.969	0.884	0.585					
7.52	0.378	0.952	0.882	0.587					
7.6	0.372	0.96	0.881	0.575					

Table B.5. Centerline downstream cooling data of Louver scheme Br = 1.0.

x/d	η	HTCR	Fn	NHFR	x/d	η	HTCR	Fn	NHFR	x/d	η	HTCR	Fn	NHFR
0	0.834	0.91	0.985	1.228	2.72	0.907	0.919	0.981	1.331	5.44	0.81	0.956	0.978	1.206
0.08	0.829	0.863	0.993	1.21	2.8	0.904	0.919	0.984	1.327	5.52	0.804	0.949	0.979	1.196
0.16	0.866	0.87	0.992	1.26	2.88	0.899	0.869	0.978	1.303	5.6	0.799	0.948	0.978	1.188
0.24	0.951	0.851	0.989	1.363	2.96	0.897	0.852	0.978	1.294	5.68	0.797	0.937	0.97	1.183
0.32	0.945	0.84	0.979	1.35	3.04	0.893	0.858	0.979	1.291	5.76	0.794	0.934	0.974	1.179
0.4	0.95	0.853	0.986	1.362	3.12	0.89	0.88	0.979	1.295	5.84	0.793	0.939	0.973	1.178
0.48	0.866	0.855	0.982	1.256	3.2	0.889	0.856	0.979	1.286	5.92	0.788	0.945	0.971	1.171
0.56	0.942	0.872	0.986	1.36	3.28	0.885	0.881	0.973	1.289	6	0.785	0.95	0.978	1.169
0.64	0.943	0.876	0.983	1.363	3.36	0.881	0.89	0.984	1.286	6.08	0.78	0.952	0.976	1.162
0.72	0.934	0.898	1	1.36	3.44	0.877	0.898	0.982	1.284	6.16	0.785	0.951	0.978	1.168
0.8	0.934	0.888	0.98	1.356	3.52	0.876	0.893	0.974	1.281	6.24	0.778	0.953	0.977	1.159
0.88	0.951	0.872	0.98	1.372	3.6	0.871	0.881	0.98	1.27	6.32	0.77	0.946	0.977	1.147
0.96	0.95	0.872	0.984	1.371	3.68	0.867	0.871	0.983	1.262	6.4	0.77	0.946	0.974	1.146
1.04	0.948	0.884	0.981	1.372	3.76	0.865	0.904	0.984	1.269	6.48	0.759	0.956	0.978	1.132
1.12	0.946	0.894	0.979	1.375	3.84	0.862	0.909	0.978	1.267	6.56	0.76	0.956	0.974	1.134
1.2	0.943	0.903	0.986	1.375	3.92	0.858	0.916	0.979	1.263	6.64	0.761	0.97	0.972	1.137
1.28	0.941	0.889	0.984	1.366	4	0.855	0.924	0.973	1.261	6.72	0.756	0.967	0.977	1.129
1.36	0.94	0.877	0.985	1.36	4.08	0.853	0.937	0.982	1.262	6.8	0.753	0.977	0.977	1.126
1.44	0.94	0.894	0.987	1.367	4.16	0.852	0.944	0.978	1.262	6.88	0.757	0.962	0.976	1.13
1.52	0.934	0.882	0.978	1.353	4.24	0.849	0.936	0.978	1.257	6.96	0.75	0.968	0.976	1.121
1.6	0.929	0.912	0.981	1.359	4.32	0.848	0.942	0.981	1.256	7.04	0.744	0.976	0.978	1.113
1.68	0.933	0.91	0.986	1.364	4.4	0.845	0.947	0.976	1.253	7.12	0.742	0.969	0.977	1.11
1.76	0.929	0.906	0.986	1.356	4.48	0.84	0.956	0.979	1.248	7.2	0.746	0.942	0.976	1.112
1.84	0.923	0.886	0.981	1.341	4.56	0.838	0.949	0.978	1.244	7.28	0.737	0.964	0.978	1.101
1.92	0.924	0.894	0.981	1.345	4.64	0.835	0.953	0.981	1.241	7.36	0.744	0.975	0.975	1.113
2	0.927	0.925	0.981	1.362	4.72	0.832	0.955	0.977	1.237	7.44	0.738	0.956	0.968	1.103
2.08	0.926	0.932	0.982	1.362	4.8	0.832	0.957	0.979	1.237	7.52	0.736	0.951	0.978	1.099
2.16	0.923	0.935	0.981	1.36	4.88	0.829	0.959	0.978	1.233	7.6	0.734	0.958	0.976	1.097
2.24	0.921	0.946	0.978	1.361	4.96	0.827	0.96	0.977	1.231	7.68	0.733	0.943	0.976	1.094
2.32	0.918	0.952	0.982	1.359	5.04	0.82	0.958	0.976	1.22	7.76	0.727	0.962	0.978	1.087
2.4	0.916	0.949	0.975	1.355	5.12	0.818	0.969	0.979	1.22	7.84	0.722	0.968	0.975	1.081
2.48	0.913	0.958	0.981	1.355	5.2	0.812	0.963	0.979	1.21	7.92	0.718	0.966	0.978	1.074
2.56	0.911	0.949	0.98	1.348	5.28	0.809	0.952	0.979	1.203	8	0.713	0.966	0.978	1.067
2.64	0.909	0.947	0.978	1.344	5.36	0.812	0.957	0.978	1.209	8.08	0.708	0.966	0.976	1.06

Table B.5. (Continue).

x/d	η	HTCR	Fn	NHFR	x/d	η	HTCR	Fn	NHFR	x/d	η	HTCR	Fn	NHFR
8.16	0.708	0.966	0.975	1.06	10.88	0.583	1.006	0.977	0.873	13.6	0.424	1.037	0.98	0.622
8.24	0.702	0.967	0.97	1.051	10.96	0.578	1.008	0.977	0.865	13.68	0.423	1.028	0.977	0.624
8.32	0.7	0.972	0.974	1.049	11.04	0.578	1.005	0.977	0.866	13.76	0.42	1.048	0.982	0.612
8.4	0.697	0.986	0.977	1.045	11.12	0.57	1.001	0.974	0.854	13.84	0.424	1.048	0.978	0.618
8.48	0.694	0.991	0.978	1.04	11.2	0.561	1.012	0.978	0.84	13.92	0.422	1.051	0.981	0.614
8.56	0.686	0.976	0.977	1.028	11.28	0.561	1.012	0.977	0.84	14	0.414	1.053	0.982	0.601
8.64	0.683	0.976	0.974	1.024	11.36	0.559	1.016	0.977	0.835	14.08	0.411	1.064	0.988	0.592
8.72	0.686	0.973	0.975	1.028	11.44	0.548	1.022	0.976	0.817	14.16	0.409	1.065	0.99	0.588
8.8	0.681	0.987	0.977	1.021	11.52	0.545	1.02	0.976	0.814	14.24	0.407	1.054	0.982	0.589
8.88	0.67	0.989	0.976	1.005	11.6	0.536	1.011	0.978	0.802	14.32	0.407	1.068	0.991	0.583
8.96	0.673	0.99	0.976	1.009	11.68	0.534	1.024	0.977	0.797	14.4	0.402	1.075	0.996	0.573
9.04	0.664	0.984	0.976	0.997	11.76	0.525	1.015	0.977	0.785	14.48	0.401	1.081	0.988	0.569
9.12	0.659	0.976	0.977	0.988	11.84	0.523	1.014	0.977	0.782	14.56	0.404	1.078	0.983	0.575
9.2	0.664	0.993	0.976	0.996	11.92	0.521	1.021	0.978	0.776	14.64	0.402	1.088	0.998	0.568
9.28	0.66	0.974	0.968	0.99	12	0.516	1.029	0.978	0.767	14.72	0.39	1.095	1.007	0.546
9.36	0.652	0.979	0.971	0.979	12.08	0.506	1.026	0.978	0.753	14.8	0.394	1.111	1.003	0.546
9.44	0.65	0.981	0.972	0.975	12.16	0.502	1.021	0.978	0.747	14.88	0.39	1.066	0.977	0.558
9.52	0.649	0.995	0.977	0.974	12.24	0.495	1.031	0.978	0.734	14.96	0.385	1.105	1.012	0.533
9.6	0.649	0.954	0.965	0.974	12.32	0.489	1.04	0.978	0.723	15.04	0.393	1.105	1.008	0.546
9.68	0.646	0.971	0.976	0.97	12.4	0.483	1.046	0.977	0.711	15.12	0.387	1.08	0.978	0.546
9.76	0.642	0.98	0.976	0.963	12.48	0.478	1.042	0.978	0.705	15.2	0.387	1.119	1.014	0.531
9.84	0.637	0.965	0.972	0.957	12.56	0.478	1.044	0.978	0.705	15.28	0.385	1.132	1.017	0.522
9.92	0.637	0.964	0.977	0.957	12.64	0.468	1.031	0.978	0.693	15.36	0.382	1.132	1.018	0.516
10	0.634	0.973	0.973	0.952	12.72	0.467	1.033	0.978	0.691	15.44	0.386	1.158	1.022	0.513
10.08	0.626	0.98	0.976	0.941	12.8	0.464	1.04	0.977	0.683	15.52	0.386	1.216	1.058	0.487
10.16	0.625	0.974	0.978	0.939	12.88	0.462	1.037	0.978	0.681	15.6	0.389	1.215	1.054	0.494
10.24	0.621	0.99	0.977	0.932	12.96	0.458	1.022	0.978	0.679	15.68	0.387	1.202	1.059	0.497
10.32	0.61	0.995	0.976	0.915	13.04	0.453	1.023	0.976	0.672	15.76	0.385	1.244	1.059	0.475
10.4	0.615	0.996	0.976	0.922	13.12	0.453	1.022	0.977	0.673	15.84	0.398	1.307	1.082	0.473
10.48	0.608	1.013	0.973	0.911	13.2	0.45	1.015	0.977	0.67					
10.56	0.599	1.02	0.973	0.896	13.28	0.445	1.024	0.977	0.66					
10.64	0.592	1.019	0.977	0.886	13.36	0.438	1.03	0.978	0.646					
10.72	0.583	1.011	0.974	0.874	13.44	0.433	1.025	0.978	0.64					
10.8	0.583	0.996	0.976	0.874	13.52	0.43	1.034	0.979	0.633					

Table B.6. Centerline downstream cooling data of Louver scheme Br = 1.5.

x/d	η	HTCR	Fn	NHFR	x/d	η	HTCR	Fn	NHFR	x/d	η	HTCR	Fn	NHFR
0	0.731	0.928	0.905	1.09	2.72	0.96	0.937	0.901	1.412	5.44	0.896	0.964	0.889	1.332
0.08	0.728	0.856	0.886	1.079	2.8	0.955	0.925	0.891	1.399	5.52	0.893	0.953	0.885	1.323
0.16	0.756	0.878	0.902	1.118	2.88	0.955	0.889	0.901	1.384	5.6	0.89	0.952	0.885	1.32
0.24	0.827	0.895	0.937	1.215	2.96	0.953	0.857	0.887	1.368	5.68	0.89	0.946	0.882	1.317
0.32	0.814	0.857	0.9	1.19	3.04	0.952	0.875	0.899	1.374	5.76	0.89	0.943	0.886	1.316
0.4	0.874	0.884	0.92	1.275	3.12	0.948	0.889	0.891	1.375	5.84	0.886	0.954	0.89	1.314
0.48	0.839	0.854	0.884	1.221	3.2	0.944	0.879	0.906	1.366	5.92	0.88	0.959	0.887	1.307
0.56	0.967	0.871	0.886	1.392	3.28	0.945	0.894	0.889	1.373	6	0.882	0.952	0.882	1.308
0.64	0.967	0.891	0.9	1.402	3.36	0.936	0.89	0.886	1.36	6.08	0.878	0.959	0.886	1.303
0.72	0.966	0.882	0.884	1.396	3.44	0.94	0.904	0.89	1.37	6.16	0.884	0.954	0.884	1.31
0.8	0.966	0.91	0.903	1.409	3.52	0.938	0.907	0.891	1.369	6.24	0.88	0.958	0.885	1.307
0.88	0.984	0.882	0.892	1.42	3.6	0.936	0.886	0.888	1.358	6.32	0.877	0.949	0.883	1.3
0.96	0.985	0.891	0.906	1.425	3.68	0.932	0.873	0.887	1.348	6.4	0.877	0.951	0.882	1.299
1.04	0.985	0.901	0.901	1.43	3.76	0.932	0.905	0.887	1.361	6.48	0.87	0.963	0.887	1.293
1.12	0.981	0.899	0.887	1.424	3.84	0.929	0.91	0.882	1.358	6.56	0.869	0.963	0.883	1.292
1.2	0.979	0.905	0.89	1.424	3.92	0.926	0.924	0.89	1.36	6.64	0.871	0.977	0.882	1.299
1.28	0.976	0.897	0.894	1.417	4	0.924	0.932	0.884	1.36	6.72	0.867	0.978	0.89	1.293
1.36	0.972	0.887	0.897	1.407	4.08	0.924	0.947	0.893	1.366	6.8	0.866	0.983	0.885	1.294
1.44	0.978	0.899	0.894	1.42	4.16	0.922	0.963	0.899	1.368	6.88	0.869	0.966	0.883	1.293
1.52	0.973	0.892	0.891	1.41	4.24	0.921	0.945	0.889	1.36	6.96	0.863	0.975	0.885	1.287
1.6	0.967	0.922	0.893	1.415	4.32	0.922	0.951	0.892	1.364	7.04	0.855	0.979	0.883	1.277
1.68	0.976	0.918	0.896	1.427	4.4	0.917	0.952	0.884	1.358	7.12	0.86	0.977	0.887	1.284
1.76	0.964	0.912	0.894	1.407	4.48	0.916	0.956	0.882	1.358	7.2	0.86	0.949	0.885	1.275
1.84	0.957	0.898	0.895	1.391	4.56	0.916	0.952	0.884	1.356	7.28	0.855	0.971	0.887	1.275
1.92	0.967	0.896	0.885	1.403	4.64	0.911	0.964	0.894	1.354	7.36	0.859	0.981	0.884	1.284
2	0.969	0.938	0.895	1.426	4.72	0.912	0.962	0.887	1.353	7.44	0.854	0.967	0.882	1.272
2.08	0.969	0.944	0.895	1.427	4.8	0.91	0.96	0.885	1.35	7.52	0.854	0.952	0.882	1.268
2.16	0.964	0.944	0.891	1.421	4.88	0.908	0.969	0.89	1.351	7.6	0.852	0.967	0.887	1.269
2.24	0.968	0.956	0.891	1.432	4.96	0.908	0.966	0.886	1.35	7.68	0.854	0.946	0.882	1.266
2.32	0.966	0.964	0.896	1.433	5.04	0.903	0.966	0.886	1.343	7.76	0.848	0.967	0.885	1.264
2.4	0.965	0.96	0.888	1.429	5.12	0.902	0.981	0.892	1.346	7.84	0.847	0.973	0.882	1.263
2.48	0.965	0.965	0.89	1.432	5.2	0.901	0.973	0.891	1.341	7.92	0.845	0.967	0.882	1.258
2.56	0.966	0.961	0.894	1.431	5.28	0.892	0.953	0.882	1.322	8	0.84	0.966	0.881	1.252
2.64	0.96	0.953	0.887	1.42	5.36	0.897	0.959	0.883	1.332	8.08	0.838	0.971	0.884	1.249

Table B.6. (Continue).

x/d	η	HTCR	Fn	NHFR	x/d	η	HTCR	Fn	NHFR	x/d	η	HTCR	Fn	NHFR
8.16	0.837	0.971	0.882	1.249	10.88	0.764	1.006	0.88	1.147	13.6	0.679	1.016	0.864	1.019
8.24	0.836	0.977	0.883	1.247	10.96	0.756	1.004	0.877	1.134	13.68	0.675	1.028	0.88	1.013
8.32	0.834	0.979	0.883	1.246	11.04	0.767	1.006	0.881	1.151	13.76	0.67	1.029	0.869	1.005
8.4	0.832	0.989	0.882	1.245	11.12	0.762	1.002	0.879	1.143	13.84	0.667	1.031	0.866	1
8.48	0.832	0.995	0.884	1.247	11.2	0.754	1.012	0.88	1.132	13.92	0.664	1.032	0.868	0.996
8.56	0.827	0.979	0.882	1.235	11.28	0.755	1.013	0.881	1.135	14	0.663	1.038	0.872	0.994
8.64	0.829	0.98	0.881	1.238	11.36	0.756	1.017	0.881	1.136	14.08	0.657	1.053	0.881	0.984
8.72	0.823	0.983	0.887	1.23	11.44	0.748	1.024	0.881	1.126	14.16	0.653	1.042	0.872	0.979
8.8	0.822	0.988	0.881	1.231	11.52	0.74	1.022	0.881	1.113	14.24	0.648	1.04	0.873	0.971
8.88	0.815	0.992	0.882	1.221	11.6	0.734	1.014	0.883	1.102	14.32	0.654	1.038	0.867	0.981
8.96	0.816	0.992	0.881	1.222	11.68	0.738	1.026	0.882	1.109	14.4	0.647	1.041	0.869	0.969
9.04	0.812	0.986	0.881	1.214	11.76	0.736	1.016	0.881	1.105	14.48	0.644	1.057	0.87	0.965
9.12	0.809	0.974	0.879	1.209	11.84	0.732	1.015	0.881	1.1	14.56	0.634	1.061	0.871	0.948
9.2	0.811	0.999	0.884	1.217	11.92	0.729	1.024	0.883	1.096	14.64	0.635	1.065	0.88	0.95
9.28	0.811	0.986	0.882	1.214	12	0.726	1.029	0.881	1.092	14.72	0.634	1.055	0.874	0.948
9.36	0.809	0.987	0.882	1.21	12.08	0.729	1.023	0.878	1.096	14.8	0.627	1.072	0.872	0.937
9.44	0.809	0.988	0.882	1.211	12.16	0.721	1.021	0.881	1.083	14.88	0.626	1.056	0.872	0.935
9.52	0.806	1	0.885	1.209	12.24	0.718	1.032	0.881	1.08	14.96	0.618	1.059	0.874	0.922
9.6	0.807	0.966	0.88	1.203	12.32	0.712	1.04	0.88	1.07	15.04	0.613	1.065	0.875	0.914
9.68	0.806	0.972	0.88	1.203	12.4	0.708	1.045	0.879	1.065	15.12	0.611	1.074	0.876	0.91
9.76	0.802	0.984	0.882	1.2	12.48	0.713	1.043	0.881	1.072	15.2	0.61	1.073	0.875	0.908
9.84	0.802	0.969	0.879	1.196	12.56	0.702	1.044	0.88	1.056	15.28	0.605	1.083	0.876	0.9
9.92	0.798	0.965	0.881	1.191	12.64	0.702	1.018	0.87	1.054	15.36	0.594	1.082	0.877	0.882
10	0.795	0.976	0.879	1.188	12.72	0.701	1.02	0.87	1.052	15.44	0.595	1.102	0.877	0.881
10.08	0.792	0.987	0.885	1.186	12.8	0.697	1.04	0.881	1.047	15.52	0.594	1.07	0.838	0.883
10.16	0.792	0.968	0.875	1.182	12.88	0.701	1.024	0.869	1.052	15.6	0.593	1.097	0.857	0.878
10.24	0.788	0.991	0.881	1.18	12.96	0.697	1.022	0.881	1.046	15.68	0.592	1.058	0.839	0.882
10.32	0.782	0.999	0.882	1.173	13.04	0.694	1.011	0.869	1.041	15.76	0.592	1.097	0.842	0.876
10.4	0.785	0.997	0.88	1.177	13.12	0.689	1.01	0.87	1.034	15.84	0.533	1.154	0.86	0.768
10.48	0.784	1.013	0.875	1.179	13.2	0.687	1.004	0.87	1.031					
10.56	0.78	1.025	0.881	1.174	13.28	0.684	1.024	0.88	1.026					
10.64	0.775	1.018	0.879	1.166	13.36	0.68	1.03	0.88	1.021					
10.72	0.772	1.015	0.881	1.161	13.44	0.68	1.025	0.88	1.02					
10.8	0.771	0.999	0.881	1.156	13.52	0.679	1.032	0.88	1.018					

Table B.7. Laterally averaged downstream cooling data of Louver scheme.

Br = 0.5					Br = 1.0					Br = 1.5				
x/d	η	HTCR	Fn	NHFR	x/d	η	HTCR	Fn	NHFR	x/d	η	HTCR	Fn	NHFR
1	0.736	0.873	0.875	1.091	1	0.843	0.883	0.982	1.234	1	0.897	0.892	0.894	1.308
2	0.568	0.912	0.883	0.866	2	0.776	0.91	0.979	1.149	2	0.852	0.92	0.891	1.256
3	0.433	0.923	0.895	0.677	3	0.683	0.913	0.984	1.022	3	0.791	0.917	0.889	1.171
4	0.342	0.957	0.908	0.534	4	0.61	0.936	0.986	0.921	4	0.74	0.934	0.886	1.102
5	0.267	0.969	0.908	0.419	5	0.544	0.947	0.985	0.826	5	0.692	0.945	0.885	1.036
6	0.214	0.969	0.914	0.342	6	0.483	0.946	0.99	0.739	6	0.649	0.937	0.884	0.975
7	0.166	0.985	0.893	0.261	7	0.441	0.975	0.982	0.671	7	0.609	0.975	0.884	0.916
8	0.117	0.986	0.898	0.186	8	0.396	0.973	0.983	0.604	8	0.576	0.971	0.884	0.868
9	0.067	0.997	0.889	0.103	9	0.373	0.987	0.978	0.564	9	0.542	0.989	0.882	0.815
					10	0.333	0.991	0.978	0.504	10	0.516	0.993	0.883	0.776
					11	0.301	1.002	0.973	0.45	11	0.487	1.011	0.884	0.728
					12	0.265	1.017	0.972	0.388	12	0.458	1.031	0.887	0.677
					13	0.246	1.034	0.978	0.347	13	0.433	1.06	0.903	0.628
					14	0.219	1.055	0.987	0.291	14	0.409	1.081	0.91	0.582
					15	0.201	1.095	0.986	0.235	15	0.389	1.138	0.923	0.527

Table B.8. Centerline downstream cooling data of Hybrid scheme Br = 0.5.

x/d	η	HTCR	Fn	NHFR	x/d	η	HTCR	Fn	NHFR	x/d	η	HTCR	Fn	NHFR
0	0.956	1.073	0.587	1.466	4.796	0.618	1.094	0.584	0.921	9.591	0.458	1.103	0.611	0.654
0.12	0.94	1.076	0.586	1.44	4.916	0.612	1.085	0.584	0.911	9.711	0.454	1.099	0.61	0.65
0.24	0.859	1.078	0.591	1.31	5.035	0.604	1.093	0.594	0.897	9.831	0.45	1.088	0.605	0.647
0.36	0.706	1.079	0.593	1.063	5.155	0.597	1.098	0.596	0.885	9.951	0.442	1.082	0.604	0.636
0.48	0.739	1.09	0.605	1.119	5.275	0.583	1.09	0.598	0.863	10.07	0.438	1.094	0.609	0.625
0.599	0.786	1.104	0.613	1.198	5.395	0.581	1.098	0.608	0.858	10.19	0.435	1.087	0.608	0.622
0.719	0.833	1.12	0.613	1.279	5.515	0.571	1.094	0.614	0.843	10.31	0.428	1.092	0.617	0.609
0.839	0.861	1.126	0.611	1.327	5.635	0.565	1.084	0.608	0.835	10.43	0.423	1.09	0.604	0.602
0.959	0.873	1.146	0.617	1.355	5.755	0.565	1.08	0.611	0.835	10.55	0.417	1.097	0.606	0.589
1.079	0.883	1.16	0.624	1.377	5.875	0.558	1.09	0.609	0.823	10.67	0.411	1.102	0.614	0.577
1.199	0.895	1.184	0.625	1.405	5.995	0.554	1.091	0.62	0.815	10.79	0.405	1.099	0.609	0.569
1.319	0.89	1.177	0.626	1.395	6.114	0.553	1.083	0.614	0.815	10.91	0.404	1.089	0.599	0.572
1.439	0.875	1.182	0.626	1.369	6.234	0.547	1.079	0.612	0.807	11.03	0.395	1.11	0.614	0.548
1.559	0.876	1.188	0.638	1.374	6.354	0.543	1.078	0.614	0.8	11.15	0.392	1.104	0.603	0.545
1.678	0.868	1.159	0.625	1.35	6.474	0.54	1.084	0.614	0.795	11.27	0.385	1.111	0.604	0.531
1.798	0.867	1.184	0.638	1.356	6.594	0.536	1.091	0.619	0.785	11.39	0.382	1.099	0.594	0.53
1.918	0.855	1.176	0.642	1.332	6.714	0.529	1.076	0.619	0.779	11.51	0.382	1.105	0.604	0.528
2.038	0.836	1.162	0.64	1.295	6.834	0.529	1.063	0.617	0.781	11.63	0.381	1.128	0.615	0.517
2.158	0.825	1.139	0.635	1.27	6.954	0.524	1.056	0.613	0.774	11.75	0.385	1.103	0.609	0.534
2.278	0.81	1.12	0.626	1.24	7.074	0.52	1.058	0.617	0.767	11.87	0.372	1.102	0.612	0.514
2.398	0.798	1.101	0.622	1.217	7.194	0.515	1.06	0.612	0.759	11.99	0.379	1.106	0.617	0.523
2.518	0.788	1.08	0.615	1.197	7.313	0.512	1.076	0.621	0.75	12.11	0.384	1.105	0.614	0.532
2.638	0.785	1.09	0.618	1.194	7.433	0.515	1.088	0.619	0.753	12.23	0.391	1.127	0.62	0.535
2.758	0.773	1.097	0.62	1.175	7.553	0.515	1.104	0.629	0.749	12.35	0.389	1.146	0.624	0.522
2.877	0.763	1.106	0.626	1.16	7.673	0.508	1.103	0.621	0.737	12.47	0.384	1.142	0.614	0.516
2.997	0.754	1.109	0.62	1.145	7.793	0.503	1.103	0.618	0.729	12.59	0.383	1.129	0.612	0.52
3.117	0.739	1.125	0.624	1.122	7.913	0.501	1.096	0.608	0.728	12.71	0.383	1.126	0.613	0.521
3.237	0.722	1.117	0.611	1.094	8.033	0.501	1.101	0.614	0.726	12.83	0.376	1.126	0.615	0.509
3.357	0.72	1.13	0.612	1.091	8.153	0.499	1.08	0.603	0.729	12.95	0.377	1.128	0.622	0.51
3.477	0.711	1.129	0.604	1.075	8.273	0.493	1.069	0.602	0.722	13.07	0.379	1.132	0.621	0.512
3.597	0.698	1.151	0.615	1.054	8.392	0.488	1.066	0.602	0.715	13.19	0.384	1.136	0.619	0.518
3.717	0.686	1.142	0.609	1.032	8.512	0.481	1.069	0.601	0.702	13.31	0.381	1.112	0.603	0.523
3.837	0.676	1.144	0.6	1.017	8.632	0.48	1.066	0.605	0.701	13.43	0.383	1.115	0.601	0.525
3.956	0.663	1.15	0.604	0.994	8.752	0.478	1.071	0.61	0.697	13.55	0.38	1.13	0.606	0.513
4.076	0.666	1.149	0.598	0.998	8.872	0.474	1.067	0.61	0.692	13.67	0.365	1.129	0.61	0.489
4.196	0.653	1.133	0.593	0.977	8.992	0.47	1.07	0.603	0.684	13.79	0.364	1.122	0.608	0.491
4.316	0.641	1.124	0.587	0.957	9.112	0.468	1.075	0.602	0.68	13.91	0.358	1.133	0.618	0.476
4.436	0.636	1.116	0.588	0.948	9.232	0.462	1.086	0.602	0.666	14.03	0.34	1.135	0.612	0.444
4.556	0.631	1.104	0.589	0.941	9.352	0.458	1.095	0.602	0.657					
4.676	0.618	1.101	0.582	0.92	9.471	0.46	1.097	0.598	0.66					

Table B.9. Centerline downstream cooling data of Hybrid scheme Br = 1.0.

x/d	η	HTCR	Fn	NHFR	x/d	η	HTCR	Fn	NHFR	x/d	η	HTCR	Fn	NHFR
0	0.791	1.139	0.623	1.212	4.676	0.759	1.154	0.611	1.16	9.352	0.528	1.093	0.602	0.773
0.12	0.853	1.139	0.622	1.319	4.796	0.759	1.153	0.616	1.16	9.471	0.515	1.106	0.603	0.748
0.24	0.75	1.136	0.623	1.142	4.916	0.746	1.151	0.62	1.138	9.591	0.516	1.102	0.611	0.752
0.36	0.865	1.122	0.617	1.333	5.035	0.734	1.14	0.621	1.115	9.711	0.51	1.088	0.605	0.744
0.48	0.893	1.114	0.619	1.378	5.155	0.739	1.124	0.611	1.123	9.831	0.501	1.085	0.604	0.731
0.599	0.909	1.127	0.627	1.411	5.275	0.735	1.109	0.609	1.113	9.951	0.494	1.09	0.609	0.718
0.719	0.917	1.125	0.616	1.423	5.395	0.729	1.097	0.608	1.102	10.07	0.487	1.096	0.61	0.705
0.839	0.919	1.153	0.626	1.436	5.515	0.728	1.086	0.61	1.101	10.19	0.479	1.086	0.608	0.694
0.959	0.912	1.153	0.622	1.425	5.635	0.723	1.09	0.612	1.092	10.31	0.471	1.087	0.614	0.681
1.079	0.916	1.143	0.616	1.428	5.755	0.715	1.08	0.611	1.078	10.43	0.464	1.088	0.603	0.67
1.199	0.908	1.146	0.606	1.414	5.875	0.713	1.077	0.603	1.076	10.55	0.464	1.097	0.607	0.667
1.319	0.908	1.149	0.612	1.416	5.995	0.707	1.063	0.605	1.064	10.67	0.456	1.106	0.617	0.65
1.439	0.902	1.131	0.6	1.399	6.114	0.701	1.068	0.606	1.055	10.79	0.454	1.096	0.609	0.65
1.559	0.895	1.137	0.611	1.39	6.234	0.695	1.079	0.613	1.046	10.91	0.445	1.108	0.611	0.632
1.678	0.885	1.116	0.603	1.365	6.354	0.691	1.072	0.611	1.039	11.03	0.443	1.114	0.617	0.627
1.798	0.881	1.109	0.599	1.356	6.474	0.688	1.064	0.604	1.035	11.15	0.435	1.112	0.608	0.614
1.918	0.877	1.103	0.603	1.348	6.594	0.682	1.065	0.604	1.024	11.27	0.436	1.1	0.599	0.62
2.038	0.869	1.088	0.6	1.33	6.714	0.678	1.043	0.6	1.018	11.39	0.434	1.108	0.6	0.614
2.158	0.864	1.084	0.604	1.321	6.834	0.667	1.041	0.605	1.001	11.51	0.427	1.111	0.608	0.6
2.278	0.857	1.075	0.601	1.307	6.954	0.657	1.049	0.609	0.984	11.63	0.419	1.093	0.597	0.594
2.398	0.851	1.069	0.604	1.296	7.074	0.651	1.048	0.611	0.976	11.75	0.415	1.109	0.613	0.581
2.518	0.848	1.073	0.611	1.292	7.194	0.652	1.048	0.606	0.977	11.87	0.413	1.103	0.612	0.58
2.638	0.84	1.068	0.606	1.277	7.313	0.64	1.06	0.613	0.958	11.99	0.411	1.085	0.605	0.584
2.758	0.836	1.07	0.605	1.273	7.433	0.641	1.072	0.611	0.959	12.11	0.414	1.096	0.61	0.584
2.877	0.833	1.071	0.607	1.268	7.553	0.631	1.057	0.603	0.944	12.23	0.408	1.093	0.602	0.577
2.997	0.826	1.092	0.611	1.26	7.673	0.631	1.067	0.601	0.943	12.35	0.402	1.106	0.603	0.562
3.117	0.822	1.089	0.604	1.254	7.793	0.62	1.082	0.606	0.924	12.47	0.398	1.11	0.598	0.553
3.237	0.813	1.112	0.608	1.245	7.913	0.616	1.066	0.591	0.918	12.59	0.397	1.112	0.603	0.549
3.357	0.801	1.123	0.609	1.227	8.033	0.603	1.083	0.605	0.897	12.71	0.395	1.111	0.605	0.548
3.477	0.796	1.134	0.608	1.22	8.153	0.601	1.09	0.609	0.893	12.83	0.392	1.105	0.604	0.545
3.597	0.801	1.14	0.61	1.23	8.273	0.59	1.082	0.61	0.876	12.95	0.388	1.1	0.607	0.54
3.717	0.799	1.149	0.613	1.228	8.392	0.586	1.085	0.613	0.869	13.07	0.386	1.1	0.604	0.536
3.837	0.791	1.159	0.608	1.216	8.512	0.575	1.082	0.609	0.852	13.19	0.38	1.103	0.602	0.526
3.956	0.788	1.175	0.617	1.215	8.632	0.567	1.085	0.617	0.839	13.31	0.372	1.121	0.609	0.505
4.076	0.783	1.174	0.612	1.205	8.752	0.563	1.082	0.617	0.831	13.43	0.374	1.122	0.605	0.507
4.196	0.775	1.163	0.609	1.188	8.872	0.554	1.073	0.614	0.819	13.55	0.374	1.12	0.601	0.508
4.316	0.77	1.166	0.61	1.181	8.992	0.544	1.081	0.609	0.801	13.67	0.376	1.13	0.611	0.507
4.436	0.767	1.157	0.61	1.175	9.112	0.541	1.079	0.605	0.796	13.79	0.373	1.12	0.608	0.507
4.556	0.758	1.151	0.615	1.157	9.232	0.535	1.092	0.606	0.784	13.91	0.369	1.135	0.619	0.494

Table B.9. (Continue).

x/d	η	HTCR	Fn	NHFR	x/d	η	HTCR	Fn	NHFR
14.03	0.369	1.138	0.614	0.493	18.22	0.285	1.131	0.589	0.353
14.15	0.369	1.143	0.616	0.489	18.34	0.281	1.15	0.609	0.336
14.27	0.364	1.145	0.609	0.48	18.46	0.277	1.162	0.618	0.321
14.39	0.363	1.14	0.607	0.482	18.58	0.278	1.138	0.602	0.336
14.51	0.361	1.141	0.609	0.476	18.7	0.279	1.128	0.603	0.343
14.63	0.36	1.14	0.607	0.475	18.82	0.28	1.115	0.599	0.352
14.75	0.357	1.128	0.61	0.477	18.94	0.275	1.141	0.616	0.329
14.87	0.356	1.123	0.607	0.477	19.06	0.275	1.129	0.611	0.336
14.99	0.356	1.145	0.618	0.467	19.18	0.272	1.129	0.601	0.331
15.11	0.353	1.123	0.604	0.471	19.3	0.268	1.149	0.619	0.313
15.23	0.353	1.139	0.614	0.465	19.42	0.264	1.144	0.615	0.309
15.35	0.348	1.139	0.61	0.455	19.54	0.263	1.148	0.618	0.304
15.47	0.344	1.142	0.615	0.446	19.66	0.263	1.121	0.606	0.322
15.59	0.343	1.139	0.613	0.447	19.78	0.258	1.127	0.61	0.309
15.71	0.341	1.135	0.608	0.445	19.9	0.258	1.13	0.609	0.307
15.83	0.337	1.144	0.614	0.434	20.02	0.263	1.163	0.625	0.297
15.95	0.332	1.142	0.603	0.427	20.14	0.263	1.142	0.611	0.309
16.07	0.331	1.139	0.603	0.426	20.26	0.265	1.147	0.612	0.309
16.19	0.329	1.14	0.604	0.422	20.38	0.265	1.139	0.623	0.314
16.31	0.325	1.128	0.599	0.423	20.5	0.263	1.131	0.614	0.315
16.43	0.326	1.127	0.601	0.423	20.62	0.263	1.116	0.607	0.324
16.55	0.325	1.14	0.613	0.415	20.74	0.26	1.126	0.618	0.313
16.66	0.323	1.132	0.598	0.417	20.86	0.261	1.121	0.615	0.318
16.78	0.316	1.139	0.601	0.401	20.98	0.263	1.09	0.604	0.341
16.9	0.315	1.13	0.6	0.404	21.1	0.258	1.105	0.614	0.323
17.02	0.31	1.15	0.614	0.386	21.22	0.264	1.099	0.608	0.336
17.14	0.307	1.15	0.614	0.38	21.34	0.263	1.092	0.607	0.339
17.26	0.307	1.141	0.606	0.385	21.46	0.26	1.096	0.607	0.332
17.38	0.303	1.148	0.613	0.374	21.58	0.26	1.102	0.613	0.327
17.5	0.299	1.145	0.61	0.369	21.7	0.262	1.1	0.605	0.332
17.62	0.297	1.144	0.6	0.366	21.82	0.261	1.128	0.622	0.313
17.74	0.296	1.161	0.61	0.355	21.94	0.258	1.121	0.607	0.314
17.86	0.293	1.154	0.6	0.353	22.06	0.253	1.123	0.602	0.303
17.98	0.29	1.13	0.592	0.361	22.18	0.23	1.146	0.612	0.25
18.1	0.288	1.152	0.613	0.345					

Table B.10. Centerline downstream cooling data of Hybrid scheme Br = 1.5.

x/d	η	HTCR	Fn	NHFR	x/d	η	HTCR	Fn	NHFR	x/d	η	HTCR	Fn	NHFR
0	0.852	1.129	0.61	1.313	4.676	0.857	1.163	0.615	1.332	9.352	0.626	1.094	0.611	0.933
0.12	0.903	1.136	0.618	1.403	4.796	0.857	1.176	0.621	1.335	9.471	0.615	1.11	0.611	0.913
0.24	0.793	1.135	0.615	1.215	4.916	0.841	1.176	0.622	1.307	9.591	0.609	1.104	0.61	0.904
0.36	0.96	1.146	0.627	1.505	5.035	0.829	1.16	0.619	1.283	9.711	0.604	1.089	0.611	0.898
0.48	0.975	1.135	0.622	1.525	5.155	0.837	1.143	0.617	1.293	9.831	0.592	1.086	0.61	0.878
0.599	0.981	1.146	0.627	1.54	5.275	0.828	1.146	0.629	1.278	9.951	0.588	1.09	0.61	0.871
0.719	0.978	1.154	0.63	1.54	5.395	0.824	1.112	0.611	1.262	10.07	0.58	1.095	0.61	0.858
0.839	0.985	1.172	0.627	1.56	5.515	0.826	1.121	0.625	1.268	10.19	0.566	1.087	0.61	0.836
0.959	0.983	1.189	0.638	1.564	5.635	0.822	1.096	0.613	1.256	10.31	0.555	1.089	0.61	0.818
1.079	0.987	1.155	0.623	1.556	5.755	0.81	1.093	0.614	1.235	10.43	0.55	1.094	0.61	0.808
1.199	0.976	1.178	0.636	1.547	5.875	0.808	1.09	0.612	1.232	10.55	0.547	1.1	0.61	0.803
1.319	0.975	1.155	0.619	1.535	5.995	0.802	1.085	0.612	1.22	10.67	0.537	1.11	0.61	0.784
1.439	0.973	1.171	0.636	1.538	6.114	0.798	1.087	0.614	1.214	10.79	0.533	1.098	0.61	0.78
1.559	0.973	1.17	0.636	1.538	6.234	0.791	1.085	0.613	1.202	10.91	0.523	1.11	0.61	0.76
1.678	0.956	1.127	0.618	1.49	6.354	0.789	1.093	0.619	1.2	11.03	0.517	1.116	0.61	0.749
1.798	0.957	1.141	0.631	1.497	6.474	0.788	1.091	0.62	1.198	11.15	0.51	1.113	0.61	0.738
1.918	0.958	1.11	0.616	1.485	6.594	0.781	1.073	0.612	1.183	11.27	0.507	1.116	0.61	0.733
2.038	0.949	1.109	0.625	1.469	6.714	0.775	1.064	0.613	1.173	11.39	0.504	1.109	0.61	0.729
2.158	0.947	1.094	0.621	1.459	6.834	0.764	1.061	0.614	1.155	11.51	0.496	1.112	0.61	0.715
2.278	0.94	1.085	0.617	1.446	6.954	0.757	1.05	0.61	1.142	11.63	0.488	1.106	0.61	0.703
2.398	0.936	1.079	0.617	1.436	7.074	0.748	1.052	0.611	1.129	11.75	0.485	1.11	0.611	0.698
2.518	0.935	1.079	0.617	1.435	7.194	0.755	1.069	0.617	1.141	11.87	0.478	1.104	0.61	0.688
2.638	0.922	1.087	0.623	1.416	7.313	0.737	1.071	0.613	1.113	11.99	0.475	1.092	0.61	0.686
2.758	0.923	1.074	0.613	1.414	7.433	0.738	1.075	0.611	1.116	12.11	0.476	1.1	0.612	0.686
2.877	0.924	1.086	0.62	1.42	7.553	0.734	1.077	0.611	1.109	12.23	0.469	1.099	0.61	0.674
2.997	0.917	1.115	0.625	1.418	7.673	0.731	1.078	0.611	1.104	12.35	0.462	1.113	0.612	0.658
3.117	0.911	1.107	0.621	1.406	7.793	0.719	1.085	0.611	1.086	12.47	0.456	1.123	0.611	0.645
3.237	0.904	1.117	0.614	1.398	7.913	0.71	1.091	0.614	1.071	12.59	0.452	1.12	0.61	0.64
3.357	0.894	1.133	0.616	1.385	8.033	0.698	1.087	0.611	1.052	12.71	0.447	1.119	0.61	0.631
3.477	0.888	1.168	0.63	1.388	8.153	0.698	1.097	0.613	1.052	12.83	0.446	1.108	0.611	0.633
3.597	0.891	1.183	0.634	1.398	8.273	0.69	1.092	0.611	1.038	12.95	0.442	1.103	0.611	0.629
3.717	0.893	1.16	0.617	1.394	8.392	0.687	1.089	0.613	1.033	13.07	0.433	1.111	0.615	0.61
3.837	0.883	1.175	0.619	1.381	8.512	0.679	1.089	0.613	1.02	13.19	0.43	1.108	0.612	0.606
3.956	0.876	1.184	0.615	1.373	8.632	0.671	1.088	0.611	1.007	13.31	0.418	1.134	0.616	0.578
4.076	0.873	1.19	0.619	1.369	8.752	0.663	1.086	0.612	0.995	13.43	0.421	1.126	0.61	0.584
4.196	0.866	1.18	0.615	1.353	8.872	0.652	1.079	0.611	0.976	13.55	0.42	1.129	0.614	0.582
4.316	0.867	1.176	0.615	1.354	8.992	0.644	1.085	0.611	0.963	13.67	0.421	1.146	0.618	0.577
4.436	0.863	1.166	0.615	1.343	9.112	0.643	1.083	0.61	0.962	13.79	0.419	1.127	0.613	0.581
4.556	0.854	1.16	0.613	1.326	9.232	0.633	1.094	0.611	0.945	13.91	0.413	1.145	0.615	0.564

Table B.10. (Continue).

x/d	η	HTCR	Fn	NHFR	x/d	η	HTCR	Fn	NHFR
14.03	0.413	1.142	0.611	0.566	18.22	0.341	1.152	0.61	0.436
14.15	0.414	1.148	0.61	0.564	18.34	0.334	1.16	0.611	0.42
14.27	0.41	1.152	0.614	0.557	18.46	0.333	1.16	0.608	0.419
14.39	0.409	1.151	0.615	0.554	18.58	0.333	1.152	0.61	0.423
14.51	0.405	1.148	0.614	0.549	18.7	0.331	1.136	0.61	0.429
14.63	0.406	1.146	0.613	0.552	18.82	0.332	1.122	0.609	0.436
14.75	0.403	1.139	0.614	0.55	18.94	0.33	1.141	0.61	0.423
14.87	0.402	1.125	0.611	0.553	19.06	0.327	1.134	0.61	0.422
14.99	0.402	1.15	0.613	0.544	19.18	0.326	1.129	0.609	0.423
15.11	0.397	1.129	0.61	0.544	19.3	0.322	1.151	0.61	0.404
15.23	0.399	1.152	0.616	0.537	19.42	0.314	1.135	0.61	0.4
15.35	0.392	1.155	0.617	0.523	19.54	0.312	1.13	0.611	0.4
15.47	0.391	1.15	0.61	0.524	19.66	0.311	1.121	0.61	0.402
15.59	0.389	1.149	0.611	0.522	19.78	0.303	1.124	0.61	0.387
15.71	0.388	1.14	0.611	0.523	19.9	0.306	1.118	0.606	0.395
15.83	0.381	1.156	0.613	0.505	20.02	0.307	1.15	0.611	0.38
15.95	0.38	1.157	0.611	0.502	20.14	0.303	1.136	0.61	0.38
16.07	0.378	1.151	0.614	0.501	20.26	0.303	1.14	0.61	0.378
16.19	0.377	1.142	0.611	0.504	20.38	0.299	1.136	0.61	0.374
16.31	0.373	1.135	0.611	0.5	20.5	0.294	1.121	0.61	0.373
16.43	0.374	1.138	0.612	0.5	20.62	0.295	1.107	0.61	0.382
16.55	0.373	1.147	0.611	0.495	20.74	0.286	1.116	0.61	0.362
16.66	0.371	1.142	0.612	0.493	20.86	0.288	1.113	0.613	0.368
16.78	0.366	1.157	0.614	0.477	20.98	0.283	1.09	0.611	0.373
16.9	0.364	1.143	0.612	0.48	21.1	0.281	1.108	0.616	0.359
17.02	0.359	1.16	0.611	0.464	21.22	0.283	1.099	0.611	0.368
17.14	0.359	1.156	0.611	0.467	21.34	0.276	1.096	0.613	0.359
17.26	0.359	1.162	0.614	0.463	21.46	0.277	1.102	0.614	0.356
17.38	0.358	1.158	0.612	0.463	21.58	0.273	1.11	0.615	0.345
17.5	0.353	1.153	0.611	0.457	21.7	0.275	1.136	0.631	0.333
17.62	0.348	1.158	0.61	0.447	21.82	0.276	1.139	0.616	0.332
17.74	0.35	1.165	0.612	0.446	21.94	0.271	1.128	0.613	0.33
17.86	0.345	1.16	0.611	0.441	22.06	0.271	1.137	0.614	0.325
17.98	0.344	1.157	0.611	0.439	22.18	0.238	1.149	0.623	0.261
18.1	0.342	1.159	0.611	0.436					

Table B.11. Laterally averaged downstream cooling data of Hybrid scheme.

Br = 0.5					Br = 1.0					Br = 1.5				
x/d	η	HTCR	Fn	NHFR	x/d	η	HTCR	Fn	NHFR	x/d	η	HTCR	Fn	NHFR
1	0.494	1.096	0.578	0.716	1	0.446	1.104	0.583	0.635	1	0.631	1.178	0.622	0.937
2	0.457	1.068	0.585	0.664	2	0.426	1.077	0.591	0.612	2	0.616	1.129	0.621	0.914
3	0.389	1.054	0.584	0.56	3	0.402	1.071	0.594	0.574	3	0.595	1.108	0.617	0.88
4	0.334	1.079	0.584	0.461	4	0.375	1.098	0.595	0.52	4	0.576	1.131	0.615	0.847
5	0.306	1.064	0.585	0.425	5	0.35	1.084	0.597	0.486	5	0.557	1.113	0.614	0.816
6	0.267	1.043	0.589	0.374	6	0.325	1.06	0.599	0.458	6	0.536	1.088	0.616	0.786
7	0.25	1.032	0.588	0.355	7	0.302	1.05	0.599	0.425	7	0.51	1.073	0.613	0.748
8	0.225	1.048	0.583	0.306	8	0.271	1.072	0.597	0.364	8	0.485	1.099	0.612	0.7
9	0.195	1.038	0.583	0.266	9	0.251	1.067	0.6	0.335	9	0.451	1.09	0.613	0.647
10	0.17	1.038	0.582	0.227	10	0.249	1.068	0.6	0.331	10	0.423	1.09	0.613	0.602
11	0.133	1.039	0.577	0.169	11	0.231	1.076	0.598	0.297	11	0.394	1.103	0.612	0.55
12	0.117	1.033	0.571	0.149	12	0.212	1.079	0.597	0.264	12	0.377	1.11	0.614	0.518
13	0.086	1.028	0.56	0.104	13	0.203	1.088	0.593	0.243	13	0.36	1.129	0.615	0.48
14	0.041	1.015	0.541	0.047	14	0.194	1.098	0.586	0.221	14	0.349	1.15	0.613	0.452
					15	0.199	1.111	0.589	0.22	15	0.34	1.156	0.612	0.434
					16	0.169	1.093	0.587	0.183	16	0.328	1.142	0.613	0.419
					17	0.163	1.099	0.584	0.17	17	0.319	1.153	0.614	0.399
					18	0.152	1.108	0.584	0.146	18	0.31	1.165	0.614	0.376
					19	0.144	1.081	0.582	0.153	19	0.303	1.138	0.613	0.38
					20	0.127	1.074	0.575	0.13	20	0.294	1.146	0.614	0.359
					21	0.095	1.035	0.575	0.111	21	0.286	1.104	0.614	0.37
					22	0.11	1.065	0.577	0.112	22	0.283	1.131	0.613	0.349